ABENGOA
RESEARCH

Compositional engineering of perovskites and charge dynamics studies for solar cells applications

Author: *Manuel Salado Manzorro*

Director:	Co-Director:	Tutor:
Dr. Shahzada Ahmad	Dr. Samrana Kazim	Dr. J. A. Anta Montalvo

University Pablo de Olavide

September 2017

The present dissertation complies with all the requirements established by the "Normativa de estudios oficiales de doctorado Universidad Pablo de Olavide de Sevilla (RD 99/2011)" to be a thesis as a compendium of the Publications 1, 2, 3, 4, 5,6 and 7 (in Part IV of this document). All of them published during my doctoral period in the Ph.D. Program in Biotechnology, Engineering and Chemical Technology of the University Pablo de Olavide.

Dedicado a
mi familia

Resumen

Esta memoria recoge un extenso estudio sobre las celdas solares de perovskita (CSP). Después de un período de investigación de aproximadamente 60 años, la tecnología utilizando perovskitas híbridas metal-orgánicas ha revolucionado el campo de la fotovoltaica tras alcanzar eficiencias por encima del 22% debido principalmente a sus excelentes propiedades optoelectrónicas y a un proceso de fabricación de bajo coste. Los dispositivos fotovoltaicos de perovskita se componen generalmente de varias capas, por lo que, para la obtención de altas eficiencias es necesario optimizar no solo los distintos materiales que componen cada capa sino también su espesor. Además, este material permite la modificación de sus propiedades cuando se incorpora o intercambian tanto los cationes orgánicos como los iones haluro. Una variación en la composición química puede resultar en un incremento de absorción y en las propiedades ópticas de la perovskita. Sin embargo, una de las principales desventajas que presenta este material es su degradación en condiciones ambientales, que se puede ver acelerada cuando además de la humedad, está expuesto a altas temperaturas o alta iluminación. En este contexto general, el primer capítulo de esta memoria se focaliza en el estudio de las capas adicionales para la extracción de cargas. Aunque el material de perovskita presenta un carácter ambipolar, (la capacidad de transportar tanto huecos como electrones), generalmente se utilizan capas adicionales transportadoras de huecos y electrones respectivamente que favorecen la extracción de cargas disminuyendo así la recombinación. En esta memoria, se investigaron varios materiales transportadores de huecos, desde polímeros semiconductores a pequeñas moléculas orgánicas y se examinó cómo afectan los distintos niveles energéticos, las propiedades transportadoras de carga, el contacto entre interfaces y su degradación. Por otro lado, el material comúnmente utilizado para la extracción de electrones consiste en nanopartículas de TiO_2 depositadas por técnicas en disolución (spin-coating). Con el objetivo de obtener una deposición homogénea y controlada, en este trabajo se utilizó la técnica de deposición física en fase vapor (PVD-OAD), Con esta técnica es posible variar el ángulo de incidencia para depositar nanocolumnas verticales 1D. Éstas estructuras 1D resultaron incrementar no solo la extracción de carga (y así la eficiencia) sino también la estabilidad frente a la estructura mesoporosa 3D. En el segundo capítulo, se realizó un estudio de la estabilidad de las fases, la morfología de la capa de perovskita, la histéresis, y el rendimiento general de los dispositivos en función de la composición química de la perovskita. Además, el empleo de la técnica de deposición de un solo paso con la adición de un disolvente apolar conlleva una mejora en la estructura cristalina de la perovskita. Ello disminuye las fronteras de grano y la recombinación lo cual mejora de manera notable la eficiencia de los dispositivos.

El objetivo final de esta tesis es la fabricación de celdas solares de perovskitas eficientes y estables, así como la comprensión de su funcionamiento a nivel fundamental. Por este motivo en el tercer capítulo se realizó un estudio del impacto de la degradación en los dispositivos. Para ello, las muestras con diferentes composiciones químicas de perovskita y diferentes materiales transportadores de huecos se expusieron a altos porcentajes de humedad y se estudiaron sus modificaciones tanto morfológicas como su variación en la dinámica de cargas. Se concluyó que aunque los materiales poliméricos presentan una mayor resistencia a la degradación por humedad, la acumulación de carga en la interfaz HTM/perovskita, puede generar una degradación más rápida. Además, como posible solución para evitar la degradación del material de perovskita, en el cuarto y último capítulo se introdujo como dopante un líquido iónico prefluorinado que posee un carácter hidrofóbico. Tras la adición y optimización de este dopante, se consiguieron capas de perovskita que eran estables más de 100 días cuando se expusieron a altos índices de humedad.

Abstract

In this dissertation a comprehensive study on hybrid organic-inorganic perovskite solar cells (PSCs) has been carried out. After sixty years of extensive research on photovoltaic (PV),PSCs has emerged and revolutionized the PV field during the last 6 years,due to its outstanding opto-electronics properties with efficiencies over 22%,and cost-effective fabrication process. PSCs has stacks of layers, thus to harvest maximum sunlight and to achieve the best performance from the devices,layers optimization in with ideal materials and thickness needs to be designed. Moreover, the active layer perovskites can be tuned with the incorporation of different organic cations or mixture of halide anion. A variation in the perovskite composition enhances its electro- optical properties. Nevertheless, one of the main drawbacks of this new born technology is the fast degradation under ambient conditions which further accelerated when other external factors such as heat or light are involved. In this context, the first chapter of this work will focus on the effect of different charge selective layers i.e. electron and hole selective layers. Although perovskite has ambipolar character, charge extraction layers are used to reduce recombination rate. For studying the effect of hole selective layer, several hole transport materials such as semiconducting polymers or organic small molecules were investigated to examine the energy level, alignment, nature of the molecules, charge transporting properties, interfacial contact and degradation. On the other hand, for electron transport layer mainly mesoporous structure made from inorganic metal oxides nanoparticles, mainly TiO_2, is being used and deposited through solution process techniques.We have undertaken physical vapour deposition at oblique angle incidence (PVD-OAD) technique to obtain a homogeneous deposition over large area and 1D-nanoforest like structure of TiO_2, which exhibits improved charge extraction as well as stability compare to 3D-mesoporous layer. In the second chapter, we have investigated phase stability, morphology of the perovskite layer, hysteresis behaviour in current–voltage curve, and overall performance by tuning the chemical composition. Employing one-step deposition method using anti-solvent entails an improvement of perovskite crystal structure, minimizing grain boundaries and charge recombination. Thus, it was considered as an important breakthrough to increase device efficiency. The ultimate goal of this thesis is the fabrication and understanding of efficient and stable PSCs. Thus, in the third chapter, a degradation study was carried out. For this purpose, samples of different perovskite composition as well as hole transport materials were exposed to high humidity conditions. Microscopy and spectroscopy techniques were employed to unravel first, morphologic degradation processes and second charge dynamics effect in degraded solar cells. Additionally, to overcome stability issue, in chapter four we have described the use of hydrophobic dopant such as perfluorinated compounds. They were added to perovskite precursor's solution and an increment in the device stability of over 100 days under ambient atmosphere was found.

Contents

Part I
Introduction

1 Introduction

1.1 General context: energy production

Global energy consumption is continuously increasing due to the population growth and fast-paced industrialization in recent decades. However, almost 90% of the current energy production is based on fossil fuels such as oil, coal and natural gas[1]. The growing concerns towards global warming together with fossil fuels limited sources are the main reasons in order to shift from fossil fuels to renewable energy sources[2]. In this context, renewable energies (hydro, marine, wind, solar, geothermal and bioenergy) are gradually replacing conventional fuels, while solar technology being the one the best bet.

1.2 Solar energy

Solar energy, which is in abundant and sustainable source of energy, has attracted enormous interest in terms of research and development during last decades. Although solar photovoltaic (PV) and onshore wind together represent in the last year 75% of global renewable electricity capacity,[3] the difficulty has always been converting solar energy in an efficient and cost-effective way. Nevertheless, this trend is changing not only due to the developments in emerging PV technology which are taking place at a rapid pace, but also due to government's commitment. As examples, India's solar power prices have fallen at May 2017 to 0.014 € per kilowatt hour[4], China is set to build a giant solar power station in the Gobi desert, which could generate enough energy to supply one million homes[5] or France who plan to triple its PV energy production before year 2023[6].

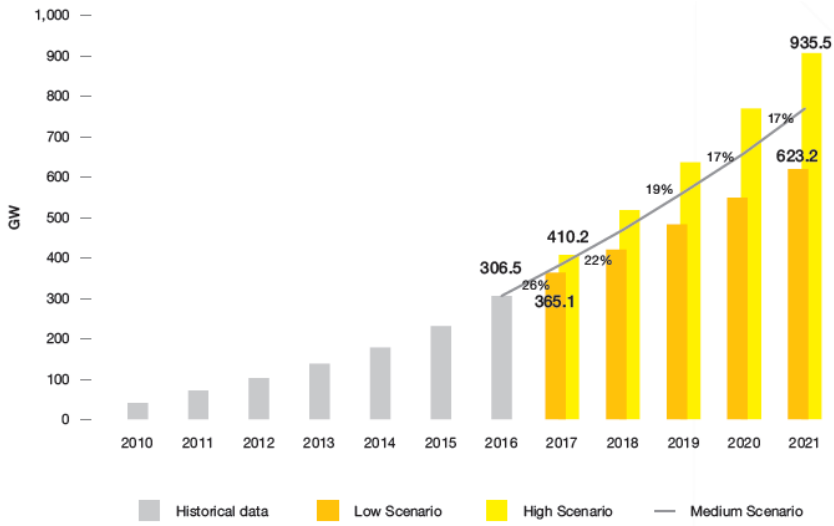

Figure 1: World total solar PV market scenarios 2017 - 2021.[7]

1.3 Progress in photovoltaic technology

Since the discovery of the PV effect by Ed Becquerel in 1839[8], several ways have been investigated for the conversion of light into electrical energy.[9] PV devices are the most promising route, which converts directly photons into electricity.The uses of semiconductors that absorb light in the solar spectrum region have been the most successful. Among them,only those semiconducting materials are being considered who can generate free carriers or excitons when exposed to photons with energies above their optical band gap. These charges, once separated are propagated through the device and extracted at the contacts, generating electricity[10].

1.3.1 Evolution: 1st, 2nd and 3rd generation

Historically, the development of PV technology has gone through numerous changes resulting in different kinds of cells that can be placed into different generations.

Silicon solar cells, known as first generation PV cells, are currently dominant in the PV with efficiencies (PCE) close to 25%. However, its high production cost, is partially compensated through government subsidies, this is due to high usage of materials(>200 microns), for being an indirect band gap semiconductor limits their large-scale application[11].

The search for alternatives to silicon has generated a second generation technologies based on thin film solar cells that reduce significantly the manufacturing cost. Among them, semiconductors such as cadmium telluride (CdTe) or copper indium gallium selenide (CIGS) achieved efficiencies close to (22.6%), comparable to mono-crystalline Si, but with the usage of exotic material[12]. The challenge was to push the efficiency further,with the use of vacuum manufacturing techniques,however the high material cost of indium limits its large-scale production.Solar cells based on the kesterite mineral structure, including Cu_2ZnSnS_4(CZTS), $Cu_2ZnSnSe_4$(CZTSe)are being explored as thin-film PV candidates as they are earth-abundant and non toxic elements.[13] However, its low V_{OC}due to high rate of recombination or poor optimized interface entails modest efficiency value such as 13.8% reported in 2016 for small-area device.[14] In the last decades, a “new concept” in PV cells based on nanostructured materials which are inexpensive and can be solution processes made great progress. The usage of low cost organic materials with high optical absorption placed them in a third generation category. In addition, Dye-sensitized solar cell (DSSCs) introduced by Grätzel[15] reduces the material quality requirements necessary with Si solar cells, owing to the separate transport of photo-generated electrons and holes in different materials. However, organic sensitizers[16] have been limited by their low light-harvesting ability and poor lifetime stability.

In order to replace conventional organic-type sensitizers, inorganic semiconductor suchas quantum dots[17] or extremely thin absorber (ETA) solar cells[18] were investigated.

Recently, the emergence and development of organic–inorganic halide PSCs have sparked tremendous research interest, dueto their ideal combination of high efficiency and low cost solution based fabrication process.

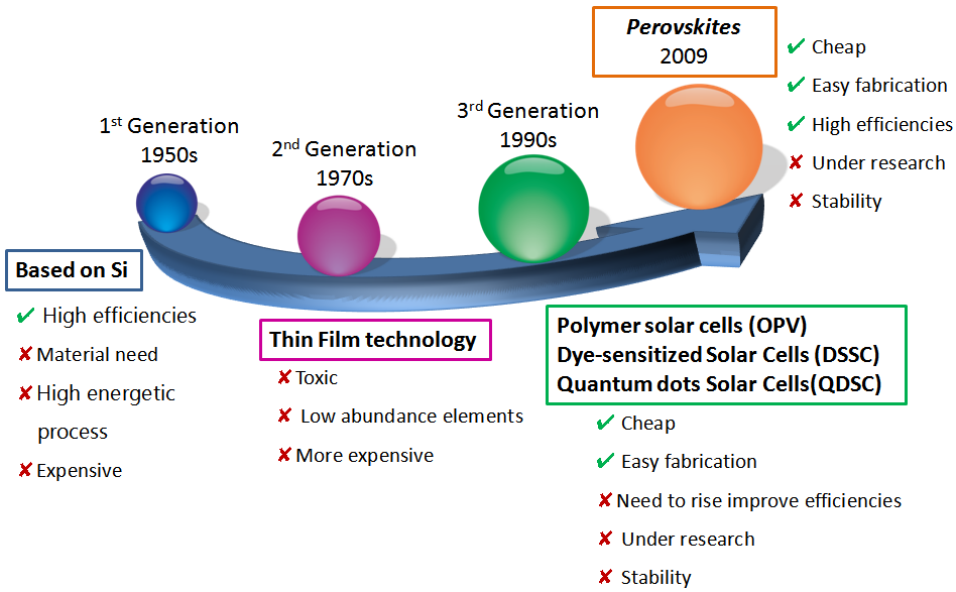

Figure 2: Evolution of photovoltaic technology.

1.3.2 Perovskite solar cell

Presently, organic-inorganic halide perovskite solar cells have been the most significant development in the field of photovoltaics in recent decades and are the competitive candidate to fulfil the need for high efficiencies at low cost.

Though perovskite-structure based hybrid halide compounds were studied by Weber in 1978[19] it was not recognised as PV materials untill 2009, when Miyasaka et al.[20] introduced methyl ammonium lead halide based perovskiteas sensitizers in a liquid electrolyte based DSSCs, obtaining a PCE of 3.8%. The devices suffered from stability and reproducibility issues due to the rapid dissolution of perovskite nanoparticles into the liquid electrolyte. In 2011, Park et al.[21] reported a higher PCE of 6.5% optimizing TiO_2 film thickness and electrolyte formulation. In a subsequent year, the efficiency was pushed to 9.7% by replacing the liquid with a solid-state hole-transporting material,while improving cell stability[22] significantly.

Since then, there has been a huge research effortin the PSCs field.In 2015, Yang et al.[23] achieved an impressive efficiency of 20.2% using an intermolecular exchange in formamidinium leadiodide ($FAPbI_3$). More recently, Saliba et al.[24] also attained a stabilized efficiency of 21.1% with the use of a mixture of Cs/MA/FA triple cation. Nevertheless, the best efficiency of 22.1% was obtained by KRICT group[25] which can be seen in NREL chart (see figure 3).

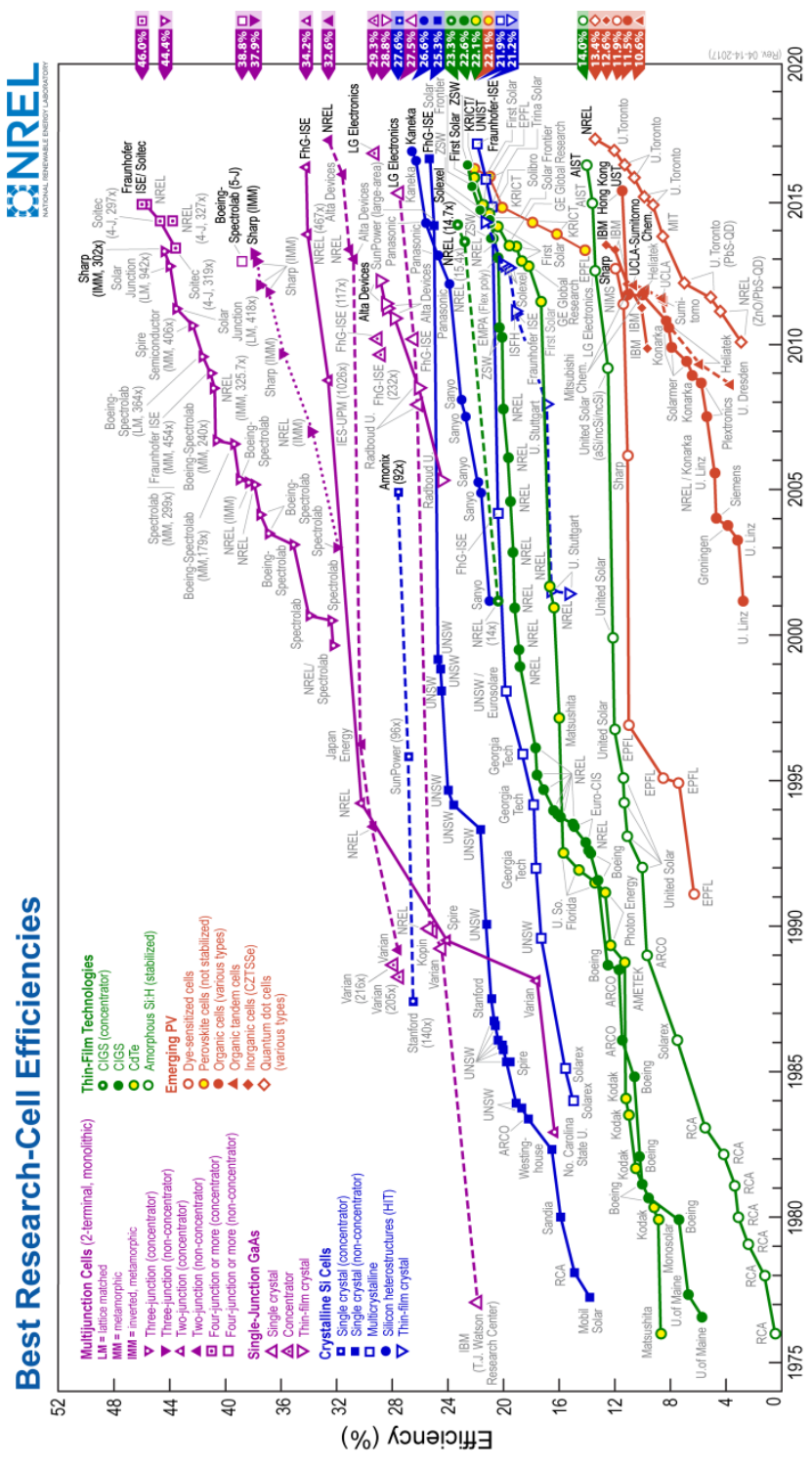

Figure 3: Best research-cell efficiencies chart for different PV technologies. Taken from www.nrel.gov[26].

Part II
Motivation and scope of this thesis

2 Motivation and scope of this thesis

The arrival of metal halide perovskite in the PV field has made revolution in terms of high efficiency and low-cost fabrication process. This material has unique advantages such as better opto-electronic properties, easy processability, being solution-processable as well as power conversion efficiency close to crystalline silicon. Despite, the technological progresses reported, some issues as the intrinsic mechanism of this material or the long-term stability under operating conditions are still under debate.The understanding of such processes is a key milestone in order to exploit this technology in real-world scenarios. The main purpose of this thesis is to unravel the whole process of a perovskite based solar cell in order to fabricate highly efficient and stable devices. For this, the thesis would be divided in four different chapters:

1.- Selective layers can introduce additional path for recombination as well as favor the charge extraction process, therefore **the study of their effect in the functioning of the cell** is a keystone to understand and improve the performance of the devices. Publications summarized for this purpose are:

- "Interface play between Perovskite and Hole Selective Layer on the Performance and Stability of Perovskite Solar Cells"

- "1-dimensional TiO_2 nano-forests as photo-anodes for efficient and stable perovskite solar cells fabrication"

2.-One of the striking properties of perovskite material is the possibility to tune its opto-electronic properties by varying the halide as well as the organic cation composition and nature. For this, **a complete study was carried out to modify perovskite composition**. Publications derived from this purpose are:

- "Influence of mixed organic cation ratio in lead iodide based perovskite on the performance of solar cells"

- " Identifying the charge generation process in a Cs^+ - based triple cation mixed perovskite solar cell"

3.- Long-term stability has become one of the key factors for up-scaling and future commercialization of perovskite solar cells. Although the degradation mechanism is not fully understood yet, many efforts have been undertaken to improve the devices stability. In this chapter, **the degradation mechanism was studied**.

- "Impact of moisture on efficiency-determining electronic processes in perovskite solar cells"

4.- Additionally, **possible future alternative for highly stable devices** were presented. The use of perfluorinated compounds as dopants in perovskite solar cells increases their stability over 100 days. Publications selected for this purpose are:

- "Extending the Lifetime of Perovskite Solar Cells using a Perfluorinated Dopant"

- "Towards extending solar cells life time: addition of a fluorous cation to triple-cation based perovskite films"

Part III
Theoretical background

3 Theoretical background

Photovoltaic energy conversion can be defined as the direct conversion of light into electricity. This was made possible due to advance materials has the capability of absorbing photons from light and releasing electrons. Generally, photovoltaic energy conversion takes place in following two steps:

- A light absorption process which causes the generation of an electron-hole pair in the absorbing material.

- A discriminating charge separation mechanism, which splits electrons (negative charges) to one contact (anode) and holes (positive charges) to the other contact (cathode).

3.1 Solar spectrum

The Sun, situated at the centre of our solar system is responsible for the Earth's climate and weather. It generates energy which fulfils the solar system; however, not the entire direct sunlight incident on earth's atmosphere (1.37 kilowatts per square meter (kW/m^2) (AM0)) arrives at the earth's surface (AM1.5G). There are many factors affecting the amount of radiation on earth that must be taken into account: absorption (X-Ray and UV), scattering,or reflection on the surface, for example.

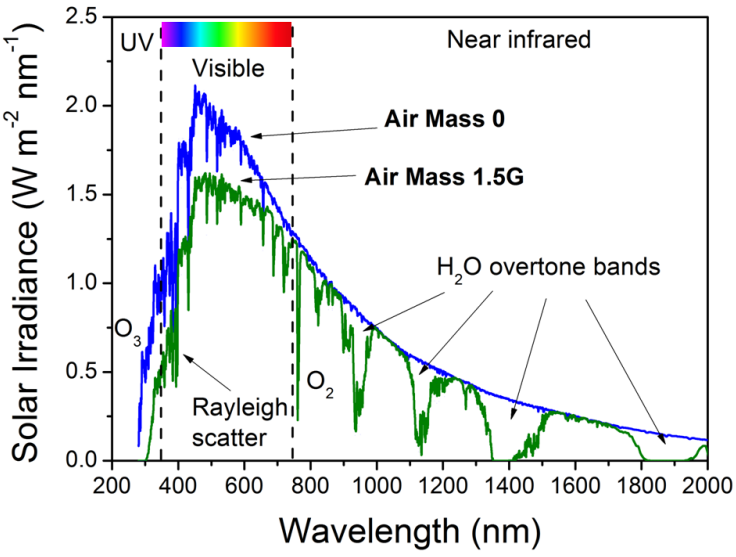

Figure 4: In blue solar spectrum at the top of atmosphere (Air Mass 0), while in green solar spectrum at Earth's surface for temperate zones (Air Mass 1.5). Modified from ASTM E-49027[27] and ASTM G-173-0328[28] respectively.

3.2 Physics in solar cells

Bonds between atoms in a crystal as well as electric transport phenomena are due to interactions between electrons, in particular those farthest from the nucleus, with electrons from other atoms determining the way in which like or dissimilar atoms combine creating a field of accessible levels (band). At T = 0K, those electrons (valence electrons) fill the lower energy band, termed valence band (VB). On the other hand, the upper energetic allowed levels in a band are known as conduction band (CB). (figure 5)

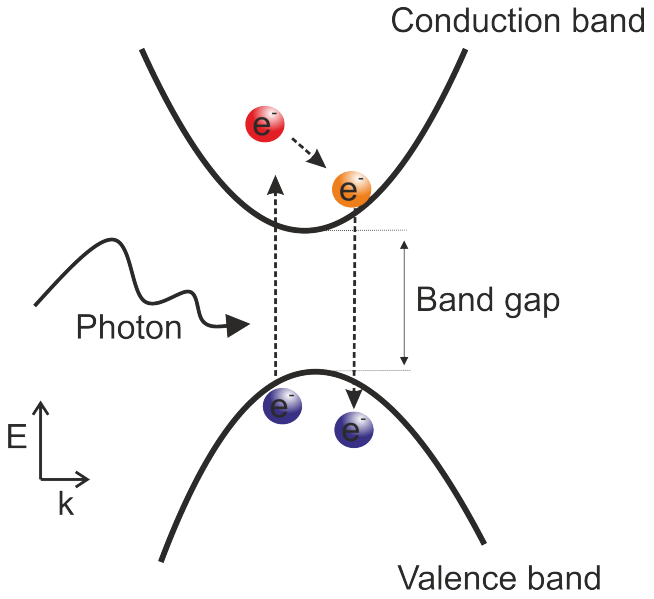

Figure 5: Excitation mechanism of an electron from the valence band (VB) to the conduction band (CB) by the absorption of a photon. The thermalization and recombination dynamics are also reported. Adapted from[29]

Earlier it was noted that the absorption of light entails the generation of an electron-hole pair. At an energy that is specific to the material and its atomic structure, light can produce an electron from its atomic bond rather than just making the bond to vibrate.In this context, a band gap is defined as a separation in energy between the highest occupied state (valence band, VB) and the lowest unoccupied state (conduction band, CB). Depending on the value of this band gap, different types of materials can be classified. An ideal crystalline semiconductor, the presence of a band gap (0.5-3 eV), allow the conversion of energy in the sunlight into usable electric energy. In this type of materials, when an electron is excited it quickly decays to the minimum energy of the conduction band (femtoseconds time process), however radiative recombination to the valence band occurs with a slower mechanism (microseconds time process) giving enough time to the solar cell to extract the electron.

Nevertheless, this process will not take place in conducting materials as it has no band gap (0 eV), thus it is not possible to collect excited electrons neither in insulating materials as its band gap is too big (≈3 eV) that will require high energy to excite the electron. Since the Sun's spectrum has a wide variety of energies and intensities (figure 4), the key is to match a material and its characteristic band gap energy with the solar spectrum so that the maximum amount of energy falls just above the characteristic energy.

3.3 Generation and Recombination processes

The two processes which generally rule the functioning of a solar cell are the electronic excitation of electrons by photons (photo-generation) and the electronic relaxation of free charges (recombination). Generation process starts with the absorption of a photon and the promotion of an electron from the VB to the CB, creating an electron-hole pair, while desirable recombination is the decay of the electron from the CB back to the lower energy state. Photons with energy higher than the band gap promote electrons to the conduction band with an excess of energy (figure 5).This is lost in a fast thermalization process, which relaxes the electron to the minimum energy of the conduction band. On the other hand charge-carrier relaxation dynamics play an important role in the electronic device as the carrier lifetime limits the time available to extract charges before recombination occurs. Recombination process includes one or more mechanisms that reduce the number of mobile electrons and holes. Generally, there are two kind of recombination: radiative and non-radiative. Recombination mechanisms include:

- Monomolecular recombination (k_1) (non-radiative): indirect recombination through a recombination center (e.g., an electron captured by a recombination center and then recombined with a hole, each process involving only one carrier). Depending on the nature of the recombination center, it can be classified into:

    *Shockley–Read–Hall (SRH) recombination: due to deep traps.
    *Surface recombination: interfaces.

- Bimolecular recombination (k_2) (radiative): direct band-to-band recombination, where an electron drops back down to its equilibrium energy band and radiates a photon

- Trimolecular recombination (k_3) (non-radiative): a three-body collision in the Auger intrinsic recombination[30] (in which one electron in the conduction band recombines with a hole in the valence band and the energy released is taken up by a third particle-electron). This energy can be used to promote an electron to a higher energy band or just emitting the energy as a phonon.

The decay of free-charge- carrier density n(t) in terms of different contributing mechanisms can be expressed as

$$\frac{dn}{dt} = -k_3 n^3 - k_2 n^2 - k_1 n \tag{1}$$

where, k1, k2 and k3 correspond to the rate constants associated to monomolecular, bimolecular and trimolecular recombination mechanisms, respectively.

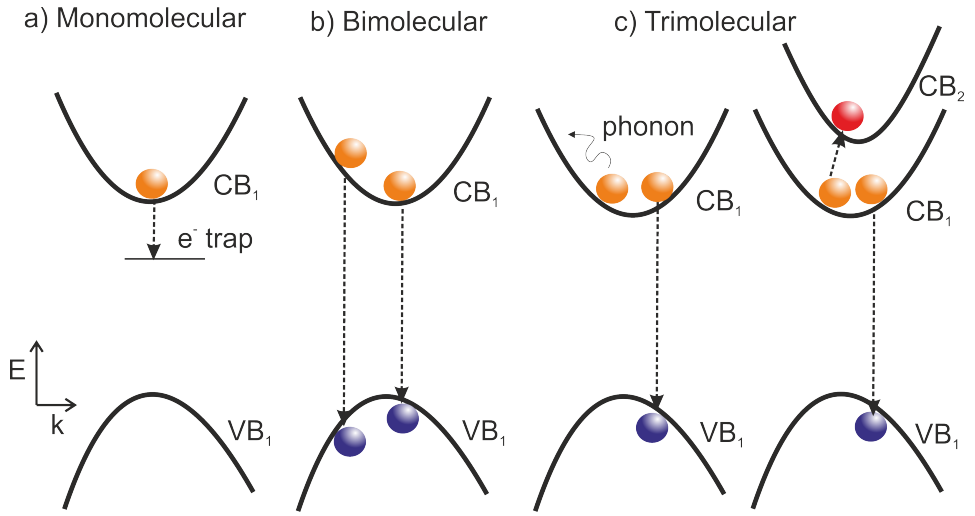

Figure 6: Schematic diagram indicating recombination mechanisms active in organic-inorganic metal halide perovskites.(a) trap-assisted recombination (b) bimolecular recombination (c) trimolecular or Auger recombination. Abbreviations: CB, conduction band; VB, valence band. Adapted from [31]

3.4 Current-Voltage (J-V) characteristics

As discussed in section 3.1, the generation of photocurrent occurs when an electron-hole pair is generated by absorption of a photon and then the charges are separated and collected forward in the selective contacts. Nevertheless, photocurrent also depends on the incident solar spectrum (figure 4), which due to its lack of uniformity, spectrum losses, non-radiative recombination and so on, reduces the maximum theoretical efficiency to 33.7% in the case of single junctions (p-n) solar cells as calculated by Schockley-Queisser.[32]

Generally a solar cell is considered as a diode, in an ideal case because it favours the current flow only in one direction. It behaviour can be described through an equivalent electrical circuit (like the one showed in figure 7,(black part). Theoretically in an ideal diode, the current absorbed by a device when a direct potential is applied between the two contacts, can be expressed as

$$I_D = I_0 * (e^{\frac{qV}{K_B T}} - 1) \tag{2}$$

Where, I_0 is defined as the saturation current density, q is the elementary charge in Coulombs, k_B is the Boltzmann's constant and T is the temperature in Kelvin degrees.

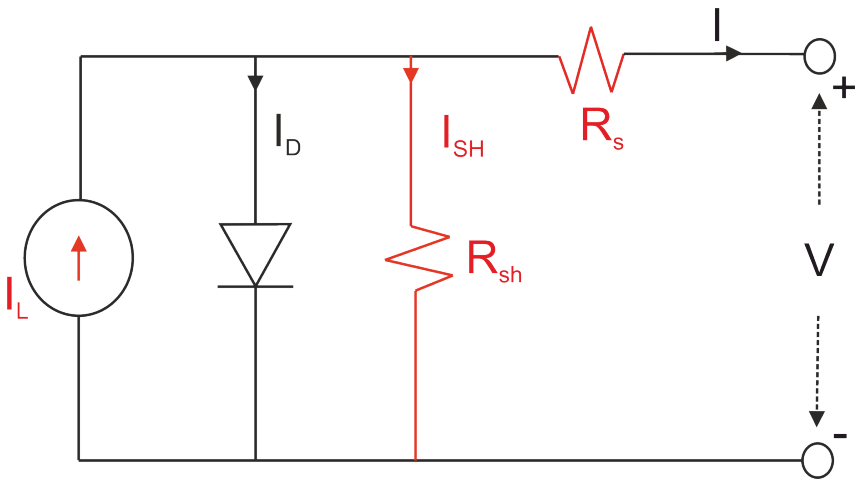

Figure 7: Equivalent circuit of an ideal solar cell (black lines), parasitic resistances (red lines) appear as results of recombination processes (real solar cell).

However, under illuminated or forward bias conditions, some recombination processes appear (figure 6), introducing parasitic resistances to the solar cells (red part in figure 7) lessening the generated photocurrent. In this configuration, R_S represents the resistance introduced by the interfaces present in the device; therefore, its value depends on charge mobility and layers thicknesses. On the other hand, R_{SH} describes the quantity of charges that recombines before it is collected, principally due to defects (recombination centres) introduced during cell fabrication. Under illuminated conditions, the net extracted photocurrent in real devices is given to,

$$I = I_L - I_D - I_{SH} \tag{3}$$

Here, I_L represents the light-generated current in the cell, I_D represents dark current, and I_{SH} represents the current lost due to shunt resistances. The last parameter from the equation is defined by,

$$I_{SH} = \frac{V + I * R_S}{R_{SH}} \tag{4}$$

To evaluate the performance of solar cell devices, three parameters are usually used. First one of them is the **Short-circuit photocurrent (I_{SC})**. As we have aforementioned, at short circuit conditions the externally measured current is I_{SC}, defined as short-circuit current. In addition, assuming no series or shunt resistances $R_S = 0$ and $R_{SH} = \alpha$, the extracted photocurrent expression gives,

$$I = I_{SC} + I_0 * (e^{\frac{qV}{K_B T}} - 1)] \tag{5}$$

The second characteristic parameter is the **Open-circuit voltage (V_{OC})**, which corresponds to the maximum voltage available from the solar cell. This is obtained when contacts are blocked (connected to an infinite series resistance) and no current is running through the device. From equation (5), we can obtain,

$$V_{OC} = \frac{K_B T}{q} ln(\frac{I_{SC}}{I_0} + 1) \tag{6}$$

V_{OC} value is characteristic on the nature of the absorber by means of I_0 (saturation current density), which depends in turn on recombination in the solar cell. In an ideal scenario, at conditions of zero non-radiative recombination, V_{OC} is equal to the optical band gap (E_g) of the absorber material minus losses.

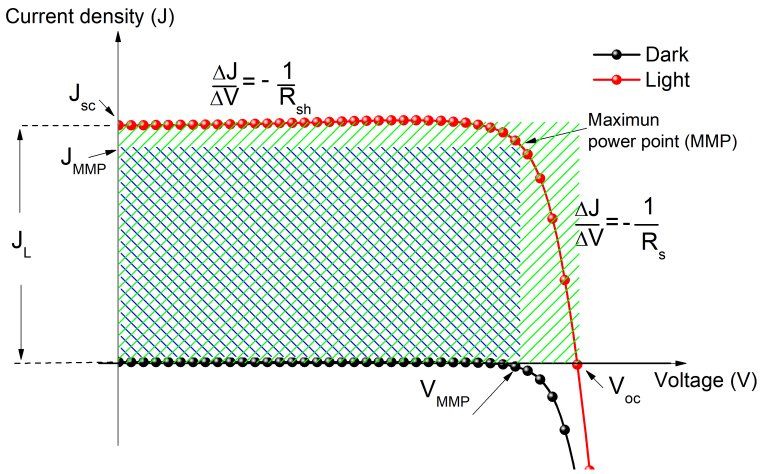

Figure 8: Current-voltage characteristic of a solar cell in light (red line) and in dark (black line). Adapted from[33]

The third parameter, the **Fill factor (FF)** represents the ratio between (I_{MMP} * V_{MMP}) [blue square] to (I_{SC} * V_{OC}) [green square] depicted in Figure 8, whose vertexes are identified by the operating points that deliver the maximum electric power attainable by the solar cell. It can be expressed by,

$$FF = \frac{I_{MMP} * V_{MMP}}{V_{OC} * I_{SC}} \tag{7}$$

Finally, energy-conversion efficiency, η, is given by

$$\eta = \frac{I_{MMP} * V_{MMP}}{P_{in}} = \frac{V_{OC} * I_{SC} * FF}{P_{in}} \tag{8}$$

where, P_{in} is the power of the incident light. Standard illumination conditions are defined by the AM 1.5 spectrum under a total integrated power density of 1000 W/m^2. It is worth to mention that the generated photocurrent intensity values are usually replaced by current density (J) as it is normalized by an area. In this way, material properties can be extracted.

3.5 Organic-Inorganic halide perovskites

As discussed in 1.3.2, organic-inorganic halide perovskites are a very promising candidates for future solar energy conversion, mainly due to its high power conversion efficiency ($\approx 22\%$) and its easy and inexpensive fabrication process.

3.5.1 Material

In 1839, Gustav Rose discovered calcium titanate ($CaTiO_3$)from Ural Mountains and named after by the Russian mineralogist Lev Perovski. Any family of material having similar crystal structures like $CaTiO_3$ are known as perovskites and can be represented by general formula ABX_3. Oxides perovskite material (ABO_3) composed by a tetravalent metal (B), a divalent cation (A) and oxygen, exhibits many interesting and intriguing properties from both the theoretical and the application point of view. Their main fields of applications are microelectronics and telecommunication, due to its superconductivity, magneto resistance, ionic conductivity, and dielectric properties. For PV applications, A and B correspond to organic and inorganic cations respectively, while X represents the halide anion. This family of perovskite presents interesting properties which make them suitable as great absorber material for PV technology[34].

3.5.1.1. Crystal structure

The crystal structure in figure 9 presents an ideal perovskite structure where B site is occupied by a divalent metal ion which is octahedrally coordinated with halides anion (X site), sharing every corner to create a three-dimensional network. The cation in A site fills the hollow form for every 8 octahedra and thus balancing the charge of the entire network. [34]

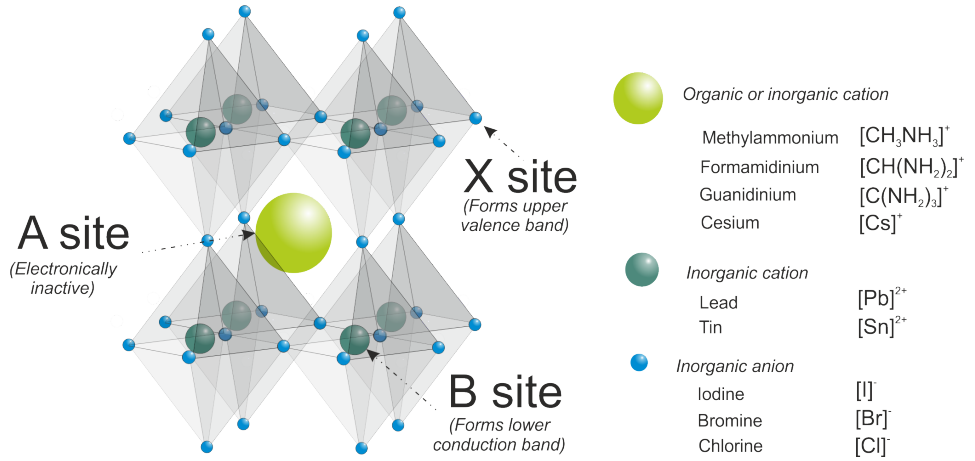

Figure 9: Schematic representation of the perovskite crystal structure with respect to A,B and X lattice sites. Adapted from[35]

The perovskite crystal structure was first described by Victor Goldschmidt in 1926, in his work on tolerance factors.[36] Although A site cations do not have any contribution to the band structure of the perovskite, their size can notably affect the symmetry of the octahedral network.[37] Goldschmidt's tolerance factor evaluates the stability and distortion of crystal structures as a function of ionic radii. It is represented by the equation,

$$t = \frac{R_A * R_X}{\sqrt{2}(R_B + R_X)} \tag{9}$$

where, subscripts indicate the position of the atom in the structure.

Depending on the value of the tolerance factor, different crystal structures can be found. Generally, it can be classified in four categories, t>1 presents hexagonal structures, 0.9>t>1 exhibits cubic structure, 0.71>t>0.9, perovskite presents octahedral rotations and finally t>0.71 the structure is composed by trigonal crystals. A second parameter known as the octahedral factor μ, defined by $\mu = \frac{r_B}{r_X}$ is used to evaluate the stability of the octahedral network and, together with the tolerance factor, provides a general idea about the geometrical perovskite stability.[37]

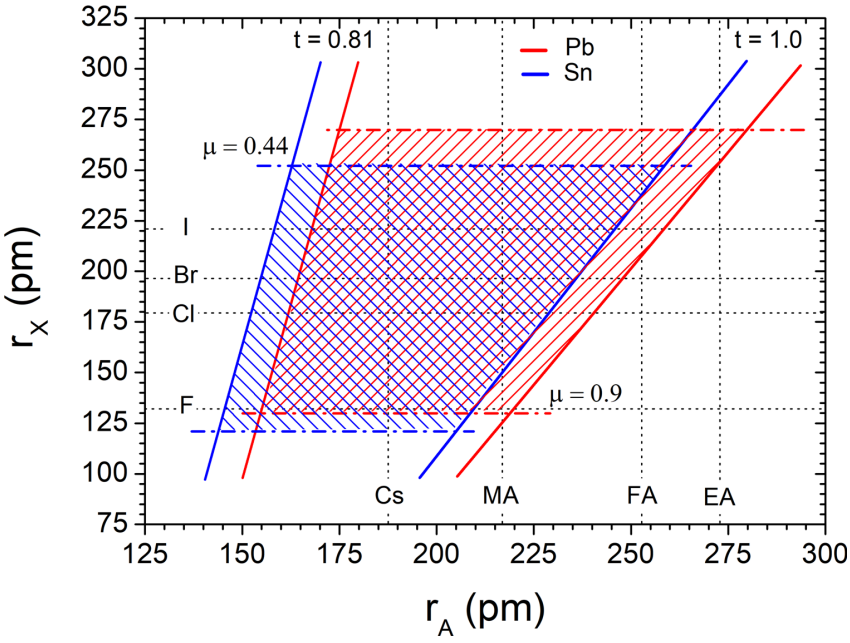

Figure 10: Formability of three-dimensional lead (red) and tin (blue) halide perovskites as a function of A-site cation and halide anion radii. Solid and dashed lines mark the bounds of the tolerance and octahedral factors, respectively. Organic cations shown in the graph are abbreviated by (MA=methylamonium; FA= formamidinium and EA= ethylamonium)[38]

Although in the crystal structure of typical $CH_3NH_3PbI_3$, methylammonium cation (2.70 Å) satisfies perfectly the tolerance factor (t=0.89), the organic cation presents an oriental disorder in the crystal with respect to the temperature. In this circumstance, three different crystal phases occurs at different temperature. At low-temperature orthorhombic phase (T <-108°C), methylammonium cation is fully ordered with a space group Pnma. When temperature increases (-108-54°C), the structure changes to the tetragonal with space group I4/mcm in which the organic cations are no longer in a fixed position but with a 2D disorder. At temperatures above 54°C, molecular disorder increases to 3D which entails a cubic phase transition with a space group Pm3m.[39, 40, 41]

Larger organic cation such as formamidinium (2.79 Å)which involve a tolerance factor close to 1, has been also employed [42], however at room temperature it has a Pm3m space group similar to high temperature $CH_3NH_3PbI_3$ cubic phase. [43] Moreover, formamidinium based perovskite exhibits a corner-sharing α perovskite structure (black colour) or a face-sharing δ phase perovskite (yellow colour) when the film is annealed above or under 150°C, respectively. A similar behaviour has been also found in cesium based perovskites.[44, 45, 46]

In order to stabilize these phases in formamidinium based perovskite, different approached were carried out. In 2014, Pellet et al.[47] studied the mixture of methylammonioum (MA^+) and formamidinium (FA^+), and they concluded that the addition of 20% MA avoided the undesirable formation of the δ-phase while maintaining the red-shifted band gap of $FAPbI_3$, obtaining their best result with an addition of 40% MA. Recently, Yi et al.[48] demonstrated that the best performance of the mixture were only with the addition of 10% MA. A stable "quasi-cubic" phase at room temperature is formed, achieving impressive efficiencies of 20.2%. Other inorganic cations were also used such as cesium[49]or rubidium,[50] paving a way towards replacement of organic cations in lead halide perovskites. In addition, triple cations (MA)/(FA)/(Cs) have been studied by different groups24,52, the addition of a low percentage of cesium, helps to stabilized the structure and increases thermal stability. Seok et al.[25] demonstrated that a careful control of the growth conditions of perovskite layers taking into account deficiency in halide anions is essential for achieving high-efficiency perovksite devices. Nevertheless, it is important to consider that, with the addition of a mixture of different cations and halides[51] devices are not constituted by a perfectly homogeneous crystalline structure, but a nanoscale segregation of multiple perovskite compositions.[52, 53]

Table 1: Summary of the highest PCEs of perovskite solar cells with different compositions.Adapted from [54]

Perovskite	Tolerance factor	RT phase	RT phase post-anneal	Band-gap (Eg)	Best PCE (%)	Ref.
$MAPbI_3$	0.89	Tetragonal	Tetragonal	1.55	20.3	[55]
$CsPbI_3$	0.79	Orthorhombic	Orthorhombic, yellow	1.72	10.77	[56]
$CsPb(I_{0.67}Br_{0.33})_2$	0.81	Orthorhombic	Cubic	1.9	6.5	[57]
$FA_{0.85}Cs_{0.15}PbI_3$	0.99	Tetragonal	Tetragonal	1.52	17.3	[58]
$FA_{0.85}MA_{0.15}Pb(I_{0.85}Br_{0.15})_3$	1.01	Cubic	Cubic	1.62	22.1	[23, 25, 26]
$FA_{0.85}Cs_{0.15}Pb(I_{0.83}Br_{0.17})_3$	1.01	Tetragonal	Tetragonal	1.74	20.0	[50]

The large versatility that presents the perovskite structure, allows the incorporation of large organic cation such as ethylammonium [59, 60], or guanidinium.[61] Although, these organic cations do not adjust the tolerance factor, authors suggest that they situate in the grain boundaries reducing the charge accumulation and increasing stability of devices.[62] These large cation mostly produce 2D[63] structure, which is more stable than 3D, due to their superior stability and water resistance.[64] Bearing this in mind, some authors proposed a multidimensional concept in order to improve stability in perovskite solar cells.[65]

3.5.1.2. Opto-electronic properties

Hybrid organic-inorganic perovskites shows very strong absorption properties in the UV-visible part of spectra. With a band edge at 780 nm of $CH_3NH_3PbI_3$ which can be red-shifted further with the addition of formamidinium cation,[47, 66] is able to absorb the entire visible spectrum. This strong optical absorption is one of the key characteristics for a PV material as it reduces the need of thicker films, avoiding recombination losses.

Electrical structure has been investigated in order to understand the properties of perovskites.[67] As it was explained before, the electronic band gap is determined by the states at the valence band maximum (VBM) and conduction band minimum (CBM). In case of perovskite, the VBM is formed of an anti-bonding Pb 6s/n p combination,where n depends on the nature of the halide.[67]On the other hand, the conduction band is created of the anti-bonding combination of empty Pb 6p orbitals, that with a formal oxidation state of 2^+ has the ground-state electronic configuration $5d^{10}$ $6s^2$ $6p^0$, and only in small portion by the halide ns orbitals. It means that,unlike organic cations, halogen anions do significantly affect the band structure of the perovskite. Solis-Ibarra et al.[68] interchanged from Cl^- to Br^- to I^-, observing as the band gap of the perovskite was gradually decreased, resulting in a gradual red shift of the optical-absorption edge.

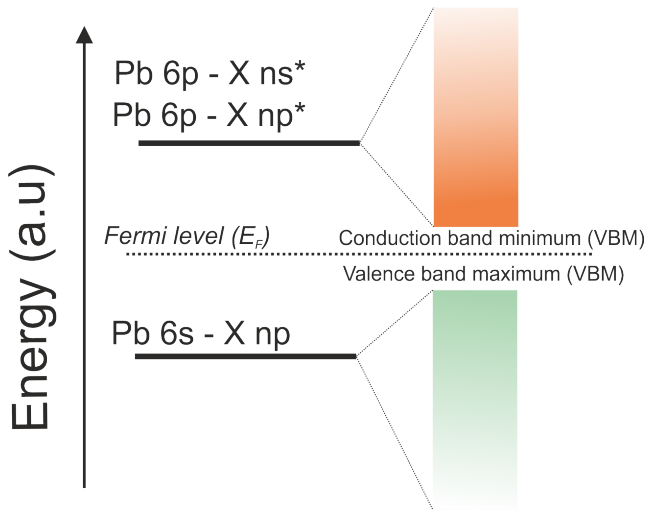

Figure 11: Bonding diagram of $CH_3NH_3PbI_3$ crystal where the value of n depends on the halide (Cl^-=3, Br^-=4 and I^-=5). Adapted from[69]

One of the main differences which have been attributed to perovskite is that it acts as a direct-band gap semiconductor.[70, 71, 72] This gives great advantage against previous known semiconductorsuch as silicon in which both absorption and recombination involve not only photons, but also phonons.

However, some works suggest[73, 74] a direct-indirect character of the band-gap in $CH_3NH_3PbI_3$ due to the presence of second-order recombination, and was attributed to direct excitation from the VB to the CBM, which forms an indirect band gap with the VBM. In addition, excess of organic cation concentration or ion migration can also cause a slightly displacement of energy bands.[75]

For efficient charge-carrier separation in a solar-cell material,besides wide absorption spectra, it is important that the binding energy (EB), which determines the fraction of free carriers, must be small. In organic–inorganic halide perovskite it is clearly difficult to measure directly the binding energy; a broad range of binding energy values from 2 to 55 meV [76, 77, 78] have been reported in the literature depending on the characterization technique used.Hirasawa, et al.[79] demonstrated that the photo-excited states can be divided in Wannier-type excitons with binding energies ranging from 20 meV to 98 meV or Frenkel excitons which have much higher binding energies (>100 meV). However, extremely low binding energy values, gives rise to the idea of spontaneous free charge carrier generation (non-excitonic process) after photo-excitation in the perovskite, which could explain the impressive performance of this kind of absorbers.[80]

Another interesting property observed in perovskite materials is the high carrier mobility together with an ambipolar character.[81] The combination of two factors, the small effective mass of carriers (electrons and holes)[82, 83] and the relative weak carrier-phonon interaction,[80] has been attributed to the origin of large carrier mobility. In addition, diffusion lengths for charge carriers have been shown to be in the order of over 100 nm in the case of $CH_3NH_3PbI_3$,[84] while in the case of mixed halides perovskite, it can be over 1 μm.[72]

Table 2: Summary of transport characteristics of perovskites and comparison to previous generations. Adapted from [85]

	$CH_3NH_3PbI_3$		$CH_3NH_3PbBr_3$		Si		GaAs	
Material	Poly crystalline	single crystal	Poly crystalline	single crystal	e^-	h^+	e^-	h^+
Diffusion length (μm)	0.1–1	2–8	0.3–1	3–17	1000	600	7	1.6
Carrier lifetime (μs)	0.01–1	0.5–1	0.05–0.16	0.3–1	1000		$\approx$ 0.01–1	
Mobility ($cm^2\ V^{-1}\ s^{-1}$)	1–10	24–105	30	24–115	1450	500	8000	400
Effective mass (m0)	$\approx$ 0.10–0.15		0.13		0.19	0.16	0.063	0.076
Trap density (cm^{-3})	$10^{15} - 10^{16}$	(1–3)*10^{10}		(0.6–3)*10^{10}				
References	[86, 87, 80, 84, 72, 88, 89, 90],	[91, 92, 93]	[87, 94, 92, 95, 96]	[91, 92]	[33]		[33, 97]	

Previously in section 3.3, main processes which are taking place into the perovskite have been discussed.The existence of different materials and layers that compose the photovoltaic device entails an emergence of desirable and undesirable process that will affect the final performance of the devices.

Although the presence of different undesirable processes injection of electron and hole in selective contacts occur on a much faster time scale that charge recombination processes leading to the high performance of the PV device.

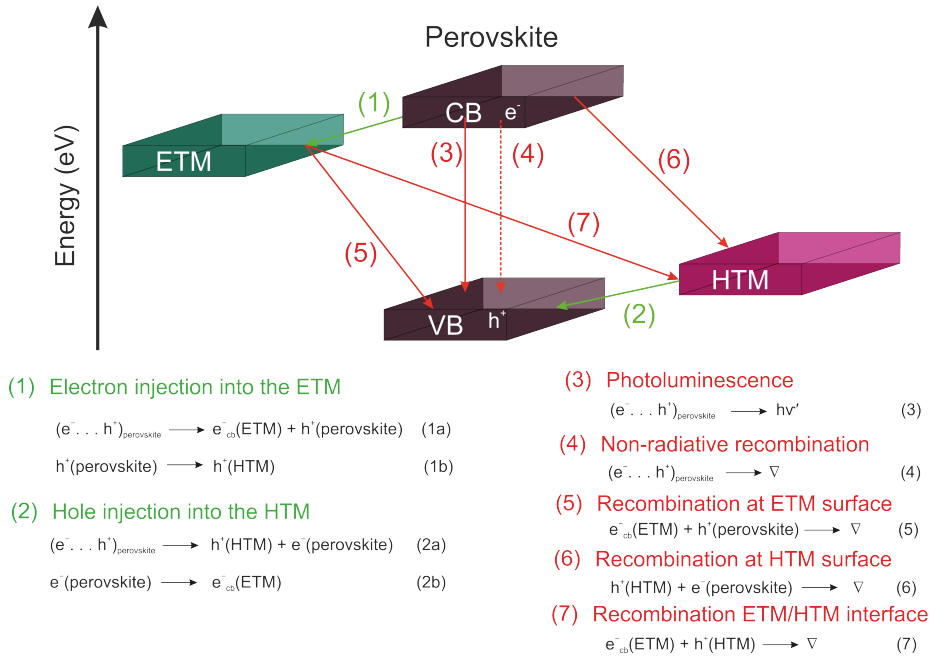

Figure 12: General review of the possible different process inside the whole devices. Adapted from[98]

3.5.2 Device architecture

Although, there exists a variety of possible device architectures and materials, but the perovskite solar cells are composed by three main functional units. The transparent front electrode (generally Fluorine doped Tin Oxide (FTO),IndiumTin Oxide(ITO) or Aluminum doped Zinc Oxide (AZO)). On top of it, a compact or blocking layer is usually deposited in order to reduce the recombination. The absorber layer is perovskite and the counter electrode (Au, Ag, Ni or C). As it has been cited, perovskite presents an ambipolar character; however, one or two auxiliary layers can be added in order to have an efficient charge extraction (electron transport layer (ETL) or hole transport layer (HTL)).

Photovoltaic characteristic parameters (section 3.4) are highly dependent on the quality ofthe perovskite film, its composition and the interfacial contact as well as the device architecture. Therefore, it is important to develop architectures where the parasitic series resistance (R_S) and shunt resistance(R_{SH}) of devices are minimized, as they are dependent in turn on the bulk conductivity of each of the layers, and the contact resistance between them.

Thus, in order to optimize charge extraction from perovskite to selective contacts,three different architectures (mesoscopic,planar and inverted) have been proposed.[99] The mesoscopic architecture consists of porous titanium oxide (TiO_2) or aluminium oxide (Al_2O_3) nanoparticles in which the perovskite is infiltrated while they are absent in planar or inverted structure. To date, several electron transport layers (ETLs) have been reported, including metal oxides (such as TiO_2, ZnO, SnO_2, SiO_2, ZrO_2), metal oxide composites, and metal oxide heterostructure nanoparticles(Al_2O_3/ZnO[100], TiO_2/MgO [101] and WO_3/TiO_2.[102]

The use of TiO_2 as electron transport layer was based on the typical structure of a dye-sensitized solar cell[15], where the liquid electrolyte is in direct contact with sintered TiO_2 nanoparticles. [103, 104] Contrary to TiO_2, mesoporous Al_2O_3[105] acts only as a scaffold as its VBM is higher than perovskite, therefore electron injection is not possible.Similar to mesoporous Al_2O_3, the use of dielectric materials such as SiO_2[106] and ZrO_2,[107] do not achieve high efficiencies, but increases the recombination resistance due to its lower CBM and higher VBM. Although some studies[108] suggest some detrimental effects, the presence of the electron transport material provides advantages such as large contact area after perovskite deposition, prolongation of light-absorption length or a reduction of charge transport length. In this context, optimized deposition characteristics as well as different shapes were studied. Ultra-thin amorphous TiO_x provides uniformity and homogeneity giving highly stable electronic properties than thicker TiO_2 layer which affects the V_{OC} due to an increase of electron transport resistance.[109] In addition, one-dimensional nanorods,[110] nanocolumns,[111] nanowires,[112] nanosheets,[113] or nanoneedles[114] provide better surface morphology, roughness, and efficient electron injection and a short carrier path for the electron, therefore a fast charge extraction occurs.The use of core-shell nanoparticles or adding dopant to the mesoporous layer are other strategies that can improve the efficiency by retarding charge recombination.

Han et al.[101] fabricated MgO-coated TiO_2 nanoparticle which improved open circuit-voltage and fill factor in the order of 4.7% and 6.1% higher respectively. Other approach involves the n-type-doping of TiO_2 in order to enhance the electronic properties by increasing its CBM and therefore reducing charge recombination processes. Most n-type dopants used for this purpose include Y,[115] Sn,[116] Mg,[117] Al,[118] or Li.[119] However, due to the need of high temperature in the TiO_2 deposition process (500°C), SnO_2 appears as a good substitute due to high electron mobility, anti-reflection properties, and deeper conduction band also with a lower temperature process (150°C).[120, 121]

The use of polymer as electron extraction layer is another possibility to fabricate flexible devices at lower temperature. Many research groups have reported organic ETL such as PET,[122, 123] PCBM,[124, 125] to achieve high efficiency in inverted architecture. However the hydrophobic nature of the polymers often leads to pinhole generation and poor surface coverage when perovskite film is grown on it.Improved coverage together with high conductivity was achieved with the incorporation of graphene oxide into PCBM [126] or the use of evaporation techniques. [122]

It is worth to mention here, that though the best performing devices reported entail the presence of TiO_2 layer,recently, planar devices have also improved their efficiencies over 21%.[120] In addition,fabrication of planar devices is relatively easier and less energy consuming compared to mesoscopic devices.

It is reported that perovskite solar cell requires an ETL but not necessarily a HTL.[127] The role of HTL is the most extensively studied as it is responsible to achieve high open circuit voltage.[128] The most used HTL can be classified into inorganic and organic, which can be divided further into polymers and small molecules.2,2',7,7'-tetrakis-(N,N-di-4-methoxyphenylamino)-9,9'spirobifluorene (Spiro - OMeTAD) is the most studied small molecule based HTM in perovskite solar cell, albeit it presents poor hole conductivity and an expensive production process due to its multi-step synthesis and difficult purification steps.[129] The need to dope it with tris[2-(1H-pyrazol-1-yl)-4-tert-butylpyridine]cobalt(III) tris[bis(trifluoromethylsulfonyl)imide] (FK209),4-tert-butylpiridine (t-BP) and bis-(trifluoromethanesulfonyl)imide lithium salt(LiTFSI) reduces its commercial application because of its instability in ambient conditions.[130] In order to mimic the good performance, similar structure to Spiro-OMeTAD were synthesized by Ko and co-workers [131] coded as OMeTPA-FA and OMeTPA-TPA. These compounds presented absorption bands at 395 and 490 nm with an efficiency of 13.6% after adding dopants. Another approach made by Ko and co-workers,[132] was to use a donor–π–acceptor (D–π–A) systems to synthesized Triazine-Th-OMeTPA and Triazine-Ph-OMeTPA. By using these molecules, similar performance to Spiro-OMeTAD based devices were achieved.

On the other hand, different core-based small molecules were investigated in order to replace Spiro-OMeTAD, such as quinolizino acridine,[133] carbazole,[134, 135] thiophenes[136] or triazatruxenes.[137, 138] Although the use of small molecules, was demonstrated as they can achieve performance over 20% PCE, further development need to be done to establish their long-term stability under high temperature conditions as well as under light stress.[139] Conducting polymers have been already applied in organic photovoltaic (OPV) technology.[140] The most used conducted polymers in perovskite solar cells include poly(3,4 ethylene dioxythiophene)(PEDOT),[122, 141, 142, 143, 144] poly (3-hexylthiophene -2,5 -diyl) (P3HT) [145, 146, 147] and poly(triarylamine) (PTAA).[148, 149, 150] Among them, the best performing HTM is PTAA, which yields an impressive PCE of over 20% when used in a PSC device.[151]

However, improvement of the quality of the interface with the perovskite, batch-to-batch reproducibility and purity, need to be addressed. Other interesting approach is the use of carbon-based materials (e.g. graphene related materials,[144, 152] carbon nanotube,[153]carbon paste,[154]) to improve interfaces of the devices. Carbon materials was also demonstrated as promising candidates for addressing stability or hysteresis problems in perovskite solar cells. For instance, employing perovskite/fullerene hetero-junction can achieve PCE of over 20% with negligible hysteresis behaviour due to a passivation of the defects of perovskite.[155, 156, 157] In addition, it can also be seen as advantage of the impressive electric properties of graphene[158] and carbon nanotubes[159] to enhance the charge transport or to replace the traditional metal electrode. Recently, Nazeerudin et al. have presented a seminal work where, PSCs with a stability of >10,000 hours was reported in ambient air under full sunlight, using conductive carbon as electrode.[65] These brilliant achievements prove the attractive perspective of carbon materials based perovskite solar cells.

Inorganic compounds have also been used as a replacement of expensive and low conductive organic HTMs.CuI was the first inorganic material tested as HTM which achieved better FF than devices fabricated with Spiro-OMeTAD due to its higher conductivity.[160, 161, 162, 163] However, it presented high recombination rate, limiting therefore the V_{OC}. Inorganic NiO thin films were employed successfully as a HTM.[164] Recently an outstanding 16.4% efficiency was achieved when an ultrathin layer was deposited by atomic layer deposition (ALD) technique with a V_{OC} of 1.04V.[165] Nevertheless, CuSCN presented the best performance due to its highly stable crystalline structure and its robustness even at high temperatures.[166] Seok et al.[167] compared thermal stability under humidity conditions with commonly used Spiro-OMeTAD. Although both materials presented efficiencies close to 18%, after 2 hours at 125°C and 40% RH, inorganic based device maintain approximately 60% of the initial value.

In the hunt for stable and efficient PSCs, different architecture were explored which provides a large number of combinations in order to reduce resistances and increase V_{OC}. Different possibilities are offered for both ETL and HTL. Nevertheless, it is important to optimize not only the different layer which compose the devices but also the ideal architecture for future commercial applications. Figure 13, summarizes the different possible architectures and their advantages/disadvantages.

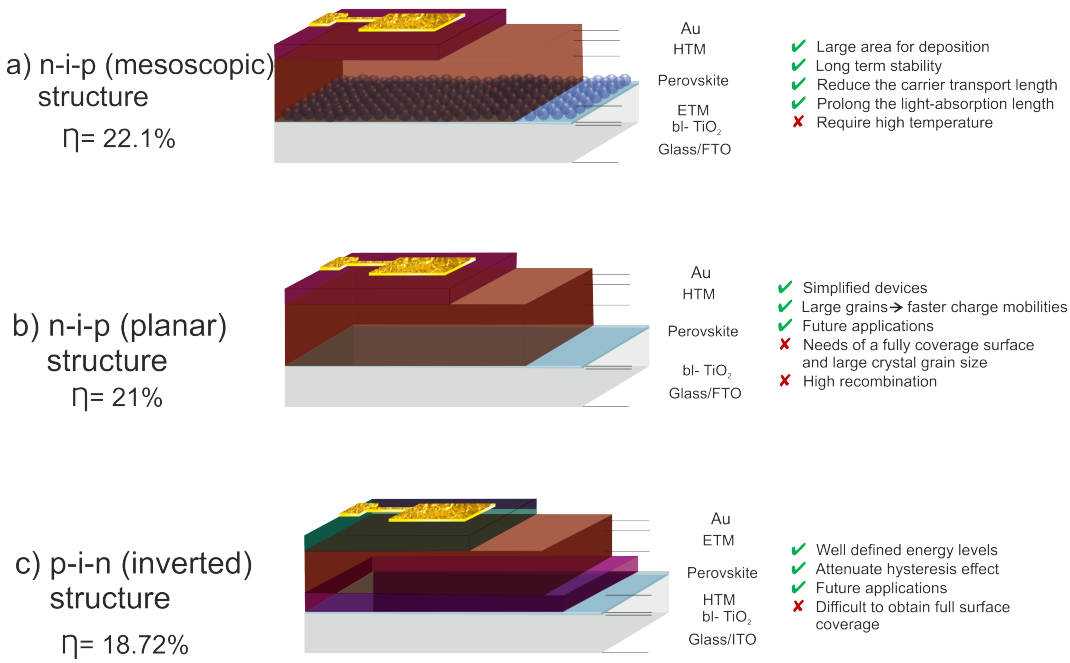

Figure 13: Different possible architectures of perovskite solar devices; a) mesoporous[26] b) Planar[120] and c) Inverted.[168] Best efficiencies achieved and advantages/disadvantages are also shown.

3.5.3 Deposition techniques

The performance of PSCs highly depends on the perovskite film quality. This involves different properties such as grain size, crystallinity, homogeneous morphology with a full surface coverage. The factors influencing the film morphology such as the deposition method, material composition, additives and film treatment are explained below.

- The ratio of organic-inorganic component largely affects perovskite film quality. However, this ratio depends on the precursors used or the method used for perovskite deposition. In 2013, sequential step deposition technique[169] was explored using 1:3 inorganic-organic ratioand high reproducibility and efficiency close to 15% was achieved. A year later, a new one step deposition method[170] came up which provides an extremely uniform and dense perovskite layer. In this case, a molar ratio of 1:1 was used. However, subsequent studies suggested that the excess of PbI_2 has positive effect in final device performance since it has been proposed to passivate the defects in perovskite grain boundaries.[171, 172, 173, 174]

- Temperature treatment has a huge influence during the PSC fabrication, in particularly in the annealing step. Over heating of perovskite can entail a loose of light harvesting properties or degradation of the perovskite.Dualeh et al.[175] studied role of the temperature used in the annealing process required to convert as deposited solution into the perovskite. It was suggested that in the case of sequential deposition process of $CH_3NH_3PbI_3$, annealing temperature must be in the range of 80-100°C. An excess of this temperature entails the formation of PbI2, which has detrimental effects of device performance. However, Khatiwada et al.[176] showed that there was a significant change in crystal formation, when annealing temperature was increasedfor mixed halide perovskite ($CH_3NH_3PbI_{3-x}Cl_x$). Besides, $(FAPbI_3)_{1-x}(MAPbBr_3)_x$ presents a complex system. Chen et al.[177]suggested that the optimal annealing temperature was 135°C in order to unstable avoid the δ-$FAPbI_3$ phase formation. Annealing step, especially when one-step deposition with solvent engineering is used, has extremely importance as the perovskite crystals are formed during spin coating while the solvent is evaporating. Some authors[178] recommend a multi-step annealing process in order to achieve a more uniform film as well as a pinhole free high surface coverage.

- The number of solvents with sufficient solubility for both components are limited therefore could highly affect the final properties of the perovskite. γ-butyrolactone (GBL), Dimethyl sulfoxide (DMSO), and Dimethylformamide (DMF) are the common polar solvents in the precursor solution. Wang et al.[179] investigated the effect of mixing halide using DMF and DMSO as precursor solvents in the sequence deposition. They demonstrated that the $PbI_2(DMSO)_x$ complex formed with the solvent mixture provides full surface coverage compared to pure DMF.The emergence of the deposition method of one-step with solvent engineering expands the range of solvent to employ in the perovskite film fabrication. Seok et al.[170] were the first to report this technique by using a mixture of GBL and DMSO as the precursor solvent and toluene as anti-solvent during the spinning step. This outstanding work improved PSCs efficiency as well as controlled the morphology. The good results obtained with this method, enforces the research of new anti-solvents in order to optimize this technique. Recently, Paek et al.[180] presented a complete work, wherea set of six anti-solvents with different dielectric constants (ϵ, solvating abilities) and other physicochemical properties were tested. Anti-solvents studied were trifluorotoluene (TFT), toluene (TL), chlorobenzene (CB), p-xylene (Xyl), diethyl ether (ether), and dichloromethane (DCM). They obtained a promising PCE of 20.3% with the use of TFT as a new anti-solvent. Moreover, ultra smooth surfaces were achieved using a novel ethyl ether/n-hexane mixed anti-solvent (MAS).[181]

Other possibility to improve the quality of perovskite films is the addition of small amounts of different chemical additives, such as diiodoctane,[182] methylammonium chloride[183] or hydroiodic acid (HI),[42] in the perovskite precursor solutions which provides advantages in terms of crystallinity and film coverage. In addition, Grätzel and Han et al.[184] reported that the addition of alkylphosphonic acid ω-ammonium also improved the device stability.

- Perovskite films are generally deposited inside a glove-box in the presence of nitrogen or dry-air, albeit there exist discrepancies if humidity affects positive or negatively in the final device performance. Some studies[185] indicate that less than 30% of humidity could improve the properties. Cronin et al.[186] reported recently the effect of humidity and annealing time. Results showed that at around 20% RH, device performance is independent of the annealing time, but at higher (30 - 40% RH) or lower (0 - 15% RH) humidity, it becomes very sensitive.On the other hand, Tai et al.[187] have obtained high-quality ($CH_3NH_3PbBr_{3-x}SCN_x$) perovskite films even when the relative humidity exceeds 70%. Moreover, humidity in the precursor solvents also could lead to films with poor morphology. Aranda et al.[188] indicated the importance of precursor´s stoichiometry during fabrication process step. Under not adequate humidity conditions, the presence of hydrates induces recombination centres, thus reducing the open circuit voltage.

Generally, the fabrication of a complete perovskite solar cell is based on a layer-by-layer process as shown figure 14. First a TiO_2 blocking layer is deposited onto the substrates by spray pyrolysis at 450 °C, using a titanium diisopropoxidebis(acetylacetonate) solution diluted in ethanol, with oxygen as carrier gas. Then a mesoporous TiO_2 layer (in case of mesoscopic structure) is deposited by spin coating using a TiO_2 paste diluted (30 nm nanoparticle) in ethanol. After drying at 100 °C for 10 min, the TiO_2 mesoporous layer is heated at 500 °C for 30 minutes using a progressive heating and later cooled to room temperature. Perovskite films can be deposited by different methods, but here one-step deposition is presented with solvent engineering. After deposition, the substrate is annealed at 100 °C for 60 minutes. Then, the perovskite film is covered with the hole-transporting material (HTM) by spin coating. Finally, a very thin layer (70 nm) of gold is thermally evaporated on top of the device to form the electrode contacts.

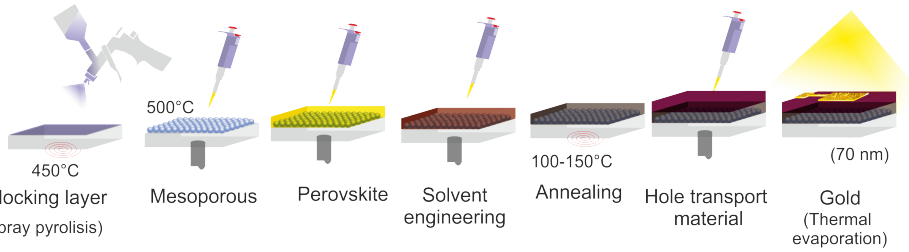

Figure 14: Typical perovskite solar cells fabrication process using one-step deposition with anti-solvent.

For the deposition of the perovskite layer, four different methods can be used so far, depending on the device architecture, substrate size, etc. selected.At first glance, deposition methods can be divided into solution-base and vapour-based deposition, besides they can be classified further into one step and two step deposition. One-step with anti-solvent (Figure 15a) is the simplest method and most commonly used, albeit the latter three methods permit a better control of the perovskite film with respect to the crystallinity, morphology, and homogeneity.In one-step both precursors components are previously dissolved in an aprotic solvent such as DMF, DMSO or GBL and then spin coated on the substrate, in case of dual-source both are evaporated in vacuum condition onto a rotating substrate.Regarding two step deposition, first the inorganic part is deposited onto the substrate and then it is created a close contact with the organic part by dipping or vapour assisted obtaining a better control of the crystal growth.

One-step solution deposition. In this method (figure 15a), the precursor solution of the perovskite is prepared by dissolving powdered organic cation halide and Pb halide at a specific mole ratio (usually at 1:1) in aprotic polar solvents such as (γ-butyrolactone (GBL), dimethyl formamide (DMF), dimethyl sulfoxide (DMSO), to get a clear solution. Secondly, the solution is spin-coated. Finally, an annealing process at approximately 100-150°C is required to transform the precursor to crystalline perovskite. This method presented low coverage and a non-uniform perovskite layer,however the use of an anti-solvent[151] during the spinning step not only improve the crystal structure as it reduces Gibbs energy but also affects the electronic properties of the perovskite.

Two-step sequential solution deposition. Burschka et al.[169](figure 15b) presented this method in order to improve pore filling of the perovskite. In this deposition procedure, the solution of PbI_2 in DMF was first spin-coated onto the nanocrystalline TiO_2 film and subsequently transformed into the perovskite by dipping into a solution of methyl ammonium (MA) halide in iso-propanol.The close contact during the dipping step permits much better control over the perovskite morphology than achieved with the common one-step method.

Dual-source vapour deposition. In this process,[81] the organic and inorganic precursor, evaporate simultaneously from separate sources under vacuum conditions with a specific molar ratio, onto a rotating substrate (figure 15c). This deposition technique can be used for large scale extremely uniform and nano crystalline perovskite films without any voids between the perovskite crystals, which is rarely observed in solution-processed films. Modified version[189] of this as vacuum-flash solution process has obtained a maximum efficiency of 20.5%.

Vapour- assisted solution process. The vapour-assisted solution process can be viewed as a modified two-step sequential solution deposition whose second step is replaced by a vapour deposition process. [190, 191, 192] The perovskite layer made by this technique featured full surface coverage, low surface roughness, grain sizes up to the microscale level, and 100% precursor transformation completeness due to the incorporation of the organic through vapour phase. (figure 15d)

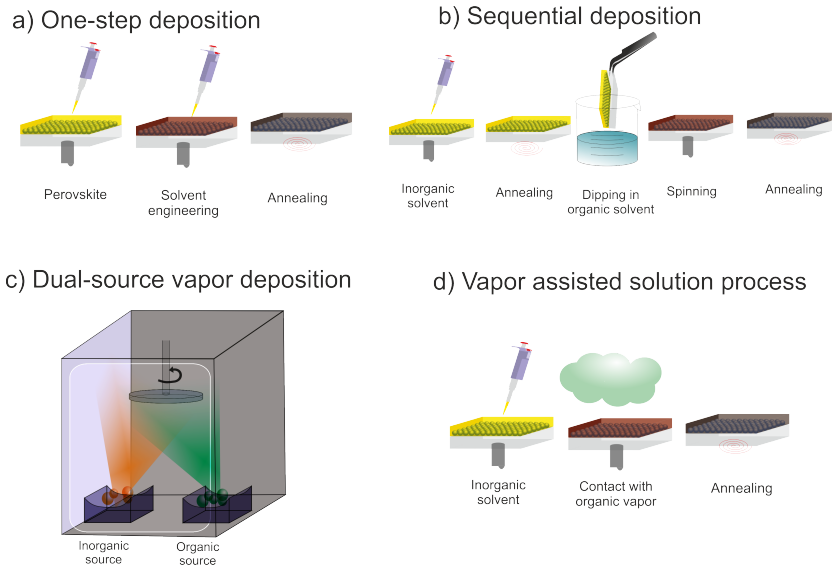

Figure 15: Different perovskite deposition method.a) and c) represents one step deposition, while b) and d) shows two step deposition process.

3.5.4 Characterization techniques

For perovskite solar cells a qualitative characterization by a standard *J-V* measurement is helpful for a brief glance whether fabricated solar cells are working or not. Nevertheless, to obtain a whole understanding of the process governed in the devices, additional characterization needs to be carried out. Below, some characterization techniques both basis and application are explained.

Incident photon-to-current efficiency (IPCE)

The incident photon-to-current efficiency (IPCE) is a measure of the ratio of the photocurrent (converted to an electron transfer rate) versus the rate of incident photons as a function of wavelength.The general equation for calculating the IPCE is,

$$IPCE(\lambda) = EQE(\lambda) = \frac{collectedelectrons(\lambda)}{incidentphotons(\lambda)} = \frac{hc}{q}\frac{J_{SC}(\lambda)}{\lambda P_{in}(\lambda)} \tag{10}$$

where, h is the Planck constant, c is the speed of light, q is the elementary charge and λ is the wavelength in nanometers.

Measuring the IPCE is also useful to determine the optical band gap. However, the band gap obtained from IPCE may be higher than that obtained by optical spectroscopy techniques, since the onset of photocurrentmay be limited by slow kinetics and/or electron transport. Optical band gap can be calculated by the following equation,

$$E_g = \frac{hc}{\lambda} = \frac{1239.8}{\lambda}(ineV) \tag{11}$$

Where λ is the threshold wavelength (in nm) that allows for absorption across the band gap.

Atomic force microscopy (AFM) and Scanning electron microscopy (SEM)

AFMs operate by measuring the attractive and repulsive forces between a probe and the sample. Generally, the probe is a sharp tip, which is a 3-6 μm tall pyramid with 15-40 nm end radius (Figure 16a). Although AFM technique was used to obtain a surface profile of the samples, new variants as Kelvin probe force microscope (KPFM) and Conductive atomic force microscopy (c-AFM) have risen as useful techniques to study charge dynamics in perovskite solar cells. Remarkable studies were performed by Bergmann et al.[193] who reported holes accumulation at the interface perovskite/HTM due to unbalanced charge transport in the devices. Li et al.[194] investigated the influence of DMF in the annealing process with both techniques in order to unravel the effect of grain boundaries as recombination sites. On the other hand, Scanning electron microscopy is extensively used in the morphological characterization of the films. Thicknesses of the different layer which composed perovskite devices are fundamental information when optimization needs to be done (figure 16b).In addition, environmental-SEM can also be used to monitor the degradation processes when perovskite samples are exposed to different humidity conditions.[195]

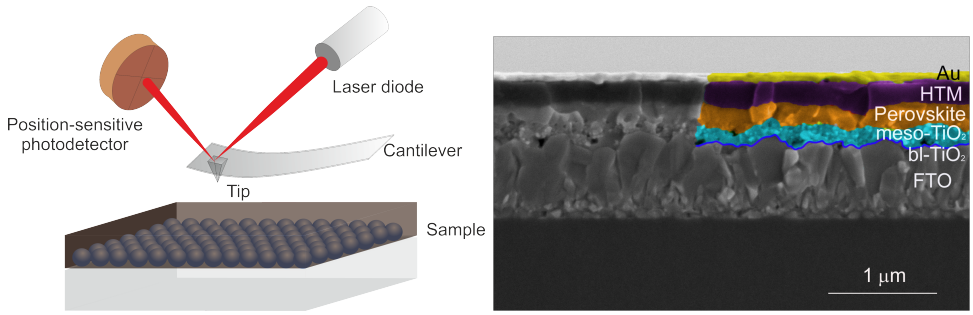

(a) Theoretical basics of AFM

(b) Cross-sectional image of a perovskite device

Figure 16: Microscopy techniques used in perovskite film characterization.

X-Ray diffraction (XRD)

As we have seen, high quality perovskite crystal formation is a key-stone in theopto-electronics and final performance of the device. Therefore, several works have investigated the crystal growth orientation by means of XRD. X-Ray characteristic peaks of $CH_3NH_3PbI_3$ are situated at 14.1° and 28.4°, which are attributed to the tetragonal structure of a 3D hybrid perovskite(I4/mcm space group). However, the existence of different crystal phases depending on the temperature, together with the fabrication of complex mixed perovskites make difficult to identify every single phase present in the films. Additionally, in order to gain more quantitative information of perovskite samples several authors have performed depth profile analysis with X-ray photoelectron spectroscopy (XPS). As a result, the oxidation states of the individual elements which composed the perovskite film as well as the energies binding can be extracted from this technique. Moreover, both techniques have been used to evaluate degradation process in perovskite films. The presence of moisture causes the formation of PbI_2, which has a characteristic peak at 12.6°. Evaluating the intensity of this peak and the extinction of the peaks a 14.1° and 28.4°, is a clear indication that degradation is taken place.

Electrochemical impedance spectroscopy (EIS)

In general, electrochemical impedance spectroscopy is a non-destructive technique that consists in applying a voltage (small perturbation) to the system and measure the ac electrical current response at a certain angular frequency. This relationship can be expressed by the equation,

$$Z(\omega) = \frac{V(\omega)}{I(\omega)} \tag{12}$$

Where, ω is the radial frequency (expressed in radians/second) which can be convert into frequency f (expressed in hertz) through the equation $\omega = 2\pi f$.

EIS was commonly applied in charge dynamic analysis on DSSCs.[196, 197] During an impedance measurement, the system is (ideally) kept at a fixed steady state by imposing stationary constraints, i.e usually under illumination. Then, the Z (ω) is measured by scanning the frequency at a multitude of values, typically over a wide range of frequencies, i.e., from 10^{-2}Hz to 10^{6} Hz. This technique makes it possible to extract physically meaningful properties of the electrochemical system by modeling the impedance data in terms of an equivalent circuit composed of ideal resistors *(R)*, capacitors *(C)*, inductors *(I)*, etc.. However, because of the lack of ideally of the system, it is needed to use more complex elements as constant phase element *(CPE)*. From the analysis of the equivalent circuit physical parameters of the charge transport in the perovskite and on the different layers interfaces can be obtained. Specifically, several authors utilize this simple technique to explain the capacitive charging of the selective contacts, as well as exploring the low-frequency 'slow' response of the perovskite layer.[198] Recombination and dielectric relaxation resistances are frequent parameters extracted from the analysis of this technique, which indicate possible collecting charges in the interfaces of the different layers.[199]

On the other hand, other spectroscopic techniques based on magnetic excitation have been used to reveal useful information concerning the device operation.As examples, *Optical pump–terahertz probe (OPTP)*, or *Time-resolved terahertz spectroscopy (TRTS)* are powerful techniques to study charge dynamics by through a magnetic excitation on femtosecond time scales in PSCs. Very recently, researchers from Ames Laboratory,[200] were able to capture the moment when a particle of light hits a solar cell and becomes energy by TRTS.

3.5.5 Device stability and hysteresis phenomena

By far, the main concern raised in the development of perovskite solar cell is their long-term stability.[201, 202] It is well documented that moisture and heat have been identified as major causes for the instability in the perovskite.[203, 204] According to some author, degradation mechanism will follow a cascade of reactions where at some point, the degradation would be irreversible.

Table 3: Proposed reactions of perovskite degradation depending on different external factors. Adapted from 207

External factor	Degradation process
Humidity [205, 206]	$CH_3NH_3PbI_3\,(s) \xrightleftharpoons{H_2O} PbI_2\,(s) + CH_3NH_3I\,(aq)$
	$CH_3NH_3I\,(aq) \rightleftharpoons CH_3NH_2\,(aq) + HI\,(aq)$
	$4\,HI\,(aq) + 02 \rightleftharpoons 2\,I_2\,(s) + 2\,H_2O\,(aq)$
	$2\,HI\,(aq) \rightleftharpoons H_2\,(g) + I_2\,(s)$
Temperature [37, 207, 208, 209]	$PbI_2\,(s) + CH_3NH_3I \rightleftharpoons CH_3NH_3PbI_3\,(s)$
	$CH_3NH_3PbI_3\,(s) \xrightleftharpoons{\triangle} PbI_2 + CH_3NH_3 + HI$
Light and humidity [201, 150, 210]	$CH_3NH_3PbI_3\,(s) \xrightarrow{h\nu} PbI_2 + CH_3NH_3 + HI$
	$2\,I^- \xrightarrow{h\nu} I_2 + 2\,e^-$ (at TiO_2 / $CH_3NH_3PbI_3$ interface)
	$3\,CH_3NH_3{}^+ \xrightarrow{h\nu} 3\,CH_3NH_2 + 3\,H^+$
	$I^- + I_2 + 3\,H^+ + 2\,e^- \xrightarrow{h\nu} 3\,HI$
Light [211, 212]	$CH_3NH_3PbI_3\,(s) \xrightarrow{h\nu} CH_3NH_3PbI_3{}^*$
	$O_2 \xrightleftharpoons{CH_3NH_3PbI_3{}^*} O^{*-}$
	$CH_3NH_3PbI_3 + O_2 \xrightarrow{\text{deprotonation}} CH_3NH_2 + PbI_2 + \frac{1}{2}\,I_2 + H_2O$

However, several advances in improving the chemical stability of perovskite materials have been achieved.[213] As mentioned in section (3.5.2) different sorts of HTMs were used with the final aim of protecting the perovskite layer from the ambient humidity. To conclude, carbon based HTM were proposed as a promising alternative for stable hole extraction material due to its hydrophobic properties. Snaith et al.[159] proposed the used of carbon nanotubes, Zhenget al.[214] used perthiolatedtrisulfur-annulated hexa-perihexabenzocoronene (TSHBC) doped with graphene and very recently Nazeerudin et al.[65] reported a very high stable cell when conductive carbon is employed as electrode.

Besides, different strategies such as shielding with molecularly designed materials or enclosing the perovskite molecular structure in a protecting chemical environment, as fluoropolymers, have also been reported for improved humidity and UV-induced degradation.[215, 216, 217, 184] However, increasing the stability generally results in a reduction of PCEs. Despite considerable research efforts, the ultimate goal of material used in optoelectronic application should be based on the “triple-E” terms: energy efficient, economically inexpensive and environmentally friendly. PSCs satisfy the first two criteria.

However, the presence of lead is undesirable because of its toxicity even if the amount of Pb is practically negligible in comparison to the amount used in car batteries.[218, 219, 220, 221, 222] Several studies proposed Sn as a great candidate due to its electronic properties, but it is unstable in the bivalent form.[120, 223, 224, 225, 226] On the other hand, working principles as hysteresis and charge carrier dynamics are still unresolved questions. Although hysteresis, which appears when we measure the device indifferent scan direction, was observed in DSSC,[227, 228, 229] Organic photovoltaic *(OPV)*[230] and Silicon.[231] When the voltage scan is too fast, PSCs presents a hysteresis more complex and anomalous.[232, 75] This complexity is attributed not only to intrinsic parameters as ferroelectric polarization, ion migration, carrier dynamic at interfaces or deep traps states in perovskite layer but also to extrinsic parameters, as device structure, process fabrication, measurement conditions.[233, 234, 235, 236, 237]

It is well documented that perovskite metal oxides ($BaTiO_3$, $PbTiO_3$...) present ferroelectric polarization.[238] Wei et al.[239] suggested a model where he explained that the excess polarization can generate a transient state. However, other authors[240] claimed that ferroelectric properties presented in perovskite material should be evaluated taking into account the others layers as well as operation conditions. Interfaces are strongly suggested as the place where hysteresis can be originated.[241] The unbalance carrier extraction as well as ion migration have been proposed as the main cause for hysteresis, as they entail charge accumulation (potential barrier) in the interfaces as instability of perovskite layer.[234, 235, 242, 243, 244, 245] The presumption that trap states could be the origin of hysteresis is not completely convincing as perovskite presents low trap density. Regarding extrinsic parameters, as devices are layered structured, their architecture as well as their fabrication method can induce hysteresis.[246] Following the ascending order; inverted, mesoscopic and planar architecture show less hysteresis, respectively. In addition, measuring conditions such as faster scan speed, light intensity (light soaking)[247]and temperaturev[248] also induce hysteresis. As it has been explained, different parameters can involve in the emergence of hysteresis behaviour in PSCs, therefore its existence cannot be attributed to a single mechanism but to a combination of all of them.

3.5.6 Future perspective and applications

Efficient light absorbing properties and the ability of transporting charges make perovskites, an excellent material for solar energy conversion. Challenges such as stability needs an enormous effort to be addressed, however the use of inverted architecture together with carbon-based or inorganic charge-transport material seems to be an option to overcome this issue.

Its versatility also makes perovskite material applicable in other energy production technologies such as water-splitting or CO_2 photo-reduction. Grätzel et al.[249] combined a perovskite tandem solar cell to achieve a solar-to-hydrogen efficiency of 12.3%. In addition, low temperature fabrication required in inverted architecture opens a wide range of commercial applications as flexible device. Fiber-shape [250, 251] as well as ultra light flexible PSCs [252, 253, 122, 125] are being studied as emerging wearable and electronic textiles for advanced next-generation devices.

Part IV
References

References

[1] BP. "Statistical Review of World Energy." In: *BP Stat. Rev. World Energy* June (2016), pp. 1–48. ISSN: 18766102. DOI: 10.1016/j.egypro.2013.06.172.

[2] Nídia S. Caetano et al. "New Trends in Energy Production and Utilization." In: *Energy Procedia* 107 (2017), pp. 7–14. ISSN: 1876-6102. DOI: https://doi.org/10.1016/j.egypro.2016.12.122.

[3] System Integration of Renewables (SIR). *Next Generation Wind and Solar Power - From cost to value*. France: Int. Energy Agency, 2016.

[4] Michael Safi. *Indian solar power prices hit record low, undercutting fossil fuels*. urlhttps://www.theguardian.com/environment/2017/may/10/ indian -solar-power-prices-hit-record-low-undercutting-fossil-fuels. 2017.

[5] Alexandra Sims. *China builds huge solar power station which could power a million homes*. http://www.independent.co.uk/environment/ china-builds-huge-solar-power-station-which-could-power-a - million - homes - 10446840.html. 2015.

[6] Ian Clover. *France eyes threefold solar target increase by 2023*. https:// www.pv- magazine.com/2016/04/18/ france- eyes -threefold-solar-target-increase-by-2023. 2016.

[7] SolarPower Europe. *Global Market Outlook For Solar Power (2016-2020)*. Brussels, Belgium: European Photovoltaic Industry Association, 2016.

[8] A.E. Becquerel. "Memoire sur les effects d ´electriques produits sous l´influence des rayons solaires." In: *Annalen der Physick und Chemie* 54 (1841), pp. 35–42.

[9] Bhubaneswari Parida, S. Iniyan, and Ranko Goic. "A review of solar photovoltaic technologies." In: *Renewable and Sustainable Energy Reviews* 15.3 (2011), pp. 1625–1636. ISSN: 1364-0321.

[10] Jeffery L. Gray. "The Physics of the Solar Cell." In: *Handb. Photovolt. Sci. Eng.* 2011, pp. 82–129. ISBN: 9780470721698. DOI: 10.1002/978-047-097-4704.ch3.

[11] S.W. Glunz, R. Preu, and D. Biro. "1.16 - Crystalline Silicon Solar Cells: State-of-the-Art and Future Developments." In: *Comprehensive Renewable Energy*. Ed. by Ali Sayigh. Oxford: Elsevier, 2012, pp. 353–387. ISBN: 978-0-08-087873-7. DOI: https://doi.org/10.1016/B978-0-08-087872-0.00117-7.

[12] A. Shah et al. "Photovoltaic Technology: The Case for Thin-Film Solar Cells." In: *Science* 285.5428 (1999), pp. 692–698. ISSN: 0036-8075. DOI: 10.1126/science.285.5428.692.

[13] Suzanne K Wallace, David B Mitzi, and Aron Walsh. "The Steady Rise of Kesterite Solar Cells." In: *ACS Energy Letters* 2.4 (2017), pp. 776–779.

[14] "Reported at PVSEC-36 by a research team led at DGIST in South Korea. A 0.181 cm2 solar cell was certified at 13.80% by KIER." In: (2016).

[15] Michael Grätzel. "Dye-sensitized solar cells." In: *Journal of Photochemistry and Photobiology C: Photochemistry Reviews* 4.2 (2003), pp. 145–153.

[16] Askari. Mohammad Bagher. "Introduction to Organic Solar Cells." In: *Sustainable Energy* 2.3 (2014), pp. 85–90. DOI: 10.12691/rse-2-3-2.

[17] AJ Nozik. "Quantum dot solar cells." In: *Physica E: Low-dimensional Systems and Nanostructures* 14.1 (2002), pp. 115–120.

[18] J Briscoe and S Dunn. "Extremely thin absorber solar cells based on nanostructured semiconductors." In: *Materials Science and Technology* 27.12 (2011), pp. 1741–1756. DOI: 10.1179/026708311X13135950699209.

[19] Dieter Weber. "$CH_3NH_3PbX_3$, ein Pb (II)-system mit kubischer perowskitstruktur/ $CH_3NH_3PbX_3$, a Pb (II)-system with cubic perovskite structure." In: *Zeitschrift für Naturforschung B* 33.12 (1978), pp. 1443–1445.

[20] Akihiro Kojima et al. "Organometal Halide Perovskites as Visible-Light Sensitizers for Photovoltaic Cells." In: *Journal of the American Chemical Society* 131.17 (2009), pp. 6050–6051. DOI: 10.1021/ja809598r.

[21] Jeong-Hyeok Im et al. "6.5% efficient perovskite quantum-dot-sensitized solar cell." In: *Nanoscale* 3.10 (2011), pp. 4088–4093.

[22] Hui-Seon Kim et al. "Lead iodide perovskite sensitized all-solid-state submicron thin film mesoscopic solar cell with efficiency exceeding 9%." In: *Scientific reports* 2 (2012).

[23] Woon Seok Yang et al. "High-performance photovoltaic perovskite layers fabricated through intramolecular exchange." In: *Science* 348.6240 (2015), pp. 1234–1237. ISSN: 0036-8075. DOI: 10.1126/science.aaa9272.

[24] Michael Saliba et al. "Cesium-containing triple cation perovskite solar cells: improved stability, reproducibility and high efficiency." In: *Energy & environmental science* 9.6 (2016), pp. 1989–1997.

[25] Woon Seok Yang et al. "Iodide management in formamidinium-lead-halide–based perovskite layers for efficient solar cells." In: *Science* 356.6345 (2017), pp. 1376–1379. ISSN: 0036-8075. DOI: 10.1126/science.aan2301.

[26] National Renewable Energy Laboratory (NREL). *NREL Efficiency Chart*. url http://www.nrel.gov/ncpv/images/efficiency/chart.jpg. 2017.

[27] ASTM International. *https://www.astm.org/Standards/E490.htm*. 2014.

[28] ASTM International. *https://www.astm.org/Standards/G173.htm*. 2012.

[29] Ma Green. *Solar Cells- Operating Principles, Technology and System Applications*. 1982. DOI: 10.1016/0038-092X(82)90265-1.

[30] H J Mathieu. "Auger Electron Spectroscopy." In: *Surf. Anal. – Princ. Tech.* (2009), pp. 9–45. ISSN: 1936-086X. DOI: 10.1002/9780470721582.ch2.

[31] Laura M Herz. "Charge-carrier dynamics in organic-inorganic metal halide perovskites." In: *Annual review of physical chemistry* 67 (2016), pp. 65–89.

[32] William Shockley and Hans J Queisser. "Detailed balance limit of efficiency of p-n junction solar cells." In: *Journal of applied physics* 32.3 (1961), pp. 510–519.

[33] Simon M Sze and Kwok K Ng. *Physics of semiconductor devices*. John wiley & sons, 2006.

[34] M. Borowski. *Perovskites: Structure, Properties, and Uses*. Chemical engineering methods and technology. Nova Science Publishers, 2010. ISBN: 9781616685256.

[35] Aron Walsh. "Principles of chemical bonding and band gap engineering in hybrid organic–inorganic halide perovskites." In: *The Journal of Physical Chemistry C* 119.11 (2015), pp. 5755–5760.

[36] V. M. Goldschmidt. "Die Gesetze der Krystallochemie." In: *Naturwissenschaften* 14 (May 1926), pp. 477–485. DOI: 10.1007/BF01507527.

[37] C. C Stoumpos, C. D Malliakas, and M. G Kanatzidis. "Semiconducting tin and lead iodide perovskites with organic cations: phase transitions, high mobilities, and near-infrared photoluminescent properties." In: *Inorganic chemistry* 52.15 (2013), pp. 9019–9038.

[38] Joseph S. Manser, Jeffrey A. Christians, and Prashant V. Kamat. *Intriguing Optoelectronic Properties of Metal Halide Perovskites*. 2016. DOI: 10.1021/acs.chemrev.6b00136.

[39] A. Poglitsch and D. Weber. "Dynamic disorder in methylammoniumtrihalogenoplumbates (II) observed by millimeter–wave spectroscopy." In: *The Journal of Chemical Physics* 87.11 (1987), pp. 6373–6378. DOI: 10.1063/1.453467.

[40] A. M. Glazer. "Simple ways of determining perovskite structures." In: *Acta Crystallographica Section A* 31.6 (Nov. 1975), pp. 756–762. DOI: 10.1107/S0567739475001635.

[41] AM Glazer. "The classification of tilted octahedra in perovskites." In: *Acta Crystallographica Section B: Structural Crystallography and Crystal Chemistry* 28.11 (1972), pp. 3384–3392.

[42] Giles E Eperon et al. "Formamidinium lead trihalide: a broadly tunable perovskite for efficient planar heterojunction solar cells." In: *Energy & Environmental Science* 7.3 (2014), pp. 982–988.

[43] Mark T. Weller et al. “Cubic Perovskite Structure of Black Formamidinium Lead Iodide, alpha-[$HC(NH_2)$]PbI_3, at 298 K.” In: *The Journal of Physical Chemistry Letters* 6.16 (2015), pp. 3209–3212. DOI: 10.1021/acs.jpclett.5b01432.

[44] Yu Geun Kim et al. “Cesium lead iodide solar cells controlled by annealing temperature.” In: *Physical Chemistry Chemical Physics* 19.8 (2017), pp. 6257–6263.

[45] Hyosung Choi et al. “Cesium-doped methylammonium lead iodide perovskite light absorber for hybrid solar cells.” In: *Nano Energy* 7 (2014), pp. 80–85.

[46] Giles E Eperon et al. “Inorganic caesium lead iodide perovskite solar cells.” In: *Journal of Materials Chemistry A* 3.39 (2015), pp. 19688–19695.

[47] Norman Pellet et al. “Mixed-organic-cation Perovskite photovoltaics for enhanced solar-light harvesting.” In: *Angewandte Chemie International Edition* 53.12 (2014), pp. 3151–3157.

[48] Yi Zhang et al. “Optimization of Stable Quasi-Cubic $FA_xMA_{(1-x)}PbI_3$ Perovskite Structure for Solar Cells with Efficiency beyond 20%.” In: *ACS Energy Letters* 2.4 (2017), pp. 802–806. DOI: 10.1021/acsenergylett.7b00112.

[49] Jin-Wook Lee et al. “Formamidinium and cesium hybridization for photo- and moisture-stable perovskite solar cell.” In: *Advanced Energy Materials* 5.20 (2015).

[50] Michael Saliba et al. “Incorporation of rubidium cations into perovskite solar cells improves photovoltaic performance.” In: *Science* 354.6309 (2016), pp. 206–209.

[51] Yong Sun et al. “Triple-cation mixed-halide perovskites: towards efficient, annealing-free and air-stable solar cells enabled by $Pb(SCN)_2$ additive.” In: *Scientific Reports* 7 (2017).

[52] Paul Gratia et al. “Intrinsic Halide Segregation at Nanometer Scale Determines the High Efficiency of Mixed Cation/Mixed Halide Perovskite Solar Cells.” In: *Journal of the American Chemical Society* 138.49 (2016), pp. 15821–15824. DOI: 10.1021/jacs.6b10049.

[53] Olivia Hentz, Zhibo Zhao, and Silvija Gradečak. “Impacts of ion segregation on local optical properties in mixed halide perovskite films.” In: *Nano Lett* 16.2 (2016), pp. 1485–1490.

[54] Shida Yang et al. “Recent advances in perovskite solar cells: efficiency, stability and lead-free perovskite.” In: *Journal of Materials Chemistry A* (2017).

[55] Qi Wang et al. "Thin Insulating Tunneling Contacts for Efficient and Water-Resistant Perovskite Solar Cells." In: *Advanced Materials* 28.31 (2016), pp. 6734–6739.

[56] Abhishek Swarnkar et al. "Quantum dot-induced phase stabilization of alfa-$CsPbI_3$ perovskite for high-efficiency photovoltaics." In: *Science* 354.6308 (2016), pp. 92–95. ISSN: 0036-8075. DOI: 10.1126/science.aag2700.

[57] Rachel E Beal et al. "Cesium lead halide perovskites with improved stability for tandem solar cells." In: *The journal of physical chemistry letters* 7.5 (2016), pp. 746–751.

[58] Zhen Li et al. "Stabilizing perovskite structures by tuning tolerance factor: formation of formamidinium and cesium lead iodide solid-state alloys." In: *Chemistry of Materials* 28.1 (2015), pp. 284–292.

[59] Jeong-Hyeok Im et al. "Synthesis, structure, and photovoltaic property of a nanocrystalline 2H perovskite-type novel sensitizer ($CH_3CH_2NH_3$) PbI_3." In: *Nanoscale research letters* 7.1 (2012), p. 353.

[60] Martin A Green, Anita Ho-Baillie, and Henry J Snaith. "The emergence of perovskite solar cells." In: *Nature Photonics* 8.7 (2014), pp. 506–514.

[61] Nicholas De Marco et al. "Guanidinium: A Route to Enhanced Carrier Lifetime and Open-Circuit Voltage in Hybrid Perovskite Solar Cells." In: *Nano Letters* 16.2 (2016), pp. 1009–1016. DOI: 10.1021/acs.nanolett.5b04060.

[62] Hsiang-Lin Hsu et al. "High-performance and high-durability perovskite photovoltaic devices prepared using ethylammonium iodide as an additive." In: *Journal of Materials Chemistry A* 3.17 (2015), pp. 9271–9277.

[63] Duyen H Cao et al. "2D homologous perovskites as light-absorbing materials for solar cell applications." In: *Journal of the American Chemical Society* 137.24 (2015), pp. 7843–7850.

[64] Ian C Smith et al. "A layered hybrid perovskite solar - cell absorber with enhanced moisture stability." In: *Angewandte Chemie* 126.42 (2014), pp. 114 14 - 11417.

[65] G Grancini et al. "One-Year stable perovskite solar cells by 2D/3D interface engineering." In: *Nature Communications* 8 (2017).

[66] Manuel Salado et al. "Influence of the mixed organic cation ratio in lead iodide based perovskite on the performance of solar cells." In: *Phys. Chem. Chem. Phys.* 18 (39 2016), pp. 27148–27157. DOI: 10.1039/C6CP03851D.

[67] Federico Brivio, Alison B Walker, and Aron Walsh. "Structural and electronic properties of hybrid perovskites for high-efficiency thin-film photovoltaics from first-principles." In: *Apl Materials* 1.4 (2013), p. 042111.

[68] D Solis-Ibarra, IC Smith, and HI Karunadasa. "Post-synthetic halide conversion and selective halogen capture in hybrid perovskites." In: *Chemical Science* 6.7 (2015), pp. 4054–4059.

[69] T Umebayashi et al. "Electronic structures of lead iodide based low-dimensional crystals." In: *Physical Review B* 67.15 (2003), p. 155405.

[70] Christian Wehrenfennig et al. "Charge-carrier dynamics in vapour-deposited films of the organolead halide perovskite $CH_3NH_3PbI_{(3-x)}Cl_x$." In: *Energy Environ. Sci.* 7 (7 2014), pp. 2269–2275. DOI: 10.1039/C4EE01358A.

[71] Chenyi Yi et al. "Perovskite photovoltaics with outstanding performance produced by chemical conversion of bilayer mesostructured lead halide/TiO_2 films." In: *Advanced Materials* 28.15 (2016), pp. 2964–2970.

[72] Samuel D Stranks et al. "Electron-hole diffusion lengths exceeding 1 micrometer in an organometal trihalide perovskite absorber." In: *Science* 342.6156 (2013), pp. 341–344.

[73] Eline M Hutter et al. "Direct-indirect character of the bandgap in methylammonium lead iodide perovskite." In: *Nature materials* 16.1 (2017), pp. 115–120.

[74] Tianyi Wang et al. "Indirect to direct bandgap transition in methylammonium lead halide perovskite." In: *Energy & Environmental Science* 10.2 (2017), pp. 509–515.

[75] Henry J Snaith et al. "Anomalous hysteresis in perovskite solar cells." In: *The journal of physical chemistry letters* 5.9 (2014), pp. 1511–1515.

[76] Le Quang Phuong et al. "Free Excitons and Exciton Phonon Coupling in $CH_3NH_3PbI_3$ Single Crystals Revealed by Photocurrent and Photoluminescence Measurements at Low Temperatures." In: *The Journal of Physical Chemistry Letters* 7.23 (2016), pp. 4905–4910. DOI: 10.1021/acs.jpclett.6b02432.

[77] Qianqian Lin et al. "Electro-optics of perovskite solar cells." In: *Nature Photonics* 9.2 (2015), pp. 106–112.

[78] Jacky Even, Laurent Pedesseau, and Claudine Katan. "Analysis of Multivalley and Multibandgap Absorption and Enhancement of Free Carriers Related to Exciton Screening in Hybrid Perovskites." In: *The Journal of Physical Chemistry C* 118.22 (2014), pp. 11566–11572. DOI: 10.1021/jp503337a.

[79] M. Hirasawa et al. "Magnetoabsorption of the lowest exciton in perovskite-type compound $(CH_3NH_3)PbI_3$." In: *Physica B: Condensed Matter* 201 (1994), pp. 427–430. ISSN: 0921-4526. DOI: http://dx.doi.org/10.1016/0921-4526(94)91130-4.

[80] Atsuhiko Miyata et al. "Direct measurement of the exciton binding energy and effective masses for charge carriers in an organic-inorganic tri-halide perovskite." In: *arXiv preprint arXiv:1504.07025* (2015).

[81] Mingzhen Liu, Michael B Johnston, and Henry J Snaith. "Efficient planar heterojunction perovskite solar cells by vapour deposition." In: *Nature* 501.7467 (2013), p. 395.

[82] Yuping He and Giulia Galli. "Perovskites for Solar Thermoelectric Applications: A First Principle Study of $CH_3NH_3AI_3$ (A = Pb and Sn)." In: *Chemistry of Materials* 26.18 (2014), pp. 5394–5400. DOI: 10.1021/cm5026766.

[83] Giacomo Giorgi et al. "Small photocarrier effective masses featuring ambipolar transport in methylammonium lead iodide perovskite: A density functional analysis." In: *The journal of physical chemistry letters* 4.24 (2013), pp. 4213–4216.

[84] Guichuan Xing et al. "Long-range balanced electron-and hole-transport lengths in organic-inorganic $CH_3NH_3PbI_3$." In: *Science* 342.6156 (2013), pp. 344–347.

[85] Thomas M Brenner et al. "Hybrid organic inorganic perovskites: low-cost semiconductors with intriguing charge-transport properties." In: *Nature Reviews Materials* 1 (2016), p. 15007.

[86] Andreas Baumann et al. "Identification of trap states in perovskite solar cells." In: *The journal of physical chemistry letters* 6.12 (2015), pp. 2350–2354.

[87] Kenichiro Tanaka et al. "Comparative study on the excitons in lead-halide-based perovskite-type crystals $CH_3NH_3PbBr_3$–$CH_3NH_3PbI_3$." In: *Solid state communications* 127.9 (2003), pp. 619–623.

[88] Christian Wehrenfennig et al. "High charge carrier mobilities and lifetimes in organolead trihalide perovskites." In: *Advanced materials* 26.10 (2014), pp. 1584–1589.

[89] Eran Edri et al. "Elucidating the charge carrier separation and working mechanism of $CH_3NH_3PbI_{(3-x)}Cl_x$ perovskite solar cells." In: *Nature communications* 5 (2014), p. 3461.

[90] Hsin-Sheng Duan et al. "The identification and characterization of defect states in hybrid organic–inorganic perovskite photovoltaics." In: *Physical chemistry chemical physics* 17.1 (2015), pp. 112–116.

[91] Makhsud I Saidaminov et al. "High-quality bulk hybrid perovskite single crystals within minutes by inverse temperature crystallization." In: *Nature communications* 6 (2015), p. 7586.

[92] Dong Shi et al. "Low trap-state density and long carrier diffusion in organolead trihalide perovskite single crystals." In: *Science* 347.6221 (2015), pp. 519–522.

[93] Qingfeng Dong et al. "Electron-hole diffusion lengths> 175 μm in solution-grown $CH_3NH_3PbI_3$ single crystals." In: *Science* 347.6225 (2015), pp. 967–970.

[94] Rui Sheng et al. “Methylammonium lead bromide perovskite-based solar cells by vapor-assisted deposition.” In: *The Journal of Physical Chemistry C* 119.7 (2015), pp. 3545–3549.

[95] Meng Zhang et al. “Composition-dependent photoluminescence intensity and prolonged recombination lifetime of perovskite $CH_3NH_3PbBr_{(3-x)}Cl_x$ films.” In: *Chemical Communications* 50.79 (2014), pp. 11727–11730.

[96] Nir Kedem et al. “Light-induced increase of electron diffusion length in ap–n junction type $CH_3NH_3PbBr_3$ perovskite solar cell.” In: *The journal of physical chemistry letters* 6.13 (2015), pp. 2469–2476.

[97] RJ Nelson and RG Sobers. “Minority-carrier lifetimes and internal quantum efficiency of surface-free GaAs.” In: *Journal of Applied Physics* 49.12 (1978), pp. 6103–6108.

[98] Arianna Marchioro et al. “Unravelling the mechanism of photoinduced charge transfer processes in lead iodide perovskite solar cells.” In: *Nature photonics* 8.3 (2014), pp. 250–255.

[99] Teddy Salim et al. “Perovskite-based solar cells: impact of morphology and device architecture on device performance.” In: *Journal of Materials Chemistry A* 3.17 (2015), pp. 8943–8969.

[100] Aravind Kumar Chandiran et al. “Quantum-confined ZnO nanoshell photoanodes for mesoscopic solar cells.” In: *Nano letters* 14.3 (2014), pp. 1190–1195.

[101] Gill Sang Han et al. “Retarding charge recombination in perovskite solar cells using ultrathin MgO-coated TiO_2 nanoparticulate films.” In: *Journal of Materials Chemistry A* 3.17 (2015), pp. 9160–9164.

[102] Khalid Mahmood et al. “Highly efficient perovskite solar cells based on a nanostructured WO_3–TiO_2 core–shell electron transporting material.” In: *Journal of Materials Chemistry A* 3.17 (2015), pp. 9051–9057.

[103] Marie-Isabelle Baraton. “Nano-TiO_2 for dye-sensitized solar cells.” In: *Recent patents on nanotechnology* 6.1 (2012), pp. 10–15.

[104] Guangda Niu et al. “Study on the stability of $CH_3NH_3PbI_3$ films and the effect of post-modification by aluminum oxide in all-solid-state hybrid solar cells.” In: *Journal of Materials Chemistry A* 2.3 (2014), pp. 705–710.

[105] Michael M Lee et al. “Efficient hybrid solar cells based on meso- superstructured organometal halide perovskites.” In: *Science* 338.6107 (2012), pp. 643–647.

[106] Sun Hye Hwang et al. “Size-controlled SiO_2 nanoparticles as scaffold layers in thin-film perovskite solar cells.” In: *Journal of Materials Chemistry A* 2.39 (2014), pp. 16429–16433.

[107] Dongqin Bi et al. “Using a two-step deposition technique to prepare perovskite ($CH_3NH_3PbI_3$) for thin film solar cells based on ZrO_2 and TiO_2 mesostructures.” In: *Rsc Advances* 3.41 (2013), pp. 18762–18766.

[108] Yantao Shi et al. “$CH_3NH_3PbI_3$ and $CH_3NH_3PbI_{(3-x)}Cl_x$ in Planar or Mesoporous Perovskite Solar Cells: Comprehensive Insight into the Dependence of Performance on Architecture.” In: *The Journal of Physical Chemistry C* 119.28 (2015), pp. 15868–15873.

[109] Byeong Jo Kim et al. “Highly efficient and bending durable perovskite solar cells: toward a wearable power source.” In: *Energy & Environmental Science* 8.3 (2015), pp. 916–921.

[110] Xin Li et al. “Efficient perovskite solar cells depending on TiO_2 nanorod arrays.” In: *ACS applied materials & interfaces* 8.33 (2016), pp. 21358–21365.

[111] F Javier Ramos et al. “Nanocolumnar 1-dimensional TiO_2 photoanodes deposited by PVD-OAD for perovskite solar cell fabrication.” In: *Journal of Materials Chemistry A* 3.25 (2015), pp. 13291–13298.

[112] Jianhang Qiu et al. “All-solid-state hybrid solar cells based on a new organometal halide perovskite sensitizer and one - dimensional TiO_2 nanowire arrays.” In: *Nanoscale* 5.8 (2013), pp. 3245–3248.

[113] Shilong Jiao et al. “Ultrathin TiO_2 nanosheets synthesized using a high pressure solvothermal method and the enhanced photoresponse performance of $CH_3NH_3PbI_3$–TiO_2 composite films.” In: *RSC Advances* 7.34 (2017), pp. 20845–20850.

[114] Rajeshkumar S Hyam et al. “Room temperature synthesis of rutile TiO_2 hierarchical nanoneedle flower morphology for dye sensitized solar cell.” In: *Journal of nanoscience and nanotechnology* 10.9 (2010), pp. 5894–5898.

[115] Peng Qin et al. “Yttrium-substituted nanocrystalline TiO_2 photoanodes for perovskite based heterojunction solar cells.” In: *Nanoscale* 6.3 (2014), pp. 1508–1514.

[116] Xiang Zhang et al. “Sn-doped TiO_2 nanorod arrays and application in perovskite solar cells.” In: *RSC Advances* 4.109 (2014), pp. 64001–64005.

[117] K Manseki et al. “Mg-doped TiO_2 nanorods improving open-circuit voltages of ammonium lead halide perovskite solar cells.” In: *RSC Advances* 4.19 (2014), pp. 9652–9655.

[118] Juan Dong et al. “Impressive enhancement in the cell performance of ZnO nanorod-based perovskite solar cells with Al-doped ZnO interfacial modification.” In: *Chemical Communications* 50.87 (2014), pp. 13381–13384.

[119] Fabrizio Giordano et al. “Enhanced electronic properties in mesoporous TiO_2 via lithium doping for high-efficiency perovskite solar cells.” In: *Nature communications* 7 (2016), p. 10379.

[120] Elham Halvani Anaraki et al. “Highly efficient and stable planar perovskite solar cells by solution-processed tin oxide.” In: *Energy & Environmental Science* 9.10 (2016), pp. 3128–3134.

[121] Weijun Ke et al. “Low-temperature solution-processed tin oxide as an alternative electron transporting layer for efficient perovskite solar cells.” In: *Journal of the American Chemical Society* 137.21 (2015), pp. 6730–6733.

[122] Cristina Roldán-Carmona et al. “Flexible high efficiency perovskite solar cells.” In: *Energy & Environmental Science* 7.3 (2014), pp. 994–997.

[123] Dianyi Liu and Timothy L Kelly. “Perovskite solar cells with a planar heterojunction structure prepared using room-temperature solution processing techniques.” In: *Nature photonics* 8.2 (2014), pp. 133–138.

[124] Kai Wang et al. “Bulk heterojunction perovskite hybrid solar cells with large fill factor.” In: *Energy & Environmental Science* 8.4 (2015), pp. 1245–1255.

[125] Jingbi You et al. “Low-temperature solution-processed perovskite solar cells with high efficiency and flexibility.” In: (2014).

[126] Chaoyang Kuang et al. “Highly efficient electron transport obtained by doping PCBM with graphdiyne in planar-heterojunction perovskite solar cells.” In: *Nano letters* 15.4 (2015), pp. 2756–2762.

[127] Eran Edri et al. “Why lead methylammonium tri-iodide perovskite-based solar cells require a mesoporous electron transporting scaffold (but not necessarily a hole conductor).” In: *Nano letters* 14.2 (2014), pp. 1000–1004.

[128] Emilio J Juarez-Perez et al. “Role of the selective contacts in the performance of lead halide perovskite solar cells.” In: *The journal of physical chemistry letters* 5.4 (2014), pp. 680–685.

[129] Kai Zhang et al. “A thermally and electrochemically stable organic hole-transporting material with an adamantane central core and triarylamine moieties.” In: *Synthetic Metals* 162.5 (2012), pp. 490–496.

[130] Rafael S Sanchez and Elena Mas-Marza. “Light-induced effects on Spiro-OMeTAD films and hybrid lead halide perovskite solar cells.” In: *Solar Energy Materials and Solar Cells* 158 (2016), pp. 189–194.

[131] Hyeju Choi et al. “Efficient perovskite solar cells with 13.63% efficiency based on planar triphenylamine hole conductors.” In: *Chemistry-A European Journal* 20.35 (2014), pp. 10894–10899.

[132] Kwangseok Do et al. “Star-shaped hole transporting materials with a triazine unit for efficient perovskite solar cells.” In: *Chemical Communications* 50.75 (2014), pp. 10971–10974.

[133] Peng Qin et al. “Perovskite solar cells with 12.8% efficiency by using conjugated quinolizino acridine based hole transporting material.” In: *Journal of the American Chemical Society* 136.24 (2014), pp. 8516–8519.

[134] Paul Gratia et al. “A Methoxydiphenylamine-Substituted Carbazole Twin Derivative: An Efficient Hole-Transporting Material for Perovskite Solar Cells.” In: *Angewandte Chemie International Edition* 54.39 (2015), pp. 11409–11413.

[135] Pei-Yang Su et al. “A multifunctional poly-N-vinylcarbazole interlayer in perovskite solar cells for high stability and efficiency: a test with new triazatruxene-based hole transporting materials.” In: *Journal of Materials Chemistry A* 5.5 (2017), pp. 1913–1918.

[136] Paramaguru Ganesan et al. “A simple spiro-type hole transporting material for efficient perovskite solar cells.” In: *Energy & Environmental Science* 8.7 (2015), pp. 1986–1991.

[137] Kasparas Rakstys et al. “Triazatruxene-based hole transporting materials for highly efficient perovskite solar cells.” In: *Journal of the American Chemical Society* 137.51 (2015), pp. 16172–16178.

[138] F Javier Ramos et al. “Rational design of triazatruxene-based hole conductors for perovskite solar cells.” In: *Rsc Advances* 5.66 (2015), pp. 53426–53432.

[139] Laura Calió et al. “Hole-Transport Materials for Perovskite Solar Cells.” In: *Angewandte Chemie International Edition* (2016).

[140] Eva Bundgaard and Frederik C Krebs. “Low band gap polymers for organic photovoltaics.” In: *Solar Energy Materials and Solar Cells* 91.11 (2007), pp. 954–985.

[141] Olga Malinkiewicz et al. “Perovskite solar cells employing organic charge-transport layers.” In: *Nature Photonics* 8.2 (2014), pp. 128–132.

[142] Yaoming Xiao et al. “Efficient bifacial perovskite solar cell based on a highly transparent poly (3, 4-ethylenedioxythiophene) as the p-type hole-transporting material.” In: *Journal of Power Sources* 306 (2016), pp. 171–177.

[143] Dibyashree Koushik et al. “Atomic Layer Deposition Enabled Perovskite/PEDOT Solar Cells in a Regular n -i -p Architectural Design.” In: *Advanced Materials Interfaces* (2017).

[144] Peng You et al. “Efficient semitransparent perovskite solar cells with graphene electrodes.” In: *Advanced Materials* 27.24 (2015), pp. 3632–3638.

[145] Yunlong Guo et al. “Enhancement in the efficiency of an organic–inorganic hybrid solar cell with a doped P3HT hole-transporting layer on a void-free perovskite active layer.” In: *Journal of Materials Chemistry A* 2.34 (2014), pp. 13827–13830.

[146] Francesco Di Giacomo et al. “High efficiency $CH_3NH_3PbI_{(3-x)}Cl_x$ perovskite solar cells with poly (3-hexylthiophene) hole transport layer.” In: *Journal of Power Sources* 251 (2014), pp. 152–156.

[147] Mahshid Ahmadi et al. “Effect of Photogenerated Dipoles in the Hole Transport Layer on Photovoltaic Performance of Organic–Inorganic Perovskite Solar Cells.” In: *Advanced Energy Materials* 7.4 (2017).

[148] Jan C Brauer et al. “Charge transfer dynamics from organometal halide perovskite to polymeric hole transport materials in hybrid solar cells.” In: *The journal of physical chemistry letters* 6.18 (2015), pp. 3675–3681.

[149] Qi Wang, Cheng Bi, and Jinsong Huang. “Doped hole transport layer for efficiency enhancement in planar heterojunction organolead trihalide perovskite solar cells.” In: *Nano Energy* 15 (2015), pp. 275–280.

[150] Jin Hyuck Heo et al. “Efficient inorganic-organic hybrid heterojunction solar cells containing perovskite compound and polymeric hole conductors.” In: *Nature photonics* 7.6 (2013), pp. 486–491.

[151] Nam Joong Jeon et al. “Compositional engineering of perovskite materials for high-performance solar cells.” In: *Nature* 517.7535 (2015), p. 476.

[152] Antonio Agresti et al. “Graphene–Perovskite Solar Cells Exceed 18% Efficiency: A Stability Study.” In: *ChemSusChem* 9.18 (2016), pp. 2609–2619.

[153] Severin N Habisreutinger et al. “Carbon nanotube/polymer composites as a highly stable hole collection layer in perovskite solar cells.” In: *Nano letters* 14.10 (2014), pp. 5561–5568.

[154] Zhiyong Liu et al. “Using a low-temperature carbon electrode for preparing hole-conductor-free perovskite heterojunction solar cells under high relative humidity.” In: *Nanoscale* 8.13 (2016), pp. 7017–7023.

[155] Jun-Yuan Jeng et al. “$CH_3NH_3PbI_3$ Perovskite/Fullerene Planar- Heterojunction Hybrid Solar Cells.” In: *Advanced Materials* 25.27 (2013), pp. 3727–3732.

[156] Jixian Xu et al. “Perovskite–fullerene hybrid materials suppress hysteresis in planar diodes.” In: *Nature communications* 6 (2015).

[157] Agnese Abrusci et al. “High-performance perovskite-polymer hybrid solar cells via electronic coupling with fullerene monolayers.” In: *Nano letters* 13.7 (2013), pp. 3124–3128.

[158] Muge Acik and Seth B Darling. “Graphene in perovskite solar cells: device design, characterization and implementation.” In: *Journal of Materials Chemistry A* 4.17 (2016), pp. 6185–6235.

[159] Severin N. Habisreutinger, Robin J. Nicholas, and Henry J. Snaith. “Carbon Nanotubes in Perovskite Solar Cells.” In: *Advanced Energy Materials* 7.10 (2017), 1601839–n/a. ISSN: 1614-6840. DOI: 10.1002/aenm.201601839.

[160] Jeffrey A Christians, Raymond CM Fung, and Prashant V Kamat. “An inorganic hole conductor for organo-lead halide perovskite solar cells. Improved hole conductivity with copper iodide.” In: *Journal of the American Chemical Society* 136.2 (2013), pp. 758–764.

[161] Saba Gharibzadeh et al. “Two-step physical deposition of a compact CuI Hole-Transport layer and the formation of an interfacial species in perovskite solar cells.” In: *ChemSusChem* 9.15 (2016), pp. 1929–1937.

[162] Gaveshana A Sepalage et al. “Copper (I) iodide as hole-conductor in planar perovskite solar cells: probing the origin of J–V hysteresis.” In: *Advanced Functional Materials* 25.35 (2015), pp. 5650–5661.

[163] Weihai Sun et al. “Room-temperature and solution-processed copper iodide as the hole transport layer for inverted planar perovskite solar cells.” In: *Nanoscale* 8.35 (2016), pp. 15954–15960.

[164] Xiaobao Xu et al. “Hole selective NiO contact for efficient perovskite solar cells with carbon electrode.” In: *Nano letters* 15.4 (2015), pp. 2402–2408.

[165] Seongrok Seo et al. “An ultra-thin, un-doped NiO hole transporting layer of highly efficient (16.4%) organic–inorganic hybrid perovskite solar cells.” In: *Nanoscale* 8.22 (2016), pp. 11403–11412.

[166] Senyun Ye et al. “CuSCN-based inverted planar perovskite solar cell with an average PCE of 15.6%.” In: *Nano letters* 15.6 (2015), pp. 3723–3728.

[167] Minsu Jung et al. “Thermal Stability of CuSCN Hole Conductor-Based Perovskite Solar Cells.” In: *ChemSusChem* 9.18 (2016), pp. 2592–2596.

[168] Senyun Ye et al. “A Breakthrough Efficiency of 19.9% Obtained in Inverted Perovskite Solar Cells by Using an Efficient Trap State Passivator Cu (Thiourea) I.” In: *Journal of the American Chemical Society* (2017).

[169] Julian Burschka et al. “Sequential deposition as a route to high- performance perovskite - sensitized solar cells.” In: *Nature* 499.7458 (2013), p. 316.

[170] Nam Joong Jeon et al. “Solvent engineering for high-performance inorganic - organic hybrid perovskite solar cells.” In: *Nature materials* 13.9 (2014), pp. 897–903.

[171] T Jesper Jacobsson et al. “Unreacted PbI_2 as a double-edged sword for enhancing the performance of perovskite solar cells.” In: *J. Am. Chem. Soc* 138.32 (2016), pp. 10331–10343.

[172] Duyen H Cao et al. “Remnant PbI_2, an unforeseen necessity in high-efficiency hybrid perovskite-based solar cells?” In: *Apl Materials* 2.9 (2014), p. 091101.

[173] C Roldan-Carmona et al. “High efficiency methylammonium lead triiodide perovskite solar cells: the relevance of non-stoichiometric precursors.” In: *Energy & Environmental Science* 8.12 (2015), pp. 3550–3556.

[174] Tian Du et al. “Formation, location and beneficial role of PbI_2 in lead halide perovskite solar cells.” In: *Sustainable Energy & Fuels* 1.1 (2017), pp. 119–126.

[175] Amalie Dualeh et al. “Effect of annealing temperature on film morphology of organic–inorganic hybrid pervoskite solid-state solar cells.” In: *Advanced Functional Materials* 24.21 (2014), pp. 3250–3258.

[176] Devendra Khatiwada et al. “Efficient perovskite solar cells by temperature control in single and mixed halide precursor solutions and films.” In: *The Journal of Physical Chemistry C* 119.46 (2015), pp. 25747–25753.

[177] Lung-Chien Chen et al. “Annealing Effect on $(FAPbI_3)_{(1-x)}(MAPbBr_3)_x$ Perovskite Films in Inverted-Type Perovskite Solar Cells.” In: *Materials* 9.9 (2016), p. 747.

[178] Like Huang et al. “Multi-step slow annealing perovskite films for high performance planar perovskite solar cells.” In: *Solar Energy Materials and Solar Cells* 141 (2015), pp. 377–382.

[179] Wenzhe Li et al. “Controllable grain morphology of perovskite absorber film by molecular self-assembly toward efficient solar cell exceeding 17%.” In: *Journal of the American Chemical Society* 137.32 (2015), pp. 10399–10405.

[180] S Paek et al. “From Nano-to Micrometer Scale: The Role of Antisolvent Treatment on High Performance Perovskite Solar Cells.” In: *Chemistry of Materials* 29.8 (2017), pp. 3490–3498.

[181] Yu Yu et al. “Ultrasmooth Perovskite Film via Mixed Anti-Solvent Strategy with Improved Efficiency.” In: *ACS applied materials & interfaces* 9.4 (2017), pp. 3667–3676.

[182] Hansol Kim, Hanbin Jeong, and Jae Kwan Lee. “Highly Efficient, Reproducible, Uniform $(CH_3NH_3)PbI_3$ Layer by Processing Additive Dripping for Solution-Processed Planar Heterojunction Perovskite Solar Cells.” In: *Chemistry–An Asian Journal* 11.17 (2016), pp. 2399–2405.

[183] Eran Edri et al. “Chloride inclusion and hole transport material doping to improve methyl ammonium lead bromide perovskite-based high open-circuit voltage solar cells.” In: *The journal of physical chemistry letters* 5.3 (2014), pp. 429–433.

[184] Anyi Mei et al. “A hole-conductor–free, fully printable mesoscopic perovskite solar cell with high stability.” In: *Science* 345.6194 (2014), pp. 295–298.

[185] Jingbi You et al. “Moisture assisted perovskite film growth for high performance solar cells.” In: *Applied Physics Letters* 105.18 (2014), p. 183902.

[186] Harry M Cronin et al. “Effects of ambient humidity on the optimum annealing time of mixed-halide Perovskite solar cells.” In: *Nanotechnology* 28.11 (2017), p. 114004.

[187] Qidong Tai et al. “Efficient and stable perovskite solar cells prepared in ambient air irrespective of the humidity.” In: *Nature communications* 7 (2016).

[188] Clara Aranda et al. “Formation criteria of high efficiency perovskite solar cells under ambient conditions.” In: *Sustainable Energy & Fuels* 1.3 (2017), pp. 540–547.

[189] Xiong Li et al. “A vacuum flash–assisted solution process for high-efficiency large-area perovskite solar cells.” In: *Science* 353.6294 (2016), pp. 58–62.

[190] Yu-Hsien Chiang et al. “Low-Pressure Vapor-Assisted Solution Process for Thiocyanate-Based Pseudohalide Perovskite Solar Cells.” In: *ChemSusChem* 9.18 (2016), pp. 2620–2627.

[191] Huanping Zhou, Qi Chen, and Yang Yang. “Vapor-assisted solution process for perovskite materials and solar cells.” In: *MRS Bulletin* 40.8 (2015), pp. 667–673.

[192] Qi Chen et al. “Planar heterojunction perovskite solar cells via vapor-assisted solution process.” In: *Journal of the American Chemical Society* 136.2 (2013), pp. 622–625.

[193] Victor W Bergmann et al. “Real-space observation of unbalanced charge distribution inside a perovskite-sensitized solar cell.” In: *Nature communications* 5 (2014), p. 5001.

[194] Jiang-Jun Li et al. “Influence of N, N-Dimethylformamide Annealing on the Local Electrical Properties of Organometal Halide Perovskite Solar Cells: an Atomic Force Microscopy Investigation.” In: *ACS applied materials & interfaces* 8.39 (2016), pp. 26002–26007.

[195] Manuel Salado et al. “Impact of moisture on efficiency-determining electronic processes in perovskite solar cells.” In: *Journal of Materials Chemistry A* (2017).

[196] J Ross Macdonald and E Barsoukov. “Impedance spectroscopy: theory, experiment, and applications.” In: *History* 1.8 (2005).

[197] Amalie Dualeh et al. “Impedance spectroscopic analysis of lead iodide perovskite-sensitized solid-state solar cells.” In: *Acs Nano* 8.1 (2013), pp. 362–373.

[198] Rafael S Sanchez et al. “Slow dynamic processes in lead halide perovskite solar cells. Characteristic times and hysteresis.” In: *The journal of physical chemistry letters* 5.13 (2014), pp. 2357–2363.

[199] Isaac Zarazua, Juan Bisquert, and Germà Garcia-Belmonte. “Light-induced space-charge accumulation zone as photovoltaic mechanism in perovskite solar cells.” In: *The journal of physical chemistry letters* 7.3 (2016), pp. 525–528.

[200] Mark Hutchins. *Ames Laboratory researchers can see light hitting a solar cell*. urlhttps://www.pv-magazine.com/2017/06/07/ames-laboratory - researchers - can - see- light-hitting-a-solar-cell. 2017.

[201] Haifeng Yuan et al. “Degradation of methylammonium lead iodide perovskite structures through light and electron beam driven ion migration.” In: *The journal of physical chemistry letters* 7.3 (2016), pp. 561–566.

[202] Antonio Guerrero et al. “Interfacial degradation of planar lead halide perovskite solar cells.” In: *ACS nano* 10.1 (2015), pp. 218–224.

[203] Ravi K Misra et al. “Temperature-and component-dependent degradation of perovskite photovoltaic materials under concentrated sunlight.” In: *The journal of physical chemistry letters* 6.3 (2015), pp. 326–330.

[204] Taame Abraha Berhe et al. “Organometal halide perovskite solar cells: degradation and stability.” In: *Energy & Environmental Science* 9.2 (2016), pp. 323–356.

[205] Ze Wang et al. “Stability of perovskite solar cells: a prospective on the substitution of the A cation and X anion.” In: *Angewandte Chemie International Edition* (2016).

[206] Shahab Ahmad et al. “In situ intercalation dynamics in inorganic–organic layered perovskite thin films.” In: *ACS applied materials & interfaces* 6.13 (2014), pp. 10238–10247.

[207] Jarvist M Frost et al. “Atomistic origins of high-performance in hybrid halide perovskite solar cells.” In: *Nano letters* 14.5 (2014), pp. 2584–2590.

[208] Bert Conings et al. “Intrinsic thermal instability of methylammonium lead trihalide perovskite.” In: *Advanced Energy Materials* 5.15 (2015).

[209] Yasmina Dkhissi et al. “Stability comparison of perovskite solar cells based on zinc oxide and titania on polymer substrates.” In: *ChemSusChem* 9.7 (2016), pp. 687–695.

[210] Daniel Bryant et al. “Correction: Light and oxygen induced degradation limits the operational stability of methylammonium lead triiodide perovskite solar cells.” In: *Energy & Environmental Science* 9.5 (2016), pp. 1850–1850.

[211] Tomas Leijtens et al. “Overcoming ultraviolet light instability of sensitized TiO_2 with meso-superstructured organometal tri-halide perovskite solar cells.” In: *Nature communications* 4 (2013), p. 2885.

[212] Nicholas Aristidou et al. “The role of oxygen in the degradation of methylammonium lead trihalide perovskite photoactive layers.” In: *Angewandte Chemie International Edition* 54.28 (2015), pp. 8208–8212.

[213] Andrew J Pearson et al. “Oxygen Degradation in Mesoporous Al_2O_3-$CH_3NH_3PbI_{(3-x)}Cl_x$ Perovskite Solar Cells: Kinetics and Mechanisms.” In: *Advanced Energy Materials* 6.13 (2016).

[214] Nam-Gyu Park et al. “Towards stable and commercially available perovskite solar cells.” In: *Nature Energy* 1 (2016), p. 16152.

[215] Jing Cao et al. “Well-defined thiolated nanographene as hole-transporting material for efficient and stable perovskite solar cells.” In: *Journal of the American Chemical Society* 137.34 (2015), pp. 10914–10917.

[216] Xiong Li et al. “Improved performance and stability of perovskite solar cells by crystal crosslinking with alkylphosphonic acid ω-ammonium chlorides.” In: *Nature chemistry* 7.9 (2015), pp. 703–711.

[217] J Calabrese et al. “Preparation and characterization of layered lead halide compounds.” In: *Journal of the American Chemical Society* 113.6 (1991), pp. 2328–2330.

[218] Federico Bella et al. “Improving efficiency and stability of perovskite solar cells with photocurable fluoropolymers.” In: *Science* (2016), aah4046.

[219] Aslihan Babayigit et al. “Toxicity of organometal halide perovskite solar cells.” In: *Nature materials* 15 (2016), pp. 247–251.

[220] Pablo P Boix et al. “Perovskite solar cells: beyond methylammonium lead iodide.” In: *The journal of physical chemistry letters* 6.5 (2015), pp. 898–907.

[221] Lucia Serrano-Lujan et al. “Tin-and Lead-Based Perovskite Solar Cells under Scrutiny: An Environmental Perspective.” In: *Advanced Energy Materials* 5.20 (2015).

[222] Feliciano Giustino and Henry J Snaith. “Toward Lead-Free Perovskite Solar Cells.” In: (2016).

[223] Andreas Binek et al. “Recycling Perovskite Solar Cells To Avoid Lead Waste.” In: *ACS applied materials & interfaces* 8.20 (2016), pp. 12881–12886.

[224] Nakita K Noel et al. “Lead-free organic–inorganic tin halide perovskites for photovoltaic applications.” In: *Energy & Environmental Science* 7.9 (2014), pp. 3061–3068.

[225] Kenneth P Marshall, Richard I Walton, and Ross A Hatton. “Tin perovskite/fullerene planar layer photovoltaics: improving the efficiency and stability of lead-free devices.” In: *Journal of Materials Chemistry A* 3.21 (2015), pp. 11631–11640.

[226] Yukari Takahashi et al. “Charge-transport in tin- iodide perovskite $CH_3NH_3SnI_3$: origin of high conductivity.” In: *Dalton Transactions* 40.20 (2011), pp. 5563–5568.

[227] Mulmudi Hemant Kumar et al. “Lead-free halide perovskite solar cells with high photocurrents realized through vacancy modulation.” In: *Advanced Materials* 26.41 (2014), pp. 7122–7127.

[228] Anders Hagfeldt et al. “Dye-sensitized solar cells.” In: *Chemical reviews* 110.11 (2010), pp. 6595–6663.

[229] Fan Wu et al. “Hysteresis analysis in dye-sensitized solar cells based on external bias field effects.” In: *Journal of Power Sources* 342 (2017), pp. 704–708.

[230] Neng-Jye Yang, Chien-Shiun Liao, and Show-An Chen. “Hysteresis in Conjugated Polymer Thin Film Transistors Generated by Chain Relaxation.” In: *Advanced Functional Materials* 20.6 (2010), pp. 1000–1004.

[231] Horng-Chih Lin et al. “Origin of hysteresis in current-voltage characteristics of polycrystalline silicon thin-film transistors.” In: *Journal of Applied Physics* 105.5 (2009), p. 054502.

[232] Bo Chen et al. “Origin of J–V hysteresis in perovskite solar cells.” In: *The journal of physical chemistry letters* 7.5 (2016), pp. 905–917.

[233] Simone Meloni et al. “Ionic polarization-induced current–voltage hysteresis in $CH_3NH_3PbX_3$ perovskite solar cells.” In: *Nature communications* 7 (2016), p. 10334.

[234] Cheng Li et al. “Iodine migration and its effect on hysteresis in perovskite solar cells.” In: *Advanced Materials* 28.12 (2016), pp. 2446–2454.

[235] Christopher Eames et al. “Ionic transport in hybrid lead iodide perovskite solar cells.” In: *Nature communications* 6 (2015), p. 7497.

[236] Yiliang Wu et al. “On the Origin of Hysteresis in Perovskite Solar Cells.” In: *Advanced Functional Materials* 26.37 (2016), pp. 6807–6813.

[237] Hui-Seon Kim et al. “Control of I–V hysteresis in $CH_3NH_3PbI_3$ perovskite solar cell.” In: *The journal of physical chemistry letters* 6.22 (2015), pp. 4633–4639.

[238] Ronald E Cohen. “Origin of ferroelectricity in perovskite oxides.” In: *Nature* 358.6382 (1992), pp. 136–138.

[239] Jing Wei et al. “Hysteresis analysis based on the ferroelectric effect in hybrid perovskite solar cells.” In: *The journal of physical chemistry letters* 5.21 (2014), pp. 3937–3945.

[240] Zhen Fan et al. “Ferroelectricity of $CH_3NH_3PbI_3$ perovskite.” In: *The journal of physical chemistry letters* 6.7 (2015), pp. 1155–1161.

[241] Bo Wu et al. “Charge Accumulation and Hysteresis in Perovskite-Based Solar Cells: An Electro-Optical Analysis.” In: *Advanced Energy Materials* 5.19 (2015).

[242] Yongbo Yuan and Jinsong Huang. “Ion migration in organometal trihalide perovskite and its impact on photovoltaic efficiency and stability.” In: *Accounts of chemical research* 49.2 (2016), pp. 286–293.

[243] Yuchuan Shao et al. “Grain boundary dominated ion migration in polycrystalline organic–inorganic halide perovskite films.” In: *Energy & Environmental Science* 9.5 (2016), pp. 1752–1759.

[244] Kenjiro Miyano et al. “Hysteresis, stability, and ion migration in lead halide perovskite photovoltaics.” In: *The journal of physical chemistry letters* 7.12 (2016), pp. 2240–2245.

[245] Jon M Azpiroz et al. “Defect migration in methylammonium lead iodide and its role in perovskite solar cell operation.” In: *Energy & Environmental Science* 8.7 (2015), pp. 2118–2127.

[246] Hui-Seon Kim and Nam-Gyu Park. “Parameters affecting I–V hysteresis of $CH_3NH_3PbI_3$ perovskite solar cells: effects of perovskite crystal size and mesoporous TiO_2 layer.” In: *The journal of physical chemistry letters* 5.17 (2014), pp. 2927–2934.

[247] EL Unger et al. “Hysteresis and transient behavior in current–voltage measurements of hybrid-perovskite absorber solar cells.” In: *Energy & Environmental Science* 7.11 (2014), pp. 3690–3698.

[248] Luis K Ono et al. “Temperature-dependent hysteresis effects in perovskite-based solar cells.” In: *Journal of Materials Chemistry A* 3.17 (2015), pp. 9074–9080.

[249] Jingshan Luo et al. “Water photolysis at 12.3% efficiency via perovskite photovoltaics and Earth-abundant catalysts.” In: *Science* 345.6204 (2014), pp. 1593–1596.

[250] Longbin Qiu et al. “Integrating perovskite solar cells into a flexible fiber.” In: *Angewandte Chemie International Edition* 53.39 (2014), pp. 10425–10428.

[251] Jue Deng et al. “Elastic perovskite solar cells.” In: *J. Mater. Chem. A* 3 (42 2015), pp. 21070–21076. DOI: 10.1039/C5TA06156C.

[252] Pablo Docampo et al. “Efficient organometal trihalide perovskite planar-heterojunction solar cells on flexible polymer substrates.” In: *Nature communications* 4 (2013).

[253] Xiaoyan Wang et al. “TiO_2 nanotube arrays based flexible perovskite solar cells with transparent carbon nanotube electrode.” In: *Nano Energy* 11 (2015), pp. 728–735.

Part V
Publication included in this Thesis

4 Publications included in this thesis

Chapter 1: "Study of the effect in the selective contacts in the charge extraction process"

Publication 1

"Interface Play between Perovskite and Hole Selective Layer on the Performance and Stability of Perovskite Solar Cells"

Manuel Salado, Jesus Idigoras, Laura Calio, Samrana Kazim, Mohammad Khaja Nazeeruddin, Juan A. Anta, and Shahzada Ahmad, ACS Applied Materials and Interfaces 2016 8 (50), 34414-34421

https://doi.org/10.1021/acsami.6b12236

Publication 2

"1-dimensional TiO_2 nano-forests as photoanodes for efficient and stable perovskite solar cells fabrication"

Manuel Salado, Manuel Oliva-Ramirez, SamranaKazim, Agustín R. González-Elipe, Shahzada Ahmad, Nano Energy, Volume 35, May 2017, Pages 215-222, ISSN 2211-2855

https://doi.org/10.1016/j.nanoen.2017.03.034

Chapter 2: "Modification of perovskite composition towards efficient and stable solar cells"

Publication 3

"Influence of the mixed organic cation ratio in leadiodide based perovskite on the performance ofsolar cells"

M. Salado, L. Calio, R. Berger, S. Kazim and S. Ahmad, Phys. Chem. Chem. Phys., 2016, 18, 27148

https://doi.org/10.1039/C6CP03851D

Publication 4

" Identifying the charge generation process in a Cs^+ based triple cation mixed perovskite solar cell"

Manuel Salado, Ramesh Kumar Kokal, Laura Calio, Samrana Kazim, Melepurath Deepa and Shahzada Ahmad. Phys. Chem. Chem. Phys., 2017. Accepted Manuscript.

https://doi.org/10.1039/C7CP03760K

Chapter 3: "Study of perovskite selective degradation mechanism under high humidity conditions"

Publication 5

"Impact of moisture on efficiency-determining electronic processes in perovskite solar cells"

M. Salado, L. Contreras-Bernal, L. Caliò, A. Todinova, C. López-Santos, S. Ahmad, A. Borras, J. Idígoras and J. A. Anta, J. Mater. Chem. A, 2017, 5, 10917

https://doi.org/10.1039/C7TA02264F

Chapter 4: "Improving the stability of the devices"

Publication 6

"Extending the Lifetime of Perovskite Solar Cells using a Perfluorinated Dopant"

M. Salado, F. J. Ramos, V. M. Manzanares, P. Gao, M. K. Nazeeruddin, P. J. Dyson, S. Ahmad, ChemSusChem 2016, 9, 2708.

https://doi.org/10.1002/cssc.201601030

Publication 7

"Towards extending solar cells life time: addition of a fluorous cation to triple-cation based perovskite films"

Salado, M., Fernández, M. A., Holgado, J. P., Kazim, S., Nazeeruddin, M. K., Dyson, P. J. and Ahmad, S. ChemSusChem. Accepted Author Manuscript.

https://doi.org/10.1002/cssc.201700797

ACS APPLIED MATERIALS & INTERFACES

Research Article

www.acsami.org

Interface Play between Perovskite and Hole Selective Layer on the Performance and Stability of Perovskite Solar Cells

Manuel Salado,[†] Jesus Idigoras,[‡] Laura Calio,[†] Samrana Kazim,[†] Mohammad Khaja Nazeeruddin,[§] Juan A. Anta,[‡] and Shahzada Ahmad*[,†]

[†]Abengoa Research, Abengoa, Campus Palmas Altas, C/Energía Solar no 1, 41014 Sevilla, Spain

[‡]Department of Physical, Chemical and Natural Systems, Universidad Pablo de Olavide, Sevilla 41013, Spain

[§]Group for Molecular Engineering of Functional Materials, Institute of Chemical Sciences and Engineering, Ecole Polytechnique Fédérale de Lausanne, CH-1951 Sion, Switzerland

Supporting Information

ABSTRACT: Perovskite solar cells with variety of hole selective contacts such as 2,2′,7,7′-tetrakis(*N*,*N*-di-*p*-methoxyphenylamine)-9,9′-spirobifluorene (Spiro-OMeTAD), poly(3-hexylthiophene-2,5-diyl), poly[bis(4-phenyl)(2,5,6-trimentlyphenyl)amine], 5,10,15-trihexyl-3,8,13-tris(4-methoxyphenyl)-10,15-dihydro-5*H*-diindolo[3,2-a:3′,2′-c]carbazole (HMPDI), and 2′,7′-bis(bis(4-methoxyphenyl)-amino)spiro[cyclopenta[2,1-b:3,4-b′]dithiophene-4,9′-fluorene] were employed to elucidate its role at the interface of perovskite and metallic cathode. Microscopy images revealed Spiro-OMeTAD and HMPDI produce smoother and intimate contact between perovskite/hole transporting materials (HTM) interfaces among others evaluated here. This morphological feature appears to be connected with three fundamental facts: (1) hole injection to the HTM is much more efficient as evidenced by photoluminescence measurements, (2) recombination losses are less important as evidenced by intensity-modulated photovoltage spectroscopy and impedance spectroscopy measurements, and (3) fabricated solar cells are much more robust against degradation by moisture. Devices with higher open-circuit photovoltages are characterized by higher values of the recombination resistance extracted from the impedance data. The variation in device hysteresis behavior can be ascribed mainly due to the molecular interaction and the core of HTM employed. In all cases, this fact is related with a larger value of the low-frequency capacitance, which indicates that the HTM can induce specific slow processes of ion accumulation at the interface. Notably, these processes tend to slowly relax in time, as hysteresis is substantially reduced for aged devices.

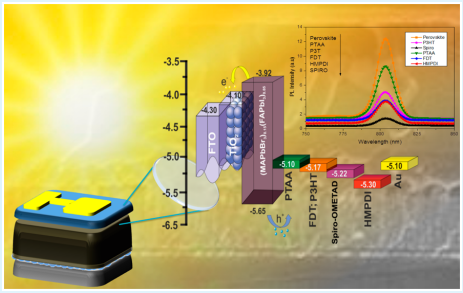

KEYWORDS: *perovskite solar cells, small perturbation techniques, interface, hole transport materials, electrochemical impedance spectroscopy*

1. INTRODUCTION

The unprecedented rise in organic−inorganic halide perovskite has astonished the thin film photovoltaics (PVs) research field. Its first usage as sensitizer in dye sensitized solar cells in 2009[1] was due to its panchromatic absorption, tunable band gap, and high absorption coefficient; subsequently, since 2012 it is being used to fabricate solar cells in solid-state configuration,[2] also due its ambipolar charge transport nature. It possesses a small binding energy, which allows efficient charge-carrier generation, transport, and collection effectively at ambient temperature. In 2012, with an attempt to replace the liquid electrolyte, solid-state hole transporting material 2,2′,7,7-tetrakis(*N*,*N*-di-*p*-methoxyphenylamine)-9,9′-spirobifluorene (*p*,*p*-Spiro-OMeTAD) was used, which has improved significantly solar cell stability, and power conversion efficiency (PCE) made a stunning jump from merely 3.8%[3] to 22.1% (http://www.nrel.gov/ncpv/).

In mesoporous perovskite solar cells (PSCs) architecture, it is distinguished by four different layers. A very thin and compact layer of TiO_2, followed by mesoporous layer (usually TiO_2 nanoparticles) is deposited before perovskite deposition. Both compact and mesoporous layers act as electron selective contacts that effectively extract electrons from the perovskite and block the recombination of electrons with holes. While light absorption and charge generation (excited electrons and holes) take place in the perovskite layer, where grain size, crystallinity, surface coverage, and homogeneity are vital parameters. A variety of techniques has been used for perovskite layer deposition such as two step (sequential deposition),[4] vapor-assisted deposition,[5] vacuum evaporation,[6]

Received: September 27, 2016
Accepted: November 28, 2016
Published: November 28, 2016

DOI: 10.1021/acsami.6b12236
ACS Appl. Mater. Interfaces 2016, 8, 34414−34421

ACS Applied Materials & Interfaces Research Article

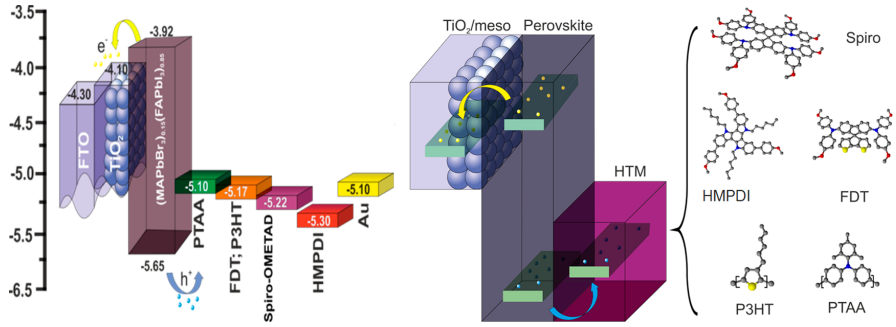

Figure 1. Energy level diagram of the perovskite solar cell and HOMO level of the different HTM studied here (left). Schematic diagram of the charge separation process and molecular structures of the HTMs (right).

or solvent engineering approach[7] to optimize the process. And the fourth layer is hole transporting layer (HTL) to work as hole selective contacts. The device can work without HTL, but for efficient hole extraction, an additional HTL is required and is used for enhanced PV performance. Spiro-OMeTAD enjoys the privilege of being the most exploited hole transporting material (HTM) in solid-state dye-sensitized solar cells as well as in perovskite solar cells.[8] In recent years, a variety of organic polymers, small-molecules-based, and inorganic p-type semiconducting materials have also been employed as HTMs such as poly[bis(4-phenyl)(2,5,6-trimentlyphenyl)amine] represented as poly[bis(4-phenyl)(2,5,6-trimentlyphenyl)amine] (PTAA),[9] small molecules such as phthalocyanine,[10] pentacene,[11] carbazole derivatives molecules,[12−14] etc, and inorganic salts such as NiO[15] or copper compounds as Cu_2O,[16] CuO,[17] CuI,[18] and CuSCN.[19,20]

In spite of the number of materials tested as HTM in perovskite solar cells, there is a paucity of understanding about the vital role played by these materials into a functioning device in a holistic manner. Generally, Spiro-OMeTAD gives high open-circuit voltage in comparison with other materials, a fact normally attributed to its adequate energy level alignment and high hole conductivity. However, it is not yet clear if the perovskite/HTM interface is a source of critical recombination losses due to molecular interaction. The selective contacts transport the charge carriers from the excited state of the absorber to the metallic charge collector (generally gold or silver) in which the carriers are at the equilibrium Fermi level. For efficient charge separation, it is a prerequisite that the electron transporting materials or HTM equilibrate its Fermi level to one type of carrier. However, some recombination processes occur in the absorber due to the excess of charge carriers, which are unavoidable due to the microscopic reversibility of the excitation process. On light irradiation, electrons and holes are generated in the carrier bands, separated by the quasi-Fermi levels of the two states in the perovskite. In this context, the selection of proper electron or hole selective layers plays a crucial role in the final performance of the device. For example, by employing Kelvin probe force microscopy we have studied the charge distribution inside a perovskite solar cell.[21] It was found that the accumulation of holes and electrons at the interfaces reduces the short-circuit current and thus the PCE.

Herein, we studied perovskite solar cells prepared with range of HTMs, including the classical Spiro-OMeTAD and other high-performance organic polymer semiconductors like PTAA and poly(3-hexylthiophene-2,5-diyl) (P3HT), and the small molecules coded as 2′,7′-bis(bis(4-methoxyphenyl)amino)-spiro[cyclopenta[2,1-b:3,4-b′]dithiophene-4,9′-fluorene] (FDT) and 5,10,15-trihexyl-3,8,13-tris(4-methoxyphenyl)-10,15-dihydro-5*H*-diindolo[3,2-a:3′,2′-c]carbazole (HMPDI). To elucidate the effect of HTM, the solar cell configuration (fluorine doped tin oxide coated glass (FTO)/bl-TiO_2/mesoporous-TiO_2/perovskite) was kept unaltered in devices, and the influence of the different HTMs was probed. We employed an array of small-perturbation electrochemical techniques to hypothesize the recombination losses caused by each HTM.

2. RESULTS AND DISCUSSION

The key for the efficient light harvesting is the optimal combination of generated charge carriers upon light absorption and their diffusion. Figure 1 represents energy level diagram of a $(FAPbI_3)_{0.85}(MABr_3)_{0.15}$-based perovskites with different high performance HTMs. On light irradiation photoexcited charge species in perovskite transfer through corresponding charge selective contact as n- and p-type materials for electrons and holes extraction, respectively, both in contact with the perovskite. To measure the PV parameters, devices were fabricated using different HTMs, and $J-V$ curves were recorded (Figure 2) under 1 sun conditions; the PV parameters are summarized in Table 1. It can be deduced that Spiro-OMeTAD

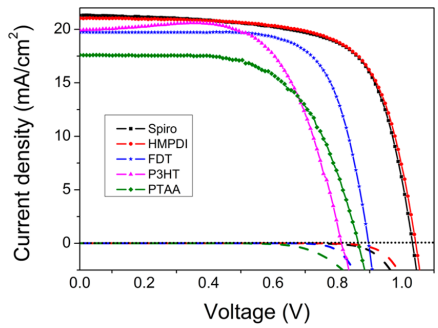

Figure 2. Current−voltage characteristics of the perovskite solar cell with different hole transporting materials.The device active area was 0.16 cm^2, and measurement was made in the direction of V_{oc} to J_{sc} at a scan rate of 100 mV/s.

DOI: 10.1021/acsami.6b12236
ACS Appl. Mater. Interfaces 2016, 8, 34414−34421

ACS Applied Materials & Interfaces Research Article

Table 1. Photovoltaic Parameters and Calculated Hysteresis Index of the Fresh Perovskite Solar Cells Prepared Using Different HTMs under 100 mW/cm^2

PV parameters	Spiro-OMeTAD	HMPDI	FDT	P3HT	PTAA
V_{oc} (mV)	1030	1040	810	810	860
J_{SC} (mA/cm^2)	21.29	21.04	21.4	19.99	17.61
fill factor (%)	65.98	69.41	70.97	65.19	62.24
R_s (ohm)	31.1	31.9	26.7	50.6	52.6
R_{sh} (ohm)	8238.5	16846.8	37295.3	5027.5	19523.3
PCE (%)	15.15	15.22	12.41	10.61	9.47
HI	0.206	0.315	0.679	0.450	0.346

and HMPDI gave good results. Table S1 in the Supporting Information represent average values and reproducibility of the devices.

The devices fabricated from HMPDI as HTM gave the best performance, and a PCE of 15.22% was measured, with the V_{oc} of 1040 mV and J_{sc} of 21.04 mA/cm^2, while similar performance was also yielded by Spiro-OMeTAD. The other HTM investigated here such as FDT, P3HT, and PTAA showed reduction in V_{oc}, which we ascribed to higher recombination processes at the interface of perovskite/HTM or unfavorable molecular interaction.

Because of hysteresis behavior in perovskite solar cells, the scan direction used in the $J-V$ measurements can give different results. On the basis of the architecture adopted for device fabrication the reverse ($V_{oc} \rightarrow J_{sc}$) or forward ($J_{sc} \rightarrow V_{oc}$) scan shows higher PCE. This irregular hysteresis behavior has been reported for diversity of PSCs configurations, irrespective of configuration (such as planar, mesoporous, or inverted) employed, and even in dye-sensitized solar cells.[22] The behavior can be quantified using the hysteresis index (HI), which we define here as

$$\mathrm{HI} = \frac{J_{rev}(0.8{*}V_{oc}) - J_{fwd}(0.8{*}V_{oc})}{J_{rev}(0.8{*}V_{oc})} \quad (1)$$

where photocurrent at 80% of the V_{oc} is assumed to work at the maximum power point.[23]

The hysteresis behavior in the PSCs has been found to depend on many factors; however, the real cause of its origin is still not quantitative. In some reports, it was suggested that ion migration together with charge accumulation at the contacts can be the cause of hysteresis.[22,24,25] These molecular processes are relatively slow in comparison with the electronic ones, and this is why the scan rate during $J-V$ characterization plays an important role in the hysteretic behavior. The nature (crystal size and shape), composition of the perovskite, and the charge selective contacts are hysteresis determining factors. Table S2 illustrates the HI as a function of time (aging) for different HTM-based devices. The Spiro-based devices show the lowest values of HI. In contrast FDT, P3HT, and PTAA tend to produce devices with much higher hysteresis, which suggests that these materials can induce specific ionic accumulation at the perovskite/HTM interface. However, it can be visualized that these HI values decreased significantly after 75 d. This can be attributed to a relaxation of the ionic charges to an equilibrium or quasi-equilibrium state after preparation.

Incident photon-to-current conversion efficiency (IPCE) spectra for the devices fabricated with the different HTMs are shown in Figure 3. IPCE values are in accordance with previous literature, and almost plateau is achieved between 400 and 750 nm with value of greater than 80% in the case of Spiro-

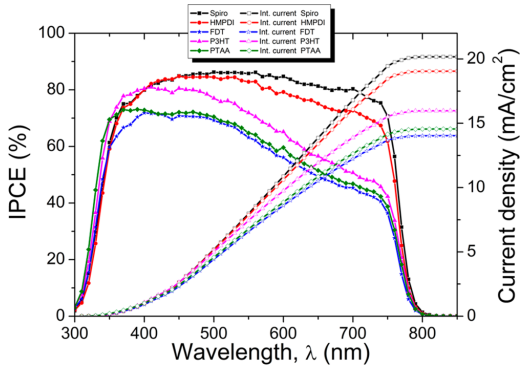

Figure 3. IPCE spectra of the perovskite solar cell devices with different hole selective materials.

OMeTAD and HMPDI. The integrating current of the devices is plotted on secondary Y-axis of Figure 2 and is well in accordance with the $J-V$ curves. The integrated current is well in agreement (20.3 mA cm^{-2}) for the Spiro-OMeTAD, which is close to the measured photocurrent density of 21.2 mA cm^{-2} at the standard solar AM1.5G intensity of 100 mW cm^{-2}.

It is notable from the IPCE spectra that there is a loss in photon conversion in the range of 550−800 nm for the FDT, P3HT, and PTAA, which is not the case for Spiro-OMeTAD or HMPDI. We attribute this loss to the existence of traps and recombination sites at the perovskite/HTL interface, compared to Spiro-OMeTAD and HMPDI. This will be discussed later in the electrical impedance spectroscopy (EIS) section. We rule out the possibility of this loss in IPCE due to parasitic absorption by the HTM. To confirm this, absorption spectra of different HTMs deposited on FTO were measured (Figure S1), and it shows similar profile for all the HTM. These HTMs absorb below 400 nm, and thus avoid any competition with perovskite absorption. However, P3HT and FDT showed absorption in the range of 400−650 nm and 420−550 nm, respectively. In our device architecture, since the light is absorbed mainly by the perovskite layer placed before the HTM, it will be having negligible effect on the IPCE spectrum.

To explore charge extraction, steady-state photoluminescence (PL) measurements were made in the pristine perovskite and between the perovskite/HTM interfaces by exciting at 532 nm (Figure 4). In general, for all the samples with HTM, the intensity of emission spectra decreases with respect to pristine perovskite. In all the cases an emission maximum appears at 803 nm, which is in agreement with the previous published results. The reduction of PL intensity or PL quenching indicates the hole injection to the HTM from perovskite, and

DOI: 10.1021/acsami.6b12236
ACS Appl. Mater. Interfaces 2016, 8, 34414−34421

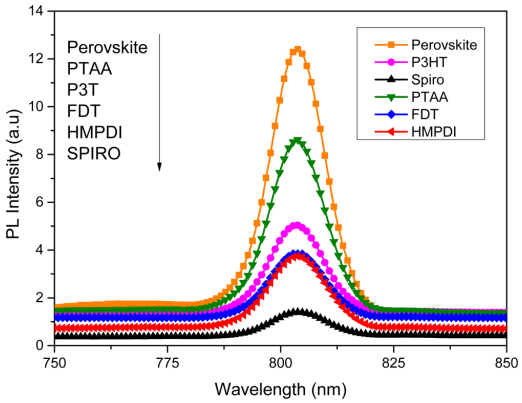

Figure 4. Steady-state PL spectra of pristine perovskite on quartz and perovskite with different HTM in bilayer configuration. The excitation wavelength was 532 nm.

enhanced PL quenching is an indication of efficient hole extraction to the highest occupied molecular orbital (HOMO) of HTM. Thus, the HTM materials appear to be more efficient in the order of Spiro > HMPDI > FDT > P3HT > PTAA, which shows similar trend as photocurrent. The relative reduction of the PL signal is in accordance with the short-circuit photocurrents measured for each device (Table 1 and Figure 2). These measurements suggest that it is basically the hole injection capability of the different HTM that is performance-determining step in a solar cell at short-circuit conditions, given that perovskite and the electron transport materials are the same.

Figure 5 represents the cross-sectional scanning electron microscopy (SEM) images across the cleaved edge of a mesoscopic solar cell device. SEM images show the effect of layers interconnection, specifically, perovskite/HTM frontier. The thickness of the perovskite layer is ~600 nm; thus, a thicker HTM is required. For this, an HTM layer between 150 and 200 nm was used in this study. An intimate contact between the different layers entails high efficiency and stability under working conditions,[26] and this was observed with selected HTMs. The SEM images reveal that Spiro-OMeTAD and HMPDI show very high homogeneity and well interlayer connection with perovskite and gold interfaces, FDT, and conductive polymers (P3HT and PTAA), show high porosity, and lack fine interconnection. This deficiency in contact is most likely related to the polymeric nature of HTM, which may or may not be stable under very high vacuum condition, a prerequisite for depositing metallic contacts.

To further investigate the dynamical processes operating under real device conditions, we employed intensity-modulated photovoltage spectroscopy (IMVS) and EIS to extract information regarding carrier lifetime and recombination processes within the device. These techniques have been used in past to study electron dynamics in perovskite solar cells.[27,28] In IMVS a small frequency-modulated optical perturbation is applied to the devices, whereas in EIS this perturbation is in the form of an excess voltage (in the order of a few mV) applied at the contacts. Because of the small amplitude of the perturbation, the response can be linearized so that specific frequencies characteristic of the device can be detected. In IMVS the measurement is carried at open circuit, and the response is a V_{oc} modulation. The complex-plane representation of the IMVS response is in the form of a semicircle, defined by a characteristic time constant (τ_{IMVS}). Since this time constant represents the voltage relaxation response of the device after an optical generation of carriers, it can be in principle related to a carrier lifetime (τ_n). The IMVS time constant was obtained by considering the minimum of the semicircle located at an angular frequency that is equal to

$$\tau_n^{(IMVS)} = \frac{1}{\omega_{min}} \quad (2)$$

As light intensity increases, the semicircle radius decreases. The frequency corresponding to the minimum in the complex plane increases with the increase in light intensity. This indicates that the carrier lifetime and hence the IMVS time constant, become shorter. Therefore, carrier (electron−hole) recombination is

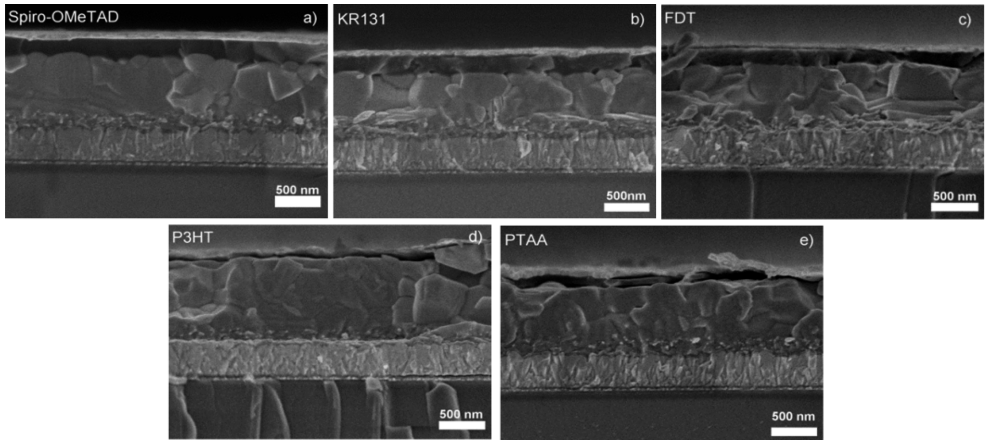

Figure 5. Cross-sectional SEM images showing different layers in a mesoscopic perovskite solar cell using different HTMs such as (a) Spiro-OMeTAD, (b) HMPDI, (c) FDT, (d) P3HT, and (e) PTAA.

DOI: 10.1021/acsami.6b12236
ACS Appl. Mater. Interfaces 2016, 8, 34414−34421

more pronounced at higher illumination intensities, due to the larger concentration of carriers generated in the device. Analogously, a time constant accounting for the lifetime of the carriers can also be obtained from EIS. In this case the response is more complex as more time constants (semicircles) show up in the spectrum. On the one hand, it is known that the time constant appearing at low frequencies is generally associated with slow processes connected to the hysteresis. On the other hand, the peak appearing at higher frequencies is related to the recombination of carriers.[28,29] The "lifetimes" can be estimated from the frequency of the maximum (in analogy to eq 2), but it can also be expressed in terms of a capacitance and a recombination resistance.

$$\tau_n^{(EIS)} = CR_{rec} \quad (3)$$

In the past it was reported[27,29] that this capacitance is normally dominated by the bulk component $C_g = \varepsilon\varepsilon_0 A/d$, where ε is the dielectric constant of the perovskite, ε_0 is the vacuum permittivity, A the effective contact area, and d is the thickness. Figure S2 shows that the capacitance extracted from the high-frequency component is indeed constant with respect to applied voltage as expected from its bulk nature. Assuming a static dielectric constant of ∼24 (reported value for pure $MAPbI_3$ is 23) the measured values of the capacitance (∼1.5×10^{-8} F) are close to the predicted values of C_g. It also roughly coincides with the high-frequency limit of the capacitance (discussed in next section). The parallel resistance that accompanies C_g is attributed to the recombination resistance. Both R_{rec} and impedance time constant are expected to decrease exponentially with voltage.[29]

In Figure S3 lifetimes obtained from the IMVS and EIS data are presented; for the most stable and efficient devices (Spiro and HMPDI), there is consistency between the IMVS and EIS data (from the maximum of the frequency and from fitting to an RC equivalent circuit element, i.e, eq 3). However, the rest of the devices present an anomalous behavior of the IMVS response. It is worth noting that, since the small-perturbation response is controlled by the geometrical capacitance of the device, the time constant extracted from eqs 2 and 3 is not a true carrier lifetime, although it is directly connected to the recombination rate. However, to avoid ambiguities, we will base our analysis on the extracted values of the recombination resistance. The anomalous behavior observed in the IMVS experiment is more likely connected to the degradation of the device as a consequence of the optical perturbation applied on the device. For this reason, only data extracted from EIS will be discussed below.

Figure 6 depicts the recombination resistance obtained from fittings to a simple $-R(R_{rec}C)$ equivalent circuit of the midfrequency region of the impedance spectra measured at open circuit. Except for FDT, which shows anomalous performance, the recombination resistance decreases exponentially with increased open-circuit voltage, as a consequence of the acceleration of the recombination rate, as more carriers are injected into the active layer of the device. The results are consistent with PV performance of the devices. Hence, at the same value of the open-circuit voltage, cells with better performance show a larger recombination resistance. In this respect, HTM based on small molecules (Spiro, HMPDI) showed minimum recombination, possibly due to the improved perovskite/HTM interface (Figure 5).

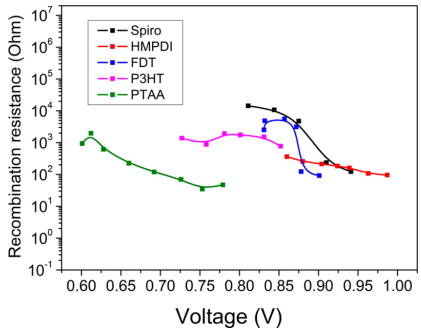

Figure 6. Recombination resistance as obtained from fittings to $-R(R_{rec}C)$ equivalent circuit of the impedance response of all studied devices.

The impedance study also makes it possible to look at the low-frequency behavior of the solar cells. In Figure 7 the

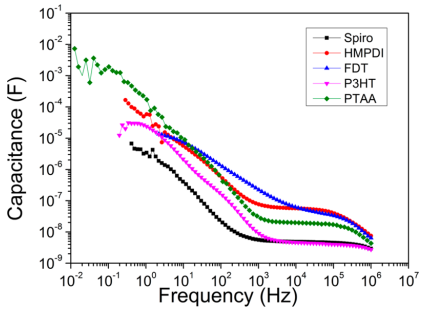

Figure 7. Apparent capacitance vs frequency as obtained from the impedance measurements.

apparent capacitance is represented as a function of the frequency. The low-frequency limit of the capacitance is related to the slow molecular processes that are behind the hysteresis behavior.[24,25] The obtained data have the typical conduct of a perovskite solar cell, showing in some cases a plateau in the midfrequency region, associated with the bulk capacitance of the perovskite.[30] Remarkably the HTMs that gave higher value of hysteresis also tend to give a larger low-frequency capacitance. This suggests that in these cases interfacial phenomena of ionic accumulation are more important, giving rise to a more intense low-frequency response.

To elucidate the role of different HTMs on stability, aging tests were performed for unencapsulated devices. Degradation either due to external factors such as moisture, oxygen, temperature, UV light, or internal factors such as ion migration and interfacial reactions is well-reported. In this work, the use of diverse p-type semiconductor molecules as HTM stress the interface differences, as observed with microstructural images. It was found that small molecules such as Spiro-OMeTAD, HMPDI, and FDT show intimate contact with the perovskite. This can also make devices unstable at higher temperatures due to the organic material degradation.[31,32] The case of polymeric HTM (P3HT and PTAA) presents better resistance with temperature;[33,34] however, the adhesion with perovskite is not

DOI: 10.1021/acsami.6b12236
ACS Appl. Mater. Interfaces 2016, 8, 34414−34421

homogeneous (Figure 5), thus, a possible pathway of moisture degradation.[35,36]

To study device degradation trend in these devices, they were kept at atmospheric humidity (~55−57% relative humidity (RH)) under dark at room temperature. Figure 8

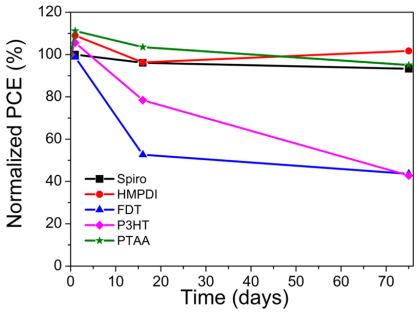

Figure 8. Evolution of PCE with time under atmospheric humidity conditions (55% RH).

shows the evolution of normalized PCE of the devices with time. It can be deducted that PSCs fabricated using P3HT and FDT shows a loss of 20% and 45%, respectively, in the first 15 d. While the devices fabricated from HMPDI, under similar conditions monitored for 75 d, show negligible loss in performance, on the contrary an increment of ~3% from the initial value. We assigned this increment in PCE value to improved interlayer contact and drying of solvent. The moisture resistance ability in these cells may be due to charge stabilization as well as a better contact between HTM and active material (perovskites). It is notable that devices with PTAA also showed good stability. As discussed in the SEM section, FDT layers possess small cavities that affect the stability of devices (loss of 50%). Figure S4 presents the PV parameters decay with time depending on the devices configuration. It can be observed that PSCs with HMPDI and Spiro-OMeTAD show a slight decay in short-circuit current (J_{sc}); however, the PSCs fabricated with FDT, P3HT, and PTAA showed decay in J_{sc} as well as loss in open-circuit voltage (V_{oc}). This decay can be interpreted as a consequence of electron−holes recombination, which can be triggered by perovskite degradation due to moisture uptake.[27]

3. CONCLUSIONS

The role of different HTMs in the mesoporous perovskite solar cells was elucidated. We demonstrate that the quality of the interface (molecular interaction) between the perovskite and the hole selective contact has a profound effect on the performance, both in terms of better hole extraction and lower recombination. Furthermore, a smooth interface makes the device more robust against degradation by moisture. Small-perturbation-based optoelectronic and electrochemical measurements (intensity modulated photovoltage and impedance spectroscopies) reveal that the HTMs that yield a higher open-circuit photovoltage and hysteresis have a larger recombination resistance and a larger value of the low-frequency capacitance, respectively. Both facts are clearly connected with the quality of the interface. Among the investigated high-performance and stable HTMs, Spiro-OMeTAD and HMPDI were found to be of significant interest for future perovskite solar cells technology.

4. EXPERIMENTAL SECTION

Fabrication of the Devices. Perovskite solar cell devices were fabricated onto FTO-coated glass (TEC15, Pilkington) patterned by laser etching. At first, the substrates were cleaned using Hellmanex solution and washed with deionized water. Next, they were ultrasonicated for 25 min at 60 °C in acetone, 2-propanol, and ethanol and, subsequently, dried finally with nitrogen. A TiO_2 compact layer was deposited by spray pyrolysis at 450 °C using a dilution of 1 mL of titanium diisopropoxide bis(acetyl acetonate) precursor solution (75% in 2-propanol, Sigma-Aldrich) in 19 mL of pure ethanol using dry air as the carrier gas. After blocking layer deposition, substrates were kept for additional 30 min at 450 °C to transform TiO_2 into anatase phase. Once the samples were cooled gradually at room temperature they were immersed into a 0.02 M $TiCl_4$ solution in deionized water at 70 °C for 30 min to obtain a regular layer. Afterward substrates were then washed with deionized water and heated at 500 °C for 30 min and then cooled to room temperature. Next, a TiO_2 mesoporous layer (Dyesol, 30NRD) was deposited by spin coating at 4000 rpm for 20 s followed by annealing the substrates up to 450 °C by heating them progressively for 2 h.

For perovskite deposition, precursor solutions of 1.4 M PbI_2, 1 M FAI, and 0.2 M MABr and $PbBr_2$, respectively, in a mixture of dimethylformamide/dimethyl sulfoxide were prepared inside an argon-filled glovebox with moisture- and oxygen-controlled conditions (H_2O level: <1 ppm and O_2 level: <10 ppm) and stirred at 80 °C overnight to completely dissolve the PbI_2. The deposition of the perovskite was performed using one-step deposition method. In this method, the perovskite precursor solution was spin-coated on top of the mesoporous layer at 1000 rpm for 10 s and then 6000 rpm for 20 s, dropping some amount of chlorobenzene during the second step. Following this the films were moved onto a hot plate and annealed at 100 °C for 1 h.

After the perovskite annealing, the substrates were cooled, and the different HTM solutions were spin coated above the perovskite layer according to literature depending on their optimized spin conditions. Solutions (60 and 70 mM) in chlorobenzene were prepared for Spiro-OMeTAD and HMPDI (Rakstys et al.),[37,38] respectively, and a 60 mM solution of FDT was prepared in toluene.[39] All the three HTM solutions were doped with lithium bis(trifluoromethylsulfonyl)imide salt (LiTFSI), 4-*tert*-butylpyridine (*t*-BP), and tris(2-(1*H*-pyrazol-1-yl)-4-*tert*-butylpyridine)cobalt(III)-tris(bis(trifluoromethylsulfonyl)-imide) (FK209) in the molar ratios of 0.5, 3.3, and 0.1 for Li-TFSI, *t*-BP, and FK209, respectively, and were spun-coated at 4000 rpm for 30 s. For PTAA 10 mg/mL solution was prepared in toluene, and to this 7.5 μL of LiTFSI, from a stock solution of 170 mg/mL in acetonitrile, and 4 μL of *t*-BP were added, while in the case of P3HT 15 mg/mL solution in chlorobenzene was prepared and doped with 6.8 μL of a 28.3 mg/mL stock solution of LiTFSI in acetonitrile. Both solutions of PTAA and P3HT were spun-coated at 3000 rpm for 30 s atop of the perovskite layer. Finally, an 80 nm layer of gold was thermally evaporated on the top of the cell as cathode under a vacuum level between 1×10^{-6} and 1×10^{-5} torr.

Characterization. Current density versus voltage ($J-V$) curves were recorded with a Keithley 2400 source-measurement-unit under AM 1.5 G, 100 mW cm^2 illumination from a 450 W solar simulator (ORIEL, 94023 A). Sun intensity was calibrated using a calibrated monocrystalline silicon solar cell. A mask (0.16 cm^2) was used to reduce the influence of scattered light during the measurement. A scan rate of 100 mV/s was used to record $J-V$ curves and to calculate the HI. IPCE measurements were performed using a 150 W xenon lamp (Newport) attached to an Oriel Cornerstone 260 motorized 1/4 m monochromator as the light source.

Steady-state PL measurements were performed on solid samples prepared on quartz for pure perovskite and perovskite with different hole transporting layer in bilayer configuration using Hitachi, F-7000 Fluorescence spectro-photometer.

DOI: 10.1021/acsami.6b12236
ACS Appl. Mater. Interfaces 2016, 8, 34414−34421

To measure the absorbance of the different HTM onto glass, a (Agilent Cary 60) spectro-photometer was used. SEM cross-sectional images were obtained using a Hitachi S-4800 field emission scanning electron microscope at power 2 kV.

The illumination for the Impedance Spectroscopy (IS) measurements was provided by a green light-emitting diode (LED) over a wide range of direct current (DC) light intensities. This allows for probing the devices at different positions of the Fermi level in the semiconductor. A response analyzer module (PGSTAT302N/FRA2, Autolab) was utilized to analyze the frequency response of the devices. To avoid voltage drop due to series resistance, IS measurements were performed at the open-circuit potential, the Fermi level (related to the open-circuit voltage) being fixed by the DC illumination intensity. A 20 mV perturbation in the 1×10^{6} to 1×10^{-2} Hz range was utilized to obtain the spectra. Intensity modulated photovoltage spectroscopy (IMVS) measurements were performed by coupling the PGSTAT302N/FRA2 module to the LED. IMVS measurements were performed at short-circuit in the 1×10^{6} to 1×10^{-2} Hz range with a light perturbation corresponding to 10% of the DC background illumination intensity. The NOVA 1.7 software was used to generate IS data. Z-view equivalent circuit modeling software (Scribner) was used to fit the IS spectra.

■ ASSOCIATED CONTENT

Supporting Information

The Supporting Information is available free of charge on the ACS Publications website at DOI: 10.1021/acsami.6b12236.

Absorption spectra, stability graphs, hysteresis index, along with impedance spectra (PDF)

■ AUTHOR INFORMATION

Corresponding Author

*E-mail: shahzada.ahmad@abengoa.com.

ORCID

Mohammad Khaja Nazeeruddin: 0000-0001-5955-4786

Shahzada Ahmad: 0000-0002-1218-2556

Funding

S.A. and L.C. thank the European Union Seventh Framework Programme under Grant No. 607232 [THINFACE] for financial support. J.A.A. thanks Junta de Andalucía for financial support via Grant No. FQM 1851, FQM 2310, and Ministerio de Economía y Competitividad of Spain under Grant No. MAT2013-47192-C3-3-R.

Notes

The authors declare no competing financial interest.

■ REFERENCES

(1) Kazim, S.; Nazeeruddin, M. K.; Grätzel, M.; Ahmad, S. Perovskite as Light Harvester: A Game Changer in Photovoltaics. *Angew. Chem., Int. Ed.* **2014**, *53*, 2812−2824; *Angew. Chem.* **2014**, *126*, 2854−2867.

(2) O'Regan, B.; Grätzel, M. A Low-Cost, High-Efficiency Solar Cell Based on Dye-Sensitized Colloidal TiO_2 Films. *Nature* **1991**, *353*, 737−740.

(3) Kojima, A.; Teshima, K.; Shirai, Y.; Miyasaka, T. J. Organometal Halide Perovskites as Visible-Light Sensitizers for Photovoltaic cells. *J. Am. Chem. Soc.* **2009**, *131*, 6050−6051.

(4) Burschka, J.; Pellet, N.; Moon, S.-J.; Humphry-Baker, R.; Gao, P.; Nazeeruddin, M. K.; Grätzel, M. Sequential Deposition as a Route to High-Performance Perovskite-Sensitized Solar Cells. *Nature* **2013**, *499*, 316−320.

(5) Chen, Q.; Zhou, H.; Hong, Z.; Luo, S.; Duan, H. S.; Wang, H. H.; Liu, Y.; Li, G.; Yang, Y. Planar Heterojunction Perovskite Solar Cells Via Vapor-Assisted Solution Process. *J. Am. Chem. Soc.* **2014**, *136*, 622−625.

(6) Liu, M.; Johnston, M. B.; Snaith, H. J. Efficient Planar Heterojunction Perovskite Solar Cells by Vapour Deposition. *Nature* **2013**, *501*, 395−398.

(7) Jeon, N. J.; Noh, J. H.; Kim, Y. C.; Yang, W. S.; Ryu, S.; Seok, S. Il. Solvent Engineering for High-Performance Inorganic−Organic Hybrid Perovskite Solar Cells. *Nat. Mater.* **2014**, *13*, 897−903.

(8) Ding, I. K.; Tétreault, N.; Brillet, J.; Hardin, B. E.; Smith, E. H.; Rosenthal, S. J.; Sauvage, F.; Grätzel, M.; McGehee, M. D. Pore-Filling of Spiro-OMeTAD in Solid-State Dye Sensitized Solar Cells: Quantification, Mechanism, and Consequences for Device Performance. *Adv. Funct. Mater.* **2009**, *19*, 2431−2436.

(9) Heo, J. H.; Im, S. H.; Noh, J. H.; Mandal, T. N.; Lim, C.-S.; Chang, J. A.; Lee, Y. H.; Kim, H.; Sarkar, A.; Nazeeruddin, M. K.; Gratzel, M.; Seok, S. Il. Efficient Inorganic-Organic Hybrid Heterojunction Solar Cells Containing Perovskite Compound and Polymeric Hole Conductors. *Nat. Photonics* **2013**, *7*, 486−491.

(10) Kumar, C. V.; Sfyri, G.; Raptis, D.; Stathatos, E.; Lianos, P. Perovskite Solar Cell With Low Cost Cu-phthalocyanine as Hole Transporting Material. *RSC Adv.* **2015**, *5*, 3786−3791.

(11) Kazim, S.; Ramos, F. J.; Gao, P.; Nazeeruddin, M. K.; Grätzel, M.; Ahmad, S. A Dopant Free Linear Acene Derivative as a Hole Transport Material for Perovskite Pigmented Solar Cells. *Energy Environ. Sci.* **2015**, *8*, 1816−1823.

(12) Sung, S. Do; Kang, M. S.; Choi, I. T.; Kim, H. M.; Kim, H.; Hong, M.; Kim, H. K.; Lee, W. I. 14.8% Perovskite Solar Cells Employing Carbazole Derivatives as Hole Transporting Materials. *Chem. Commun.* **2014**, *50*, 14161−14163.

(13) Gratia, P.; Magomedov, A.; Malinauskas, T.; Daskeviciene, M.; Abate, A.; Ahmad, S.; Grätzel, M.; Getautis, V.; Nazeeruddin, M. K. A Methoxydiphenylamine-Substituted Carbazole Twin Derivative: An Efficient Hole-Transporting Material for Perovskite Solar Cells. *Angew. Chem., Int. Ed.* **2015**, *54*, 11409−11413.

(14) Wang, H.; Sheikh, A. D.; Feng, Q.; Li, F.; Chen, Y.; Yu, W.; Alarousu, E.; Ma, C.; Haque, M. A.; Shi, D.; Wang, Z.-S.; Mohammed, O. F.; Bakr, O. M.; Wu, T. Facile Synthesis and High performance of a New Carbazole-Based Hole Transporting Material for Hybrid Perovskite Solar Cells. *ACS Photonics* **2015**, *2*, 849.

(15) Xu, X.; Liu, Z.; Zuo, Z.; Zhang, M.; Zhao, Z.; Shen, Y.; Zhou, H.; Chen, Q.; Yang, Y.; Wang, M. Hole Selective NiO Contact for Efficient Perovskite Solar Cells with Carbon Electrode. *Nano Lett.* **2015**, *15*, 2402−2408.

(16) Yu, W.; Li, F.; Wang, H.; Alarousu, E.; Chen, Y.; Lin, B.; Wang, L.; Hedhili, M. N.; Li, Y.; Wu, K.; Wang, X.; Mohammed, O. F.; Wu, T. T. Ultrathin Cu_2O as an Efficient Inorganic Hole Transporting Material for Perovskite Solar Cells. *Nanoscale* **2016**, *8*, 6173−6179.

(17) Zuo, C.; Ding, L. Solution-Processed Cu_2O and CuO as Hole Transport Materials for Efficient Perovskite Solar Cells. *Small* **2015**, *11*, 5528−5532.

(18) Christians, J. a.; Fung, R. C. M.; Kamat, P. V. An Inorganic Hole Conductor for Organo-Lead Halide Perovskite Solar Cells. Improved Hole Conductivity with Copper Iodide. *J. Am. Chem. Soc.* **2014**, *136*, 758−764.

(19) Ye, S.; Sun, W.; Li, Y.; Yan, W.; Peng, H.; Bian, Z.; Liu, Z.; Huang, C. CuSCN-based Inverted Planar Perovskite Solar Cell with an Average PCE of 15.6%. *Nano Lett.* **2015**, *15*, 3723−3728.

(20) Zhao, K.; Munir, R.; Yan, B.; Yang, Y.; Kim, T.-S.; Amassian, A. Solution-Processed Inorganic Copper(I) thiocyanate (CuSCN) Hole Transporting Layers for Efficient p−i−n Perovskite Solar Cells. *J. Mater. Chem. A* **2015**, *3*, 20554−20559.

(21) Bergmann, V. W.; Weber, S. A. L.; Javier Ramos, F.; Nazeeruddin, M. K.; Grätzel, M.; Li, D.; Domanski, A. L.; Lieberwirth, I.; Ahmad, S.; Berger, R. Real-Space Observation of Unbalanced Charge Distribution Inside a Perovskite-Sensitized Solar Cell. *Nat. Commun.* **2014**, *5*, 5001.

(22) Tress, W.; Correa Baena, J. P.; Saliba, M.; Abate, A.; Graetzel, M. Inverted Current−Voltage Hysteresis in Mixed Perovskite Solar Cells: Polarization, Energy Barriers, and Defect Recombination Adv. *Energy Mater.* **2016**, *6*, 1600396.

DOI: 10.1021/acsami.6b12236
ACS Appl. Mater. Interfaces 2016, 8, 34414−34421

(23) Kim, H. S.; Park, N. G. Control of I-V Hysteresis in $CH_3NH_3PbI_3$ Perovskite Solar Cell. *J. Phys. Chem. Lett.* **2014**, *5*, 2927−2934.
(24) Chen, B.; Yang, M.; Priya, S.; Zhu, K. Origin of J-V Hysteresis in Perovskite Solar Cells. *J. Phys. Chem. Lett.* **2016**, *7*, 905−917.
(25) Kim, H. S.; Jang, I. H.; Ahn, N.; Choi, M.; Guerrero, A.; Bisquert, J.; Park, N. G. Control of I-V Hysteresis in $CH_3NH_3PbI_3$ Perovskite Solar Cell. *J. Phys. Chem. Lett.* **2015**, *6*, 4633−4639.
(26) Shi, J.; Xu, X.; Li, D.; Meng, Q. Interfaces in Perovskite Solar Cells. *Small* **2015**, *11*, 2472−2486.
(27) Pockett, A.; Eperon, G. E.; Peltola, T.; Snaith, H. J.; Walker, A.; Peter, L. M.; Cameron, P. J. Characterization of Planar Lead Halide Perovskite Solar Cells by Impedance Spectroscopy, Open-Circuit Photovoltage Decay, and Intensity-Modulated Photovoltage/Photocurrent spectroscopy. *J. Phys. Chem. C* **2015**, *119*, 3456−3465.
(28) Guillén, E.; Ramos, F. J.; Anta, J. A.; Ahmad, S. Elucidating Transport-Recombination Mechanisms in Perovskite Solar Cells by Small-Perturbation Techniques. *J. Phys. Chem. C* **2014**, *118*, 22913−22922.
(29) Todinova, A.; Idígoras, J.; Salado, M.; Kazim, S.; Anta, J. A. Universal Features of Electron Dynamics in Solar Cells with TiO_2 Contact: From Dye Solar Cells to Perovskite Solar Cells. *J. Phys. Chem. Lett.* **2015**, *6*, 3923−3930.
(30) Guerrero, A.; Garcia-Belmonte, G.; Mora-Sero, I.; Bisquert, J.; Kang, Y. S.; Jacobsson, T. J.; Correa-Baena, J.-P.; Hagfeldt, A. Properties of Contact and Bulk Impedances in Hybrid Lead Halide Perovskite Solar Cells Including Inductive Loop Elements. *J. Phys. Chem. C* **2016**, *120*, 8023−8032.
(31) Dualeh, A.; Moehl, T.; Nazeeruddin, M. K.; Grätzel, M. Temperature Dependence of Transport Properties of Spiro-OMeTAD as a Hole Transport Material in Solid-State Dye-Sensitized Solar Cells. *ACS Nano* **2013**, *7*, 2292−2301.
(32) Niu, G.; Guo, X.; Wang, L. J Review of Recent Progress in Chemical Stability of Perovskite Solar Cells. *J. Mater. Chem. A* **2015**, *3*, 8970−8980.
(33) Habisreutinger, S. N.; Leijtens, T.; Eperon, G. E.; Stranks, S. D.; Nicholas, R. J.; Snaith, H. J. Carbon Nanotube/Polymer Composites as a Highly Stable Hole Collection Layer in Perovskite Solar Cells. *Nano Lett.* **2014**, *14*, 5561−5568.
(34) Misra, R. K.; Aharon, S.; Li, B.; Mogilyansky, D.; Visoly-Fisher, I.; Etgar, L.; Katz, E. A. Temperature- and Component-Dependent Degradation of Perovskite Photovoltaic Materials Under Concentrated Sunlight. *J. Phys. Chem. Lett.* **2015**, *6*, 326−330.
(35) Berhe, T. A.; Su, W.-N.; Chen, C.-H.; Pan, C.-J.; Cheng, J.-H.; Chen, H.-M.; Tsai, M.-C.; Chen, L.-Y.; Dubale, A. A.; Hwang, B.-J. Organometal Halide Perovskite Solar Cells: Degradation and Stability. *Energy Environ. Sci.* **2016**, *9*, 323−356.
(36) Li, B.; Li, Y.; Zheng, C.; Gao, D.; Huang, W. Advancements in Stability of Perovskite Solar cells: Degradation Mechanisms and Improvement Approaches. *RSC Adv.* **2016**, *6*, 38079−38091.
(37) Ramos, F. J.; Rakstys, K.; Kazim, S.; Gratzel, M.; Nazeeruddin, M. K.; Ahmad, S. Rational Design of Triazatruxene-Based Hole Conductors for Perovskite Solar Cells. *RSC Adv.* **2015**, *5*, 53426−53432.
(38) Rakstys, K.; Abate, A.; Dar, M. I.; Gao, P.; Jankauskas, V.; Jacopin, G.; Kamarauskas, E.; Kazim, S.; Ahmad, S.; Grätzel, M.; Nazeeruddin, M. K. Triazatruxene-Based Hole Transporting Materials for Highly Efficient Perovskite Solar Cells. *J. Am. Chem. Soc.* **2015**, *137*, 16172−16178.
(39) Saliba, M.; Orlandi, S.; Matsui, T.; Aghazada, S.; Cavazzini, M.; Correa-Baena, J.-P.; Gao, P.; Scopelliti, R.; Mosconi, E.; Dahmen, K.-H.; et al. A molecularly engineered hole-transporting material for efficient perovskite solar cells. *Nature Energy* **2016**, *1*, 15017.

DOI: 10.1021/acsami.6b12236
ACS Appl. Mater. Interfaces 2016, 8, 34414−34421

Nano Energy 35 (2017) 215–222

Contents lists available at ScienceDirect

Nano Energy

journal homepage: www.elsevier.com/locate/nanoen

Full paper

1-dimensional TiO_2 nano-forests as photoanodes for efficient and stable perovskite solar cells fabrication

Manuel Salado[a], Manuel Oliva-Ramirez[b], Samrana Kazim[a], Agustín R. González-Elipe[b], Shahzada Ahmad[a,*]

[a] Abengoa Research, Abengoa, c/ Energía Solar nº. 1, Campus Palmas, Altas, 41014 Sevilla, Spain
[b] Instituto de Ciencia de Materiales de Sevilla, (CSIC-Universidad de Sevilla), c/ Americo Vespucio 49, 41092 Sevilla, Spain

ARTICLE INFO

Keywords:
Solar cells
Perovskite solar cells
1-Directional structures
Photoanode
Charge transfer

ABSTRACT

During the last years, perovskite solar cells have gained increasing interest among the photovoltaic community, in particularly after reaching performances at par with mature thin film based PV. This rapid evolution has been fostered by the compositional engineering of perovskite and new device architectures. In the present work, we report the fabrication of perovskite solar cells based on highly ordered 1-dimensional vertically oriented TiO_2 nano-forests. These vertically oriented porous TiO_2 photoanodes were deposited by physical vapor deposition in an oblique angle configuration, a method which is scalable to fabricate large area devices. Mixed $(MA_{0.15}FA_{0.85})Pb(I_{0.85}Br_{0.15})_3$ or triple cation $Cs_{0.05}(MA_{0.15}FA_{0.85})_{0.95}Pb(I_{0.85}Br_{0.15})_3$ based perovskites were then infiltrated into these 1-dimensional nanostructures and power conversion efficiencies of 16.8% along with improved stability was obtained. The devices fabricated using 1D-TiO_2 were found to be more stable compare to the classical 3-dimensional TiO_2 photoanodes prepared by wet chemistry. These 1-D photoanodes will be of interest for scaling up the technology and in other opto-electrical devices as they can be easily fabricated utilizing industrially adapted methodologies.

1. Introduction

Currently, the field of Photovoltaics (PV) is dominated by silicon PV technology. Among possible alternatives are thin-film based technologies and molecular solar cells. In recent years hybrid inorganic-organic perovskite based solar cells have positioned themselves very well as viable option and are now at par with mature thin film based CIGS {Cu(In,Ga)(Se,S)$_2$}or CdTe technology in terms of efficiencies [1–6]. A light to electricity conversion efficiency in excess of 22% has been reported for this emerging solar cells, and high expectations arisen with respect to a near future transfer and adaptation of laboratory based processes to a pre-commercial stage. In perovskite solar cells, the active materials acting as light absorber have an ABX_3 type perovskite structure. The use of perovskite has transformed through time and methylammonium lead iodide ($MAPbI_3$) and other compositional engineered mixed perovskites are being employed for the fabrication of highly efficient solar cells [7,8].

The high charge carrier mobilities in perovskites together with its conduction and valence band energy levels are well suited for applications in solar energy [4,7]. The perovskite layer is sandwiched between two charge selective contacts which generate the driving force for the charge separation. Upon illumination of light, electrons are transferred to the conduction band of an electron-transport layer while the holes are transferred to a hole-transport material (HTM) [7]. Commercially available anatase TiO_2 colloidal particles are the most exploited metal oxide used as electron transporting material [1,3] (ETM). The thickness of the ETM and their interfaces are key parameters for the fabrication of efficient and stable solar cells. The electron selective contact not only transports the electronic charges but also influences the growth of perovskite crystals. The use of one-dimensional metal oxides (e.g. TiO_2, ZnO) structures can be an attractive strategy to get uni-directional and fast charge collection, higher absorption of active materials and light management due to scattering within 1-dimensional structures. In the past, TiO_2 based nano-tubes were subject to intense investigation in sensing and other electro-optical application [9–14].

1-D based structures provides large surface-to-volume ratio, unidimensionality along with high surface reactivity, and are widely used in electro-catalysis, photo-catalysis, sensing and for other energy storage applications. Anodization [12] of metal plate remains a classical approach to produce 1-D structures, however they need to be transferred on a foreign substrate and contains defects. Moreover,

* Corresponding author.
E-mail address: shahzada.ahmad@abengoa.com (S. Ahmad).

http://dx.doi.org/10.1016/j.nanoen.2017.03.034
Received 9 November 2016; Received in revised form 14 March 2017; Accepted 16 March 2017
Available online 18 March 2017

uniformity over a large area and uniform pore size control also remain tricky aspects, limiting their use to lab curiosity. Using template methods and wet chemistry approaches, it is also possible to produce 1-D structures, although large area uniformity and batch to batch reproducibility of 1-D structures was difficult to achieve [13].

In the most studied perovskite solar cells, a mesoporous structure is coated atop of a blocking (dense) layer of TiO_2. Reports suggest this as nucleating site for perovskite growth, which allows fabricating continuous perovskite layers, thus influencing the charge selective properties of the ETM. However, the existence of grain boundaries between the nano-particles of the porous layer increases the trapping sites and the electron recombination rate. One-dimensional (1D) TiO_2 nanostructures (nano-wires, nano-tubes or nano-rods) were earlier found to have lower charge recombination rates at the grain boundaries and to provide a facile electron injection pathway due to unidirectional axis charge transport in dye sensitized solar cells (DSSCs). The enhanced performance in 1D-TiO_2 perovskite solar cells has been possibly due to their higher light harvesting abilities and lower recombination losses with respect to 3D-TiO_2 as measured by impedance spectroscopy [14].

The versatility to deposit perovskites using wet chemistry, [1,3,4,7] vapor deposition or in a mix process utilizing a solution method for the inorganic precursor and vapor assisted for the organic component have made it possible the manufacturing of a variety of device architectures.

The use of 1-D nanostructures (nano-columns, nano-rods, nano-wires) reported to be effective in enhancing electron transport properties for different solar cells including silicon [15], III-V semiconductors [16], organic photovoltaics [17] and DSSCs [18–22]. Additionally, the use of 1-D nanostructures will not only benefit the transport properties [23] along the axis but, contribute to minimize the reflection of light due to their generally low-refractive index, thus favoring the absorption of light by the active components and enhancing the light harvesting efficiency. In DSSCs the use of 1-D nanostructures was found to have a positive effect in increasing the amount of dye absorption, improved transport properties and carriers lifetime and as a result give rise to photocurrents comparable to those of equivalent mesoporous nanoparticle based devices [24,25]. Utilizing these strategy, in the present work we have prepared porous photoanodes based on vertically aligned 1D-TiO_2 thin films prepared by the physical vapor deposition method at oblique incidences angles (PVD-OAD) [26–28] and used them for the fabrication of perovskite solar cells in a similar fashion. To improve the device performance, herein we have optimized mixed {Formamidinium (FA), methylammonium (MA)} and triple cation (FA/MA/Cs) based perovskites. In addition, we have tuned the thickness of the photoanode to influence morphological parameters such as porosity of the 1-D TiO_2 with an aim of increasing photovoltaic performance magnitudes such as short circuit current (J_{SC}), open-circuit voltage (V_{OC}), fill factor (*FF*) and, ultimately, PCE.

It is worth noting regarding the future scaling up of the technology the use of the uniform 1-directional nano-forests photoanodes can be easily prepared over larger areas using PVD-OAD technique [28]. Recently nanostructured [29–32] based photoanodes (thickness 500–1500 nm) were utilized for solar cells fabrication, while thinner photoanodes of nano-structured TiO_2 were also found by us to be rather effective for device fabrication [26,27]. It is expected that nano-forests based photoanodes can show even better light harvesting efficiencies by enhancing the light scattering properties of the devices. Then, as a consequence of the effective transport of charge along the nano-forests an increase in PCE could be obtained. Thus, combining the benefits of light–scattering centers and low ionic diffusion resistance, the performance of solar cell was improved to a great extent. To the best of our understanding this is the best result so far reported for any 1D-nanostructured photoanodes in perovskite solar cells. Large area uniform 1D structures as ETM in perovskite solar cells has neither been reported so far. These successful attempts to simplify the manufacturing operation of charge selective contacts is an encouraging step for their large-scale implementation in a plethora of other opto-electrical devices.

2. Experimental

2.1. Materials

All chemicals were commercial products either from Sigma Aldrich or Agros and were employed without any treatment or purification. 2,2′,7,7′-tetrakis(*N*,*N*-di-p-methoxyphenyamine)-9,9-spirobifluorene (Spiro-OMeTAD) was acquired from Merck KGaA. Methylammonium iodide (MAI), formamidinium iodide (FAI), methylammonium bromide (MABr) were bought from Dyesol while PbI_2 and $PbBr_2$ were bought from Tokyo Chemical Industry (TCI).

2.2. Preparation of TiO_2 nano-forests photoanode

1-Dimensional nanostructured TiO_2 depicting a nano-forests microstructure were used as photoanodes. They consisted of a porous structured layer made of vertically aligned nano-columns with an approximate thickness of either 100 or 200 nm. These TiO_2 porous photoanodes were prepared at room temperature by physical vapor deposition at oblique incidence (PVD-OAD) in an electron beam evaporator using a similar procedure than in previous publications [24–28]. Basically, the method entails placing the substrate surface at a glancing angle with respect to the evaporation source. Operational conditions such as beam current, oxygen partial pressure during deposition or distance from the target are kept similar than those reported in these previous works. In the present experiment the zenithal evaporation angle (α) defined between the normal to the substrate and the flux of evaporation material was fixed at 80°. Varying the zenithal angle can be used to tailor the tilting angle of the nano-columns, as well as the porosity and other properties of the films [28]. In the present investigation, to obtain vertically aligned nano-forests and an increased layer porosity, we azimuthally rotated the substrate during deposition (40 rpm) and controlled the deposition time to prepare the two utilized layer thicknesses, i.e., 100 or 200 nm.

2.3. Device fabrication

Transparent conducting coated glasses (TEC15, 15 Ω/sq) were used as substrate. They were cleaned by ultrasonication in 2% Hellmanex water solution for 30 min followed by rinsing with deionized water and ethanol. Then, a ~40 nm TiO_2 compact layer was deposited on FTO (TEC15) substrate via spray pyrolysis at 450 °C from a precursor solution of titanium diisopropoxidebis-(acetylacetonate) in anhydrous ethanol. After the spraying, the substrates were left at 450 °C for 45 min and allowed to cool down till room temperature. These substrates were then used for the deposition of the TiO_2 nano-forests by PV-OAD and, for comparative purposes, a standard mesoporous layer of TiO_2 deposited by spin coating for 30 s at 4000 rpm. As starting material, we used a TiO_2 paste (Dyesol 30 NR-D) diluted in ethanol (1:7) to achieve a 150–200 nm thick layer. After the deposition of the TiO_2, either by spin coating or PV-OAD, the substrates were dried at 100 °C for 10 min and then annealed again at 450 °C for 30 min under a dry air flow. This thermal treatment aims at transforming the otherwise amorphous TiO_2 layers into anatase. After cooling down to 150 °C, these TiO_2 photoanodes were transferred to an glovebox for depositing the perovskite layers. The perovskite films were deposited from a precursor solution containing FAI (1 M), PbI_2 (1.2 M), MABr (0.2 M), and $PbBr_2$ (0.2 M) in anhydrous DMF:DMSO 4:1 (v:v). The perovskite solution was spin coated in a two-step sequence at 1000 and 4000 rpm for 10 and 30 s, respectively. During the second step, 100 μL of chlorobenzene was used as an antisolvent approach and poured on the substrate, 15 s prior the end of the spinning. The substrates were then annealed at 100 °C for 1 h in a glovebox. For the triple cation based perovskite $Cs_{0.05}(MA_{0.15}FA_{0.85})_{0.95}Pb(I_{0.85}Br_{0.15})_3$, CsI was separately dissolved (1.5 M stock solution in dimethyl sulfoxide (DMSO)), and added to the mixed perovskite precursor to achieve the 5% composition.

After the perovskite formation, the hole transport layer, consisting

of Spiro-OMeTAD (70 mM in chlorobenzene), was spun coated at 4000 rpm for 20 s. Spiro-OMeTAD was doped with bis- (trifluoro-methylsulfonyl)imide lithium salt (Li-TFSI), tris(2-(1H-pyrazol-1-yl)-4-tert-butylpyridine)cobalt(III)-tris(bis- (trifluoro-methylsulfonyl) imide) (FK209, from Dynamo), and 4-tert-Butylpyridine (*t-BP*). The molar ratio of additives for HTMs was: 0.5, 0.03, and 3.3 for Li-TFSI, FK209, and *t-BP*, respectively. To complete the device fabrication, the cathode, made of, 70–80 nm of gold, was thermally evaporated under low vacuum (10^{-5}×10^{-6}). All solutions were prepared inside an argon glove box with controlled moisture and oxygen conditions (O_2 and H_20 < 10 ppm).

2.4. Characterization

Current density–voltage (*J–V*) curves were recorded with a Keithley 2400 source-measurement-unit under AM 1.5 G, 100 mW cm^2 illumination from a certified Class AAA, 450 W solar simulator (ORIEL, 94023 A). Light output power was calibrated using a NREL certified calibrated mono-crystalline silicon solar cell. A black metal mask (0.16 cm^2) was placed over the square shaped device (active area 0.5 cm^2) to reduce the influence of scattered light. An optimized scan rate of 10 mV/s was used for measuring the devices to calculate the accurate value for efficiencies without having hysteresis effects. For IPCE measurements, a 150 W xenon lamp coupled to an Oriel Cornerstone 260 motorized ¼ m monochromator was used as the light source, while a 2936-R power meter was used to measure the short circuit current. Cross-sectional microscopy and normal topography images were taken with a Hitachi S5200 field-emission microscope operating at 5.0 keV.

The transmittance and reflectance spectra of the TiO_2 nano-forests deposited on FTO before and after perovskite deposition were measured using Perkin Elmer, UV–vis–NIR lambda 1050 spectrophotometer equipped with a 160 mm integrating sphere. Refractive index and thickness of the nano-forests TiO_2 films were calculated by fitting their transmittance spectra using a home-made code software based on the well-known transfer-matrix procedure [33]. The code considered a typical Cauchy dispersion for the wavelength dependence of the refractive index of the films. The reported thicknesses of the porous layers obtained as an output of the fitting procedure is in agreement with the values determined experimentally by SEM micrographs analysis.

3. Results and discussion

A schematic design of the fabricated perovskite solar cells is shown in Fig. 1. It represents a device incorporating a nano-forests TiO_2 acting as photoanode in the perovskite solar cell.

Fig. 2a shows experimental and simulated UV–vis transmission spectra of the TiO_2 layers deposited on silicon, both of them running in good accord. The simulation analysis rendered thickness values for these two layers of 109 and 216 nm, a refraction index of 1.74 for the samples and an estimated porosity in the order of 60% of the total volume of the films (rough calculation by taking into account that compact TiO_2 thin films have a refraction index of around 2.4 and that the pores are filled with air during the analysis).

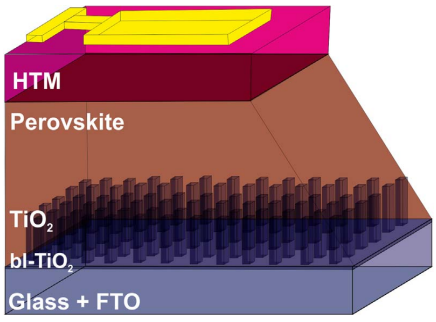

Fig. 1. Schematic diagram of TiO_2 nano-forests based perovskite solar cells.

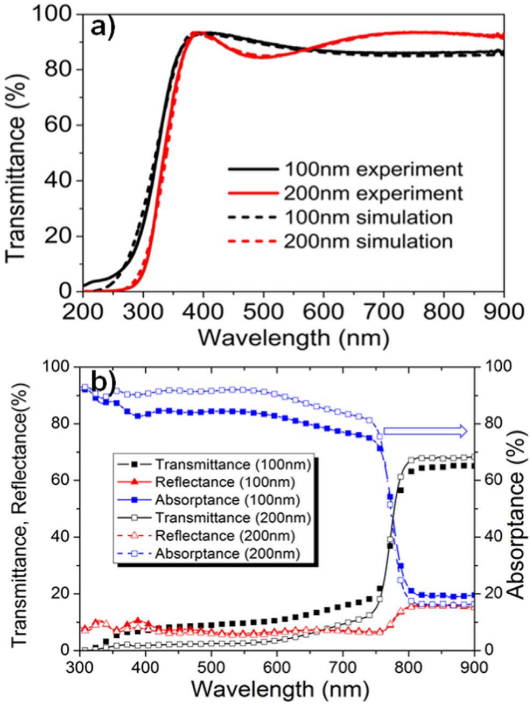

Fig. 2. a) Experimental and simulated transmission spectra for different thickness of TiO_2 nano-forests grown on quartz, b) absorptance (A=1-R-T) calculated from the measured transmittance (T) and reflectance (R) spectra of the device measured with the integrating sphere for different thickness of TiO_2 nano-forests grown on FTO after the perovskite impregnation.

Fig. 2b depicts the transmittance (T) and reflectance (R) spectra measured with the integrating sphere after deposition of perovskite. (i.e. over a FTO glass covered by a thin compact layer of TiO_2 and the nano-forests layer). Absorptance was calculated by subtracting reflectance and transmittance using the equation 1-R-T.

In both 100 and 200 nm TiO_2 nano-forests based photonaode, the absorptance (A) maxima appeared at 500–550 nm due to the high extinction coefficient of perovskite in this region, while in the spectral region from 400 to 750 nm, absorptance reaches up to 80% and 70% for the 100 and 200 nm thick nano-forests photoanode, respectively (Fig. 2b). However, the highest absorptance up to 90% was found for the 200 nm nano-forests device due to larger grain sizes and porosity. A thicker TiO_2 will also allow better infiltration of perovskite inside the pores.

Fig. 3a–f shows the topography and a series of cross section micrographs for the nano-forests TiO_2 as well as for the entire devices. Fig. 3 b and e show cross section of the nano-forests TiO_2 layers of 100 nm and 200 nm grown on a silicon substrate. The micrographs show that the films microstructure consists of vertically oriented uniform 1-dimensional nanocolumns defining a forest-like structure. Comparing the two films, it is also apparent that the nano-forests in the photoanode made up of 200 nm thick TiO_2 film have thickened as they have grown in length. This columnar thickening effect is typical of OAD films [28] and gives rise to a surface topography (c.f. normal SEM

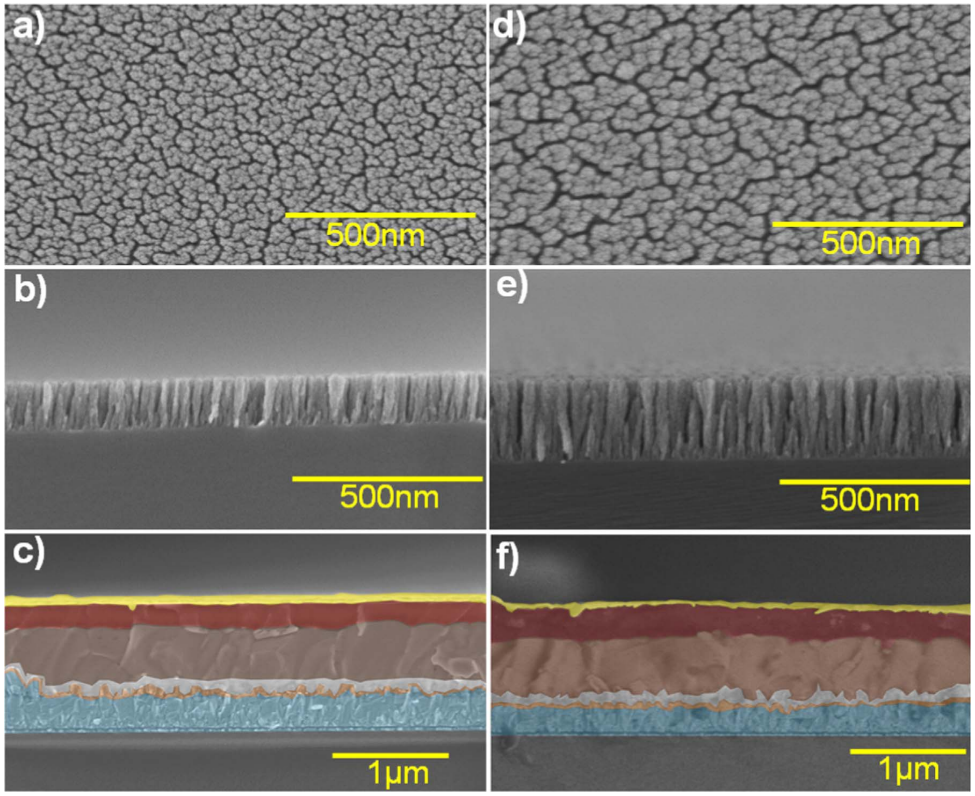

Fig. 3. a) Top view scanning electron microscopy (SEM) image of the 100 nm thick TiO_2 nano-forests, b) SEM cross section image of the 100 nm thick TiO_2 nano-forests film grown on a silicon substrate, c) SEM cross section image of a device with 100 nm TiO_2 nano-forests, d) top view SEM image of a 200 nm thick TiO_2 nano-forests, e) cross section of 200 nm thick TiO_2 nano-forests grown on a silicon substrate and f) cross section of device fabricated with 200 nm TiO_2 nano-forests.

micrographs in Fig. 3a–d) consisting of bigger grains and larger pore entrances at the surface. Moreover, these two normal images of nano-forest TiO_2 layers reveal that the individual nano-columnar structures are extremely well ordered and homogeneously distributed over the substrate. Fig. S1 depicts the magnified image of TiO_2 nano-forests. Similar microstructures are difficult to achieve with TiO_2 thin films deposited by wet chemistry routes, which generally possess an uneven dispersion and considerable aggregation of nano-particles and a poor interfacial contact between the layers material and the substrate. Some undesirable consequences of these microstructures in solar cells are poor electron transfer and a high charge recombination rate, both effects contributing to decrease the overall device efficiency.

Device cross-section image (Fig. 3c and f), depict that, a thick conformal capping layer of perovskites formed atop of perovskite infiltrated TiO_2 structures.

A very intimate and sharp interface can be seen in the cross sectional image of the fabricated solar cells (Fig. 3c and f). From bottom to top of these images, layers due to FTO (400 nm), compact TiO_2 (ca. 40–60 nm), TiO_2 nano-forests (ca. 100 or 200 nm) and perovskite (ca. 400 nm) are clearly distinguished. Atop the perovskite capping layer the 150 thick hole transporting material (Spiro-OMeTAD) and the gold cathode layer (c.a. 80 nm) can be easily distinguished. The device cross sectional image is in well agreement with the architecture of this type of devices (Fig. 1), and the layers are stacked accordingly without any defects or large inhomogeneities. It is noteworthy that large area uniform 1-D porous structures were fabricated using the PV-OAD technique.

Earlier, with the help of ToF-SIMS, we proved a homogeneous infiltration [27] of the perovskite in the pores of 1D-nanostructured TiO_2 films prepared by PV-OAD without azimuthal rotation and a thickness higher than > 500 nm. In the 100–200 nm thick photo-anodes with vertical orientation resembles as nano-forests in the present work, we can reasonably assume that the perovskite has effectively filled the inter-columnar space in the films.

Table 1
Performance of the perovskite solar cells fabricated employing vertical TiO_2 nano-forests as photoanodes.

Thickness[a] (nm)	Perovskites	J_{SC} (mA cm^{-2})	V_{OC} (mV)	FF	PCE (%)
100	$Cs_{0.05}(MA_{0.15}FA_{0.85})_{0.95}Pb(I_{0.85}Br_{0.15})_3$	20.78	1077	72.18	16.17
200	$Cs_{0.05}(MA_{0.15}FA_{0.85})_{0.95}Pb(I_{0.85}Br_{0.15})_3$	21.24	1061	74.53	16.80
1:7 TiO_2	$Cs_{0.05}(MA_{0.15}FA_{0.85})_{0.95}Pb(I_{0.85}Br_{0.15})_3$	20.68	1046	68.68	14.86

[a] Thickness of the PVD-OAD TiO_2 based photoanode.

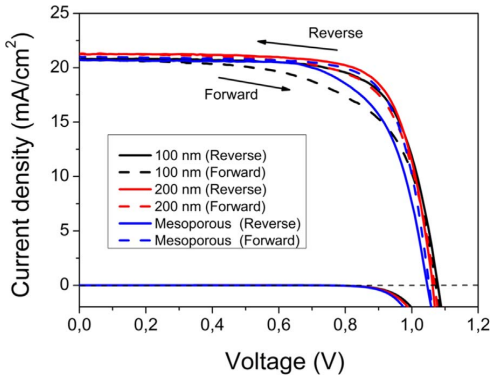

Fig. 4. Current-voltage curve for different photoanode based perovskite solar cells at 1 sun conditions.

The device photovoltaic parameters are summarized in the Table 1 and the *J-V* curves are shown in Fig. 4. We found that the devices based on a nano-forests based structure performed better than the devices fabricated from 3-dimensional TiO_2 deposited through wet chemistry techniques (spin coating of diluted TiO_2 paste). Increments in V_{OC} and in J_{SC} were observed when compared to 3-dimensional TiO_2 structures. More importantly, the FF of the devices increased significantly, reaching 74.5% for 200 nm thick TiO_2 nano-forests, a highly competitive value for perovskite solar cells. This increase in FF points towards a low electron-hole recombination in these devices. No significant differences were found between the devices with 100 or 200 nm thick TiO_2 nano-forests photoanode. 100 nm thick nano-forests gave a slightly higher V_{OC} (1077 mV) as compared with that of 200 nm (1046 mV), due to low series resistance. In the past, using TiO_2 nano-columnar structures prepared by PV-OAD without rotation, the best PV properties were obtained for 200 nm thick layers, which yielded a PCE of 10.53% with $MAPbI_3$ based perovskites [27]. Fig. S2 depicts the device statistics and which are reproducible. We speculate that for a relatively thicker TiO_2 nano-forests photoanode, the thickness of the perovskite layer (infiltrated+capping layer) will be higher and therefore a more efficient photon collection and conversion into electrons will be obtained. Fig. 5 shows that the IPCE spectra of the fabricated perovskite solar cells presents a very flat IPCE profile in the 400–700 nm region and a value close to 80%. The integrated current is in agreement with the *J-V* curves and is represented on the secondary Y-axis of Fig. 5. A similar profile was depicted by the 200 nm- thick nano-forest and the mesoporous TiO_2 based solar cells.

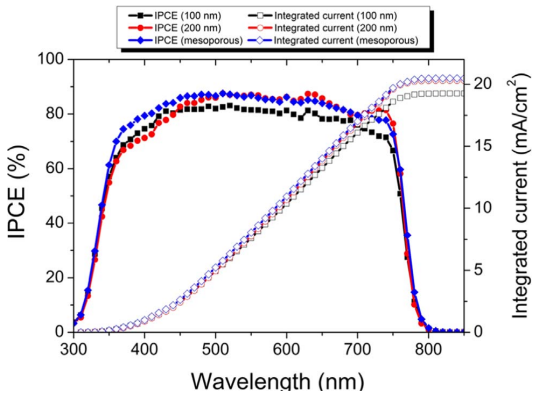

Fig. 5. IPCE curves for the solar cells with different types of TiO_2 photoanode.

Meanwhile, the 100 nm thick nano-forests shows a slightly lower photo-to-electron conversion. The 200 nm thick TiO_2 nano-forests based photoanode were the best in terms of current. In addition, the 200 nm thick photoanodes showed a significantly better voltage (V_{OC}) performance and a higher *FF* and, as a result, it gave the best PCE of 16.8%. Notably, the PCE of nano-forests based devices supersede the mesoporous based perovskite solar cells. The main difference can be seen in the increase of the FF value originated from the lower recombination in ETM as discussed in device kinetics section.

We can account for these effects in the following way. Since light has to travel through the ETM, the different thickness and transmittance of the photoanode will influence the IPCE profiles, particularly at the wavelengths of their absorbance. The slightly improved IPCE profile was shown by 200 nm thick nano-forests with an improvement in 550–750 nm range and with a peak value of 83.2% at 514 nm. The obtained improvements in IPCE values at specific wavelengths are due to the lower recombination losses.

Though we expect a facile charge injection between photoanode and perovskite layers, there is no clue to relate that the excitons generated in the HTMs layer are dissociated into photocurrent in the comparison between the IPCE profiles and the spectra in Fig. 2. We can speculate that nano-forests photoanode play the roles of extracting and transportating the charge carriers.

Fig. 6 represents, the PV parameters plotted as a function of time to prove the stability of the solar cells fabricated using the TiO_2 nano-forest and the standard mesoporous photoanodes. The un-encapsulated devices were subjected to periodically *J-V* measurements and, in-between, they were kept in dark conditions under ambient atmosphere (< 50–60% R.H.). Significant improvement in the stability was observed in the case of the devices with 1-D vertically oriented TiO_2 nano-forest photoanode. In general, an improvement of V_{OC} was observed over the time period of 50 days. Notably, the devices were significantly stable due to the addition of cesium (triple cation), which is known to retard the back conversion of perovskites into PbI_2 and also prohibits halide segregation. Improved PCEs with time (age) were obtained for TiO_2 nano-forests based photoanodes. Relatively stable solar cells were obtained with the photoanodes prepared by PV-OAD due to its one-directional orientation and slow recombination losses. The calculated drop in efficiency after 50 days was only 3.87% in the case of 200 nm, while for the standard (mesoporous) photoanode device, the drop was about 13.35%. This suggests that nano-forests photoanodes due to its facile charge collection, minimizes the traps sites (recombination center) over the period of time and in comparison with the mesoporous TiO_2 layers contributes to increase its stability.

In order to explore the dynamical processes occurring in the devices under real operation conditions, we have employed electrochemical impedance sspectroscopy (EIS) to obtain information regarding recombination processes and carrier lifetime. In the past these techniques have been used to unravel electron dynamics, first in DSSCs and lately in perovskite solar cells different types of perovskite solar cells [35]. In EIS, we prove the system response with the application of a sinusoidal signal, e.g.: $E=E_0\sin(\omega t)$, where E_0 is the signal amplitude, $\omega=2\pi f$ is the angular frequency, and f is the signal frequency. This signal is in the order of few mVs and therefore the response can be linearized so as to detect the specific frequencies which are characteristic of the device [34].

For the three different types of fabricated devices, Fig. 7 shows the plots of recombination resistance as a function of voltage. An equivalent circuit (Fig. 8, inset) was used to obtain the recombination resistance and capacitance values of the devices. It has been reported [35–37] that capacitance in the perovskite layer is typically controlled by a geometrical component, which can be expressed by the relation, $C_g=\varepsilon\varepsilon_O A/d$, where ε is the dielectric constant of the perovskite, ε_O is the vacuum permittivity, A the effective contact area and d is the thickness. R_{rec} is expected to decrease exponentially with voltage, while the capacitance extracted from the high frequency component is

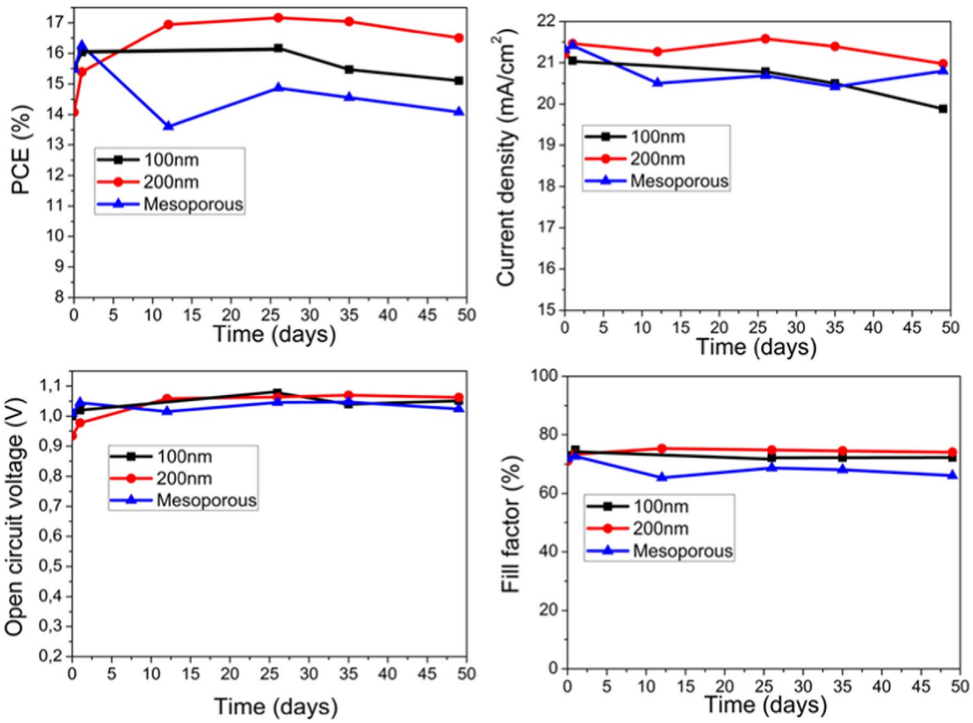

Fig. 6. Evolution of the photovoltaic parameters (PCE, J_{SC}, V_{OC} and *FF*) for the nano-forests TiO_2 and standard mp-TiO_2 photoanodes at one sun illumination conditions.

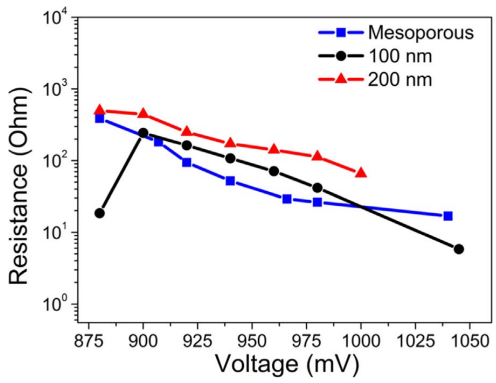

Fig. 7. Recombination resistance as obtained from the fittings of $-R(R_{rec}C)$- equivalent circuits of the impedance response for all studied devices.

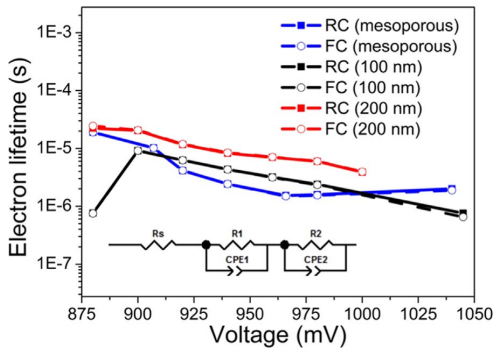

Fig. 8. Electron lifetimes versus voltage obtained by two different methods. FC=fit circle of the semicircle (w) and RC=recombination resistance and capacitance. Inset shows the equivalent circuit used to analyze impedance measurements.

constant, independently on the applied voltage as expected from a geometrical dependence. This is ratified by the results reported in Fig. 7 and in the supporting information S3. In addition, it can be deduced that the nano-forests microstructure possesses a higher recombination resistance than the mesoporous one, which could be attributed to a better interconnection between the perovskite and the electron transport layer, where the unidirectional flow of charges would render a better carrier extraction.

Time constants for the lifetime of the carriers can also be elucidated from EIS. Fig. S4 shows the Nyquist plot of the solar cells with different TiO_2 photoanode as ETM selective contacts. Taking into account only the time constants (semicircles) appeared in the plot, the analysis can be tricky. Nevertheless, the peak appearing at higher frequencies is associated to the recombination of carriers [38]. Considering this into account, from EIS results, time constants can be estimated by means of two different formulas. First, from the inverse of the maximum angular frequency, although it can also be expressed in terms of recombination resistance and capacitance. Eq. (1) represents time constant extracted from the maximum angular frequency and Eq. (2) time constant from the recombination resistance and capacitance.

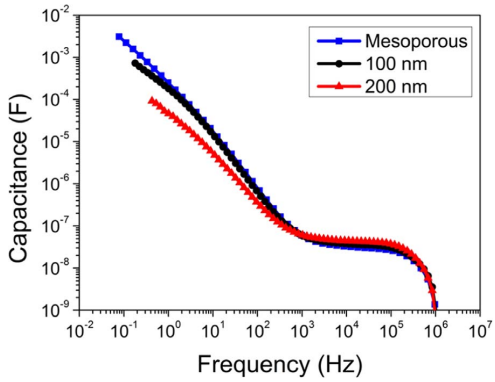

Fig. 9. Capacitance spectra for the three studied TiO_2 nanostructures measured at the same voltage.

$$\tau_n = \frac{1}{\omega_{\max}} \quad (1)$$

$$\tau_n = R_{rec} C \quad (2)$$

Electron lifetimes follow the same trend as of recombination resistance (Fig. 8), and shows decays exponentially with voltage. On the other hand, when plotting (Fig. 9) the capacitance as a function of frequency, the trend followed the typical behavior of a perovskite solar cells, characterized by a plateau at the mid-frequency region which can be associated to the bulk capacitance of the perovskite [39–41]. The existence of different types of charge carriers inside the hybrid perovskite solar cell is well known. Ionic movement inside the perovskite at low-frequency ranges was observed. Additionally, electrode polarization caused due to ion interfacial accumulation, can be the possible cause of a hysteresis behavior due to the perovskite layer´s excess capacitance. Past experiments revealed that capacitance values at low-frequencies indicate the presence of high hysteresis [39,41–45]. This effect is in accordance with the results obtained in our study (Fig. S5 and Table S1) for different TiO_2 structures. Thus, it was found that 200 nm thick nano-forests presents lower slope values for the capacitance at low-frequencies, as well as lower values of hysteresis index (HI). By using transient photovoltage analysis longer charge recombination lifetime was also reported for 1-directional photoanode w.r.t to randomly packed 3-dimensional TiO_2 scaffold. [13].

4. Conclusions

A facile and industrially scalable method is reported for the deposition of 1-dimensional TiO_2 nano-forests. This was then used as photoanode in perovskite solar cells. Porous and homogeneous 1D-TiO_2 thin films were fabricated through this proven methodology and gave competitive power conversion efficiencies. This performance proves that the presented methodology can meet the standards required for practical application and large area integration.

They are vertically aligned, ordered and transparent 1-D TiO_2 structures. Photocurrent density values as high as of 22.6 mA cm^{-2} and an encouraging photovoltaic performance of 15% for mixed $\{(MA_{0.15}FA_{0.85})Pb(I_{0.85}Br_{0.15})_3\}$ and c.a. 17% for triple cation $\{(Cs_{0.05}(MA_{0.15}FA_{0.85})_{0.95}Pb(I_{0.85}Br_{0.15})_3\}$ based perovskites under standard full sun illumination were obtained. To the best of our knowledge, to date this is the highest reported power conversion efficiency reported for any 1-dimensional TiO_2 photoanode. Using these 1-D structures, improved photovoltaic performance were obtained, pointing towards more efficient charge collection/extraction as supported by the impedance spectroscopy. Furthermore, ageing tests carried out on unsealed devices suggests improved stability as compared to 3-dimensional mesoporous structures. The facile electron collection in these 1-dimensional nano-forests devices resulted in relatively stable system than mesoporous ones deposited by spin coating of TiO_2. We believe that the reported thin film process techniques bring about new dimensions for perovskite solar cells fabrication and facilitate an easy integration.

Acknowledgements

We thank Laura Calio for help with coloration of SEM images and ARG thanks EU-FEDER funds and the MINECO (projects MAT2013-40852-R and MAT2016-79866-R) for financial support.

Author contribution: M.S made all the experiments and graphs, MOR fabricated nano-forests structures and performed microscopy experiments, SK made electro-optical characterization and revised the MS, ARG supervised the nano-forests structures preparation and revised the MS, and S.A supervised and coordinate the research, made the initial draft of the manuscript. All authors contributed to the completion of the final document.

Appendix A. Supporting information

Supplementary data associated with this article can be found in the online version at doi:10.1016/j.nanoen.2017.03.034.

References

[1] H.-S. Kim, C.-R. Lee, J.-H. Im, K.-B. Lee, T. Moehl, A. Marchioro, S.-J. Moon, R. Humphry-Baker, J.-H. Yum, J.E. Moser, M. Grätzel, N.-G. Park, Sci. Rep. 2 (2012) 591.
[2] M. Liu, M.B. Johnston, H.J. Snaith, Nature 501 (2013) 395–398.
[3] J. Burschka, N. Pellet, S.-J. Moon, R. Humphry-Baker, P. Gao, M.K. Nazeeruddin, M. Grätzel, Nature 499 (2013) 316–319.
[4] a) S. Kazim, M.K. Nazeeruddin, M. Grätzel, S. Ahmad, Angew. Chem. Int. Ed. 53 (2014) 2812–24;
b) Angew. Chem. 126 (2014) 2854–2867.
[5] N.J. Jeon, J.H. Noh, Y.C. Kim, W.S. Yang, S. Ryu, S. Il Seok, Nat. Mater. 13 (2014) 897–903.
[6] J.-H. Im, I.-H. Jang, N. Pellet, M. Grätzel, N.-G. Park, Nat. Nanotechnol. 9 (2014) 927–932.
[7] a) L. Calio, S. Kazim, M. Grätzel, S. Ahmad, Angew. Chem. Int. Ed. 55 (2016) 14522–14545;
b) Angew. Chem. 128 (2016) 14740–14764.
[8] M. Salado, F.J. Ramos, V.M. Manzanares, P. Gao, M.K. Nazeeruddin, P.J. Dyson, S. Ahmad, ChemSusChem 9 (2016) 2708–2714.
[9] M.H. Kumar, N. Yantara, S. Dharani, M. Grätzel, S. Mhaisalkar, P.P. Boix, N. Mathews, Chem. Commun. 49 (2013) 11089–11091.
[10] F.J. Ramos, M.C. López-Santos, E. Guillén, M.K. Nazeeruddin, M. Grätzel, A.R. González-Elipe, S. Ahmad, ChemPhysChem 15 (2014) 1148–1153.
[11] J.T.-W. Wang, J.M. Ball, E.M. Barea, A. Abate, J.A. Alexander-Webber, J. Huang, M. Saliba, I. Mora-Sero, J. Bisquert, H.J. Snaith, R.J. Nicolas, Nano Lett. 6 (2013) 1739–1743.
[12] P. Qin, M. Paulose, M.I. Dar, T. Moehl, N. Arora, P. Gao, O.K. Varghese, M. Grätzel, M.K. Nazeeruddin, Small 11 (2015) 5533–5539.
[13] M.-S. Seo, I. Jeong, J.-S. Park, J. Lee, I.K. Han, W.I. Lee, H.J. Son, B.-H. Sohn, M.J. Ko, Nanoscale 8 (2016) 11472–11479.
[14] O.A. Jaramillo-Quintero, M.S. de la Fuente, R.S. Sanchez, I.B. Recalde, E.J. Juarez-Perez, M.E. Rincón, I.M. Seró, Nanoscale 8 (2016) 6271–6277.
[15] B. Tian, X. Zheng, T.J. Kempa, Y. Fang, N. Yu, G. Yu, J. Huang, C.M. Lieber, Nature 449 (2007) 885–889.
[16] P. Krogstrup, H.I. Jørgensen, M. Heiss, O. Demichel, J.V. Holm, M. Aagesen, J. Nygard, A. Fontcuberta i Morral, Nat. Photonics. 7 (2013) 306–310.
[17] Y. Liu, F. Zhang, J. Wang, Int. J. Photoenergy 34 (2013) 1–6.
[18] X. Feng, K. Shankar, O.K. Varghese, M. Paulose, T.J. Latempa, C.A. Grimes, Nano Lett. 8 (2008) 3781–3786.
[19] W.-Q. Wu, B.-X. Lei, H.-S. Rao, Y.-F. Xu, Y.-F. Wang, C.-Y. Su, D.-B. Kuang, Sci. Rep. 3 (1352) (2013) 1–7.
[20] G.S. Han, S. Lee, J.H. Noh, H.S. Chung, J.H. Park, B.S. Swain, J.-H. Im, N.-G. Park, H.S. Jung, Nanoscale 6 (2014) 6127–6132.
[21] F. Shao, J. Sun, L. Gao, S. Yang, J. Luo, J. Mater. Chem. 22 (2012) 6824–6830.
[22] F. Sauvage, F. Di Fonzo, A. Li Bassi, C.S. Casari, V. Russo, G. Divitini, C. Ducati, C.E. Bottani, P. Comte, M. Grätzel, Nano Lett. 10 (2010) 2562–2567.
[23] X. Sheng, D. He, J. Yang, K. Zhu, X. Feng, Nano Lett. 14 (2014) 1848–1852.
[24] L. González-García, I. González-Valls, M. Lira-Cantu, A. Barranco, A.R. González-Elipe, Energy Environ. Sci. 4 (2011) 3426–3435.

[25] L. González-García, J. Parra-Barranco, J.R. Sánchez-Valencia, A. Barranco, A. Borrás, A.R. González-Elipe, M.-C. García-Gutiérrez, J.J. Hernández, D.R. Rueda, T.A. Ezquerra, Nanotechnology 23 (2012) 205701.
[26] F.J. Ramos, M. Oliva-Ramirez, M.K. Nazeeruddin, M. Grätzel, A.R. González-Elipe, S. Ahmad, J. Mater. Chem. A 4 (2016) 4962–4970.
[27] F.J. Ramos, M. Oliva-Ramirez, M.K. Nazeeruddin, M. Grätzel, A.R. González-Elipe, S. Ahmad, J. Mater. Chem. A 3 (2015) 13291–13298.
[28] A. Barranco, A. Borras, A.R. Gonzalez-Elipe, A. Palmero, Prog. Mater. Sci. 76 (2016) 50–153.
[29] L. González-García, J. Idígoras, A.R. González-Elipe, A. Barranco, J.A. Anta, J. Photochem. Photobiol. A 241 (2012) 58–66.
[30] J. Qiu, Y. Qiu, K. Yan, M. Zhong, C. Mu, H. Yan, S. Yang, Nanoscale 5 (2013) 3245–3248.
[31] H.-S. Kim, J.-W. Lee, N. Yantara, P.P. Boix, S.A. Kulkarni, S. Mhaisalkar, M. Grätzel, N.-G. Park, Nano Lett. 13 (2013) 2412–2417.
[32] X. Gao, J. Li, J. Baker, Y. Hou, D. Guan, J. Chen, C. Yuan, Chem. Commun. 50 (2014) 6368–6371.
[33] M. Bass, Handbook of Optics, Fundamentals, Techniques and Design 1, McGraw-Hill Inc, New York, 1995, p. 34.
[34] M-G. Olivier, M. Poelman, in: R.S. Razavi (Ed.), InTech, 2012, DOI: http://dx.doi.org/10.5772/33844, ISBN: 978-953-307-920-2.
[35] M. Salado, J. Idigoras, L. Calio, S. Kazim, M.K. Nazeeruddin, J.A. Anta, S. Ahmad, ACS Appl. Mater. Interfaces 8 (2016) 34414–34421.
[36] J. Bisquert, L. Bertoluzzi, I. Mora-sero, G. Garcia-belmonte, J. Phys. Chem. C 118 (2014) 18983–18991.
[37] A. Pockett, G.E. Eperon, T. Peltola, H.J. Snaith, A. Walker, L.M. Peter, P.J. Cameron, J. Phys. Chem. C 119 (2015) 3456–3465.
[38] E. Guillén, F.J. Ramos, J.A. Anta, S. Ahmad, J. Phys. Chem. C 118 (2014) 22913–22922.
[39] O. Almora, I. Zarazua, E. Mas-Marza, I. Mora-Sero, J. Bisquert, G. Garcia-Belmonte, J. Phys. Chem. Lett. 6 (2015) 1645–1652.
[40] A. Guerrero, G. Garcia-Belmonte, I. Mora-Sero, J. Bisquert, Y.S. Kang, T.J. Jacobsson, J.-P. Correa-Baena, A. Hagfeldt, J. Phys. Chem. C 120 (2016) 8023–8032.
[41] H.S. Kim, I.H. Jang, N. Ahn, M. Choi, A. Guerrero, J. Bisquert, N.G. Park, J. Phys. Chem. Lett. 6 (2015) 4633–4639.
[42] O. Almora, A. Guerrero, G. Garcia-Belmonte, Appl. Phys. Lett. (2016) 108.
[43] I. Zarazua, J. Bisquert, G. Garcia-Belmonte, J. Phys. Chem. Lett. 7 (2016) 525–528.
[44] L. Li, F. Wang, X. Wu, H. Yu, S. Zhou, N. Zhao, J. Phys. Chem. C 120 (2016) 2536–2541.
[45] B. Chen, M. Yang, X. Zheng, C. Wu, W. Li, Y. Yan, J. Bisquert, G. Garcia-Belmonte, K. Zhu, S. Priya, J. Phys. Chem. Lett. 6 (2015) 4693–4700.

Mr. Manuel Salado Manzorro born in Cadiz. He studied Chemical Engineering at University of Cádiz and Master in "Nanostructured material for Nanotechnology Applications" at University of Zaragoza (Spain). During his Masters, he gained multidisciplinary education in the synthesis, assembly and characterization of nanostructured materials. Since 2014, he is a Ph.D. candidate at Abengoa Research developing and studying hybrid perovskite material for solar cells application.

Dr. Manuel Oliva-Ramírez received his Ph.D. degree in Material Science from the University of Seville in 2016 from his work in the Institute of Material Science of Seville. His research was related to the design and fabrication of nanostructured porous thin films of different oxides for their implementation in optofluidic and photovoltaic devices. He is currently a postdoctoral researcher at the Leibniz-Institute for New Materials in Saarbruecken, and working on the development of conductive composites.

Samrana Kazim is currently working as Senior Scientist in Abengoa Research, Seville (Spain). After finishing her Ph.D. in 2008 in Materials chemistry; she moved to Institute of Macromolecular Chemistry (IMC), Prague on IUPAC/UNESCO fellowship. Since then, she had been working at IMC as research scientist before moving to Abengoa Research. Her interests are in the synthesis of metal nanoparticles and conducting polymers, hybrid inorganic–organic solar cells, organic semiconductors, and SERS.

Prof. Agustín R. González-Elipe has been director of the Institute of Material Science of Seville (ICMSE, joint center between the CSIC and the University of Seville) and responsible for the Science and Engineering area of CSIC. At present, he is the head of the Nanotechnology on Surfaces laboratory of ICMSE. His current research interests focus on thin film, plasma technology and surface analysis. He has published more than 400 SCI papers on different topics including catalysis, surface analysis, photovoltaic solar cells, photonics, surface wetting, sensors, thin film optofluidic or plasma-catalysis. The development of the oblique angle deposition technique utilized in the present work has been one of his more recent achievements in the field of surface engineering.

Shahzada Ahmad is a Principal Scientist at Abengoa Research. He finished his Ph.D. (2006) and later moved to the Max Planck Institute for Polymer Research, as Alexander von Humboldt Fellow to work with Prof. H.-J. Butt (surface and interface studies of electrodeposition in ionic liquids). He was a regular visitor to Prof. Michael Grätzel's group at École polytechnique fédérale de Lausanne, where he developed nanoporous films for metal-free electro-catalysis and new redox shuttle. His research targets are in energy conversion, conservation, and storage materials.

PCCP

PAPER

View Article Online
View Journal | View Issue

Cite this: Phys. Chem. Chem. Phys., 2016, 18, 27148

Influence of the mixed organic cation ratio in lead iodide based perovskite on the performance of solar cells†

Manuel Salado,[a] Laura Calio,[a] Rüdiger Berger,[b] Samrana Kazim*[a] and Shahzada Ahmad*[a]

Received 3rd June 2016,
Accepted 26th August 2016

DOI: 10.1039/c6cp03851d

www.rsc.org/pccp

Lead halide based perovskite solar cells are presently the flagship among the third generation solution-processed photovoltaic technologies. The organic cation part in the perovskite plays an important role in terms of crystal structure tuning from tetragonal to trigonal or pseudocubic or *vice versa* depending on the organic cations used, while it also displays different microstructure. In this paper, we demonstrate the influence of the organic cation part with respect to optical properties, hysteresis behavior, and stability. This study offers a clear understanding of the perovskite properties and how they can be modulated by compositional engineering. With a rational choice, light harvesting abilities and hysteresis behavior can be controlled in these systems. The substitution of formamidinium cation by methylammonium cation allows achieving low temperature annealing and inducing stability in perovskites together with enhanced photovoltaic properties. By the use of *in-situ* scanning force microscopy experiments the conversion of precursors to perovskite at a particular temperature can be visualized.

Introduction

Since the discovery of the photovoltaic (PV) effect in the nineteenth century, researchers have shown keen interest in the development of cost effective and efficient materials to convert solar energy into electricity. Currently, the major market share (*ca.* 91%) is being controlled by silicon solar cells, among which monocrystalline silicon solar cells offer power conversion efficiencies (PCE) of >25%. Their high production cost and excessive usage of raw materials escalate their energy payback time and limit their wide application for grid parity. Over the last few decades, different technologies such as dye-sensitized solar cells (DSSCs), organic solar cells and inorganic thin film based solar cells have been extensively studied mainly due to their low amount of material needs, solution processable nature and cost competitiveness.[1]

In recent years, perovskite solar cells (PSCs) have stunned the PV field, given the tremendous research interest in them, owing to the unique combination of their high performance and the low-cost fabrication process. Compared with the existing technology, PSCs have demonstrated their potential by establishing an unprecedented increment in the PCE from 3.8%[2] to >22% (http://www.nrel.gov/ncpv/) in a short time frame. The panchromatic light-absorption ability along with high absorption coefficient, tuneable direct band gap and charge separation and transport capability of the organohalide perovskite materials makes them suitable as light absorber materials for PV applications.[3,4] However, one of the concerns that need to be addressed is the stability and hysteresis behaviour in the devices.[5] In a broader context the term perovskite refers to any material which follows the crystal structure of ABX_3. In the case of hybrid organic–inorganic perovskite, A and B corresponds to organic and inorganic cations respectively, while X represents the halide anion. In order to balance the charge in the structure, the organic cation (A) occupies the cuboctahedral cavity formed by eight PbI_6 octahedra. The size of the cation "A" can notably affect the symmetry of the octahedral network and alter the band gap.[6] Theoretically, it is known that the three-dimensional (3D) perovskite is formed when its tolerance factor (t) falls in the range of 0.7 to 1 as described by Goldschmidt.[7]

Methylammonium ($CH_3NH_3^+$, MA, ionic radius 2.70 Å) and formamidinium ($HC(NH_2)^+$, FA, ionic radius 2.79 Å) both satisfy the tolerance factor (t) to form a 3D network. However, due to the slightly larger cation size of FA than MA, FA provides red shift of the absorption onset due to the change in the metal–halide–metal bond angle and leads to a narrower band gap (1.48 eV)[8,9] compared to $MAPbI_3$ (1.57 eV).[10] Additionally, formamidinium lead iodide ($FAPbI_3$) shows almost equal or higher charge carrier

[a] Abengoa Research, C/Energía Solar nº 1, Campus Palmas Altas-41014, Sevilla, Spain. E-mail: shahzada.ahmad@abengoa.com, samrana.kazim@abengoa.com
[b] Max Planck Institute for Polymer Research, Ackermannweg 10, Mainz 55128, Germany

† Electronic supplementary information (ESI) available. See DOI: 10.1039/c6cp03851d

View Article Online

Paper PCCP

mobility ($\sim$75 cm^2 V^{-1} s^{-1}) depending on the processing method,[11–13] better thermal stability at high temperature and negligible hysteresis during *J–V* measurements as compared to $MAPbI_3$.[9,14,15] However, it is difficult to prepare a uniform, fully covered surface of stable photoactive black polymorph (α-phase) of $FAPbI_3$ perovskite due to its phase transition into yellow non-perovskite (δ-phase) at room temperature. The conversion to α-phase of $FAPbI_3$ is achieved at high temperature (>140 °C).

The microstructure and phase purity of the thin film rely on the perovskite crystal formation processes. A variety of different deposition techniques have been used with the aim to achieve a high quality perovskite layer, such as a two step (sequential deposition) method,[16] vacuum evaporation,[17] vapour-assisted deposition[18] or the recently developed solvent engineering approach.[19] To establish a synergistic effect of both FA and MA organic cations opto-electrical properties, one of the suggested alternative was partial replacement of the MA cation by FA. So far, only a few studies have reported on the mixed organic cation of $MAPbI_3$ and $FAPbI_3$ using a two-step sequential method.[14,20,21]

These mixed organic cations exhibited PV performance superior to that of pure $MAPbI_3$, due to their extended absorption in the red part of the spectrum, better semiconducting properties and high structural and thermal stability provided by the incorporation of the FA cation in the MAI lattice matrix.[14,20] The band gap can be tuned by changing the mixed cation ratio and it has been found that it varies depending on the perovskite processing method.[22] However, none of these studies addressed the hysteresis behaviour in the solar cells, which is crucial to understand the real figure of merit for PV devices.

In this paper, we have studied the structural, surface, optical, and photovoltaic properties of 3-dimensional mixed cation perovskites having a range of composition $MA_xFA_{(1-x)}PbI_3$ (x = 0–1) as light-harvesting materials in a mesoscopic solar cell configuration. The mesoscopic configuration was found to be ideal for the formation of α-phase of $FAPbI_3$. By utilizing the anti-solvent approach, during the one step deposition process of perovskites, it is possible to obtain dense morphology with high crystallinity and large crystals in a mixed cation environment. This deposition method also allows us to transform the rough perovskite film into a smooth and glossy perovskite, with the aim to obtain homogeneous and high surface coverage with a favourable interface. In this approach, non-polar solvents (*e.g.* toluene or chlorobenzene) which are miscible with the perovskite precursor solution but do not dissolve the perovskite film were used for dripping. PbI_2 and the mixture of MAI and FAI were used as perovskite precursors and dissolved in dimethylsulfoxide (DMSO). During the preparation of this article, Jacobsson *et al.* reported mixed cation (FA and MA) and anion (Br and I) based perovskite using a one step solvent engineering method.[23] In our study only mixed cations were used with the composition $MA_xFA_{(1-x)}PbI_3$ (x = 0–1) and prepared by a one step solvent engineering method showing good air stability and less hysteresis in the case of selected compositions. An array of techniques were employed to characterize the devices in order to unravel the physical and electrical properties of the perovskite solar cells and their hysteresis behaviour.

Results and discussion

X-ray diffraction measurements were made to investigate the phase purity of mixed cation perovskite and incorporation of the FA cation into the $MAPbI_3$ perovskite lattice. The XRD spectra were recorded for all mixed organic cation perovskites $MA_xFA_{(1-x)}PbI_3$ (x = 0–1) and are shown in Fig. 1. The perovskite film was deposited onto coarse glass as substrate and was subject to measurements after annealing the sample for one hour at 100 °C for x = 0.6 to 1 and at 120 °C and 150 °C for x = 0.5 and x = 0 respectively. At room temperature, pure $MAPbI_3$ has a tetragonal structure while $FAPbI_3$ (black α-phase) has a cubic structure due to slight rotation of lead iodide octahedra.[10,24] The main diffraction peaks in pure $MAPbI_3$, where structural changes were detected, were found at $\sim$14°, 19.95°, 24.41°, 28.5° and 31.9° and belong to the characteristic peak of a tetragonal perovskite structure while peaks at 13.7° and 27.8° in pure $FAPbI_3$ correspond to the cubic black stable phase of α-$FAPbI_3$.[24] The peak present at 12.63° reflects the presence of non-converted PbI_2, for which the intensity decreases in the mixed cation (x = 0–1) environment except in $MA_{0.5}FA_{0.5}PbI_3$ perovskite which shows a strong peak of PbI_2.

Fig. S1a–c (ESI†) are focused on the characteristic peaks of the tetragonal structure of perovskite. The peaks at 14.17°, 28.33° and 31.9° gradually shift to a lower diffraction angle (2θ) with increasing amount of the FA cation. Mainly due to the relatively large size of the FA cation lattice expansion occurs. Instead of the appearance of separate and individual two peaks with different intensity of two cations, the slow shift in the diffraction angle indicates the presence of a mixed phase, where both cations were incorporated in the same lattice.

On closer visualization of the characteristic tetragonal peak at 14°, a high intense and narrow peak was observed in the case

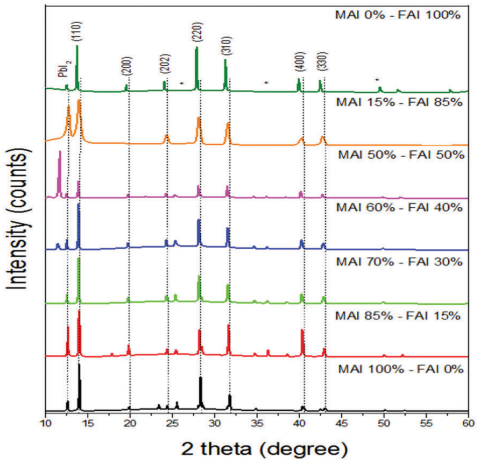

Fig. 1 X-ray diffraction spectra for the $MA_xFA_{(1-x)}PbI_3$ perovskite film, where x = 0, 0.15, 0.5, 0.6, 0.7, 0.85, 1. These films were annealed for one hour at 100 °C for x = 0.6 to 1, at 120 °C for x = 0.5 while at 150 °C for x = 0 and 0.15. A closer view of the characteristic peaks at 14.17°, 28.33° and 31.9° is shown in Fig. S1 (ESI†).

View Article Online

PCCP Paper

of $MAPbI_3$, which suggests its larger crystallite size than mixed cation perovskite. Fig. S2 (ESI†) represents the calculated average crystallite size calculated by using XRD software *versus* FA composition. The intensity of the peak decreases with increasing amount of FA in $MA_xFA_{(1-x)}PbI_3$ (x = 0–1) while the full width at half maximum (FWHM) increases up to x = 0.85 in $MA_xFA_{(1-x)}PbI_3$, while in the case of x = 0.5 it decreases. The decrease in FWHM indicates an increase of X-ray crystallite size. For pure $FAPbI_3$, the FWHM was found to be the highest (Fig. S1a, ESI†).

In mixed cation perovskite, $MA_xFA_{(1-x)}PbI_3$ (x = 0.85–0.6), no characteristic diffraction peak of δ-phase of $FAPbI_3$ was observed (which is a photo-inactive phase) except in x = 0.5, where the high intense peak at 11.7° represents the δ-phase of $FAPbI_3$.[20,25] It is well known that the annealing temperature of the perovskite affects its final structure and its electro-optical properties. In pure methylammonium iodide (MAI) conversion to perovskite takes place between 80 and 100 °C while in the case of formamidinium black α-phase perovskite is formed at 135–150 °C.[26,27] It is worth mentioning that δ-phase of formamidinium is present only in a 50 : 50 ratio, which might be due to the high annealing temperature required to convert into black α-phase of $FAPbI_3$. Due to the higher amount of $FAPbI_3$ in $MA_{0.5}FA_{0.5}PbI_3$, these crystals are not confined in the mesoporous scaffold which limits the crystallite size to ~50 nm; therefore these crystals randomly arrange themselves on the surface of the mesoporous scaffold rather than infiltrating inside and thus form large crystallites.[10] Bein *et al.*[20] studied the stabilization of the trigonal high-temperature phase of formamidinium lead iodide. It was shown that the crystal structure of MA degrades at 125 °C; however black α-phase formed at a higher temperature (135 °C). Therefore we assume that, annealing temperature plays an important role in the preparation of mixed organic cation perovskites. In order to reveal the optimal annealing temperature in the case of $MA_{0.5}FA_{0.5}PbI_3$, it was heated at different temperatures (120 °C, 135 °C and 150 °C) and subjected to X-ray diffraction and absorption spectra measurements (Fig. S3 and S4, ESI†). From XRD (Fig. S3, ESI†), it can be seen that at 120 °C, the strong peak present at ~14° corresponds to the tetragonal structure of $MAPbI_3$ along with the strong peak at ~12° indicating that PbI_2 is not fully converted to perovskite. On increasing the temperature to 135 °C, the peak at ~14° becomes less intense which finally disappears when the annealing temperature reaches 150 °C indicating degradation of the $MAPbI_3$ phase. At 135 °C and 150 °C, the emergence of the peak at ~11° confirms the presence of δ-phase of $FAPbI_3$ and the peak corresponding to PbI_2 becomes more intense at this stage. The inadequate conversion into perovskite phase indicates the presence of a thermodynamically stable point beyond which the substitution of FA does not occur.[10] The presence of yellow δ-phase of $FAPbI_3$ as observed in XRD also coincides with the SEM images of the perovskite shown in ESI† (Fig. S5). The appearance of white crystals on the surface can be observed at 135 °C and it increases on increasing the temperature to 150 °C. Recently similar observations were reported.[10,20] This may be assigned to the preferred yellow phase of $FAPbI_3$ at room temperature. However, in absorption measurements (Fig. S4, ESI†), we did not observe any significant changes except that the absorbance intensity of $MA_{0.5}FA_{0.5}PbI_3$ decreases in the case of samples annealed at 135 °C and 150 °C, which might be due to the conversion of δ-phase yellow perovskite. In our conditions we found that the optimal annealing temperature for this ratio was 120 °C (Fig. S3, ESI†), to avoid the degradation of MA cations in the matrix. Nevertheless, the geometry of the crystals depend on the mixed cation perovskite ratio to dictate the final performance of the PSCs.[25]

The conversion of the precursors into perovskite can be observed by absorption spectra of mixed organic cation perovskite. Perovskite films were deposited onto the mesoporous TiO_2 layer to mimic the crystal growth as in devices. Fig. 2 shows the absorption spectra of mixed cation perovskite measured using an integrating sphere for all different compositions. A systematic shift of the absorption band edge to longer wavelengths was observed with increasing amount of the FA cation in the $MA_xFA_{(1-x)}PbI_3$, where x = 0 to 1. The addition of the FA cation red shifts the absorption onset from 780 nm in pure $MAPbI_3$ to 815 nm in the case of pure $FAPbI_3$. Thus the energy band gap (E_g) can be easily tuned by varying the mixed cation ratio. For mixed cation perovskite with x = 0.5 and pure $FAPbI_3$, the absorbance decreases with increasing wavelength compared to other compositions.

Maximum absorbance was observed for $MA_{0.6}FA_{0.4}PbI_3$ perovskite, with red-shift of the absorption onset. Fig. 3 shows the linear dependence of the optical band gap on added FA cation composition in the $MA_xFA_{(1-x)}PbI_3$ perovskite, where x = 0 to 1. As the amount of the FA cation is increased in the $MAPbI_3$ lattice, the band gap decreases from 1.59 eV (pure $MAPbI_3$) to 1.5 eV for pure $FAPbI_3$, while the mixed cations show an intermediate value. It is to be mentioned that these perovskite films were prepared on mesoporous TiO_2; thus due to perovskite confinement in the mesoporous scaffold, it may affect the crystal structure of perovskite and thus its band gap.[21,28]

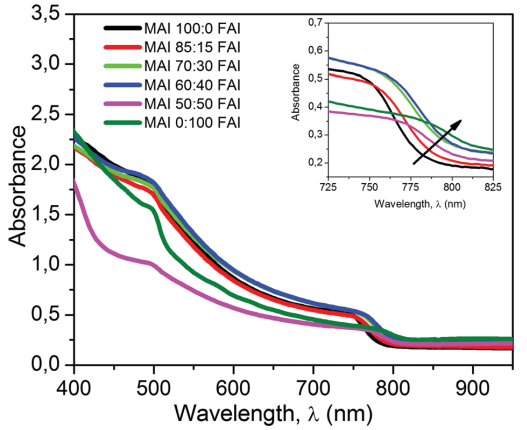

Fig. 2 UV-vis absorbance spectra of a perovskite $(MA)_x(FA)_{1-x}PbI_3$ layer on FTO including compact and mesoporous TiO_2.

View Article Online

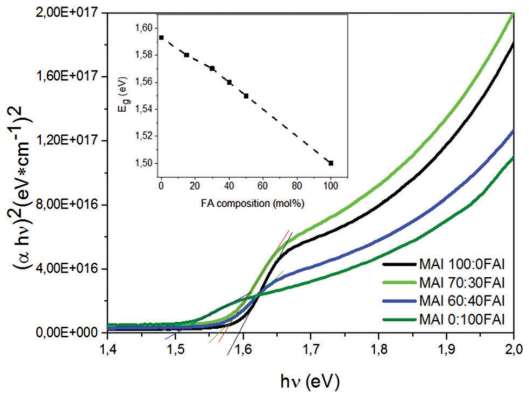

Fig. 3 Tauc plots for perovskite $(MA)_x(FA)_{1-x}PbI_3$ (x = 0, 0.6, 0.7, 1) and the inset shows the band gap (eV) for all compositions (x = 0, 0.5, 0.6, 0.7, 0.85, 1) plotted *versus* amount of formamidinium added in molar percentage.

For calculating the optical band gap, the absorption coefficient (α) was calculated by measuring total transmittance and reflectance spectra using an integrating sphere. Then the Tauc plot method was applied to estimate the direct band gap, *i.e.* linear extrapolation of the $(\alpha h\nu)^2$ *vs.* $h\nu$ curve to intercept the horizontal energy axis as shown in Fig. 3.

An optimal ratio exists which offers a compromise between absorption shift and perovskite crystal quality, and will be explained in the following sections. The morphologies of the mixed perovskites were characterized by scanning electron microscopy (SEM) and scanning force microscopy (SFM) in order to visualize the crystallization process and distribution of grains in different compositions of MAI:FAI. The perovskite film was deposited atop a mesoporous layer to reproduce similar crystal growth as in devices. Fig. 4 shows the surface microstructure of pure $MAPbI_3$, $FAPbI_3$, $MA_{0.6}FA_{0.4}PbI_3$ and the cross sectional image of the $MA_{0.6}FA_{0.4}PbI_3$ perovskite based device.

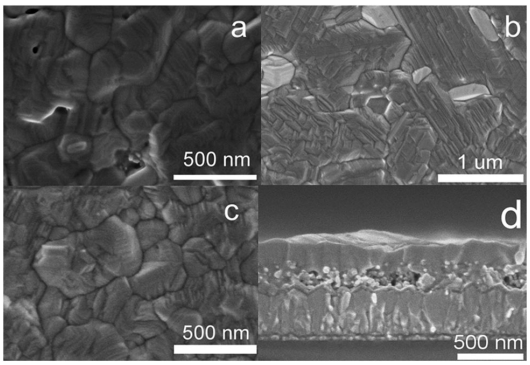

Fig. 4 (a–c) SEM images of different organic cation ratio perovskite films ($MAPbI_3$, $FAPbI_3$ and $MA_{0.6}FA_{0.4}PbI_3$ respectively) and (d) cross section image of the $TiO_2/MA_{0.6}FA_{0.4}PbI_3$/Spiro-OMeTAD solar cell. Panels a–c reveal the morphological evolution of the perovskite films when the organic cation composition was changed.

Fig. S5 and S6 (ESI†) represent SEM images of the remaining composition. The morphology of the perovskite significantly changes with the inclusion of the FA cation. SEM images depict adequate surface coverage and densely packed grains with a less number of pinholes. In the case of $FAPbI_3$, crystal edges were observed which led to the formation of lamellar structures. Furthermore the grain size varied with the MA:FA composition in perovskite. The crystallite size was larger in the case of pure $MAPbI_3$ and $FAPbI_3$ perovskite as confirmed by XRD measurements showing a narrow peak. Smaller, compact, regular and ordered crystallites with preferential orientation were observed with an average crystallite size ranging from 60 to 62 nm (Fig. S2, ESI†) in the case of x = 0.7 and 0.6 and in close agreement with the literature value.[29] These crystallites are much smaller than those observed by SEM indicating that these crystals are composed of several small grains. It is reported that during the crystallization process, if there is no lattice strain in the structure, it leads to the formation of large crystals due to more relaxation in the crystal lattice[30,31] as shown in XRD measurements where the peak shifted to a lower angle with increasing amount of the FA cation. Pure $MAPbI_3$, $FAPbI_3$ and $MA_{0.85}FA_{0.15}PbI_3$ show larger crystallite size as calculated by XRD measurements.

As the amount of FAI increases in the $MAPbI_3$ lattice, the lattice strain increases due to the comparatively larger cation size of FA and crystallization slows down and consequently, small crystals were formed in the case of x = 0.7 and 0.6 (60–62 nm) and confined in the pores of the mesoporous scaffold with preferential orientation and a high degree of order.[32] The improved and controlled crystallization of the perovskite film may reduce the density of defects and the quality of perovskite crystals can affect the charge carrier diffusion length, efficiency of charge dissociation and transport.[33–45] Subsequently, this will influence the performance of the devices as the presence of defects creates the trapping site for recombination of electrons and holes. Therefore the larger crystals at the interface are beneficial owing to a reduction of grain boundaries and trap sites and they also act as scattering centers for the incoming light and increase the effective optical path length of light in the device.

Notably, in some of the perovskite compositions, more specifically, in $MA_{0.5}FA_{0.5}PbI_3$ and pure $FAPbI_3$, individual grains exhibit higher brightness compared with the adjacent area. Fig. S3 (ESI†) shows the SEM images of $MA_{0.5}FA_{0.5}PbI_3$ with different annealing temperature. It can be observed that bright contrast was present in all the perovskite samples annealed at different temperature. In all likelihood, this could have possibly originated due to the non-perovskite δ-phase of $FAPbI_3$, which was also confirmed by the XRD measurement made at different annealing temperature.

We observed that the $MA_{0.6}FA_{0.4}PbI_3$ ratio shows almost negligible hysteresis in J–V measurements. In such samples we investigated the role of annealing temperature on perovskite film morphology and its crystal formation by means of *in-situ* SFM as the samples are sensitive to humidity.[46,47] Pure methyl ammonium iodide (MAI) at room temperature forms an active β-phase. At around 55–60 °C, this active β-phase is converted into α-$CH_3NH_3PbI_3$. At the initial stage, *i.e.* prior to annealing, the

View Article Online

PCCP Paper

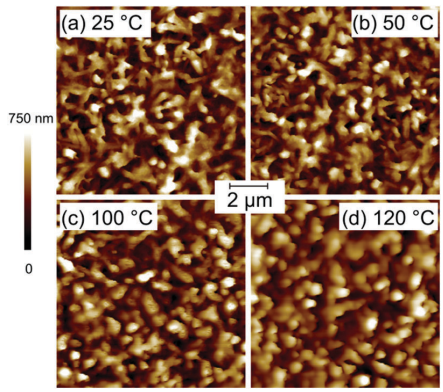

Fig. 5 SFM topographic images of FTO/$MA_{0.6}FA_{0.4}PbI_3$, during *in situ* temperature annealing. The images were recorded at (a) 25, (b) 50, (c) 100 and (d) 120 °C. At each temperature we waited 20 minutes to allow the sample to thermally equilibrate.

deposited layer formed a surface with a root-mean-square (rms) roughness of 147 nm at a 10 × 10 μm^2 scale. The deposited layer showed a 3-dimensional network like structure (Fig. 5a).

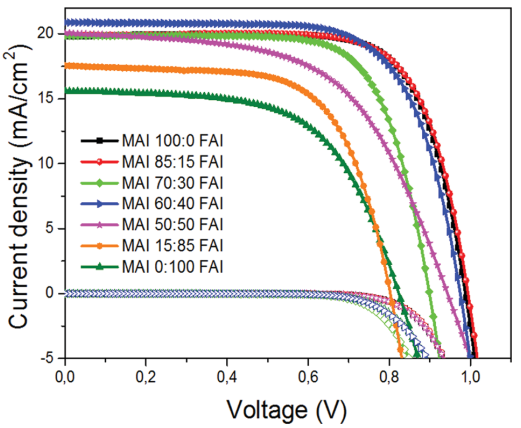

Fig. 6 *J–V* characteristics for mesoscopic devices with mixed cation perovskite $MA_xFA_{(1-x)}PbI_3$ (where x = 0, 0.5, 0.6, 0.7, 0.85, 1) as a light absorber.

On increasing the temperature to 50 °C we observed closing of small pores, and we attribute this to the intercalation induced volume expansion of inorganic materials in the organic phase. Upon further increasing the annealing temperature to 100 °C and 120 °C slight changes in morphology were observed (Fig. 5c and d). These microstructural changes reflect the conversion of the deposited layer into the perovskite structure, which is very prominent at or above 100 °C.

Photovoltaic properties

To calculate the figure of merit for the fabricated PV devices, the *J–V* curves were recorded in the dark and under simulated air mass 1.5 global (AM1.5G) sunlight. Fig. 6 shows the *J–V* characteristics in the dark and under illumination (100 mW cm^{-2}) for the best performing devices from V_{oc} to J_{sc} at 100 mV s^{-1}. Table 1 summarizes the average PV parameters with standard deviation along with the best-performing devices prepared for different compositions of MAI:FAI together with series and shunt resistance. An increase in short circuit current (J_{sc}) after the inclusion of FA in $MA_xFA_{(1-x)}PbI_3$ perovskite can be observed, which was expected due to the shift of the absorption onset to a longer wavelength. The average J_{sc} and fill factor (FF) increased gradually from 19.57 to 21 mA cm^{-2} and from 64.8 to 70% respectively with increasing FA concentration from 0 to 40 mol%. The lowest value of J_{sc} was observed for $MA_{0.5}FA_{0.5}PbI_3$, $MA_{0.15}FA_{0.85}PbI_3$ and pure $FAPbI_3$, which coincides with the optical absorption of these perovskite materials (Fig. 2). A drop in V_{oc} was observed on increasing the concentration of FA beyond 40%, for pure $MAPbI_3$ V_{oc} of 950 mV was obtained, while the lowest V_{oc} was obtained in the case of pure $FAPbI_3$ (V_{oc} = 750 mV). In the case of pure $FAPbI_3$, the drop in V_{oc} might be due to the presence of non-perovskite δ-phase which destroys the crystal lattice and crystal structure of perovskite and hence modifies the band gap.[21,28] On the other hand, in the case of $MA_{0.6}FA_{0.4}PbI_3$, the high value of V_{oc} could be related to the better confinement of the small sized perovskite crystals in the pores of the mesoporous scaffold with preferential orientation and a high degree of order.[32]

Similarly, low FF was observed in the case of $MA_{0.5}FA_{0.5}PbI_3$, $MA_{0.15}FA_{0.85}PbI_3$ and pure $FAPbI_3$, due to the presence of yellow δ-phase of $FAPbI_3$ causing a sudden drop in PV performance. This feature can be related to the increase in series resistance and the decrease in shunt resistance (Fig. S8, ESI†). The series and shunt resistance values were evaluated using the software

Table 1 Average photovoltaic parameters and calculated hysteresis index (HI) of the devices under 100 mW cm^{-2}. The scan direction was from V_{oc} to J_{sc}. The values in parentheses are reported for the best devices

Organic cation ratio	Annealing T (°C)	R_s Ohm cm^2	R_{sh} Ohm cm^2	J_{sc} (mA cm^{-2})	V_{oc} (V)	FF (%)	PCE (%)	HI
MAI 100 : FAI 0	100	5.10	1487.48	19.57 ± 0.74 (19.79)	0.95 ± 0.03 (0.987)	64.79 ± 6.37 (74.18)	12.11 ± 0.97 (14.49)	0.16
MAI 85 : FAI 15	100	4.93	7947.37	19.78 ± 0.07 (19.90)	0.97 ± 0.01 (0.994)	70.61 ± 1.69 (73.32)	13.62 ± 0.42 (14.50)	0.10
MAI 70 : FAI 30	100	5.40	9033.63	19.69 ± 0.36 (19.84)	0.89 ± 0.01 (0.899)	66.63 ± 3.21 (71.39)	11.85 ± 0.58 (12.73)	0.05
MAI 60 : FAI 40	100	5.25	3738.2	20.99 ± 0.32 (20.87)	0.983 ± 0.01 (0.975)	69.26 ± 1.17 (69.97)	14.30 ± 0.49 (14.23)	0.005
MAI 50 : FAI 50	120	12.62	591.60	16.64 ± 2.36 (19.92)	0.86 ± 0.02 (0.929)	56.77 ± 6.33 (54.99)	8.16 ± 1.54 (10.18)	0.28
MAI 15 : FAI 85	150	6.18	882.08	17.55	0.802	65.5	9.22	0.12
MAI 0 : FAI 100	150	10.50	1461.65	13.91 ± 1.60 (15.66)	0.75 ± 0.02 (0.805)	52.01 ± 2.95 (59.80)	5.42 ± 1.00 (7.53)	0.20

View Article Online

Paper PCCP

from the slope of the *J–V* curve and are reported in Table 1. We observed a decrease in series resistance, while an increase in shunt resistance for up to 40 mol% of FA cation, this can be related to the increased grain size of the perovskite and better confinement of perovskite inside the pores for intimate connectivity with the TiO_2 layer.[9]

The grain size increases with the inclusion of $FAPbI_3$, but also decreases up to a certain concentration of FAI (40 mol%, x = 0.6) and beyond that concentration, the grain size again increased for $MA_{0.5}FA_{0.5}PbI_3$ and pure $FAPbI_3$ (x = 0.5 and 0) as supported by the XRD and SEM studies. Changes in series and shunt resistance values are correlated with the morphological changes in mixed perovskite after inclusion of $FAPbI_3$. It is reported that the large-sized grain reduces the grain boundaries and thus series resistance might decrease. Similarly, the decrease in shunt resistance might be a result of the shunting pathway created due to the inadequate connectivity between the blocking layer and the perovskite interface. The decreased V_{oc} and low FF point towards high charge recombination losses (low shunt resistance and high series resistance) in the case of x = 0.5–0.[48] Pure $MAPbI_3$ based devices gave good performance; however, they suffered from hysteresis behaviour (Table S1, ESI†). It can be deduced from Fig. 6 that there is an improvement in the average PCE in the case of mixed perovskite compared to pure MAI (η = 12.11 ± 0.97%) or pure FAI (5.42 ± 1.00%). An improvement in PCE was achieved for $MA_{0.85}FA_{0.15}PbI_3$ (η = 13.62 ± 0.42%); however $MA_{0.6}FA_{0.4}PbI_3$ gave the best PV performance.

One of the main concerns in perovskite solar cell behavior is the presence of hysteresis in the current–voltage curve depending on the measurement direction (forward or reverse) and scan rate.[49–51]

J–V curves were measured at various scan rates for both reverse and forward directions at different dwell time and we found that in our case, 100 mV s^{-1} was the optimized scan rate.

The hysteresis effect has been quantified as a hysteresis index as reported by Kim *et al.* (Table S1, ESI†). To calculate the degree of hysteresis (Fig. S7, ESI†) and the PV parameters and HI are presented in Table S1 (ESI†). The hysteresis index can be lowered by increasing the FAI ratio. It was found that the degree of hysteresis decreases with increasing amount of FAI up to 40 mol%. Beyond this composition, the degree of hysteresis increases.

A rational match can be obtained for $MA_{0.6}FA_{0.4}PbI_3$, where the PCE is the best with a negligible degree of hysteresis. The lowest series resistance was noticed in $MA_{0.85}FA_{0.15}PbI_3$ which is justified by its high FF and performance. Hysteresis behaviour in PSCs is generally associated with high capacitance (on the order of mF cm^{-2}) compared to Si cells (on the order of μF cm^{-2}).[52] This capacitance effect was attributed by some authors to (i) the ferroelectricity or polarization of the perovskite layer; (ii) contact conductivity; (iii) diffusion of excess ions as interstitial defects; and/or (iv) trapping/de-trapping of charge carriers.

Even though recent studies have pointed ion migration (I^- and MA^+) and charge trapping at the interface as a presumptive cause of hysteresis in perovskite solar cells, the mechanism of ion transportation and origin of these traps are still scarcely understood.[51,53] Recently, reports on the generation of ion migration channels[54] were reported. One of them is the local lattice distortion due to confinement in the mesoporous scaffold. Mostly 70% of pure $MAPbI_3$ within the mesoporous scaffold was found to be disordered with more lattice defects, which is undetectable in XRD measurements.[55] This may explain severe photocurrent hysteresis in mesoporous devices in addition to the trapping effect. In our case, the calculated crystallite size was the least in the case of x = 0.6 and 0.7 (60–62 nm) which shows better confinement in the scaffold and probably preferred orientation with less distortion in the lattice and thus experiencing negligible hysteresis. However in the case of larger crystal size in the remaining compositions studied here, a comparatively high degree of hysteresis was observed. However, the local rearrangement of charges at the interfaces or in defects in the perovskite layer could give rise to the reported capacitive effects, while the existence of ionic vacancies is influenced by the process adopted for crystal growth.[54]

To elucidate the device performance, we measured the devices at different scan rates in both the forward and reverse direction and almost negligible hysteresis could be identified in some devices. In other words, the hysteresis behaviour could be controlled by finding an appropriate ratio due to optimal crystal formation as well as reduction of trap sites. Fig. S7 (ESI†) shows current density–voltage (*J–V*) curves in the reverse and forward direction to see the hysteresis depending on the organic cation ratio. The shape of the crystals and the direction of crystal growth induce the creation of trap states in the perovskite structure.[25,56] In accordance with the absorbance measurements, the inclusion of formamidinium cation results in shifting of the incident photon-to-current efficiencies (IPCE) onset towards longer wavelength (inset Fig. 7). By increasing the FAI concentration, it is expected to absorb more light in the near IR part of the spectrum, which can be deduced from the IPCE graph (inset Fig. 7).[14]

For all the compositions studied here, except pure $FAPbI_3$, *ca.* 80–85% light to electricity conversion can be observed in the visible part of the spectra. The incident photon-to-current efficiency (IPCE) spectra were recorded in the wavelength range of

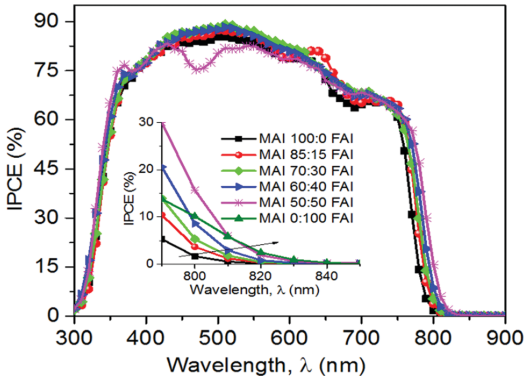

Fig. 7 Incident photon-to-current efficiency of the devices. Inset shows the closer view of the shifting of IPCE onset towards longer wavelength with increasing amount of the FA cation in $MA_xFA_{(1-x)}PbI_3$ perovskite film, where (x = 0 to 1).

300–850 nm, where the PSCs showed photon-to-current conversion. This indicates that excitons and/or free charges were effectively generated in the perovskite layers upon light illumination. In the case of pure $FAPbI_3$, the rapid degradation of devices did not permit the measurement of good IPCE spectra.

Impedance measurements

To understand the correlation between charge carrier extraction dynamics and crystallographic properties of perovskite films, we performed impedance spectroscopy (IS) which provides information concerning the performance of PSCs at different charge-carrier densities.[57] Previous reports suggest that the device architecture and particularly the perovskite layer play an important role in the interpretation of the impedance response.[58] Thus, to study the charge dynamics of the different layers in the devices, samples were analysed from maximum power point voltage to lower voltage. The measurements were performed by varying the illumination intensity under V_{oc} conditions. On increasing light intensity, the charge carrier concentration increases and an increase in V_{oc} was obtained. An equivalent circuit used for the fitting[60] of impedance measurements is shown in Fig. S9 (ESI†).

As reported, the hysteresis behaviour of the device is linked to the dielectric properties of the perovskite material.[59]

Device capacitance is an important parameter to explain the mechanisms which control undesired effects such as hysteresis behaviour.[61] Recently, Bisquert[62] reported how the acceptance or release of additional charges has repercussions on capacitance due to the change in the Fermi level of the system. The authors found that capacitance is independent of voltage for both interfaces (perovskite/TiO_2 or perovskite/Spiro-OMeTAD) but is dependent on the perovskite layer itself. Capacitance reflects the density of states (DOS) of a material, and thus a high capacitance value in perovskite shows a high DOS. Fig. 8 illustrates the value of capacitance for different organic cation compositions in PSCs.

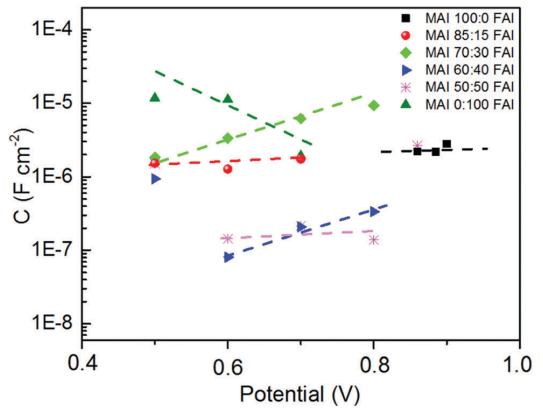

Fig. 8 Capacitance values for $MA_xFA_{(1-x)}PbI_3$. Dash lines serve as a visual aid only. Impedance measurements were performed at open-circuit in the 2–50 MHz frequency range. The equivalent circuit used and the typical impedance spectra are shown in Fig. S8 (ESI†).

The capacitance is almost independent of the applied voltage, and depending on the ratio, they possess different capacitance values. Here also, the 60 : 40 ratio shows the lowest capacitance value, which is in agreement with the lowest hysteresis. As it is well known, the semicircle observed in the impedance spectra is related with the diffusion–recombination process. In all cases, the magnitude of the impedance response generally increases with a decrease in the applied voltage. This trend is due to the fact that an increase of voltage entails a reduction of the recombination resistance, and therefore the size of the semicircle. The Nyquist plot (Fig. S10, ESI†) shows the existence of a unique semicircle or two depending on the perovskite. It has been reported that the distinct impedance features may originate from the distribution of trapping states within the perovskite band gap due to the inclusion of formamidinium cations in the structure.

Stability

The low stability of perovskite based solar cells under high moisture is the current bottleneck to upscale this technology. In general, the critical step in the fabrication of the devices is the perovskite layer deposition. A perovskite film deposited under controlled conditions exhibits good pinhole-free film coverage; additionally some researchers have reported that a small percentage (less than 30%) of humidity during the fabrication process could be beneficial to accelerate the growth of perovskite crystals in order to obtain a homogeneous film.[63–65] Mainly, this instability is based on the facile phase transitions at room temperature and formation of hydrated phases owing to its hydrophilic character. The FA cation exhibits lower stability than MA; however the presence of the smaller MA cation in mixed perovskite with FA improves stability even in high humidity conditions, which could be attributed to ten times higher dipole moment of the small sized MA cation than FA. MA stabilizes the 3D network of PbI_6 octahedra through hydrogen bonding between the hydrogen of the ammonium moiety and iodide ions, or another possible reason for stability is the strong coulomb interaction between the MA cation and PbI_6 octahedra.[20]

Fig. 9 represents the evolution of the solar cell parameters V_{oc}, J_{sc} and FF, PCE plotted as a function of time to evaluate the stability. The un-encapsulated devices were kept in the dark and humidity conditions (<60% RH) and monitored by measuring J–V characteristics. In general, the devices were found to be relatively stable, and in some cases, the device performance was found to be increased after 5 days of storage, which we assign as due to the improved intimate contact with the perovskites and HTM, or better infiltration of active materials inside the three dimensional TiO_2 structure. However, in most of the cases the device performance stabilizes after 10 days and relatively uniform output can be observed. It was noted that the substitution of FA by MA induces perovskite stability. The stable value of PCE were exposed for x = 0.85 composition, after 5 days. The calculated drop in PCE after a period of four months was only 14.41% (from 14.5% to 12.41%).

View Article Online

Paper PCCP

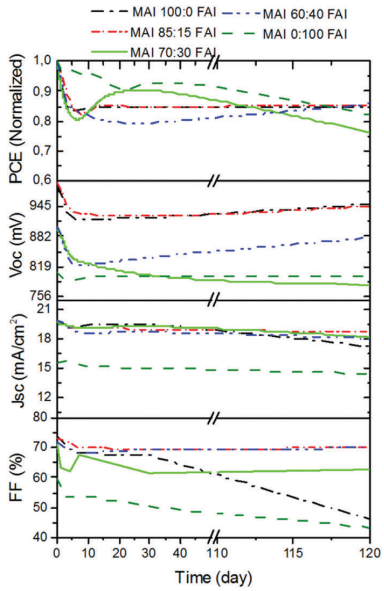

Fig. 9 Evolution of stability data for the solar cells with different organic cation ratios.

Conclusions

To summarize, we have studied varying compositions of mixed-cation perovskite $MA_xFA_{1-x}PbI_3$ (where x = 0–1) for solar cell fabrication using a one step solvent engineering approach. It was found that the addition of the formamidinium cation in the MAI slows down the crystal formation in perovskites and allows the formation of large crystals and a high degree of order. Devices fabricated using pure FAI gave the lowest performance here, while all the mixed and pure MAI showed superior PV performance. The addition of 15–40% FAI in MAI was found to influence the PV performance and dramatically reduced the hysteresis behaviour. The mixed-cation perovskite $MA_{0.6}FA_{0.4}PbI_3$ exhibited hysteresis free behaviour along with the best PV performance. By using the solvoneering (solvent engineering) approach, we were able to fabricate devices with >15% photon-to-current conversion efficiency. The strategy of mixing organic ammonium compounds opens up new prospects for further optimization and understanding of hysteresis free behaviour.

Experimental section

All chemicals were procured from Sigma Aldrich and used as such. PbI_2 was obtained from TCI, while MAI and FAI were procured from Dyesol and employed without any treatment or purification. 2,2′,7,7′-Tetrakis(*N*,*N*-di-*p*-methoxyphenyamine)-9,9-spirobifluorene (Spiro-OMeTAD) was acquired from Merck KGaA.

Device fabrication

Perovskite solar cells were fabricated on FTO-coated glass (TEC15, Pilkington) patterned by laser etching. Before any deposition, the substrates were cleaned using Hellmanex solution and rinsed with deionized water and ethanol and finally ultrasonicated in 2-propanol and air dried. The TiO_2 compact layer was deposited by spray pyrolysis at 450 °C using 1 mL of titanium diisopropoxide bis(acetyl acetonate) precursor solution (75% in 2-propanol, Sigma Aldrich) in 19 mL of pure ethanol using dry air as carrier gas. After the blocking layer deposition, the substrates were kept for further 30 minutes at 450 °C for the formation of anatase phase. Once the samples were cooled down at room temperature, they were treated with $TiCl_4$ (dipping in a 0.02 M $TiCl_4$ solution in deionized water at 70 °C for 30 minutes) with the aim to obtain a homogeneous layer. Next, the samples were washed with deionized water, heated at 500 °C for 10 minutes and were cooled down to room temperature. After this, a TiO_2 mesoporous layer (Dyesol, 30NRD) was deposited by spin coating (4000 rpm for 30 s) and then samples were heated progressively up to 450 °C for 2 hours.

Atop this, $MA_xFA_{1-x}PbI_3$ (x = 0–1) was deposited by the one step method followed by the toluene solvoneering (solvent engineering) method. The solution and perovskite films were prepared inside an argon glove box under moisture and oxygen controlled conditions (H_2O level: <1 ppm and O_2 level: <10 ppm) and kept under stirring at 80 °C overnight in order to dissolve completely PbI_2. Perovskite precursor solution composed of lead iodide (1.25 M) (PbI_2) and a mixture of formamidinium iodide (FAI) and methyl ammonium iodide (MAI) were dissolved in dimethylsulfoxide (DMSO) and the precursor solution was spin coated on top of the mesoporous layer at 1000 rpm for 10 s and then at 6000 rpm for 30 s. During the second step, toluene (900 μL) was dripped at the centre of the substrate in the last 15 seconds. After solvent treatment, the films were transferred onto a hotplate and annealed at 100–150 °C for 60 minutes depending on the cation composition. Spiro-OMeTAD was then spun coated at 4000 rpm for 30 s by dissolving 72.3 mg of Spiro-OMeTAD in 1 mL of chlorobenzene; 21.9 μL of tris(2-(1*H*-pyrazol-1-yl)-4-*tert*-butylpyrydine)cobalt(III) bis(trifluoromethylsulphonyl)imide (FK209) from stock solution (400 mg of FK209 in 1 mL of acetonitrile), 17.5 μL of lithium bis-(trifluoromethylsulphonyl)imide (LiTFSI) stock solution (520 mg of LiTFSI in 1 mL of acetonitrile) and 28.8 μL of 4-*tert*-butylpyridine were also added to the solution as dopants. Finally, 80 nm of gold (Au) was thermally evaporated on the top of the cell as a cathode under a vacuum level between 1×10^{-6} and 1×10^{-5} Torr.

Characterization

For structural characterization, thick films were prepared by spin coating of $MA_xFA_{(1-x)}PbI_3$ (x = 0–1) solutions onto coarse glass. X-ray diffractograms were recorded on a Rigaku powder diffractometer using a CuKα source. The measurements were performed in the Bragg–Brentano geometry. The samples were mounted without any further modification and the divergence slit was adjusted to the dimension of the films. A scan range of 10°–60° was selected with an acquisition time of 1 degree per min.

A baseline correction was applied to diffractograms to compensate for the noise arising from the substrate.

Transmittance and reflectance spectra of the perovskite films were collected using a Perkin Elmer UV-vis-NIR lambda 1050 spectrophotometer using a 160 mm integrating sphere. Surface morphology and cross-sectional images were obtained using a Hitachi S-4800 field emission scanning electron microscope at power 2 kV.

Current density–voltage (J–V) curves were recorded with a Keithley 2400 source-measurement-unit under AM1.5G, 100 mW cm^2 illumination from a certified Class AAA, 450 W solar simulator (ORIEL, 94023 A). Light output power was calibrated using a NREL certified calibrated mono-crystalline silicon solar cell. A black metal mask (0.16 cm^2) was used over the square solar cell active area (0.5 cm^2) to reduce the influence of scattered light.

Photovoltaic parameters including J_{sc}, V_{oc}, fill factor (FF), and power conversion efficiency (PCE) were extracted from the photocurrent–voltage (J–V) curves of the solar cells and are listed in Table 1. The scan rate and the active area used for measuring the devices were optimized as such to calculate the real value for efficiencies without having any hysteresis effect (active area: 0.16 cm^2, scan rate: 100 mV s^{-1}, pre sweep delay: 20 s). The IPCE measurements were performed using a Newport 150 W xenon lamp coupled to an Oriel Cornerstone 260 motorized 1/4 m monochromator as the light source and a 2936-R power meter to measure the short circuit current. The impedance measurements were carried under illumination in order to approach the operation conditions for solar cells. Samples were illuminated by a 530 nm LED (LUXEON) over a wide range of DC light intensities. Spectra were recorded with the application of a bias equal to the potential induced by the light. The bias close to V_{oc} and applied during the measurements was chosen to minimize the current running through the cell during the measurements and to avoid the voltage drop due to series resistance. Z-view (Scribner) was used for equivalent circuit modelling of the EIS spectra.

SFM measurements were performed using an EnviroScope (Bruker Nano Surfaces) which allows controlling the environmental condition such as humidity, oxygen content and sample temperature. The samples were deposited on glass substrates following the procedure described above. The glass substrates were much smoother than the FTO substrates. Therefore the roughness of the perovskite layers could be measured more accurately.

Acknowledgements

This project has received funding from the European Union Seventh Framework Programme under grant agreement no. 607232 [THINFACE].

Notes and references

1 B. O'Regan and M. Grätzel, *Nature*, 1991, **353**, 737–740.
2 A. Kojima, K. Teshima, Y. Shirai and T. Miyasaka, *J. Am. Chem. Soc.*, 2009, **131**, 6050–6051.
3 M. Grätzel, R. A. J. Janssen, D. B. Mitzi and E. H. Sargent, *Nature*, 2012, **488**, 304–312.
4 S. Kazim, M. K. Nazeeruddin, M. Grätzel and S. Ahmad, *Angew. Chem., Int. Ed.*, 2014, **53**, 2812–2824 (*Angew. Chem.*, 2014, **126**, 2854–2867).
5 X. Liu, W. Zhao, H. Cui, Y. Xie, Y. Wang, T. Xu and F. Huang, *Inorg. Chem. Front.*, 2015, **2**, 315–335.
6 S. Brittman, G. W. P. Adhyaksa and E. C. Garnett, *MRS Commun.*, 2015, **5**, 7–26.
7 V. M. Goldschmidt, *Naturwissenschaften*, 1926, **14**, 477–485.
8 G. E. Eperon, S. D. Stranks, C. Menelaou, M. B. Johnston, L. M. Herz and H. J. Snaith, *Energy Environ. Sci.*, 2014, **7**, 982.
9 J.-W. Lee, D.-J. Seol, A.-N. Cho and N.-G. Park, *Adv. Mater.*, 2014, **6**, 1–8.
10 G. E. Eperon, C. E. Beck and H. J. Snaith, *Mater. Horiz.*, 2016, **3**, 63–71.
11 P. Piatkowski, B. Cohen, C. S. Ponseca, M. Salado, S. Kazim, S. Ahmad, V. Sundström and A. Douhal, *J. Phys. Chem. Lett.*, 2015, **7**, 204–210.
12 V. Adinolfi, M. Yuan, R. Comin, E. S. Thibau, D. Shi, M. I. Saidaminov, P. Kanjanaboos, D. Kopilovic, S. Hoogland, Z.-H. Lu, O. M. Bakr and E. H. Sargent, *Adv. Mater.*, 2016, **28**, 3406–3410.
13 A. A. Zhumekenov, M. I. Saidaminov, M. A. Haque, E. Alarousu, S. P. Sarmah, B. Murali, I. Dursun, X.-H. Miao, A. L. Abdelhady, T. Wu, O. F. Mohammed and O. M. Bakr, *ACS Energy Lett.*, 2016, **1**, 32–37.
14 N. Pellet, P. Gao, G. Gregori, T.-Y. Yang, M. K. Nazeeruddin, J. Maier and M. Grätzel, *Angew. Chem., Int. Ed.*, 2014, **53**, 3151–3157.
15 S. Pang, H. Hu, J. Zhang, S. Lv, Y. Yu, F. Wei, T. Qin, H. Xu, Z. Liu and G. Cui, *Chem. Mater.*, 2014, **26**, 1485–1491.
16 J. Burschka, N. Pellet, S.-J. Moon, R. Humphry-Baker, P. Gao, M. K. Nazeeruddin and M. Grätzel, *Nature*, 2013, **499**, 316–320.
17 M. Liu, M. B. Johnston and H. J. Snaith, *Nature*, 2013, **501**, 395–398.
18 Q. Chen, H. Zhou, Z. Hong, S. Luo, H. S. Duan, H. H. Wang, Y. Liu, G. Li and Y. Yang, *J. Am. Chem. Soc.*, 2014, **136**, 622–625.
19 N. J. Jeon, J. H. Noh, Y. C. Kim, W. S. Yang, S. Ryu and S. Il Seok, *Nat. Mater.*, 2014, **13**, 897–903.
20 A. Binek, F. C. Hanusch, P. Docampo and T. Bein, *J. Phys. Chem. Lett.*, 2015, **6**, 1249–1253.
21 J. Liu, Y. Shirai, X. Yang, Y. Yue, W. Chen, Y. Wu, A. Islam and L. Han, *Adv. Mater.*, 2015, **27**, 4918–4923.
22 C. C. Stoumpos, C. D. Malliakas and M. G. Kanatzidis, *Inorg. Chem.*, 2013, **52**, 9019–9038.
23 T. J. Jacobsson, J. P. Correa-Baena, M. Pazoki, M. Saliba, K. Schenk, M. Grätzel and A. Hagfeldt, *Energy Environ. Sci.*, 2016, **9**, 1706–1724.
24 M. T. Weller, O. J. Weber, J. M. Frost and A. Walsh, *J. Phys. Chem. Lett.*, 2015, **6**, 3209–3212.
25 D. H. Cao, C. C. Stoumpos, C. D. Malliakas, M. J. Katz, O. K. Farha, J. T. Hupp and M. G. Kanatzidis, *APL Mater.*, 2014, **2**, 091101.

26 P. Using, X. Di, T. J. Jacobsson, L. J. Schwan, M. Ottosson, A. Hagfeldt and T. Edvinsson, *Inorg. Chem. Front.*, 2015, **54**, 10678–10685.

27 S. Aharon, A. Dymshits, A. Rotem and L. Etgar, *J. Mater. Chem. A*, 2015, **3**, 9171.

28 Y. Chen, M. He, J. Peng, Y. Sun and Z. Liang, *Adv. Sci.*, 2016, **3**, 1500392.

29 J. M. Ball, M. M. Lee, A. Hey and H. J. Snaith, *Energy Environ. Sci.*, 2013, **6**, 1739.

30 V. D'Innocenzo, A. R. Srimath Kandada, M. De Bastiani, M. Gandini and A. Petrozza, *J. Am. Chem. Soc.*, 2014, **136**, 17730–17733.

31 G. Grancini, S. Marras, M. Prato, C. Giannini, C. Quarti, F. De Angelis, M. De Bastiani, G. E. Eperon, H. J. Snaith, L. Manna and A. Petrozza, *J. Phys. Chem. Lett.*, 2014, **5**, 3836–3842.

32 D. J. Seol, J. W. Lee and N. G. Park, *ChemSusChem*, 2015, **8**, 2414–2419.

33 L. Wang, C. McCleese, A. Kovalsky, Y. Zhao and C. Burda, *J. Am. Chem. Soc.*, 2014, **110**, 12205–12208.

34 Y. Yamada, T. Nakamura, M. Endo, A. Wakamiya and Y. Kanemitsu, *J. Am. Chem. Soc.*, 2014, **136**, 11610–11613.

35 S. D. Stranks, V. M. Burlakov, T. Leijtens, J. M. Ball, A. Goriely and H. J. Snaith, *Phys. Rev. Appl.*, 2014, **2**, 034007.

36 G. J. A. H. Wetzelaer, M. Scheepers, A. M. Sempere, C. Momblona, J. Ávila and H. J. Bolink, *Adv. Mater.*, 2015, **27**, 1837–1841.

37 W. Tress, N. Marinova, O. Inganäs, M. K. Nazeeruddin, S. M. Zakeeruddin and M. Graetzel, *Adv. Energy Mater.*, 2015, **5**, DOI: 10.1002/aenm.201400812.

38 N. Marinova, W. Tress, R. Humphry-Baker, M. I. Dar, V. Bojinov, S. M. Zakeeruddin, M. K. Nazeeruddin and M. Grätzel, *ACS Nano*, 2015, **9**, 4200–4209.

39 S. D. Stranks, G. E. Eperon, G. Grancini, C. Menelaou, M. J. P. Alcocer, T. Leijtens, L. M. Herz, A. Petrozza and H. J. Snaith, *Science*, 2013, **342**, 341–344.

40 G. Xing, N. Mathews, S. Sun, S. S. Lim, Y. M. Lam, M. Grätzel, S. Mhaisalkar and T. C. Sum, *Science*, 2013, **342**, 344–347.

41 P. W. Liang, C. Y. Liao, C. C. Chueh, F. Zuo, S. T. Williams, X. K. Xin, J. Lin and A. K. Y. Jen, *Adv. Mater.*, 2014, **26**, 3748–3754.

42 Y. Wu, A. Islam, X. Yang, C. Qin, J. Liu, K. Zhang, W. Peng and L. Han, *Energy Environ. Sci.*, 2014, **7**, 2934.

43 P. Docampo, F. C. Hanusch, S. D. Stranks, M. Döblinger, J. M. Feckl, M. Ehrensperger, N. K. Minar, M. B. Johnston, H. J. Snaith and T. Bein, *Adv. Energy Mater.*, 2014, **4**, 1400355.

44 Z. Xiao, C. Bi, Y. Shao, Q. Dong, Q. Wang, Y. Yuan, C. Wang, Y. Gao and J. Huang, *Energy Environ. Sci.*, 2014, **7**, 2619.

45 J. You, Y. (Michael) Yang, Z. Hong, T.-B. Song, L. Meng, Y. Liu, C. Jiang, H. Zhou, W.-H. Chang, G. Li and Y. Yang, *Appl. Phys. Lett.*, 2014, **105**, 183902.

46 P. F. Ndione, W.-J. Yin, K. Zhu, S.-H. Wei and J. J. Berry, *J. Mater. Chem. A*, 2015, **3**, 21940–21945.

47 D. Li, S. A. Bretschneider, V. W. Bergmann, I. M. Hermes, J. Mars, A. Klasen, H. Lu, W. Tremel, M. Mezger, H.-J. Butt, S. A. L. Weber and R. Berger, *J. Phys. Chem. C*, 2016, **120**, 6363–6368.

48 H. S. Kim and N.-G. Park, *J. Phys. Chem. Lett.*, 2014, **5**, 2927–2934.

49 R. S. Sanchez, V. Gonzalez-Pedro, J. W. Lee, N. G. Park, Y. S. Kang, I. Mora-Sero and J. Bisquert, *J. Phys. Chem. Lett.*, 2014, **5**, 2357–2363.

50 H. J. Snaith, A. Abate, J. M. Ball, G. E. Eperon, T. Leijtens, N. K. Noel, S. D. Stranks, J. T. W. Wang, K. Wojciechowski and W. Zhang, *J. Phys. Chem. Lett.*, 2014, **5**, 1511–1515.

51 S. Van Reenen, M. Kemerink and H. J. Snaith, *J. Phys. Chem. Lett.*, 2015, **6**, 3808–3814.

52 B. Chen, M. Yang, X. Zheng, C. Wu, W. Li, Y. Yan, J. Bisquert, G. Garcia-Belmonte, K. Zhu and S. Priya, *J. Phys. Chem. Lett.*, 2015, **6**, 4693–4700.

53 C. Motta, F. El-Mellouhi, S. Kais, N. Tabet, F. Alharbi and S. Sanvito, *Nat. Commun.*, 2015, **6**, 7026.

54 Y. Yuan and J. Huang, *Acc. Chem. Res.*, 2015, **49**, 286–293.

55 J. J. Choi, X. Yang, Z. M. Norman, S. J. L. Billinge and J. S. Owen, *Nano Lett.*, 2014, **14**, 127–133.

56 M. B. Johnston and L. M. Herz, *Acc. Chem. Res.*, 2015, **49**, 146–154.

57 E. Guillén, F. J. Ramos, J. A. Anta and S. Ahmad, *J. Phys. Chem. C*, 2014, **118**, 22913–22922.

58 A. R. Pascoe, N. W. Duffy, A. D. Scully, F. Huang and Y.-B. Cheng, *J. Phys. Chem. C*, 2015, **119**, 4444–4453.

59 E. J. Juarez-Perez, R. S. Sanchez, L. Badia, G. Garcia-Belmonte, Y. S. Kang, I. Mora-Sero and J. Bisquert, *J. Phys. Chem. Lett.*, 2014, **5**, 2390–2394.

60 J. Bisquert, L. Bertoluzzi, I. Mora-sero and G. Garcia-belmonte, *J. Phys. Chem. C*, 2014, **118**, 18983–18991.

61 O. Almora, I. Zarazua, E. Mas-Marza, I. Mora-Sero, J. Bisquert and G. Garcia-Belmonte, *J. Phys. Chem. Lett.*, 2015, **6**, 1645–1652.

62 J. Bisquert, *Phys. Chem. Chem. Phys.*, 2003, **5**, 5360.

63 H. Zhou, Q. Chen, G. Li, S. Luo, T.-B. Song, H.-S. Duan, Z. Hong, J. You, Y. Liu and Y. Yang, *Science*, 2014, **345**, 542–546.

64 T. Leijtens, G. E. Eperon, N. K. Noel, S. N. Habisreutinger, A. Petrozza and H. J. Snaith, *Adv. Energy Mater.*, 2015, **5**, 1500563.

65 N.-G. Park, *Mater. Today*, 2015, **18**, 65–72.

PCCP

PAPER

Cite this: Phys. Chem. Chem. Phys., 2017, 19, 22905

Identifying the charge generation dynamics in Cs^+-based triple cation mixed perovskite solar cells†

Manuel Salado,[a] Ramesh K. Kokal,[b] Laura Calio,[a] Samrana Kazim,[a] Melepurath Deepa[b] and Shahzada Ahmad*[a]

Received 5th June 2017,
Accepted 27th July 2017

DOI: 10.1039/c7cp03760k

rsc.li/pccp

Triple cation based perovskite solar cells offer enhanced moisture tolerance and stability compared to mixed perovskites. Slight substitution of methyl ammonium or formamidinium cation by cesium (Cs^+), was also reported to eliminate halide segregation due to its smaller size. To elucidate the device kinetics and understand the role of the Cs, we undertook different modes of scanning probe microscopy and electrochemical impedance spectroscopy (EIS) experiments. Kelvin probe force microscopy revealed that the incorporation of the Cs cation increases the contact potential difference (CPD), this CPD further increases when Spiro-OMeTAD is used as a hole transport material. The current at the nanoscale level shows improvement with Cs inclusion and further enhancement by the Spiro-OMeTAD deposition, studied under light illumination, which supports the high photocurrent density obtained from the cells. EIS demonstrates that in a triple cation environment, reduced carrier recombination at the TiO_2/perovskite interface was also obtained which in turn allow us to achieve a higher V_{oc} value.

Introduction

In recent years, perovskite solar cells have emerged as a disruptive technology, if successful, then they can be deployed on a wide scale. Owing to their notable opto-electrical properties, such as tunable direct band-gap, broad light-absorption, charge separation and transport capability along with an easy and inexpensive fabrication processes, perovskites are competitive candidates as light absorber materials for photovoltaic applications.[1,2] Concerted efforts have been made in their development, which has led to a spectacular rise in device power conversion efficiency (PCE) from 3.8 to 22.1%.[3] This progress has been achieved using two fundamental aspects; materials engineering[4] and optimization of perovskite deposition techniques.[5] Perovskite materials, as such is composed of an inorganic part (generally a metal halide) and an organic part. The material properties can be tuned, simply by following the Goldschmidt[6] rule in order to alter the electrical properties and thereby the final performance of the devices. The methylammonium lead triiodide ($MAPbI_3$) based perovskite solar cell is the most investigated configuration, however it has been now established that the mixture of organic cations and anions enhances not only its photovoltaic properties but also results in improved stability.[7] Grätzel *et al.* reported a remarkable 20% PCE using perovskite with a formula of $((FAPbI_3)_{0.87}(MAPbBr_3)_{0.13})$.[8] The use of the mixed organic cations thermally stabilize the perovskite, apart from extending the absorption spectrum,[9] the inclusion of bromine though increases the band gap but significantly improves the humidity tolerance of the devices.

Adequate preparation methods need to be established, in order to achieve precise control of physical parameters such as crystallinity and morphology, which are required to fabricate efficient and defect free stable solar cells. Approaches such as solvent engineering,[5] vacuum[10] or gas drying[11] were reported in order to achieve homogeneous films and large size perovskite crystals. These approaches control the nucleation of perovskites in the precursor solutions, and decrease crystal growth rate, thus allowing formation of large crystals.

However, the ambient condition stability of perovskite remains a key point with regard to future scale-up and industrial commercialization.[12] Different strategies have been applied in order to address this problem, such as fluorinated compounds in the matrix of perovskites,[13] the use of hydrophobic polymers,[14] or the inclusion of cesium in the perovskite stoichiometry.[8,15,16] The latter resulted in an outstanding improvement of the device stability over 1000 h. Substitution of the mixed organic cation by a small amount of Cs, eliminates

[a] Abengoa Research, Abengoa, Campus, Palmas Altas, C/ Energia Solar n°. 1, Sevilla-41014, Spain. E-mail: shahzada.ahmad@abengoa.com
[b] Department of Chemistry, Indian Institute of Technology Hyderabad, Kandi-502285, Sangareddy, Telangana, India

† Electronic supplementary information (ESI) available: Line traces data for KPFM and CFM together with EIS results and X-ray diffratogram. See DOI: 10.1039/c7cp03760k

halide segregation.[17] Nevertheless, there is a lack of understanding of the process that entails the inclusion of such elements inside the perovskite structure. In this work, we report our findings on perovskite based solar cells with the addition of cesium in varying weight percentages (0–15%). Samples have been prepared following one-step deposition process combined with solvent engineering techniques with different precursor concentration as well as different thicknesses of hole transport material (HTM). An array of techniques together with different modes of scanning probe microscopy and electrochemical impedance spectroscopy (EIS) was used to untangle the properties and improvements after the addition of cesium.

Scanning force microscopy (SFM) and its electrical operative mode, such as Kelvin probe force microscopy (KPFM), is being employed here to investigate the homogeneities of the electrical properties of the fabricated solar cells at the nanoscale level.

Using KPFM, concurrent mapping of the topography and the value of the contact potential difference (CPD) between the tip and the sample at nanometer scale can be logged in real-time. In the past, we have also used KPFM to study the potential distribution across the interfaces of a working solar cell. We have found that the open circuit potential (V_{oc}) is built up at the interface of the $MAPbI_3$ layer to the gold (Au) electrode and when probed atop of the p-type (HTM) layer, the V_{oc} at nanometer scale was in accordance with the bulk measurements.[18] These findings are in contradiction to device models that regard the internal electric field as the main driving force for the spatial separation of charges.[19,20]

Here we probed a triple cation based solar cell with SFM measurements on different working layers. The full device was also subjected to investigation. The mapping of CPD atop the layers in a state of the art device was performed. Upon illumination and under short-circuit conditions, the sample exhibited an accumulation of charges (higher CPD) at grain boundaries in the case of the perovskite layer. The potential distribution across the surface before and after illumination was studied and correlated with separate layers. Conducting force microscopy (CFM) mode was also used to study the trend of dark- and photo-current alteration with Cs incorporation at the nanoscale level. To elucidate the internal carrier dynamics occurring inside a device, electrochemical impedance spectroscopy (EIS) was also used, whereas the analysis of EIS data is subject to fitting into complex models that neglect key elements such as interlayer interface and molecular phenomena occurring due to the interaction between the layers. These local energetic landscapes (Scheme 1) in a working nanostructured device (thickness $\leq$ 1 μm) will allow developing a methodology for correlation of figures of merit with bulk properties. Moreover a correlation of the knowledge of the charge distribution through direct visualization of the surface and internal dynamics will facilitate better understanding.

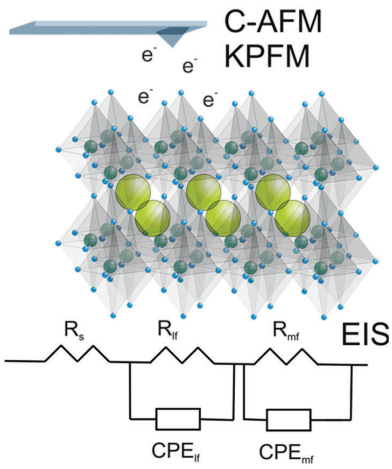

Scheme 1 Characterization techniques used in this work to study the role of cesium incorporation inside the perovskite structure.

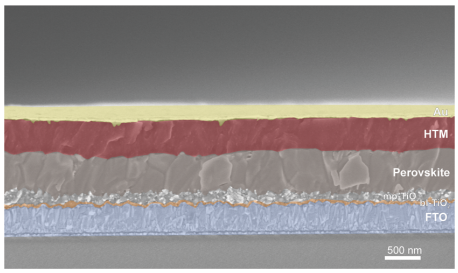

Fig. 1 Cross sectional scanning electron microscopy image of typical perovskite solar cells. The device was prepared using 1.4 M perovskite and 90 mM Spiro-OMeTAD solutions.

Results and discussion

Fig. 1 shows the cross-sectional image of a typical perovskite solar cell. The micrograph shows that all the layers are well interconnected and have well defined interfaces. From the bottom to the top of these images, layers due to FTO (400 nm), compact TiO_2 (*ca.* 50–60 nm), meso-porous TiO_2 (*ca.* 100 or 200 nm) and perovskite (*ca.* 400 nm) of $Cs_{0.05}(MA_{0.15}FA_{0.85})_{0.95}Pb(I_{0.85}Br_{0.15})_3$ are clearly distinguished. Atop the perovskite layer, the 200 nm thick Spiro-OMeTAD (HTM) and the gold as cathode layer (*ca.* 80 nm) are observed. It is to be noted that here, the thickness of the perovskite layer is relatively higher due to the 1.4 M concentration being used and the relatively thick HTM layer is due to the use of 90 mM of Spiro-OMeTAD.

Incident photon to current conversion efficiency (IPCE) spectra and their corresponding integrated current densities as a function of wavelength plots are shown for the fabricated solar cells with the $(MA_{0.15}FA_{0.85})Pb(I_{0.85}Br_{0.15})_3$ (control device), and with 5, 10, and 15% Cs^+ based perovskites (Fig. 2). Hereafter, the mixed methylammonium formamidinium, *i.e.* $(MA_{0.15}FA_{0.85})Pb(I_{0.85}Br_{0.15})_3$ is abbreviated as perovskite. We then varied the thickness of perovskite by using 1.4 M concentration and it was observed that IPCE values were improved w.r.t to 1.2 M perovskite. To find a synergy between charge extraction and the higher thickness of perovskites and hole transport layer (HTL), we then used 90 mM

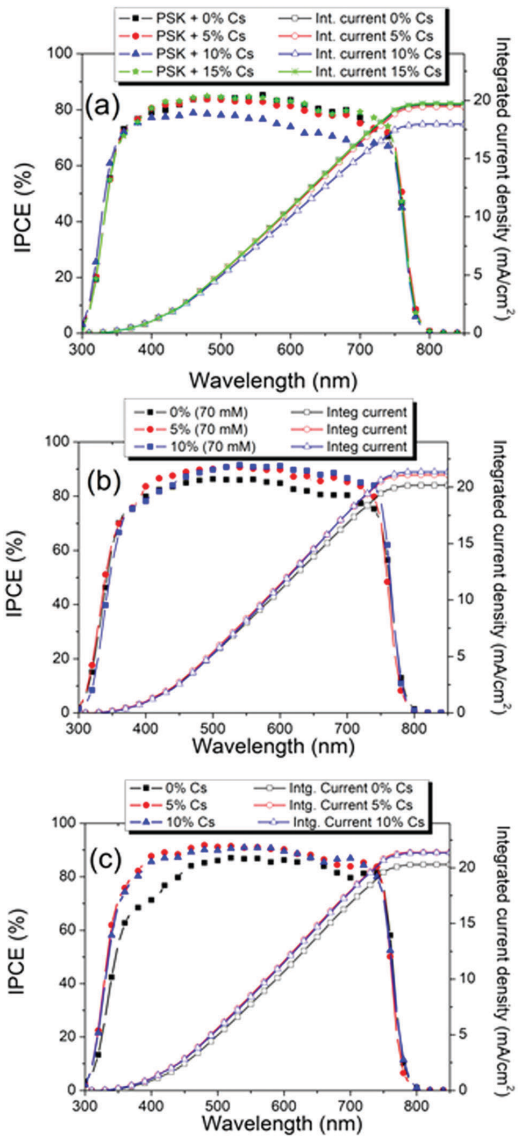

Fig. 2 IPCE spectra and integrated current densities *versus* wavelength plots of perovskite solar cells: (a) 1.2 M perovskite concentrations + Cs^+ addition, (b) 1.4 M perovskite concentrations + Cs^+ addition, with 70 mM of Spiro-OMeTAD concentration and (c) 1.4 M perovskite concentrations + Cs^+, with 90 mM of Spiro-OMeTAD concentration.

of Spiro-OMeTAD, together with 1.4 M of perovskite (with 5% Cs^+ content) concentration, and the resulting solar cell delivers the best performance studied here. Table 1 provides the solar cell parameters of cells with different compositions. The best device was composed of (with 5% Cs^+): $Cs_{0.05}(MA_{0.15}FA_{0.85})_{0.95}Pb(I_{0.85}Br_{0.15})_3$, and the concentration of the perovskite used was 1.4 M, and the Spiro-OMeTAD concentration was fixed to 90 mM. The cell parameters are: open circuit voltage (V_{oc}): 1060 mV, short circuit current density (J_{SC}: 21.92 mA cm^{-2}), fill factor (FF): 75.06%, and PCE: 17.53%. *J–V* characteristics are summarized in Table 1.

Electrical mode of scanning probe microscopy

To elucidate the role of Cs^+ inclusion, and of Spiro-OMeTAD, CFM and KPFM studies were performed. Fig. 3 shows simultaneous topographic and current images for the $(MA_{0.15}FA_{0.85})Pb(I_{0.85}Br_{0.15})_3$, $Cs_{0.05}(MA_{0.15}FA_{0.85})_{0.95}Pb(I_{0.85}Br_{0.15})_3$, $Cs_{0.05}(MA_{0.15}FA_{0.85})_{0.95}Pb(I_{0.85}Br_{0.15})_3$ + Spiro-OMeTAD (90 mM concentration) samples and their respective section profiles are shown in the ESI† (Fig. S1). Perovskite concentration was fixed to 1.4 M. The topography of the control sample, in the dark is shown in Fig. 3a, and it shows large particles, which are shapeless and a few hundred nanometers in size. In the corresponding current image (Fig. 3a′), the bright regions arise due to high currents and the dark regions correspond to lower current regions of the sample. The average value of current flowing across the film was in the range of 50–60 pA whereas a maximum current flow value of 130 pA was observed. The topography of the same sample under light irradiance is represented in Fig. 3b, and the corresponding current image (Fig. 3b′), shows an average current flow of 250 pA with a maximum current flow of 500 pA. A number of high current domains (bright regions) were observed more on illumination compared to the dark and the photocurrent magnitude was found to be larger than the dark current, thus providing evidence for charge separation under illumination. Fig. 3c and c′ illustrates the topography and current images of $Cs_{0.05}(MA_{0.15}FA_{0.85})_{0.95}Pb(I_{0.85}Br_{0.15})_3$, in the dark. The value of the current lies in the range of 50 to 160 pA, with a maximum current flow of 230 pA. The value of the current flowing through the sample made from the triple cation in dark was higher compared to the control sample.

For the triple cation perovskite, topography and current images under illumination are shown in Fig. 3d and d′, and the photocurrent varies between 150 to 400 pA, with a maximum current of 1.2 nA. Upon inclusion of 5% Cs^+ in the perovskite, the photocurrent improves, indicating that Cs^+ addition enhances both the average and the maximum current. However, in the case of both mixed and triple cation perovskites, under dark and light conditions, the high current regions are localized, randomly distributed and well-separated. The samples with Spiro-OMeTAD deposited atop of triple cation perovskites, produce significantly different current and topography maps. The maps of the Cs^+ doped and the Spiro-OMeTAD coated control sample $Cs_{0.05}(MA_{0.15}FA_{0.85})_{0.95}Pb(I_{0.85}Br_{0.15})_3$ + Spiro-OMeTAD (Cs-FAMA-Spiro) are shown in Fig. 3e and e′. Fig. S1 (ESI†) shows the line tracings of these scans. On Spiro-OMeTAD deposition, a smoother surface relative to the other two samples was found. The maximum and the minimum in height profiles are the lower for this sample. The corresponding current flow is observed to be in the range of 40 to 160 pA, with a maximum current of 290 pA, which is higher than that observed for the other two perovskites under dark conditions. The corresponding topography and current images under irradiance are displayed in Fig. 3f and f′.

Table 1 Solar cell parameters of fabricated perovskite solar cells

Cs^+ (%)	V_{oc} (mV)	J_{sc} (mA cm^{-2})	FF (%)	PCE (%)	Conditions	Ref.
0	1027	21.47	69.16	15.24	1.2 M perovskites	17
5	1054	21.7	75.48	17.10	1.2 M perovskites	17
10	1061	21.28	69.55	15.71	1.2 M perovskites	17
15	1050	17.19	66.82	12.10	1.2 M perovskites	This work
5	1050	21.90	73.07	16.81	1.4 M perovskites	This work
10	1040	21.55	66.25	14.83	1.4 M perovskites	This work
15	1070	21.03	69.18	15.60	1.4 M perovskites	This work
5	1060	21.92	75.06	17.53	1.4 M perovskites + 90 mM Spiro-OMeTAD	This work

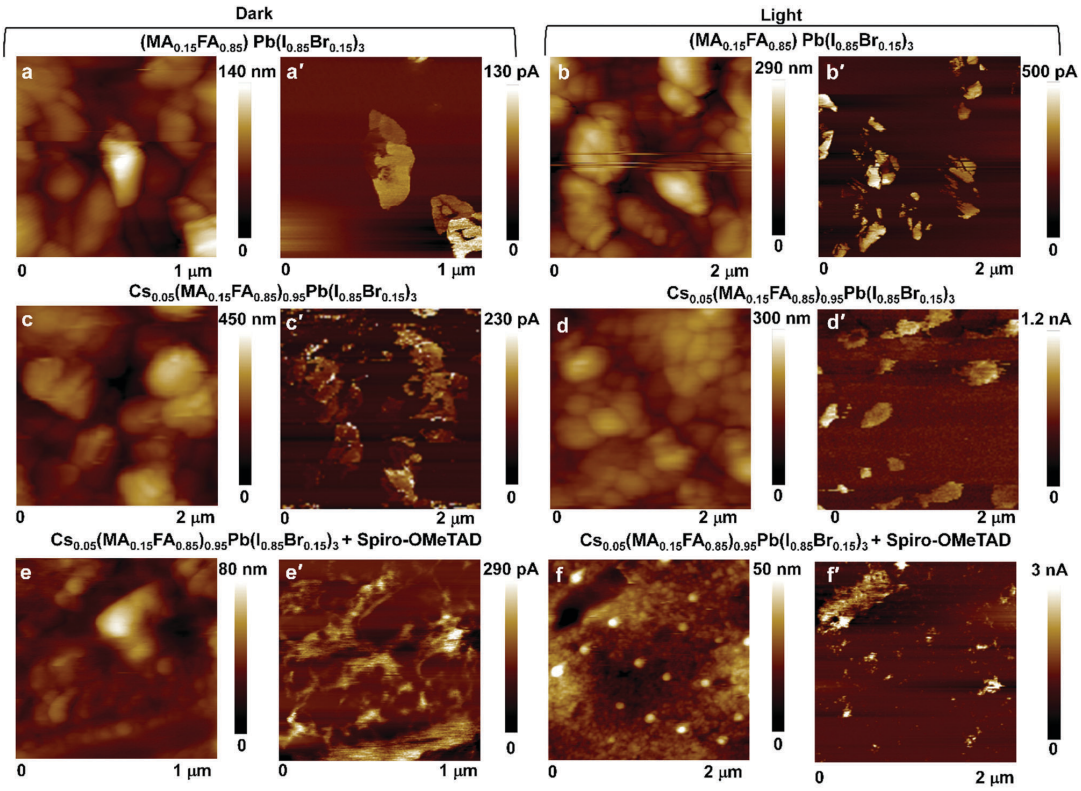

Fig. 3 Simultaneous topography: (a, c and e) in the dark, (b, d and f) under green light, and current: (a′, c′ and e′) in the dark, (b′, d′ and f′) under green light-maps of $(MA_{0.15}FA_{0.85})Pb(I_{0.85}Br_{0.15})_3$, $Cs_{0.05}(MA_{0.15}FA_{0.85})_{0.95}Pb(I_{0.85}Br_{0.15})_3$ and Spiro-OMeTAD (90 mM) coated $Cs_{0.05}(MA_{0.15}FA_{0.85})_{0.95}Pb(I_{0.85}Br_{0.15})_3$ (all at 1.4 M perovskite concentrations).

The current flow shows a maximum value of 3 nA, which is the highest among all the above-stated samples. The grain sizes of perovskites vary from tens of nanometers to ~100 nm (Fig. 3f′). A similar photocurrent effect was observed when TiO_2 was doped.[21] The grain sizes at the Spiro-OMeTAD coated surface are much smaller, compared to the only perovskite based surfaces, which aligns with the smoother surface of the hole transport layer (HTL), originating due to its small molecule nature, which covers the perovskite crystals. Notably, both under the dark and illuminated states, the high current domains are more uniformly distributed over micron length scales when Spiro-OMeTAD is coated, compared to the pristine surfaces without the HTL. It can also be deduced that on light irradiance, perovskites scavenge the holes more efficiently in the case of triple cation based samples, which is supported by a higher surface photocurrent relative to the perovskites without HTLs. Current distribution across the perovskite surface was also found to be favorably impacted by the HTL deposition, as the HTL forms excellent interfacial contact with the triple perovskite under-layer.

In a previous report, Kutes *et al.*,[22] studied the photocurrent response of $MAPbI_3$ thin films in the dark and under 0.07 mW cm^{-2}

white light (LED) illumination. The authors observed that the distribution of dark I_{SC} was homogeneous and the current showed values below 6 pA with a mean of 0.06 pA. Under illumination, the current showed a heterogeneous distribution and was found to lie in the range of 41.8 to 100 pA. I_{SC} increased by approximately 10 times on going from dark to light illumination. MacDonald *et al.*,[23] used photoconductive atomic force microscopy to investigate the electrical properties and electrical property heterogeneity at grain boundaries of a FTO/TiO_2/$MAPbI_3$ assembly under darkness and under an irradiance of 100 mW cm^{-2} with a 523 nm LED. The current in the dark and under light was found to be 200 and 300 pA respectively with an increase of 1.5 times on going from darkness to light. In this work, currents under darkness and light (using a green LED of 1.5 mW cm^{-2} intensity illumination) were measured for all the three thin films. The light intensity was measured with an ILT 1400 radiometer–photometer. The photocurrent increased for all the samples, perovskites, 5% Cs^+-perovskites and Spiro-OMeTAD (90 mM) coated 5% Cs^+-perovskites (at 1.4 M perovskite concentrations). The maximum current increases approximately 4, 5 and 10 times respectively on changing the conditions from darkness to light. These values are very much comparable to the reported magnitudes of current enhancement upon illumination in perovskite films.

The topography and the surface potential images of the perovskites under darkness and light are shown in Fig. 4. For the perovskite (mixed), in the dark (Fig. 4a and a′), the contact potential difference (CPD) is 50 mV. The respective topography and surface potential maps in the presence of light are shown in Fig. 4b and b′. The CPD was increased to 170 mV (Fig. 3e and e′). Fig. S2 (ESI†) displays the line tracings of these scans. Topographical comparison shows that the mixed perovskite grains have distinct shapes under dark conditions, but they appear to be incoherent under illumination. The area (grains) which showed a bright contrast in topography possesses high CPDs in the corresponding surface potential image. However, on light illumination, over the whole scan area, high CPDs were observed. The high surface potential domains (contrary to current distribution) are more evenly distributed across the perovskite surface and are not necessarily influenced by the height variations. From the dark to the illuminated state, the increase in CPD indicates that the photogenerated carriers are more effectively separated under light.

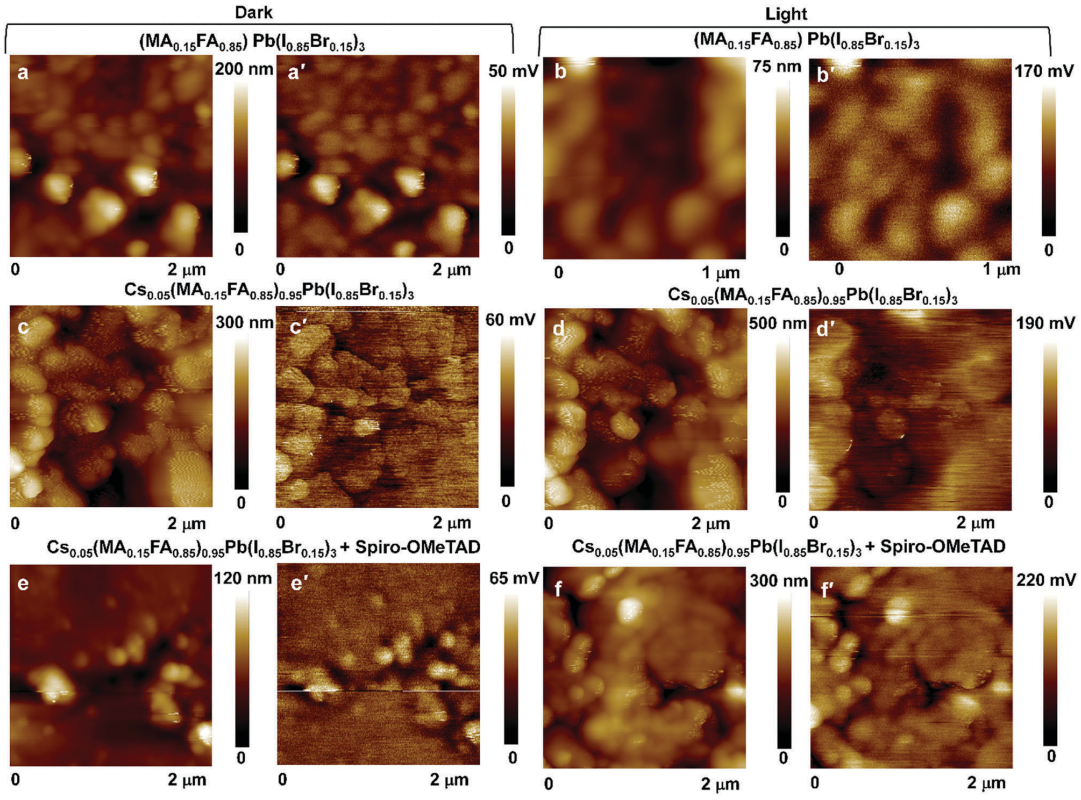

Fig. 4 Topography: (a, c and e) in dark, (b, d and f) under green light, and surface potential: (a′, c′ and e′) in the dark, (b′, d′ and f′) under green light-maps of $(MA_{0.15}FA_{0.85})Pb(I_{0.85}Br_{0.15})_3$, $Cs_{0.05}(MA_{0.15}FA_{0.85})_{0.95}Pb(I_{0.85}Br_{0.15})_3$ and Spiro-OMeTAD (90 mM) coated $Cs_{0.05}(MA_{0.15}FA_{0.85})_{0.95}Pb(I_{0.85}Br_{0.15})_3$ (at 1.4 M perovskite concentrations).

The topography and the surface potential images of the triple cation perovskite in darkness and light are shown in Fig. 4c, c′ and d, d′. The CPD is 60 mV (in the dark) whereas it achieved a value of 190 mV (under light). Cs^+ doping increases the overall photovoltage, but here, under dark and light conditions, the grains with a dark contrast (in topography) are characterized by lower CPDs in the corresponding surface potential map and the grains with a bright contrast (in topography) are characterized by higher CPDs. Photovoltage augmentation is induced by Cs^+ incorporation, which leads to a higher open circuit voltage for the triple cation perovskite compared to the pristine mixed perovskite solar cells. In a recent study on mixed and triple cation Cs–Rb-perovskites, CPDs increases upon Cs doping.[24] The triple cation with Spiro-OMeTAD deposited layer topography and potential maps are presented in Fig. 4e, e′ and f, f′ (under dark and light conditions). The CPDs are 65 and 220 mV under darkness and light respectively. Both under dark and light conditions, the surface potential images, especially under light, show very few "ultra-dark" domains. Over a lateral span of 2 μm, the bright regions which are attributed to higher CPDs are contiguous and evenly distributed, thus ratifying the role of Spiro-OMeTAD in efficiently collecting holes from the perovskite, and improving it's CPD, and boosting the open circuit voltage, thus improving it's PCE.

The CPDs are also be used for determining the work functions of the samples. The work functions are approximated to the fermi energy levels (E_F). The average values of the surface potentials in the dark for the samples: perovskites, 5% Cs^+-perovskites, and 5% Cs^+-perovskites with Spiro-OMeTAD are 50, 60 and 65 mV respectively. The following equation is used for the estimation of E_F.

$$E_F(\text{Sample}) = \phi(\text{Sample}) = 4.6 + V_{CPD}(\text{HOPG}) - V_{CPD}(\text{Sample})$$

The tip used was calibrated with a sample of highly oriented pyrolytic graphite (HOPG), which is taken as a reference, prior to the measurements on the perovskite films. The topography and surface potential images for HOPG are shown in Fig. S3a and b (ESI†). Fig. S3a (ESI†) shows the HOPG topography, wherein the aligned graphitic layers are clearly visible. Fig S3b (ESI†) shows the surface potential map of HOPG and the average surface potential is deduced to be 500 mV.

From the above equation, the magnitudes of E_F for perovskites, 5% Cs^+-perovskites, and 5% Cs^+-perovskites with Spiro-OMeTAD electrodes are 5.305, 5.30 and 5.29 eV respectively. The Fermi levels are depicted through an energy band diagram in Fig. 5. The conduction and valence band positions for the perovskite with and without 5% Cs^+, are taken from our previous study.[17] As CPD decreases, the E_F shifts deeper. In the presence of the only Cs^+, the E_F shifts to lower values and this is because of the strong p-doping nature of the cesium salt. Further addition of Spiro-OMeTAD, upshifts the E_F, because of p-type behaviour and the hole transport layer. The energy gradient between the Fermi level of 5% Cs^+-perovskites and the work function of Spiro-OMeTAD is lower than the gradient between the E_F of perovskites and the work function of Spiro-OMeTAD. A lower gradient facilitates hole transfer to this layer.

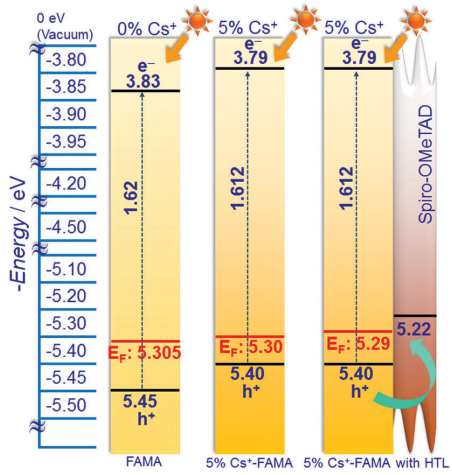

Fig. 5 Energy level diagram of the perovskites, with Fermi levels deduced from CPDs in the dark. Here the term FAMA represents $(MA_{0.15}FA_{0.85})Pb(I_{0.85}Br_{0.15})_3$ perovskites.

Electrochemical impedance spectroscopy

The fact that the organic constituent of perovskite (MA/FA) will not influence the electronic properties of perovskite solar cells will be of less significance, if we compare the metal cation with the halide anion. Nevertheless, some studies suggest the importance of the organic part and its bearing on opto-electrical properties and stability. Specifically, recent research has pointed out the possibility of ion migration (I^-, MA^+, or less probable Pb^{2+}) to contact barriers can be one of the plausible reasons for the hysteresis behavior reported in perovskite solar cells.[25,26] However with the formation of larger perovskite crystals, hysteresis behavior diminishes.

The use of mixed organic cation perovskite (MA/FA) reduces the migration of MA^+, as FA stabilizes the crystal structure due to its relatively larger size (radii MA^+ = 0.270 nm, FA^+ = 0.279 nm)[27] and the formation of hydrogen bonds with Pb octahedra. In the case of Cs^+ (radii Cs^+ = 0.118 nm),[28] though arguable, the cation has high movement, however it has been shown that the presence of strong electrostatic attractive interactions between Cs^+, I^- and Br^- contribute to stabilizing the lattice.[17] In order to unravel the charge dynamics in these cesium perovskite based solar cells, EIS experiments were carried out. It can be observed that the resistance to recombination (R_{rec}), obtained from fitting the impedance response shows a decrease in value with the addition of Cs. (Fig. 6a) The inclusion of 10% or 15% Cs in the perovskite stoichiometry shows an almost similar profile regardless of the open circuit voltage. In contrast to this, no significant changes were observed for devices with and without 5% Cs. At a higher voltage, (close to V_{oc}), all the devices represented similar values of R_{rec}. For higher Cs inclusion, lower values of electron recombination resistance were found.

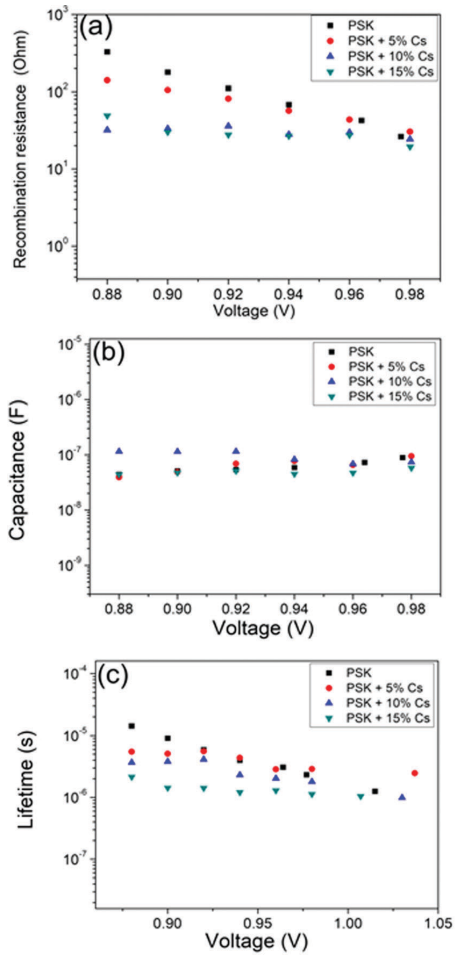

Fig. 6 Different electrical parameters derived from EIS studies using a concentration of 1.2 M perovskite solution.

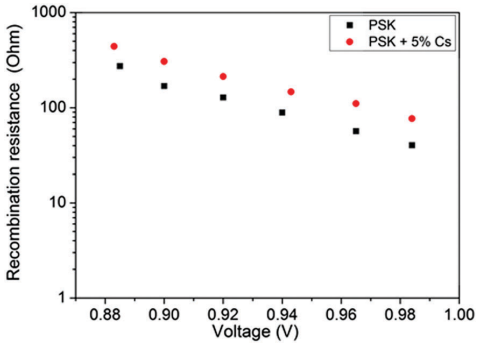

Fig. 7 Recombination resistance value for 1.4 M perovskite solution based devices.

At a lower voltage, the slope for the recombination resistance is more pronounced which diminishes at a voltage close to V_{oc} of the devices. From this, we assume that the recombination process is mediated *via* a trap-limited mechanism in the bulk of the perovskite, and at a short circuit condition close to 1 Sun; the device resistance decreases significantly.[29] A similar behavior was also obtained when 1.4 M precursor solution was used (Fig. 7). By and large the value of capacitance remains unchanged, when measured across the voltage range.[30] (Fig. 6b) This capacitance behavior is attributed to the dependence by its geometrical component. The capacitance–frequency response (Fig. S4, ESI†) measured under the range of (0.1–10^6 Hz), shows the presence of a narrow plateau appearing at medium frequencies (10^5–10^4 Hz). All the samples with cesium inclusion show a different profile, with the appearance of a sharp slope at a lower frequency range (0.1–10^3 Hz). This suggests that the electron–hole pair generation profile is altered with the presence of Cs.

Lower electron lifetime values were obtained from the Cs^+ based devices (Fig. 6c). Cs^+ inclusion gives lower electron life times, and the results are consistent with the percentage of Cs^+ in the perovskite stoichiometry. At a voltage close to the open circuit voltage, similar lifetimes are observed for all the devices, except that a slightly better electron lifetime was obtained by 5% Cs^+ inclusion, which is in accordance with the photovoltaic performances. The interface between perovskite and charge selective contacts represents the main recombination pathway in perovskite solar cells.[31] Nevertheless, the interaction between the perovskite and TiO_2 selective contact could affect the performance of the devices.

In other words, if we analyze the behavior of the devices at low frequencies, we can correlate it to the charge accumulation at the perovskite/TiO_2 interface. Some authors suggested[32] that this charge accumulation together with the ionic motion, possibly explain the hysteresis behavior in the perovskite solar cell.

This charge accumulation of electrons at the TiO_2 interface, follows a $(2k_BT)^{-1}$ slope when it is represented in the semi-logarithmic plot of capacitance at low frequencies *versus* voltage. The charge accumulation/ion motion is reduced with the inclusion of cesium cations (Fig. 8). This is in accordance with our previous results, where it was explained that the inclusion of cesium stabilized the crystal structure and helps the charge extraction as well as thermal stability.[17]

According to previous reports, the stability of perovskite solar cells is attributed to three main factors: moisture, heat, and UV light, with moisture being the most critical factor.[33] However, a combination of these factors accelerate fast degradation in perovskite devices. Additionally, intrinsic instability also affects device degradation due to charge accumulation as mentioned above. To address this issue, UV^+ and humidity degradation tests were performed in order to study structure degradation in cesium based perovskite films. After degrading for different periods of time, X-ray diffractograms were recorded. Results (Fig. S5, ESI†) showed that after 60 min UV exposure time, the ratio of the PbI_2 (12.6°) and perovskite

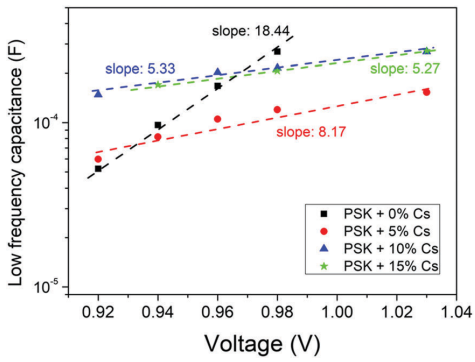

Fig. 8 Low-frequency capacitance as a function of open-circuit potential for the different cesium based perovskite compositions.

(14.1°) peaks increased, which is a clear indication that degradation is taking place in the film, whereas the sample with cesium content (15%) remains unaltered. This suggests that the incorporation of an inorganic cation (Cs^+) improve the long-term stability of perovskite solar cells.

Experimental

Materials

Unless otherwise mentioned, all chemicals were procured from either Sigma Aldrich or Acros and used as such. Methylammonium iodide (MAI), formamidinium iodide (FAI), methylammonium bromide (MABr) were bought from Dyesol, whereas PbI_2 and $PbBr_2$ were bought from TCI, Japan. 2,2′,7,7′-Tetrakis(*N*,*N*-di-*p*-methoxyphenyamine)-9,9-spirobifluorene (Spiro-OMeTAD) was acquired from Merck KGaA, whereas chlorobenzene, anhydrous dimethylformamide (DMF), dimethyl sulfoxide (DMSO) and cesium iodide (CsI) were procured from Sigma-Aldrich.

Device fabrication

Transparent conducting coated glasses (TEC15, 15 Ω sq^{-1}) were used as substrates. They were cleaned by ultrasonication in a 2% Hellmanex water solution for 30 minutes followed by rinsing with deionized water and ethanol. Then, a ∼40 nm TiO_2 compact layer was deposited on a FTO substrate *via* spray pyrolysis at 450 °C from a precursor solution of titanium diisopropoxide bis-(acetylacetonate) in anhydrous ethanol. After the spraying, the substrates were left at 450 °C for 45 minutes and allowed to cool to room temperature. The mesoporous layer of TiO_2 was deposited using spin coating (30 s at 4000 rpm). For this, a TiO_2 paste (Dyesol 30 NR-D) was first diluted in ethanol (1 : 7), so that a 150–200 nm thick layer was achieved. Following this, the photoanodes were annealed at 450 °C for 30 min under dry air flow. This annealing process converts the rutile phase (amorphous) TiO_2 layers into anatase and allows interconnection of particles. After cooling to 150 °C, these photoanodes were transferred to a glovebox for perovskite deposition. The perovskite films were deposited from a precursor solution containing FAI (1 M), PbI_2 (1.2 M), MABr (0.2 M), and $PbBr_2$ (0.2 M) in anhydrous DMF : DMSO 4 : 1 (v : v). The perovskite solution was spin coated in a two-step sequence at 1000 and 4000 rpm for 10 and 30 s, respectively. During the second spinning step, 100 μL of chlorobenzene was used as an antisolvent approach and was dripped on the substrate, 15 s prior to the end of the program (spinning). The substrates were then annealed at 100 °C for 1 h in a glovebox. For the triple cation based perovskite, $Cs_x(MA_{0.15}FA_{0.85})_{100-x}Pb(I_{0.85}Br_{0.15})_3$, cesium iodide (CsI) was separately dissolved (1.5 M stock solution in dimethyl sulfoxide (DMSO)), and added to the perovskite precursor to achieve 5–15% composition.

After perovskite formation, Spiro-OMeTAD (70 mM in chlorobenzene) was spin coated (4000 rpm for 20 s) as the hole transport layer. For better performance, routine doping of Spiro-OMeTAD was carried out using lithium bis-(trifluoromethylsulfonyl)imide salt (Li-TFSI), tris(2-(1*H*-pyrazol-1-yl)-4-*tert*-butylpyridine)cobalt(III)-tris(bis-(trifluoro-methylsulfonyl)imide) (FK209, from Dynamo), and 4-*tert*-butylpyridine (*t*-BP). The molar ratio of additives for HTMs was: 0.5, 0.03, and 3.3 for Li-TFSI, FK209, and *t*-BP, respectively. The device fabrication was completed by the deposition of 70–80 nm of gold as cathode, this was thermally evaporated under low vacuum ($10^{-5} \times 10^{-6}$). All the solutions were prepared inside an argon-controlled glovebox.

Characterization

Current density–voltage (*J*–*V*) curves were recorded with a Keithley 2400 source-measurement-unit under AM 1.5 G, 100 mW cm^2 illumination from a certified Class AAA, 450 W solar simulator (ORIEL, 94023 A). Light output power was calibrated using a NREL certified calibrated mono-crystalline silicon solar cell. A black metal mask (0.16 cm^2) was placed over the square shaped device (active area 0.5 cm^2) to reduce the influence of scattered light. An optimized scan rate of 10 mV s^{-1} was used for the measurements so that accurate values for efficiencies can be calculated without having hysteresis. For IPCE measurements, a 150 W xenon lamp coupled to an Oriel Cornerstone 260 motorized frac1/4; m monochromator was used as the light source, whereas a 2936-R power meter was used to measure the short circuit current. Cross-sectional microscopy and normal topography images were taken with a Hitachi S5200 field-emission microscope operating at 5.0 keV.

Impedance spectroscopy (IS) measurements was carried out by means of a white LED over a wide range of DC light intensities. This allowed us to measure devices at different positions of the Fermi level. A response analyzer module (SP300, Bio-Logic Science Instrument) was utilized to analyze the frequency response of the devices. To avoid voltage drop due to series resistance, IS measurements were performed at the open circuit potential, the Fermi level being fixed by the DC illumination intensity. A 20 mV perturbation in the range 2 MHz–1 mHz was used to obtain the spectra. After measurement, data were fitted by Z-view software in order to extract the characteristic parameters of the cells.

Conductive force microscopy (C-FM), and Kelvin probe force microscopy (KPFM) measurements were performed on

the electrodes using a Veeco, Multimode 8 with a Scan Asyst (Nanoscope 8.10 software) microscope. The conductive probes used in this study were made of antimony doped silicon (n-doped; resistivity ~ 0.01–0.025 Ω cm) coated with platinum–iridium from Bruker (SCM-PIC-V2). The probe tip had a radius of 10 nm, with a spring constant of 0.1 N m^{-1}. The sample was deposited on the FTO substrate and was affixed on a stainless steel disk with the help of conducting carbon tape. A thin strip of silver paste was glued for taking the contacts. All the images were recorded at room temperature under both dark and green light illumination. A green LED with an irradiance of 1.5 mW cm^{-2} was used.

For CFM measurements, a current sensitivity of 1 nA V^{-1} and a load force of 47.6 nN is maintained between the tip and the sample. The contact tip is scanned in contact with the sample surface. The z-feedback loop uses the dc cantilever defending a signal to maintain a constant force between the tip and the sample to generate topographic images. Concurrently, a dc bias of 500 mV is applied to the tip. The sample is held at ground potential. The built-in pre-amplified scanner head measured the current passing through the tip and sample and imaged the current profiles. For KPFM measurements, the distance (lift scan height) between the tip and the sample was maintained at 50 nm. Applied sample bias was 1 V in order to obtain decent images.

Conclusions

Conductive force microscopy studies show that the average current carrying ability of the mixed-perovskite is enhanced by 5% Cs^+ substitution, both in the dark and under the irradiance state. The photocurrents were further improved, and have a more uniform delocalized distribution across the surface, when the perovskite samples are coated with Spiro-OMeTAD, confirming that the HTL/perovskite interface is most conducive for producing high photocurrents and therefore a high J_{SC} ensues. KPFM analysis reveals that the CPDs increase with Cs^+ doping and further with Spiro-OMeTAD layer deposition atop of the perovskites. The high open circuit voltage for the solar cells obtained by 5% Cs^+ substitution[17] is correlated to the uniformly distributed and interlinked high CPD domains, which spread over multiple length scales. Incorporation of Cs ions into mixed halide perovskites reduces the recombination resistance at a voltage close to open circuit, and it also increases the electron lifetime, both properties are beneficial for extending the device photovoltaic parameters.

Acknowledgements

This project has received funding from the European Union Seventh Framework Programme under grant agreement no. 607232 [THINFACE].

References

1 S. Kazim, M. K. Nazeeruddin, M. Grätzel and S. Ahmad, *Angew. Chem., Int. Ed.*, 2014, **53**, 2812–2824 (*Angew. Chem.*, 2014, **126**, 2854–2867); L. Calió, S. Kazim, M. Grätzel and S. Ahmad, *Angew. Chem., Int. Ed.*, 2016, **55**, 14522–14545 (*Angew. Chem.*, 2016, **128**, 14740–14764).
2 J.-P. Correa-Baena, A. Abate, M. Saliba, W. Tress, T. Jesper Jacobsson, M. Grätzel and A. Hagfeldt, *Energy Environ. Sci.*, 2017, **10**, 710–727.
3 http://www.nrel.gov/pv/assets/images/efficiency_chart.jpg.
4 N. J. Jeon, J. H. Noh, W. S. Yang, Y. C. Kim, S. Ryu, J. Seo and S. Il Seok, *Nature*, 2015, **517**, 476–480.
5 N. J. Jeon, J. H. Noh, Y. C. Kim, W. S. Yang, S. Ryu and S. Il Seok, *Nat. Mater.*, 2014, **13**, 897–903.
6 V. M. Goldschmidt, *Naturwissenschaften*, 1926, **14**, 477–485.
7 Y. Zhang, G. Grancini, Y. Feng, A. M. Asiri and M. K. Nazeeruddin, *ACS Energy Lett.*, 2017, **2**, 802–806.
8 M. Saliba, T. Matsui, J.-Y. Seo, K. Domanski, J.-P. Correa-Baena, M. K. Nazeeruddin, S. M. Zakeeruddin, W. Tress, A. Abate, A. Hagfeldt and M. Grätzel, *Energy Environ. Sci.*, 2016, **9**, 1989–1997.
9 C. Yi, J. Luo, S. Meloni, A. Boziki, N. Ashari-Astani, C. Grätzel, S. M. Zakeeruddin, U. Röthlisberger and M. Grätzel, *Energy Environ. Sci.*, 2016, **9**, 656–662.
10 X. Li, D. Bi, C. Yi, J.-D. Decoppet, J. Luo, S. M. Zakeeruddin, A. Hagfeldt and M. Gratzel, *Science*, 2016, **353**, 58–62.
11 P. Luo, Z. Liu, W. Xia, C. Yuan, J. Cheng and Y. Lu, *ACS Appl. Mater. Interfaces*, 2015, **7**, 2708–2714.
12 Y. Rong, L. Liu, A. Mei, X. Li and H. Han, *Adv. Energy Mater.*, 2015, **5**, 1501066.
13 Q. Jiang, D. Rebollar, J. Gong, E. L. Piacentino, C. Zheng and T. Xu, *Angew. Chem., Int. Ed.*, 2015, **54**, 7617–7620.
14 F. Bella, G. Griffini, J.-P. Correa-Baena, G. Saracco, M. Grätzel, A. Hagfeldt, S. Turri and C. Gerbaldi, *Science*, 2016, **354**, 203–206.
15 R. E. Beal, D. J. Slotcavage, T. Leijtens, A. R. Bowring, R. A. Belisle, W. H. Nguyen, G. Burkhard, E. T. Hoke and M. D. McGehee, *J. Phys. Chem. Lett.*, 2016, 746–751.
16 H. Choi, J. Jeong, H. B. Kim, S. Kim, B. Walker, G. H. Kim and J. Y. Kim, *Nano Energy*, 2014, **7**, 80–85.
17 M. Deepa, M. Salado, L. Calio, S. Kazim, S. M. Shivaprasad and S. Ahmad, *Phys. Chem. Chem. Phys.*, 2017, **19**, 4069–4077.
18 V. W. Bergmann, S. A. L. Weber, F. Javier Ramos, M. K. Nazeeruddin, M. Grätzel, D. Li, A. L. Domanski, I. Lieberwirth, S. Ahmad and R. Berger, *Nat. Commun.*, 2014, **5**, 5001.
19 U. Wurfel, A. Cuevas and P. Wurfel, *IEEE J. Photovoltaics*, 2015, **5**, 461–469.
20 C.-S. Jiang, M. Yang, Y. Zhou, B. To, S. U. Nanayakkara, J. M. Luther, W. Zhou, J. J. Berry, J. van de Lagemaat, N. P. Padture, K. Zhu and M. M. Al-Jassim, *Nat. Commun.*, 2015, **6**, 8397.
21 P. Qin, A. L. Domanski, A. K. Chandiran, R. Berger, H.-J. Butt, M. I. Dar, T. Moehl, N. Tetreault, P. Gao, S. Ahmad, M. K. Nazeeruddin and M. Grätzel, *Nanoscale*, 2014, **6**, 1508–1514.

22 Y. Kutes, Y. Zhou, J. L. Bosse, J. Steffes, N. P. Padture and B. D. Huey, *Nano Lett.*, 2016, **16**, 3434–3441.
23 G. A. MacDonald, M. Yang, S. Berweger, J. P. Killgore, P. Kabos, J. J. Berry, K. Zhu and F. W. DelRio, *Energy Environ. Sci.*, 2016, **9**, 3642–3649.
24 M. Zhang, J. S. Yun, Q. Ma, J. Zheng, C. F. J. Lau, X. Deng, J. Kim, D. Kim, J. Seidel, M. A. Green, S. Huang and A. W. Y. Ho-Baillie, *ACS Energy Lett.*, 2017, **2**, 438–444.
25 Z. Xiao, Y. Yuan, Y. Shao, Q. Wang, Q. Dong, C. Bi, P. Sharma, A. Gruverman and J. Huang, *Nat. Mater.*, 2014, **14**, 193–198.
26 Y. Yuan and J. Huang, *Acc. Chem. Res.*, 2016, **49**, 286–293.
27 R. D. Shannon, *Acta Crystallogr., Sect. A: Cryst. Phys., Diffr., Theor. Gen. Crystallogr.*, 1976, **32**, 751–767.
28 A. Amat, E. Mosconi, E. Ronca, C. Quarti, P. Umari, M. K. Nazeeruddin, M. Grätzel and F. De Angelis, *Nano Lett.*, 2014, **14**, 3608–3616.
29 E. Guillén, F. J. Ramos, J. A. Anta and S. Ahmad, *J. Phys. Chem. C*, 2014, **118**, 22913–22922.
30 J. Bisquert, L. Bertoluzzi, I. Mora-sero and G. Garcia-belmonte, *J. Phys. Chem. C*, 2014, **118**, 18983–18991.
31 A. R. Pascoe, N. W. Duffy, A. D. Scully, F. Huang and Y.-B. Cheng, *J. Phys. Chem. C*, 2015, **119**, 4444–4453.
32 I. Zarazua, J. Bisquert and G. Garcia-Belmonte, *J. Phys. Chem. Lett.*, 2016, **7**, 525–528.
33 T. A. Berhe, W.-N. Su, C.-H. Chen, C.-J. Pan, J.-H. Cheng, H.-M. Chen, M.-C. Tsai, L.-Y. Chen, A. A. Dubale and B.-J. Hwang, *Energy Environ. Sci.*, 2016, **9**, 323–356.

Journal of Materials Chemistry A

PAPER

View Article Online
View Journal | View Issue

Cite this: J. Mater. Chem. A, 2017, 5, 10917

Impact of moisture on efficiency-determining electronic processes in perovskite solar cells†

Manuel Salado,‡[ab] Lidia Contreras-Bernal,‡[a] Laura Caliò,[b] Anna Todinova,[a] Carmen López-Santos,[c] Shahzada Ahmad,[b] Ana Borras,[c] Jesús Idígoras *[a] and Juan A. Anta *[a]

Received 14th March 2017
Accepted 10th May 2017

DOI: 10.1039/c7ta02264f

rsc.li/materials-a

Moisture-induced degradation in perovskite solar cells was thoroughly investigated by structural (SEM, EDS, XRD and XPS) and device characterization (impedance and intensity modulated photocurrent spectroscopy) techniques. Both the influence of the perovskite composition and the nature of the hole selective material were analyzed. The degradation rate was found to be significantly slower for mixed perovskites and P3HT-based devices. However, for a fixed degradation degree (defined as a 50% drop from the initial photocurrent), all configurations show similar features in small-perturbation analysis. Thus, a new mid-frequency signal appears in the impedance response, which seems to be related to charge accumulation at the interfaces. In addition, faster recombination, with a more important surface contribution, and slower transport were clearly inferred from our results. Both features can be associated with the deterioration of the contacts and the formation of a higher number of grain boundaries.

Introduction

Over the last few decades, the research community has shown special interest in the development of efficient and low-cost photovoltaic technologies. In this context, hybrid organic–inorganic metal halide perovskite materials have attracted huge attention owing to their excellent optoelectronic properties.[1–5] As a result, since the first report of perovskite materials as a sensitizer in dye-sensitized solar cells ($\eta = 3.8\%$),[6] a significant improvement of the photovoltaic conversion efficiency has been achieved with a current efficiency record of $\eta = 22.1\%$ for a perovskite solar cell.[7] This figure is comparable to the photovoltaic performances of other thin-film photovoltaic technologies based on Si, CdTe and GaAs. This remarkable development was possible due to intensive research focused on device engineering and material design.[8–12] However, in spite of this progress, the lack of long-term stability restricts its outdoor photovoltaic applications[13] and as a consequence its commercialization.

It is well-known that the stability of perovskite solar cells (PSCs) and therefore their photovoltaic performance are intimately associated with the degradation of the perovskite layer. As was previously reported, the main causes behind perovskite degradation are related to different environmental factors,[14–16] such as moisture, temperature, oxygen and UV light, which could give rise to different degradation pathways. Niu *et al.* suggested that perovskite degradation starts with the deprotonation of the methylammonium cation by water to produce methylamine, hydrogen iodide and lead iodide.[17] Yang *et al.* proposed the formation of colorless hydrated $(CH_3NH_3)_4PbI_6 \cdot 2H_2O$ as a result of perovskite hydration and the formation of lead iodide as the final product.[18] Haque *et al.* described perovskite degradation by the coupled effect of molecular oxygen and light suggesting that reactive oxygen species and the organic cation of perovskite react among themselves.[19] More recently, Wang *et al.* have proposed a self-degradation process caused by the I_2 vapor generated under working conditions due to chemical chain reactions.[20] In any case, many approaches have been developed in order to prevent perovskite degradation and guarantee device stability. Among them stand out the effective passivation of devices by the use of hydrophobic polymer layers and the employment of photopolymerized fluorinated coatings, hydrophobic hole-selective materials, hydrophobic carbon electrodes and a thin blocking layer between perovskite and electron-selective layers.[21–27]

However, the impact of these environmental factors on perovskite degradation kinetics depends on other intrinsic

[a]Área de Química Física, Universidad Pablo de Olavide, E-41013, Seville, Spain. E-mail: anta@upo.es; jaidileo@upo.es

[b]Abengoa Research, C/Energía Solar No. 1, Campus Palmas Altas, 41014 Sevilla, Spain

[c]Nanotechnology on Surfaces Laboratory, Instituto de Ciencia de Materiales de Sevilla (CSIC-Univ. Seville), Seville ES-41092, Spain

† Electronic supplementary information (ESI) available: Scanning electron microscopy images, EDS spectra and maps, current–voltage characteristic and photovoltaic parameters, Nyquist impedance spectra, impedance–frequency plots, electron recombination resistances, HF time constant *versus* potential, static water contact angle and XPS characterization before and after moisture exposure. See DOI: 10.1039/c7ta02264f

‡ Manuel Salado and Lidia Contreras-Bernal have contributed equally to the paper.

properties such as thermal and electrical stability, which are determined by the perovskite composition. Hybrid organic–inorganic metal halide perovskites are defined by the chemical formula ABX_3, where A is an organic or inorganic cation ($MA = CH_3NH_3^+$; $FA = HC(NH_2)_2^+$ and Cs^+), B is a metal (Pb and Sn) and X is a halide (I^-, Br^- and Cl^-). The chemical nature of these elements influences not only the photoelectronic behavior, but also the structural properties defined by the tolerance factor (t)[28]

$$t = \frac{(r_A + r_X)}{\left(\sqrt{2}\,(r_B + r_X)\right)}$$

where r_A, r_B and r_X are the ionic radii of the different elements A, B and X, respectively. Empirically, for the most stable perovskite, t shows values between 0.8 and 1 giving rise to a cubic crystal structure. However, for t <0.8 the tetragonal or the orthorhombic crystal structure is more probable.[28,29] As a consequence, special attention has been paid to the perovskite composition in order to achieve a more stable crystal structure and guarantee long-term stability by the entire or partial inclusion of different ions with different sizes. For instance, the beneficial effect in terms of stability of a partial insertion of bromine into the perovskite structure was reported.[30,31] Similar results were found for the inclusion of chloride.[32] In both cases, the smaller ionic radii of Br and Cl with respect to I lead to a more compact structure in which the organic cations are less exposed. More recently, Petrus and coworkers reported the impact of the excess of PbI_2 as the precursor on perovskite stability against moisture exposure.[33] In relation to the organic cations, t values of 0.88 and 0.83 were found for perovskites containing MA and FA, respectively.[34] The higher thermal stability found for $FAPbI_3$ was associated with the more-stable cubic crystal phase with respect to the tetragonal one attributed to $MAPbI_3$, which could be related to the different interactions of these cations with the inorganic matrix.[29] Similar results were found by Snaith *et al.* when they compared $CsPbI_2Br$ and $MAPbI_2Br$ and demonstrated the stability of the former owing to the appropriate ionic radius of Cs^+.[35] The stability of a triple cation perovskite (containing MA, FA and Cs) has also been investigated.[36]

To date, previous studies related to perovskite stability have mainly investigated the different perovskite degradation mechanisms under environmental conditions or different approaches to prevent perovskite degradation. SEM and STEM images, EDS mapping, UV-Vis absorbance, XRD patterns, and Raman and IR spectroscopy techniques were commonly used to determine the extent of perovskite degradation and its kinetics. However, to the best of our knowledge, this is the first report where small-perturbation optoelectronic techniques have been used to investigate the impact of moisture on the electronic processes that determine the photovoltaic performance. This is important to better assess how the perovskite improvements investigated in the literature really affect the functioning of the device in terms of stability and efficiency. In order to correlate the moisture effect to this, we have analyzed the electron transport and recombination processes using impedance spectroscopy (IS) and intensity-modulated photocurrent spectroscopy (IMPS). In this work, we have investigated both the influence of the perovskite composition ($MAPbI_3$ = MAI and $Cs_{0.05}(MAPbBr_3)_{0.15}(FAPbI_3)_{0.85}$ = MIX) and the influence of the hole selective material (HSL: 2,2′,7,7′-tetrakis(*N*,*N*-di-*p*-methoxyphenylamine)-9,9′-spirobifluorene = Spiro-OMeTAD and poly(3-hexylthiophene-2,5-diyl) = P3HT) on the device stability. In particular, a faster degradation rate was found for MAI perovskite and Spiro-based devices. Regardless of the device configuration, our results point to a faster recombination after moisture exposure due to the coupled effect of the bulk recombination and the surface-mediated recombination. The greater contribution of the latter in degraded devices is revealed by interfacial charge accumulation processes and slower electron transport inside the perovskite layer.

Experimental

Fabrication of perovskite solar cells

Perovskite solar cells were fabricated on FTO-coated glass (Pilkington-TEC15) patterned by laser etching. Before use, the substrates were cleaned using Hellmanex® solution and rinsed with deionized water and ethanol. Followed this they were ultrasonicated in acetone, rinsed using 2-propanol and dried with compressed air. A TiO_2 compact layer was deposited by spray pyrolysis at 450 °C using titanium diisopropoxide bis(acetylacetonate) precursor solution (75% in 2-propanol, Sigma Aldrich) using dry air as a carrier gas. The TiO_2 blocking layer was then annealed for a further 30 minutes at 450 °C for the formation of the anatase phase. Once the samples achieved room temperature, a TiO_2 mesoporous layer (Dyesol, 30NRD) was deposited by spin coating (4000 rpm for 30 s) and the samples were annealed at 450 °C. Subsequently, pure methylammonium ($MAPbI_3$ = MAI) or mixed cation perovskite ($Cs_{0.05}(MAPbBr_3)_{0.15}(FAPbI_3)_{0.85}$ = MIX) was then deposited (Fig. S1†). The pure methylammonium perovskite precursor solution was prepared by mixing 1.2 M MAI and PbI_2 (1 : 1.15) in DMSO. The mixed cation perovskite was prepared by dissolving FAI (1.01 M), MABr (0.20 M), PbI_2 (1.21 M) and $PbBr_2$ (0.20 M) in a mixture of solvents DMSO/DMF (1 : 4, v/v). After this, CsI (5 wt%) was added (from a 1.5 M stock solution in DMSO) to the precursor solution. The perovskite solution was spin coated in a two step setup at 1000 and 6000 rpm for 10 and 20 s respectively. During the second step, chlorobenzene was dropped on the spinning substrate 15 seconds before the end of the program. The samples were then annealed (100 °C) for 1 h in an argon filled glovebox. After perovskite deposition, 35 μL of a Spiro-OMeTAD or P3HT solution was spin coated at 4000 rpm for 20 seconds as the HSL. The Spiro-OMeTAD material (70 mM) was dissolved in 1 mL of chlorobenzene using standard additives namely 17.5 μL of a lithium bis(trifluoromethylsulphonyl) imide (LiTFSI) stock solution (520 mg of LiTFSI in 1 mL of acetonitrile), 21.9 μL of a FK209 (tris(2-(1*H*-pyrazol-1-yl)-4-*tert*-butylpyridine)cobalt(III)tris(bis(trifluoromethylsulfonyl)imide)) stock solution (400 mg in 1 mL of acetonitrile) and 28.8 μL of 4-*tert*-butylpyridine (*t*-BP). In the case of the P3HT material, a 15 mg mL^{-1} solution in chlorobenzene was prepared and doped with 6.8 mL of a 28.3 mg mL^{-1} stock solution of LiTFSI in

View Article Online
Paper Journal of Materials Chemistry A

acetonitrile. Finally, 80 nm of gold was deposited by thermal evaporation at a vacuum level between 1 v10^{-6} and 1 an10^{-5} Torr. All solutions were prepared inside an argon glovebox under controlled moisture and oxygen conditions. For simplicity we will use the following notations to refer to the different device configurations: MAI/Spiro, MAI/P3HT, MIX/Spiro and MIX/P3HT.

Characterization of films and devices

The devices were characterized using current–voltage characteristics with two different light sources: (1) a solar simulator (ABET-Sun2000) under 100 mW cm^{-2} illumination with an AM 1.5G filter and (2) a white light emitting diode (LED, LUXEON). The light intensity was recorded using a reference solar cell with temperature output (Oriel, 91150). The current–voltage characteristics were determined by applying an external potential bias to the cell and measuring the photocurrent using an Autolab/PGSTAT302N potentiostat.

The illumination for the different Impedance Spectroscopy (IS) measurements was provided by white, red ($\lambda = 635$ nm) and blue ($\lambda = 465$ nm) LEDs over a wide range of DC light intensities. This allows for probing the devices at different positions of the Fermi level in the semiconductor and for different optical generation profiles.[37,38] A response analyzer module (PGSTAT302N/FRA2, Autolab) was utilized to analyze the frequency response of the devices. To avoid voltage drop due to series resistance, IS measurements were performed at the open circuit potential, the Fermi level (related to the open-circuit voltage) being fixed by the DC illumination intensity. A 20 mV perturbation in the 10^6 to 10^{-2} Hz range was utilized to obtain the spectra. IMPS measurements were performed under short-circuit conditions in the 10^6 to 10^{-2} Hz range with a light perturbation corresponding to 10% of the DC background illumination intensity. To avoid any additional degradation process related to the moisture, the measurements were carried out under a N_2 atmosphere. NOVA 1.7 software was used to generate IS data. Z-view equivalent circuit modeling software (Scribner) was used to fit the spectra.

For the structural characterization, perovskite films were prepared by spin coating onto Si wafers. Scanning electron microscope (SEM) images of the samples were recorded using a Zeiss GeminiSEM-300 microscope operating at 2 keV. Electron Backscatter Diffraction (EBSD) images were obtained using a NordlysMax3 detector (Oxford Instruments). Energy Dispersive Spectroscopy (EDS) was performed using a Silicon Drift Detector (Oxford Instruments). X-ray diffractograms were recorded on a Rigaku diffractometer using a CuKα source. The measurements were performed in a grazing angle geometry. The samples were mounted without any further modification and the divergence slit was adjusted to the dimension of the films. The scan range of 10–60° was selected with an acquisition time of 3 degree min^{-1}. A baseline correction was applied to the diffractograms to compensate for the noise arising from the substrate. X-Ray Photoelectron Spectroscopy (XPS) characterization was performed on a Phoibos 100 DLD X-ray spectrometer from SPECS. The spectra were collected in the pass energy constant mode at a value of 50 eV for the general spectra and 30 eV for the different peaks using a Mg Kα source. The C 1s signal at 284.5 eV was utilized for the calibration of the binding energy in the spectra. Static water contact angle (WCA) measurements were provided by a Data Physics setup by depositing bidistilled water drops of 1 μL. The given values correspond to statistics over 10 values. The WCAs were evaluated for pinning droplets several seconds after the contact with the surfaces.

Results and discussion

Power conversion efficiencies in the range of 12–16% were obtained under standard conditions (1 sun – AM 1.5 illumination) for the different PSCs studied here (Fig. S2†). The current–voltage characteristics of the different PSCs were measured in reverse scan (from open-circuit conditions to short-circuit conditions) at a scan rate of 100 mV s^{-1}. In particular, average efficiencies of 15.3%, 13.2%, 13% and 12.5% were obtained for MAI/Spiro, MAI/P3HT, MIX/Spiro and MIX/P3HT devices, respectively (Table S1†). In line with the literature,[39–41] these results highlight the impact of the perovskite composition and the material used as the HSL on the photovoltaic performance. For both perovskite compositions, better efficiencies were obtained when Spiro-OMeTAD was used as the HSL with respect to P3HT as a result of the higher V_{OC}. Additionally, in spite of showing similar J_{SC} and V_{OC} for both HSLs, worse efficiencies were obtained for MIX devices due to their lower fill factor. These different devices will be used for the following discussion.

In order to investigate the impact of the moisture exposure on the device stability, the photovoltaic characteristics of the different PSCs were measured inside a hermetic chamber with a constant flow of air with RH >90%. Fig. 1 shows the current–

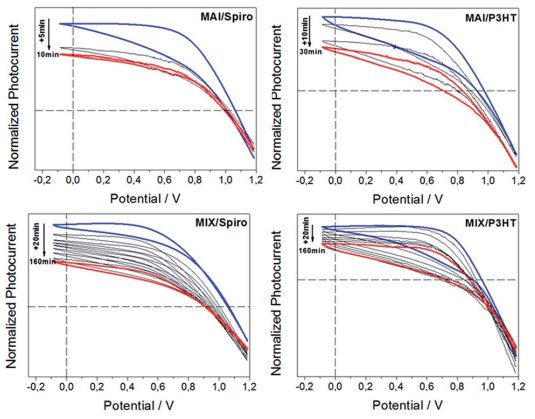

Fig. 1 Normalized I–V curves of the different PSCs (blue) before and (black and red) during the moisture exposure measured in the reverse and forward scans (cyclic voltammetry) under a light intensity of 10 mW cm^{-2} (white LED). The measurements were performed with a scan rate of 100 mV s^{-1} at room temperature and the photocurrent was normalized with respect to the short-circuit photocurrents obtained before the moisture exposure.

View Article Online
Journal of Materials Chemistry A Paper

voltage characteristics of PSCs measured by cyclic voltammetry before and during the moisture exposure. The measurements were started with a reverse scan after a dwelling time of 10 s at 1.2 V, and were then continued with a forward scan. According to preliminary results (not shown), the measurements were recorded at different exposure times to follow the degradation kinetics of the different PSC configurations.

As shown in Fig. 1, moisture exposure induces negative effects in the photovoltaic performance of the different PSCs. Both V_{OC} (open-circuit photovoltage) and J_{SC} (short-circuit photocurrent) tend to decrease with respect to the moisture exposure time. In particular, efficiency drops of 51% and 19% after 10 min for MAI-based devices and 60% and 42% after 160 min for MIX-based devices were recorded when Spiro and P3HT were used as the HSL, respectively. From these results (Fig. 1), the following trend was extracted. Firstly, focusing on the impact of the perovskite composition, the degradation process was faster when pure perovskite (MAI) was employed as the active layer compared to the degradation rate found for MIX perovskite. The same result was found when Spiro as well as P3HT were used as the HSL. As has been previously reported, the longer device stability obtained for MIX samples was not only due to the partial inclusion of bromine anions,[30,31] but also due to the combination of MA, FA and Cs cations.[36,42] This combination gives rise to a more thermally and structurally stable perovskite. And secondly, in relation to the nature of the HSL, Spiro-based devices are significantly less stable than those with P3HT as the HSL.

In order to cast light on the perovskite degradation kinetics obtained for the different PSCs, a scanning electron microscope (SEM) was used to investigate the effect of moisture exposure on the device stability. Fig. 2 shows plane-view SEM images obtained for bare perovskites (MAI and MIX) and MAI/HSL (Spiro and P3HT) films deposited on Si/cTiO_2/mTiO_2 before and after moisture exposure.

Before moisture exposure, both uncovered perovskites layers formed homogeneous and pinhole-free films, with a larger grain size in the case of MIX perovskite (Fig. S1†). However, after moisture exposure remarkable morphological changes were observable in both cases as shown in Fig. 2. In the case of bare MAI layers, large perovskite crystals with well-defined faces appeared leading to extensive pinholes after 1 hour of moisture exposure. For longer times (5 hours), larger structures with a dendritic shape were formed. In contrast, as was expected according to the literature,[30,31,36] no significant change was observed for MIX layers after at least 1 hour of moisture exposure. However, after 5 hours of exposure, large perovskite crystals with reduced pinholes around them were formed. The formation of these large perovskite structures seems to be related to the perovskite aggregation process (Fig. S3†). Similar structural changes were also observed by Wang *et al.*, in whose study perovskite films were exposed to I_2 vapor.[20] However, in contrast to a previous report,[43] EDS analysis showed the same Pb/I ratio for the fresh and degraded samples.

To investigate the influence of the HSL on the device stability, MAI perovskite was used as the active layer. Longer moisture exposure times (5 hours) were used. No significant changes appeared after only 1 hour of exposure. As shown in Fig. 2, as a result of the perovskite degradation, an increased number of emerging structures coming from the underlying

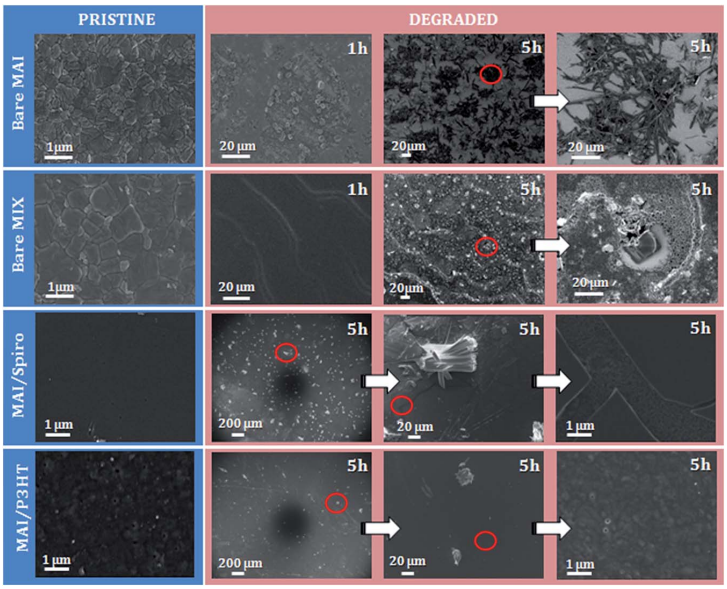

Fig. 2 Plane-view scanning electron microscopy (SEM) images of the MAI, MIX, MAI/Spiro and MAI/P3HT layers after moisture exposure (RH = 90%) for 1 and 5 h at room temperature. For more detailed analysis, SEM images of different zones (red circles) were taken using a higher magnification.

perovskite layer appeared when Spiro was used as the HSL. These newly formed crystals are a possible reason for the fracture of the Spiro layer. In contrast, after 5 hours of moisture exposure the P3HT layer appears unchanged. This behavior can be ascribed to the hydrophobic character of the P3HT layer,[26] which makes the penetration/percolation of water molecules towards the underlying perovskite layer more difficult. A similar behavior was previously reported using UV-Vis and FTIR spectroscopy.[18,44] The water contact angles (WCAs) for the different configurations are reported in Table S2.† WCAs >100° and <80° were found for perovskite/P3HT and perovskite/Spiro configurations, respectively. These results demonstrate the hydrophobic and hydrophilic character of the P3HT and Spiro layers, respectively.

Therefore, it seems reasonable to assume that the short-term stability obtained for MAI/Spiro devices was connected to both the perovskite decomposition process and higher affinity to water and the consequent degradation of the Spiro layer.

Fig. 3 shows the XRD patterns of the two perovskites (MAI and MIX) with and without the HSL (Spiro and P3HT) before and after moisture exposure. The characteristic diffraction peaks of the tetragonal perovskite phase (14.1°, 28.5° and 31.9°)[33,45] were obtained for the fresh samples, which remained at the same position when the samples were subjected to humidity (RH > 90%) exposure for 1 hour. As was previously reported, any additional peak appears as a consequence of HSLs.[44] Nevertheless, additional diffraction peaks previously related to the formation of the hydrated perovskite complex and PbI_2 were found after moisture exposure at 10.5° and 12.7°, respectively.[33,45–47] Focusing on these two diffraction peaks, different behaviors can be observed depending on the perovskite composition and/or HSL. Firstly, for uncovered perovskite layers these two peaks were only observable for MAI perovskite after moisture exposure. And secondly, contrary to expectation, higher signal intensities for these two diffraction peaks were found for MAI/Spiro with respect to the uncovered MAI sample. A similar behavior was found for MIX perovskite. In this case, the signal previously attributed to PbI_2 was only found for the MIX/Spiro sample after moisture exposure, whereas it was not observed for bare MIX and MIX/P3HT samples. Therefore, the rapid degradation kinetics found for MAI/Spiro samples (Fig. 1) could be related not only to the perovskite composition and/or the degradation of the Spiro (Fig. 2), but also to a possible interfacial interaction of both layers.[48] We have further analyzed the chemical composition of the fresh and degraded devices by XPS. The comparison of the atomic percentages of different elements (Pb, I, O, C, N, S, F and Ti) at the surface is shown in Table S3.† In line with Fig. 2, a part of the TiO_2 layer was observed for uncovered MAI after moisture exposure suggesting the high Ti percentage. A decrease of the Pb/I ratio was found for both uncovered perovskites. However, the difference was higher for MAI perovskite. In particular, after moisture exposure the Pb/I ratio changed from 0.85 to 0.5 and 0.6 to 0.4 for uncovered MAI and MIX perovskites. Finally, after moisture exposure, a percentage below 1% of I only appears in Spiro-based devices, whereas it is not detected in P3HT-based devices. Considering these results, the following trend can be established to define device stability: MAI/Spiro < MAI/P3HT < MIX/Spiro < MIX/P3HT.

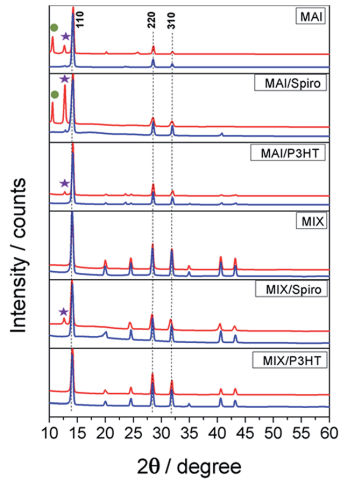

Fig. 3 X-ray diffraction of the different (MAI and MIX) perovskite layers with and without the HSL (Spiro and P3HT) deposited on the top (blue line) before and (red line) after moisture exposure for 1 hour. The positions of the XRD peaks for (purple star) PbI_2 and (green circle) the hydrated complex are marked in the graphs.

Once the impact of the moisture exposure on the device stability has been assessed according to the perovskite composition and the material employed as the HSL, we focus our attention on the electronic processes determining the photovoltaic performance. To study the effect of moisture exposure on the device performance, we analyze the impedance response in the form of Nyquist and frequency-dependent capacitance plots (Fig. 4). At this point, it is important to remark that the different PSCs were subjected to different moisture exposure times bearing in mind the different degradation kinetics demonstrated above. Therefore, in order to safely isolate the effect of the degradation rate, a photocurrent drop of 50% was employed as the criterion for the exposure time. After the moisture exposure, the PCSs were flushed with dry nitrogen for 1 hour before starting the characterization by impedance spectroscopy.

As shown in Fig. 4A, the impedance spectra obtained for the fresh PSCs were characterized by two signals (semicircles or arcs). These two signals will only be well-detected when the peak maxima on the impedance frequency plots are sufficiently well separated (Fig. S4†). As was previously reported,[49–53] the signal appearing at high frequencies (HF), the one closest to the origin and the largest semicircle, has been attributed to electronic transport/recombination processes, whereas the signal appearing at low frequencies (LF) has been related to ionic motion and charge accumulation at contacts. These two signals exhibit significant changes in the impedance spectra after moisture exposure. In particular, a distortion of the HF semicircle was found for the degraded PSCs (Fig. 4B). This behavior seems to be more remarkable for the degraded P3HT-based

View Article Online
Journal of Materials Chemistry A Paper

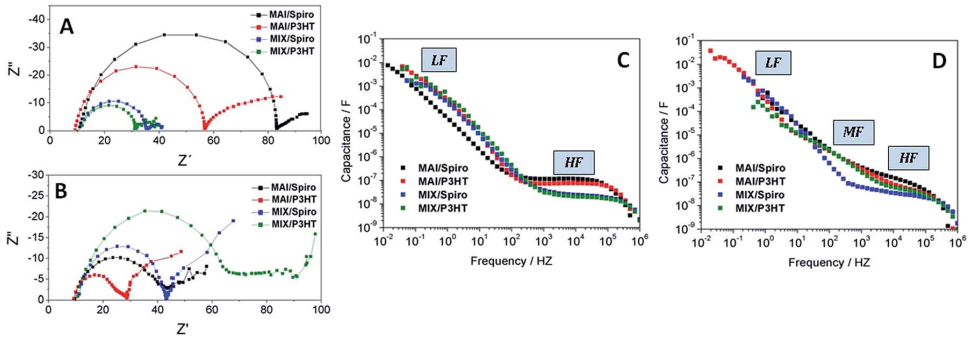

Fig. 4 (A and B) Impedance spectra and (C and D) frequency-dependent capacitance obtained under open-circuit conditions and under white light illumination for (A and C) fresh and (B and D) degraded PSCs. The illumination intensity was fixed in a way such that a photopotential close to the 1-sun V_{OC} is generated (Table S1†). In particular, the applied potentials for the fresh Spiro and P3HT-based devices were 980 mV and 870 mV, respectively, whereas for all degraded devices the applied potential was 850 mV.

devices. This feature could explain the non-symmetric shape of the HF peak in the impedance frequency plots that was found for the degraded PSCs (Fig. S4†). The non-symmetric shape suggests that the time constant of a process previously hidden under the HF semicircle after degradation now becomes resolved or, alternatively, the appearance of a new capacitive process. The general response of the frequency-dependent capacitance for the fresh and degraded devices is shown in Fig. 4C and D, respectively. According to the literature,[49,52,54,55] each plateau is related to a certain specific polarization process. In particular, the LF plateau was attributed to the accumulation of majority carriers at the TiO_2/perovskite interface, which seems to be related to the characteristic hysteretic behavior found in PSCs.[55,56] On the other hand, the HF plateau was associated with the dielectric polarization of the perovskite in the bulk. In accordance with the different thicknesses of the perovskite layers (d) (Fig. S5†) and the expression for the bulk capacitance $C = A\varepsilon/d$, higher HF capacitance values were found for MAI-based devices. Focusing on the effect of the moisture exposure, although the capacitance values observed for HF and LF plateaus are in the same range ($\approx 10^{-7}$ F and $\approx 10^{-2}$ F, respectively) for the fresh and degraded devices, the fact is that a new polarization process in the range of $\approx 10^{-6}$ to 10^{-5} F was found at mid frequencies after moisture exposure. This effect seems to be more pronounced for P3HT-based devices.

A similar behavior has previously been reported for PSCs with less efficient external contacts. In particular, impedance spectra and frequency-dependent capacitance plots were characterized by the presence of an additional MF component when TiO_2 and Nb_2O_5 were employed as the electron selective layer (ESL) in aged devices.[49] Guerrero and coworkers assigned this characteristic feature to the charge accumulation at the ESL/perovskite interface due to the low charge extraction efficiency of these selective contacts. Additionally, an interfacial recombination enhancement was suggested as a consequence of this charge accumulation process. Nevertheless, it should be noted that this charge separation/extraction process is determined not only by the ESL, but also by the perovskite itself and the material used as the HSL. As reported, the interfacial interactions between the selective contacts and the perovskite layer affect the energetic barriers that determine the charge separation/extraction processes.[55,57–60] Considering that the devices are characterized by the same ESL, the MF component could be associated with an interfacial charge accumulation process due to the perovskite composition and the material employed as the HSL which can determine the charge extraction not only at the ESL/perovskite interface, but also at the perovskite/HSL interface. This interpretation could explain the difference found for Spiro and P3HT-based devices (Fig. 4 and S4†).

To cast light on the origin of this new feature appearing at mid frequencies after moisture exposure, impedance spectroscopy was performed using two different illumination wavelengths to modify the charge generation profile inside the perovskite layer. Bearing in mind the absorption spectra widely reported in the literature and taking into account the Beer–Lambert law, a different spatial penetration of the optical excitation inside the perovskite layer is expected for blue and red illumination. The photogenerated charge would show a concentration gradient governed by the absorption coefficient.[37] In particular, a higher concentration of photogenerated charge would be expected at the ESL/perovskite interface than at the perovskite/HSL one under blue illumination. In contrast, the profile of photogenerated charge is more uniform under red illumination. A similar methodology was previously used to analyze the recombination processes.[38]

Fig. 5 shows the capacitance–frequency response under blue and red illumination for MAI/Spiro, MAI/P3HT and MIX/Spiro devices before and after moisture exposure. In line with Fig. 4C and D, the capacitance–frequency response obtained under blue and red illumination was characterized by the presence of a characteristic polarization process appearing at mid frequencies (10^4 to 10^2 Hz) which overlaps with the HF plateau (bulk capacitance) after moisture exposure. For the fresh devices the capacitance–frequency response was not affected by the electron–hole generation profile produced as a result of the different optical excitation wavelengths employed

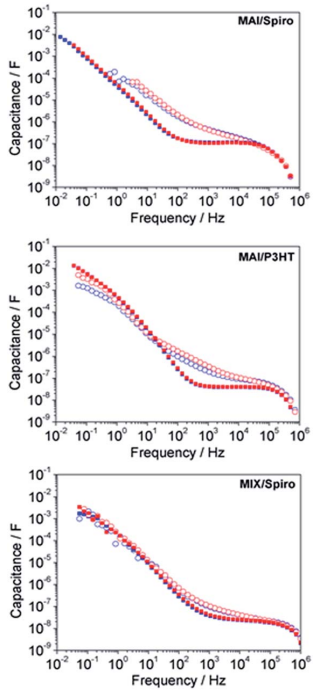

Fig. 5 Frequency-dependent capacitance obtained under open-circuit conditions and under illumination for (squares) fresh and (circles) degraded MAI/Spiro, MAI/P3HT and MIX/Spiro devices using the two excitation wavelengths of (blue) $\lambda_{blue} = 465$ nm and (red) $\lambda_{red} = 635$ nm.

during the impedance spectroscopy measurement. A similar behavior was found for the degraded MAI/Spiro and MIX/Spiro devices. In contrast, a significant difference was found at mid frequencies for the degraded MAI/P3HT devices when the electron–hole generation profile was modified. In particular, higher MF capacitance values were found when the availability of the photogenerated charges was higher at the perovskite/HSL interface (red illumination) with respect to when charge was photogenerated preferentially in the vicinity of the ESL (blue illumination). This behavior is also brought to light in the Nyquist plots by the presence of the MF semicircle for the degraded MAI/P3HT devices under red illumination (Fig. S6†). Therefore, a more important interfacial charge accumulation process seems to take place after moisture exposure when P3HT was used as the HSL and consequently, a poorer hole extraction is expected at the perovskite/P3HT interface with respect to perovskite/Spiro. This possible interpretation could explain not only the distorted HF semicircle and/or the apparent MF semicircle found in the Nyquist plot of impedance response for the degraded devices, respectively (Fig. 4B and S6†), but also the more remarkable MF capacitive process observed for P3HT-based devices (Fig. 4D). On the other hand, as mentioned above, the energetic barriers that determine the charge extraction/separation process also depend on the perovskite material. As shown in Fig. 5, when the Spiro was used as the HSL the capacitance–frequency response obtained under blue and red illumination shows the same behavior before and after moisture exposure. Similar results were found for MAI/Spiro devices (Fig. 5). Nevertheless, this MF capacitive process seems to be less visible after moisture exposure which suggests a better electron and hole extraction at both interfaces even after moisture exposure. This robustness of the electronic properties of the Spiro contact explains the normally better photocurrents obtained in devices when such a material was used.

In order to understand the differences found in the Nyquist plot of the impedance spectra at different optical excitation wavelengths for the degraded devices (Fig. S6†), the recombination (HF) kinetics were investigated. Fig. 6 shows the electron recombination resistance extracted by fitting the impedance response under blue and red illumination for the fresh and degraded MAI/Spiro devices to a simple -R_{Ser}-(R_{LF},CPE_1)-(R_{HF},-CPE_2)- equivalent circuit. To be sure about the fitting, the time constant (τ) was estimated as (1) $\tau = R_{rec} \times C_b$, where R_{rec} is the electron (HF) recombination resistance and C_b is the bulk capacitance; and (2) $\tau = 1/2\pi f$, where f is the frequency peak maximum directly extracted from impedance frequency plots. The same behavior was obtained for both fresh and degraded devices (Fig. S7†). On the other hand it is important to note that although degraded perovskites absorb much less light[18] and hence produce a comparatively lower potential, the comparison in Fig. 6 and the inset in Fig. 7 is done at the same value of the photogenerated potential so that this difference in absorption is implicitly taken into account.

Specifically, the recombination resistance shows the same behavior for the fresh devices regardless of the electron–hole generation profile. In contrast, a minor difference was found after moisture exposure when the optical excitation wavelength was changed. For the degraded devices, lower values of electron recombination resistance were found when the red illumination was used for optical excitation. In other words, the photogenerated charge at the perovskite/HSL interface seems to

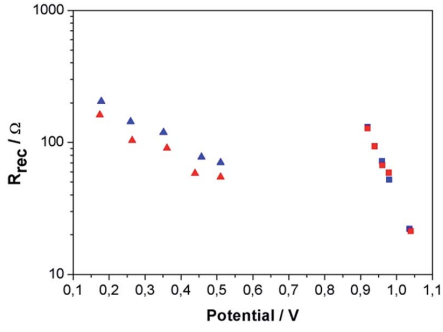

Fig. 6 Recombination (HF) resistance *versus* open-circuit potential as extracted from fittings of the impedance spectra using the two excitation wavelengths of (blue) $\lambda_{blue} = 465$ nm and (red) $\lambda_{red} = 635$ nm for (squares) fresh and (triangles) degraded MAI/Spiro devices.

View Article Online
Journal of Materials Chemistry A Paper

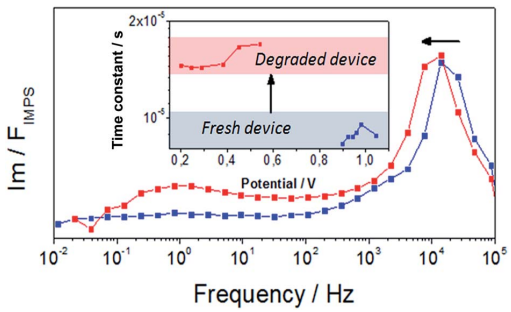

Fig. 7 IMPS frequency plot of the imaginary part for the MAI/Spiro device (blue) before and (red) after moisture exposure obtained at a photopotential close to the 1-sun V_{OC} under white light illumination. The inset shows the time constants extracted as $\tau = 1/2\pi f$, where f is the frequency peak maximum directly extracted from the IMPS frequency plots.

recombine more strongly than the photogenerated charge at the ESL/perovskite interface for a degraded device. On the other hand, a remarkable change of the slope of the recombination resistance for both optical excitations was observed with respect to fresh devices. Similar results were obtained for the different devices when a white LED was employed as the illumination source before and after moisture exposure (Fig. S8†). This observation suggests that the charge that has been mainly photogenerated at the ESL/perovskite and perovskite/HSL interfaces is subjected to different recombination mechanisms after moisture exposure. As was previously reported by us,[38] the results obtained for fresh devices suggest that the main recombination process is mediated *via* a trap-limited mechanism in the bulk of the perovskite.[61–65] However, surface recombination could be more important as a consequence of the perovskite degradation by moisture.[45,66,67] Therefore, the increase of this surface-mediated recombination seems to be intimately related to the larger interfacial charge accumulation described (Fig. 5). Similar results were expected for the rest of the devices studied in this work as revealed by the Nyquist and impedance frequency plots, which showed the same behavior under both optical excitations (Fig. S6 and S9,† respectively).

This interpretation seems to be in line with the conclusions previously reported by A. Leguy and coworkers.[45] In particular, they related the efficiency drop after moisture exposure to the isolation of the perovskite grains which would reduce the charge transport leading to an increased recombination at the grain interfaces. In other words, the grain insulating effect could limit the charge transport and improve the charge recombination giving rise to shorter charge diffusion lengths.[66,67] In order to consolidate this assumption, IMPS was performed to provide information on the different charge transport processes (Fig. 7).

As shown in Fig. 7, the IMPS frequency plot shows two well differentiated peaks with respect to the frequency scale which have previously been related to different charge transport processes characterized by different time constants.[50,56,68] In particular, the HF peak ($\approx 10^4$ Hz) was associated with the electron transport inside the perovskite layer, whereas the LF peak (≈ 1 Hz) was attributed to ionic motion. In addition, a peak at mid frequencies was also found and related to the electron transport process in the mesoporous TiO_2 matrix.[56,68] Nevertheless, this MF peak was not resolved in our case (Fig. 7). Considering the HF peak only and the associated time constants ($\tau = 1/2\pi f$) shown in the inset of Fig. 7, a lower charge diffusion coefficient (D_n) is expected for the degraded devices, since the HF peak appears at lower frequencies ($D_n = L_d^2/\tau_{HF}$, where L_d is the thickness of the perovskite layer and τ_{HF} is the HF time constant).[69] A smaller diffusion coefficient gives rise to shorter charge diffusion lengths, in line with the faster recombination observed in the degraded samples.

Conclusions

We have investigated the effect of the moisture-induced degradation of perovskite solar cells using a combination of structural characterization (SEM, EDS, XRD and XPS) and small-perturbation optoelectronic (impedance and intensity modulated photocurrent spectroscopy) techniques. We studied the influence of the perovskite composition and HSL employed on the device stability. In particular, our results reveal a lower degradation rate for perovskite solar cells based on $(Cs_{0.05}(MAPbBr_3)_{0.15}(FAPbI_3)_{0.85})$ as the active layer and P3HT as the HSL. On the other hand, the effect of the moisture-induced degradation on the electronic processes that determine the photovoltaic performance of perovskite solar cells was also investigated. Regardless of the device configuration, the charge recombination is governed by the bulk of the perovskite layer *via* a trap-limited mechanism. However, the moisture-induced degradation modifies the charge recombination mechanism. The additional mid-frequency component recorded in both Nyquist and frequency plots after moisture exposure suggests an interfacial charge accumulation. This charge accumulation process can accelerate the charge recombination rate due to a greater contribution of a surface-mediated recombination route. As a consequence of the moisture-induced degradation, a slower electron transport in perovskite layers was also observed, which can be traced back to the formation of more grain boundaries.

Conflict of interest

The authors declare no competing financial interest.

Acknowledgements

We thank Junta de Andalucía for financial support *via* grant FQM 1851 and FQM 2310. We thank the Ministerio de Economía y Competitividad of Spain (MAT2013-47192-C3-3-R and MAT2016-76892-C3-2-R) and the EU through the Cohesion Fund and FEDER programs (MAT2013-42900-P and MAT2016-79866-R) for financial support and Red de Excelencia "Emerging photovoltaic Technologies". We also thank the Servicio de Microscopía Electrónica (Universidad Pablo de Olavide) and

View Article Online
Paper Journal of Materials Chemistry A

Prof. Juan P. Espinos and the service for Surfaces Photoemission Analysis in the Materials Science Institute of Seville for the XPS characterization of the samples. SA and LC are thankful for the "Thinface" project from the European Union Seventh Framework Programme, under grant agreement no. 607232, for financial support.

References

1 G. Xing, N. Mathews, S. Sun, S. S. Lim, Y. M. Lam, M. Grätzel, S. Mhaisalkar and T. C. Sum, Long-Range Balanced Electron- and Hole-Transport Lengths in Organic–Inorganic $CH_3NH_3PbI_3$, *Science*, 2013, **342**(6156), 344–347.

2 S. D. Stranks, G. E. Eperon, G. Grancini, C. Menelaou, M. J. P. Alcocer, T. Leijtens, L. M. Herz, A. Petrozza and H. J. Snaith, Electron-Hole Diffusion Lengths Exceeding 1 Micrometer in an Organometal Trihalide Perovskite Absorber, *Science*, 2013, **342**(6156), 341–344.

3 W. Tress, N. Marinova, O. Inganäs, M. K. Nazeeruddin, S. M. Zakeeruddin and M. Graetzel, Predicting the Open-Circuit Voltage of $CH_3NH_3PbI_3$ Perovskite Solar Cells Using Electroluminescence and Photovoltaic Quantum Efficiency Spectra: The Role of Radiative and Non-Radiative Recombination, *Adv. Energy Mater.*, 2015, **5**(3), 1400812.

4 N. Pellet, P. Gao, G. Gregori, T.-Y. Yang, M. K. Nazeeruddin, J. Maier and M. Grätzel, Mixed-Organic-Cation Perovskite Photovoltaics for Enhanced Solar-Light Harvesting, *Angew. Chem., Int. Ed.*, 2014, **53**(12), 3151–3157.

5 Y. Ogomi, A. Morita, S. Tsukamoto, T. Saitho, N. Fujikawa, Q. Shen, T. Toyoda, K. Yoshino, S. S. Pandey, T. Ma, *et al.* $CH_3NH_3SnxPb_{(1-x)}I_3$ Perovskite Solar Cells Covering up to 1060 Nm, *J. Phys. Chem. Lett.*, 2014, **5**(6), 1004–1011.

6 A. Kojima, K. Teshima, Y. Shirai and T. Miyasaka, Novel Photoelectrochemical Cell with Mesoscopic Electrodes Sensitized by Lead–Halide Compounds (5), *Meet. Abstr.*, 2007, **MA2007–02**(8), 352.

7 Photovoltaic Research | NREL https://www.nrel.gov/pv/, accessed Feb 10, 2017.

8 J. M. Ball, M. M. Lee, A. Hey and H. J. Snaith, Temperature Processed Meso Superstructured to Thin-Film Perovskite Solar Cells, *Energy Environ. Sci.*, 2013, **6**(6), 1739–1743.

9 H. Zhou, Q. Chen, G. Li, S. Luo, T. Song, H.-S. Duan, Z. Hong, J. You, Y. Liu and Y. Yang, Interface Engineering of Highly Efficient Perovskite Solar Cells, *Science*, 2014, **345**(6196), 542–546.

10 J. Burschka, N. Pellet, S.-J. Moon, R. Humphry-Baker, P. Gao, M. K. Nazeeruddin and M. Grätzel, Sequential Deposition as a Route to High-Performance Perovskite-Sensitized Solar Cells, *Nature*, 2013, **499**(7458), 316–319.

11 M. Liu, M. B. Johnston and H. J. Snaith, Efficient Planar Heterojunction Perovskite Solar Cells by Vapour Deposition, *Nature*, 2013, **501**(7467), 395–398.

12 N. J. Jeon, J. H. Noh, Y. C. Kim, W. S. Yang, S. Ryu and S. I. Seok, Solvent Engineering for High-Performance Inorganic–organic Hybrid Perovskite Solar Cells, *Nat. Mater.*, 2014, **13**(9), 897–903.

13 Y. Reyna, M. Salado, S. Kazim, A. Pérez-Tomas, S. Ahmad and M. Lira-Cantu, Performance and Stability of Mixed $FAPbI_3(0.85)MAPbBr_3(0.15)$ Halide Perovskite Solar Cells under Outdoor Conditions and the Effect of Low Light Irradiation, *Nano Energy*, 2016, **30**, 570–579.

14 B. Li, Y. Li, C. Zheng, D. Gao and W. Huang, Advancements in the Stability of Perovskite Solar Cells: Degradation Mechanisms and Improvement Approaches, *RSC Adv.*, 2016, **6**(44), 38079–38091.

15 Z. Wang, Z. Shi, T. Li, Y. Chen and W. Huang, Stability of Perovskite Solar Cells: A Prospective on the Substitution of the A Cation and X Anion, *Angew. Chem., Int. Ed.*, 2017, **56**(5), 1190–1212.

16 T. A. Berhe, W.-N. Su, C.-H. Chen, C.-J. Pan, J.-H. Cheng, H.-M. Chen, M.-C. Tsai, L.-Y. Chen, A. A. Dubale and B.-J. Hwang, Organometal Halide Perovskite Solar Cells: Degradation and Stability, *Energy Environ. Sci.*, 2016, **9**(2), 323–356.

17 G. Niu, W. Li, F. Meng, L. Wang, H. Dong and Y. Qiu, Study on the Stability of $CH_3NH_3PbI_3$ Films and the Effect of Post-Modification by Aluminum Oxide in All-Solid-State Hybrid Solar Cells, *J. Mater. Chem. A*, 2014, **2**(3), 705–710.

18 J. Yang, B. D. Siempelkamp, D. Liu and T. L. Kelly, Investigation of $CH_3NH_3PbI_3$ Degradation Rates and Mechanisms in Controlled Humidity Environments Using *in situ* Techniques, *ACS Nano*, 2015, **9**(2), 1955–1963.

19 D. Bryant, N. Aristidou, S. Pont, I. Sanchez-Molina, T. Chotchunangatchaval, S. Wheeler, J. R. Durrant and S. A. Haque, Light and Oxygen Induced Degradation Limits the Operational Stability of Methylammonium Lead Triiodide Perovskite Solar Cells, *Energy Environ. Sci.*, 2016, **9**(5), 1655–1660.

20 S. Wang, Y. Jiang, E. J. Juarez-Perez, L. K. Ono and Y. Qi, Accelerated Degradation of Methylammonium Lead Iodide Perovskites Induced by Exposure to Iodine Vapour, *Nat. Energy*, 2016, **2**, 16195.

21 S. M. Kang, N. Ahn, J.-W. Lee, M. Choi and N.-G. Park, Water-Repellent Perovskite Solar Cell, *J. Mater. Chem. A*, 2014, **2**(47), 20017–20021.

22 S. Guarnera, A. Abate, W. Zhang, J. M. Foster, G. Richardson, A. Petrozza and H. J. Snaith, Improving the Long-Term Stability of Perovskite Solar Cells with a Porous Al_2O_3 Buffer Layer, *J. Phys. Chem. Lett.*, 2015, **6**(3), 432–437.

23 L. Zheng, Y.-H. Chung, Y. Ma, L. Zhang, L. Xiao, Z. Chen, S. Wang, B. Qu and Q. Gong, A Hydrophobic Hole Transporting Oligothiophene for Planar Perovskite Solar Cells with Improved Stability, *Chem. Commun.*, 2014, **50**(76), 11196–11199.

24 I. Hwang, I. Jeong, J. Lee, M. J. Ko and K. Yong, Enhancing Stability of Perovskite Solar Cells to Moisture by the Facile Hydrophobic Passivation, *ACS Appl. Mater. Interfaces*, 2015, **7**(31), 17330–17336.

25 F. Bella, G. Griffini, J.-P. Correa-Baena, G. Saracco, M. Grätzel, A. Hagfeldt, S. Turri and C. Gerbaldi, Improving Efficiency and Stability of Perovskite Solar Cells with Photocurable Fluoropolymers, *Science*, 2016, **354**(6309), 203–206.

26 Y. S. Kwon, J. Lim, H.-J. Yun, Y.-H. Kim and T. A. Park, Diketopyrrolopyrrole-Containing Hole Transporting Conjugated Polymer for Use in Efficient Stable Organic–Inorganic Hybrid Solar Cells Based on a Perovskite, *Energy Environ. Sci.*, 2014, **7**(4), 1454–1460.

27 M. Salado, F. J. Ramos, V. M. Manzanares, P. Gao, M. K. Nazeeruddin, P. J. Dyson and S. Ahmad, Extending the Lifetime of Perovskite Solar Cells Using a Perfluorinated Dopant, *ChemSusChem*, 2016, **9**(18), 2708–2714.

28 M. A. Green, A. Ho-Baillie and H. J. Snaith, The Emergence of Perovskite Solar Cells, *Nat. Photonics*, 2014, **8**(7), 506–514.

29 A. Amat, E. Mosconi, E. Ronca, C. Quarti, P. Umari, M. K. Nazeeruddin, M. Grätzel and F. De Angelis, Cation-Induced Band-Gap Tuning in Organohalide Perovskites: Interplay of Spin–Orbit Coupling and Octahedra Tilting, *Nano Lett.*, 2014, **14**(6), 3608–3616.

30 J. H. Noh, S. H. Im, J. H. Heo, T. N. Mandal and S. I. Seok, Chemical Management for Colorful, Efficient, and Stable Inorganic–Organic Hybrid Nanostructured Solar Cells, *Nano Lett.*, 2013, **13**(4), 1764–1769.

31 R. K. Misra, S. Aharon, B. Li, D. Mogilyansky, I. Visoly-Fisher, L. Etgar and E. A. Katz, Temperature- and Component-Dependent Degradation of Perovskite Photovoltaic Materials under Concentrated Sunlight, *J. Phys. Chem. Lett.*, 2015, **6**(3), 326–330.

32 A. Poglitsch and D. Weber, Dynamic Disorder in Methylammoniumtrihalogenoplumbates(II) Observed by Millimeter-wave Spectroscopy, *J. Chem. Phys.*, 1987, **87**(11), 6373–6378.

33 M. L. Petrus, Y. Hu, D. Moia, P. Calado, A. M. A. Leguy, P. R. F. Barnes and P. Docampo, The Influence of Water Vapor on the Stability and Processing of Hybrid Perovskite Solar Cells Made from Non-Stoichiometric Precursor Mixtures, *ChemSusChem*, 2016, **9**(18), 2699–2707.

34 Y. Zhao and K. Zhu, Organic-Inorganic Hybrid Lead Halide Perovskites for Optoelectronic and Electronic Applications, *Chem. Soc. Rev.*, 2016, **45**(3), 655–689.

35 R. J. Sutton, G. E. Eperon, L. Miranda, E. S. Parrott, B. A. Kamino, J. B. Patel, M. T. Hörantner, M. B. Johnston, A. A. Haghighirad, D. T. Moore and H. J. Snaith, Bandgap-Tunable Cesium Lead Halide Perovskites with High Thermal Stability for Efficient Solar Cells, *Adv. Energy Mater.*, 2016, **6**(8), 1502458.

36 M. Saliba, T. Matsui, J.-Y. Seo, K. Domanski, J.-P. Correa-Baena, M. K. Nazeeruddin, S. M. Zakeeruddin, W. Tress, A. Abate, A. Hagfeldt, *et al.* Cesium-Containing Triple Cation Perovskite Solar Cells: Improved Stability, Reproducibility and High Efficiency, *Energy Environ. Sci.*, 2016, **9**(6), 1989–1997.

37 Y. Yang, M. Yang, D. T. Moore, Y. Yan, E. M. Miller, K. Zhu and M. C. Beard, Top and Bottom Surfaces Limit Carrier Lifetime in Lead Iodide Perovskite Films, *Nat. Energy*, 2017, **2**, 16207.

38 L. Contreras Bernal, M. Salado, A. Todinova, L. Calio, S. Ahmad, J. Idígoras and J. A. Anta, Origin and Whereabouts of Recombination in Perovskite Solar Cells, *J. Phys. Chem. C*, 2017, **121**(18), 9705–9713.

39 D. Bi, L. Yang, G. Boschloo, A. Hagfeldt and E. M. J. Johansson, Effect of Different Hole Transport Materials on Recombination in $CH_3NH_3PbI_3$ Perovskite-Sensitized Mesoscopic Solar Cells, *J. Phys. Chem. Lett.*, 2013, **4**(9), 1532–1536.

40 N. J. Jeon, J. H. Noh, W. S. Yang, Y. C. Kim, S. Ryu, J. Seo and S. I. Seok, Compositional Engineering of Perovskite Materials for High-Performance Solar Cells, *Nature*, 2015, **517**(7535), 476–480.

41 M. Salado, J. Idigoras, L. Calio, S. Kazim, M. K. Nazeeruddin, J. A. Anta and S. Ahmad, Interface Play between Perovskite and Hole Selective Layer on the Performance and Stability of Perovskite Solar Cells, *ACS Appl. Mater. Interfaces*, 2016, **8**(50), 34414–34421.

42 M. Deepa, M. Salado, L. Calio, S. Kazim, S. M. Shivaprasad and S. Ahmad, Cesium Power: Low Cs^+ Levels Impart Stability to Perovskite Solar Cells, *Phys. Chem. Chem. Phys.*, 2017, **19**(5), 4069–4077.

43 N. Aristidou, I. Sanchez-Molina, T. Chotchuangchutchaval, M. Brown, L. Martinez, T. Rath and S. A. Haque, The Role of Oxygen in the Degradation of Methylammonium Lead Trihalide Perovskite Photoactive Layers, *Angew. Chem., Int. Ed.*, 2015, **54**(28), 8208–8212.

44 J. Idigoras, A. Todinova, J. R. Sanchez-Valencia, A. Barranco, A. Borras and J. A. Anta, The Interaction between Hybrid Organic–Inorganic Halide Perovskite and Selective Contacts in Perovskite Solar Cells: An Infrared Spectroscopy Study, *Phys. Chem. Chem. Phys.*, 2016, **18**(19), 13583–13590.

45 A. M. A. Leguy, Y. Hu, M. Campoy-Quiles, M. I. Alonso, O. J. Weber, P. Azarhoosh, M. van Schilfgaarde, M. T. Weller, T. Bein, J. Nelson, *et al.* Reversible Hydration of $CH_3NH_3PbI_3$ in Films, Single Crystals, and Solar Cells, *Chem. Mater.*, 2015, **27**(9), 3397–3407.

46 X. Guo, C. McCleese, C. Kolodziej, A. C. S. Samia, Y. Zhao and C. Burda, Identification and Characterization of the Intermediate Phase in Hybrid Organic–Inorganic $MAPbI_3$ Perovskite, *Dalton Trans.*, 2016, **45**(9), 3806–3813.

47 X. Guo, C. McCleese, W.-C. Lin and C. Burda, Curing of Degraded $MAPbI_3$ Perovskite Films, *RSC Adv.*, 2016, **6**(65), 60620–60625.

48 J. Carrillo, A. Guerrero, S. Rahimnejad, O. Almora, I. Zarazua, E. Mas-Marza, J. Bisquert and G. Garcia-Belmonte, Ionic Reactivity at Contacts and Aging of Methylammonium Lead Triiodide Perovskite Solar Cells, *Adv. Energy Mater.*, 2016, **6**(9), 1502246.

49 A. Guerrero, G. Garcia-Belmonte, I. Mora-Sero, J. Bisquert, Y. S. Kang, T. J. Jacobsson, J.-P. Correa-Baena and A. Hagfeldt, Properties of Contact and Bulk Impedances in Hybrid Lead Halide Perovskite Solar Cells Including Inductive Loop Elements, *J. Phys. Chem. C*, 2016, **120**(15), 8023–8032.

50 E. Guillén, F. J. Ramos, J. A. Anta and S. Ahmad, Elucidating Transport-Recombination Mechanisms in Perovskite Solar

Cells by Small-Perturbation Techniques, *J. Phys. Chem. C*, 2014, **118**(40), 22913–22922.

51 A. Todinova, J. Idígoras, M. Salado, S. Kazim and J. A. Anta, Universal Features of Electron Dynamics in Solar Cells with TiO_2 Contact: From Dye Solar Cells to Perovskite Solar Cells, *J. Phys. Chem. Lett.*, 2015, **6**(19), 3923–3930.

52 M. Bag, L. A. Renna, R. Y. Adhikari, S. Karak, F. Liu, P. M. Lahti, T. P. Russell, M. T. Tuominen and D. Venkataraman, Kinetics of Ion Transport in Perovskite Active Layers and Its Implications for Active Layer Stability, *J. Am. Chem. Soc.*, 2015, **137**(40), 13130–13137.

53 A. Dualeh, T. Moehl, N. Tétreault, J. Teuscher, P. Gao, M. K. Nazeeruddin and M. Grätzel, Impedance Spectroscopic Analysis of Lead Iodide Perovskite-Sensitized Solid-State Solar Cells, *ACS Nano*, 2014, **8**(1), 362–373.

54 H.-S. Kim, I.-H. Jang, N. Ahn, M. Choi, A. Guerrero, J. Bisquert and N.-G. Park, Control of *I–V* Hysteresis in $CH_3NH_3PbI_3$ Perovskite Solar Cell, *J. Phys. Chem. Lett.*, 2015, **6**(22), 4633–4639.

55 I. Zarazua, J. Bisquert and G. Garcia-Belmonte, Light-Induced Space-Charge Accumulation Zone as Photovoltaic Mechanism in Perovskite Solar Cells, *J. Phys. Chem. Lett.*, 2016, **7**(3), 525–528.

56 L. Contreras, J. Idigoras, A. Todinova, M. Salado, S. Kazim, S. Ahmad and J. A. Anta, Specific Cation Interactions as the Cause of Slow Dynamics and Hysteresis in Dye and Perovskite Solar Cells: A Small-Perturbation Study, *Phys. Chem. Chem. Phys.*, 2016, **18**(45), 31033–31042.

57 S. N. Habisreutinger, T. Leijtens, G. E. Eperon, S. D. Stranks, R. J. Nicholas and H. J. Snaith, Enhanced Hole Extraction in Perovskite Solar Cells Through Carbon Nanotubes, *J. Phys. Chem. Lett.*, 2014, **5**(23), 4207–4212.

58 J. P. Correa Baena, L. Steier, W. Tress, M. Saliba, S. Neutzner, T. Matsui, F. Giordano, T. J. Jacobsson, A. R. Srimath Kandada, S. M. Zakeeruddin, *et al.* Highly Efficient Planar Perovskite Solar Cells through Band Alignment Engineering, *Energy Environ. Sci.*, 2015, **8**(10), 2928–2934.

59 K. Pydzińska, J. Karolczak, I. Kosta, R. Tena-Zaera, A. Todinova, J. Idígoras, J. A. Anta and M. Ziółek, Determination of Interfacial Charge-Transfer Rate Constants in Perovskite Solar Cells, *ChemSusChem*, 2016, **9**(13), 1647–1659.

60 Y. Zou and R. J. Holmes, Temperature-Dependent Bias Poling and Hysteresis in Planar Organo-Metal Halide Perovskite Photovoltaic Cells, *Adv. Energy Mater.*, 2016, **6**(7), 1501994.

61 C. Wehrenfennig, M. Liu, H. J. Snaith, M. B. Johnston and L. M. Herz, Charge-Carrier Dynamics in Vapour-Deposited Films of the Organolead Halide Perovskite $CH_3NH_3PbI_{3-x}Cl_x$, *Energy Environ. Sci.*, 2014, **7**(7), 2269–2275.

62 J. S. Manser and P. V. Kamat, Band Filling with Free Charge Carriers in Organometal Halide Perovskites, *Nat. Photonics*, 2014, **8**(9), 737–743.

63 Y. Yang, M. Yang, Z. Li, R. Crisp, K. Zhu and M. C. Beard, Comparison of Recombination Dynamics in $CH_3NH_3PbBr_3$ and $CH_3NH_3PbI_3$ Perovskite Films: Influence of Exciton Binding Energy, *J. Phys. Chem. Lett.*, 2015, **6**(23), 4688–4692.

64 W. Rehman, R. L. Milot, G. E. Eperon, C. Wehrenfennig, J. L. Boland, H. J. Snaith, M. B. Johnston and L. M. Herz, Charge-Carrier Dynamics and Mobilities in Formamidinium Lead Mixed-Halide Perovskites, *Adv. Mater.*, 2015, **27**(48), 7938–7944.

65 J.-P. Correa-Baena, S.-H. Turren-Cruz, W. Tress, A. Hagfeldt, C. Aranda, L. Shooshtari, J. Bisquert and A. Guerrero, Changes from Bulk to Surface Recombination Mechanisms between Pristine and Cycled Perovskite Solar Cells, *ACS Energy Lett.*, 2017, 681–688.

66 D. Li, S. A. Bretschneider, V. W. Bergmann, I. M. Hermes, J. Mars, A. Klasen, H. Lu, W. Tremel, M. Mezger, H.-J. Butt, *et al.* Humidity-Induced Grain Boundaries in $MAPbI_3$ Perovskite Films, *J. Phys. Chem. C*, 2016, **120**(12), 6363–6368.

67 W. Nie, H. Tsai, R. Asadpour, J.-C. Blancon, A. J. Neukirch, G. Gupta, J. J. Crochet, M. Chhowalla, S. Tretiak, M. A. Alam, *et al.* High-Efficiency Solution-Processed Perovskite Solar Cells with Millimeter-Scale Grains, *Science*, 2015, **347**(6221), 522.

68 J. P. Correa-Baena, M. Anaya, G. Lozano, W. Tress, K. Domanski, M. Saliba, T. Matsui, T. J. Jacobsson, M. E. Calvo, A. Abate, *et al.* Unbroken Perovskite: Interplay of Morphology, Electro-Optical Properties, and Ionic Movement, *Adv. Mater.*, 2016, **28**(25), 5031–5037.

69 F. Fabregat-Santiago, G. Garcia-Belmonte, I. Mora-Seró and J. Bisquert, Characterization of Nanostructured Hybrid and Organic Solar Cells by Impedance Spectroscopy, *Phys. Chem. Chem. Phys.*, 2011, **13**(20), 9083–9118.

Extending the Lifetime of Perovskite Solar Cells using a Perfluorinated Dopant

Manuel Salado,[a] F. Javier Ramos,[a] Valentin M. Manzanares,[b] Peng Gao,[c] Mohammad Khaja Nazeeruddin,[c] Paul J. Dyson,[b] and Shahzada Ahmad*[a]

The principle limitation of perovskite solar cells is related to their instability and, hence, their limited lifetime. Herein, we employ an imidazolium iodide dopant, 1-methyl-3-(1H,1H,2H,2H-nonafluorohexyl)-imidazolium iodide, containing a perfluorous appendage, which leads to prolonged (unencapsulated, under Ar atmosphere) device activities exceeding 100 days without compromising the power conversion efficiency and other photovoltaic parameters. The extended lifetime of the device can be attributed, at least in part, to the hydrophobic nature of the imidazolium iodide salt. The functionalization of the perovskite material was found to have negligible influence on the perovskite crystal structure.

Introduction

The use of hybrid organic–inorganic-based perovskites as light harvesters in a liquid electrolyte- based solar cell was first reported in 2009.[1] Subsequently, the use of a p-type semiconductor as the hole-transporting layer ignited the interest of the photovoltaic (PV) community and power conversion efficiencies (PCEs) rapidly improved from 3.8% to over 22% within a few years.[1–5] Perovskite PV efficiencies are now on a par with other mature thin-film technologies.[6] Currently, the most developed perovskite material for solar cell applications is methylammonium lead triiodide ($MAPbI_3$). $MAPbI_3$ can be readily produced using solution-processing or sublimation techniques, rendering polycrystalline films with a direct band gap of 1.57 eV, a small exciton binding energy, and extremely long carrier diffusion lengths (>1 μm) with high electron–hole mobility.[7–10] Unfortunately, despite these attractive properties, chemical stability remains a major drawback preventing the immediate widespread application of such first-generation $MAPbI_3$ or mixed perovskite materials.[11]

Despite considerable and successful research efforts to increase the PCE, relatively little progress has been made towards increasing the stability of these materials.[12–15] Different strategies, such as crosslinking,[16] doping,[17] shielding with molecularly designed materials, or enveloping the perovskite molecular structure in a foreign chemical environment,[18] have been reported for improved humidity and UV-induced degradation. However, increased stability generally results in reduced PCEs. The problem of stability was partially overcome with the use of mixed perovskites,[19] but these materials still cannot meet commercial requirements.

The bottleneck of perovskite solar cells is their sensitivity towards environmental humidity, heat and UV light, which may greatly influence their reliability under real operating conditions. Addressing these problems is of paramount importance. Perovskite materials are salts and are sensitive to humidity. Increasing the tolerance limit for humidity will help to minimize humidity-induced instability. Recently, the partial substitution of I^- with a pseudohalide ion (SCN^-) was reported as an alternative approach to increase the stability of first-generation $MAPbI_3$-based devices.[19] The incorporation of SCN^-, which has a similar ionic radius to I^-, to form $MAPbI_{3-x}(SCN)_x$ was reported to result in larger crystal sizes, while minimizing trap sites, with a PCE of 11% in a planar device configuration.[21] It was found that 5% SCN^- loading was the optimum in the tested range of 1–10%, with the resulting perovskites displaying higher stability.[22] Subsequently, it was found that incorporation of SCN^- as a dopant opens the fundamental band gap versus $MAPbI_3$ by 8 meV and was much more stable after 4 h in air with 95% humidity.[23] However, the device PCE was limited to 8.3%.

Another approach for improved perovskite stability that was recently reported involves the reaction of MAI and $Pb(SCN)_2$ to afford $(MA)_2Pb(SCN)_2I_2$.[24] The material crystallizes in a layered orthorhombic motif with the space group $Pnm2_1$, in which the Pb^{II} ions are in an octahedral environment coordinated to four

[a] M. Salado, F. J. Ramos, Dr. S. Ahmad
Abengoa Research, Abengoa
C/Energía Solar n° 1, Campus Palmas Altas
41014, Sevilla (Spain)
E-mail: shahzada.ahmad@abengoa.com

[b] Dr. V. M. Manzanares, Prof. P. J. Dyson
Institute of Chemical Sciences and Engineering
Swiss Federal Institute of Technology Lausanne (EPFL)
CH 1015, Lausanne (Switzerland)

[c] Dr. P. Gao, Prof. M. K. Nazeeruddin
Group for Molecular Engineering of Functional Materials
Swiss Federal Institute of Technology Lausanne (EPFL), EPFL Valais Wallis
CH-1951 Sion (Switzerland)

Supporting Information for this article can be found under: http://dx.doi.org/10.1002/cssc.201601030.

This publication is part of a Special Issue focusing on the "Stability of Perovskite Solar Cells & Devices". A link to the issue's Table of Contents will appear here once it is complete.

axial I^- and two apical (or trans) S-bonded SCN^- ions. $(MA)_2Pb(SCN)_2I_2$ has an optical band gap of 1.56 eV, similar to quasi-cubic $MAPbI_3$, but it has a 2D structure.

Fluorinated cation compounds possess a bulky structure and can lead to the formation of 1D or 2D perovskite structures, which by themselves are currently not seen as viable candidates for PV applications. For example, there have been several reports on the application of fluorinated ammonium-based cations for 2D perovskites[25–27] with some fluorinated aromatic ammonium iodides leading to an observed increased photostability.[28,29] Therefore, they may be used as additives to improve the properties of perovskite materials.[30] Fluorinated compounds are known to be hydrophobic and are frequently used as water-proof surface coating materials. Recently, the use of trifluoroethyl ammonium iodide as an additive to improve the stability of $MAPbI_3$ cells was reported.[17] Herein, we report on the use of a fluorinated imidazolium-based dopant that significantly increases the stability of perovskite-based solar cells. The electron-withdrawing character of the fluorinated salt together with its hydrophobicity is believed to be responsible for the observed stability enhancements. These fluorinated imidazolium-based functional additives are easy to prepare in a few synthetic steps using commercial reactants. They induce structural and functional changes to the resultant perovskite, and may act as surfactant to promote and stabilize perovskite intercalation.

Results and Discussion

Figure 1 depicts the structure of the fluorinated imidazolium salt and control compound used to functionalize the perovskite (the former was prepared as described in the Experimental Section). A sequential method was employed for the deposition of $MAPbI_3$, and a solvent engineering based one step process was adopted for mixed-cation mixed-anion $(FAPbI_3)_{0.85}(MAPbBr_3)_{0.15}$ perovskite deposition (Scheme 1). $MAPbI_3$ and the mixed $(FAPbI_3)_{0.85}(MAPbBr_3)_{0.15}$ perovskite were doped with different concentrations of the 1-methyl-3-(1H,1H,2H,2H-nonafluorohexyl)-imidazolium iodide (FIm) or 1-methy-3-butyl-imidazolium iodide (BMIm) and their XRD patterns were recorded (Figures 2 and S1 in the Supporting Information). The perovskite film was deposited onto a glass substrate and measured after annealing the sample.

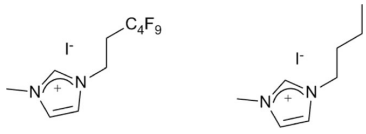

Figure 1. Structures of the dopants used in the perovskite layers: (left) FIm and (right) BMIm.

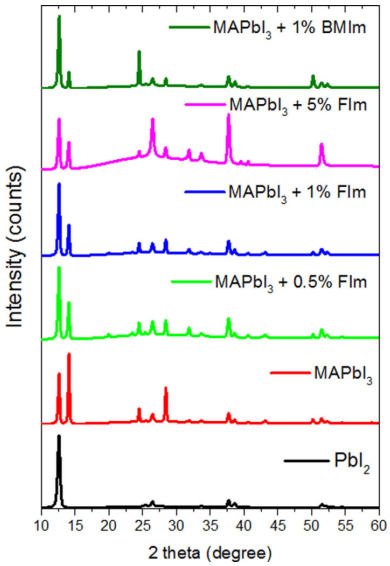

Figure 2. XRD data for PbI_2 and $MAPbI_3$ perovskite films with different concentrations of dopants.

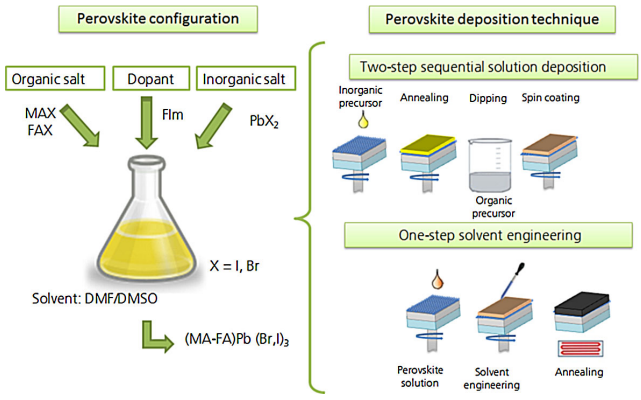

Scheme 1. One step and two step perovskite deposition processes used to generate the perovskite materials.

The XRD data show that incorporation of FIm or BMIm into the $MAPbI_3$ perovskite has negligible influence to the lattice structure. The peak at $2\theta = 12.5^\circ$, which indicates the presence of unreacted PbI_2, increases in intensity, whereas the peak appearing at $2\theta = 28.5^\circ$, characteristic of the tetragonal perovskite structure, decreases upon doping. In addition, the relative intensities of peaks at $2\theta = 26^\circ$ and 36° increase with doping. Excess PbI_2 was found to be beneficial in some cases for PV parameters, but it has negligible role to play in the stability of perovskites.[31] Similar spectra were recorded for the mixed materials $(FAPbI_3)_{0.85}(MAPbBr_3)_{0.15}$ indicating that changes in the crystallite orientation of tetragonal perovskite structure and an increase in the content of PbI_2 take place (Figure S1).

To evaluate the stability of the doped perovskites, we periodically recorded XRD patterns (Figure S2 and S3). No noticeable changes were observed with time in the doped perovskite structures; however, in the case of the $(FAPbI_3)_{0.85}(MAPbBr_3)_{0.15}$-based perovskites, FIm doping led to the decrease in the intensity of PbI_2 signature peak. The 1% and 0.5% FIm doping was found to have beneficial effect on the stability of perovskite. This also explains the enhanced PV performance upon ageing (Figure S8). Figure 3 and Figure S4 shows the visual appearance of perovskite layer deposited on fluorine-doped tin oxide (FTO)-coated glass; $(FAPbI_3)_{0.85}(MAPbBr_3)_{0.15}$ doped with 0.5 and 1% FIm showed notable behavior and the perovskite layer was found to be intact even after 103 days of exposure to air. Figure 4 shows the absorption spectra of the $MAPbI_3$-based photo anode with different concentrations of dopants. The optical properties of the materials show that neat $MAPbI_3$ and $MAPbI_3$ doped with 0.5% FIm, 1% FIm, or 1% BMIm have similar profiles. In contrast, the absorption of $MAPbI_3$ doped with 5% FIm has a lower absorption intensity for the wavelengths measured. This observation was also valid in the case of $(FAPbI_3)_{0.85}(MAPbBr_3)_{0.15}$-based perovskites (Figure S5), which is also in accordance with the optical image of the 5% doped FIm, irrespective of the perovskite used. For both the perovskites, $MAPbI_3$ and $(FAPbI_3)_{0.85}(MAPbBr_3)_{0.15}$, a 5% loading resulted in un-uniform deposition of perovskites. This could be because at the higher loading of the fluorinated compound, the surface tension increases abruptly and hinders conversion in the perovskite structure.

The morphologies of the $MAPbI_3$-based perovskites were characterized by SEM to visualize any possible changes in the crystal size or shape. It was found that the doping has no observable influence on the distribution of grains. Figure 5a and b shows the microstructure of pure $MAPbI_3$ at different magnifications, whereas Figure 5c and d shows $MAPbI_3$ with 1% FIm dopant. The doping induces a change in the microstructure and the crystal appears to be coated with an external layer. Figure 5e and f shows the material doped with 1% BMIm, and no changes were observed between both the doped perovskites. Here the perovskite layer was deposited on a mesoporous TiO_2 layer to reproduce the type of crystal growth used to prepare devices. The fluorinated compounds are seen to be grafted on the surface of $MAPbI_3$ (Figure 5c and e), which is foreseen to increase the environmental stability. All the microstructure images show adequate surface coverage, with uniform grain size and shape. With the introduction of the functionalization approach a smoother and continuous surface was achieved, in contrast to pure $MAPbI_3$. Figure 5g shows the cross sectional image of the $MAPbI_3$-based perovskite solar cells. The different layers can be easily visualized and the TiO_2 mesoporous particle appears to be completely covered with perovskite layers.

Photovoltaic properties

Devices were fabricated with the functionalized perovskites and current density–voltage (*J–V*) curves were recorded under simulated AM1.5G sunlight. Table 1 summarizes the PV properties for the different compositions of dopant, and the hysteresis index (HI) was calculated according to the following equation:

$$HI = \frac{J_{rev}(0.85{*}V_{oc}) - J_{fwd}(0.85{*}V_{oc})}{J_{rev}(0.85{*}V_{oc})}$$

Table 1. Summary of device photovoltaic parameters.

Perovskites	Dopant	J_{SC} [mA cm^{-2}]	V_{OC} [mV]	FF [%]	PCE [%]	Sun intensity
$MAPbI_3$	0	17.84	923	74	12.48	0.978
$MAPbI_3$	1% FIm	17.34	915	71	11.55	0.978
$MAPbI_3$	5% FIm	11.24	835	75.1	7.2	0.979
$MAPbI_3$ (double coated PbI_2)	0	18.90	939	76.5	13.93	0.975
$MAPbI_3$ (double coated PbI_2)	1% FIm	18.77	957	73.5	13.49	0.978
$MAPbI_3$ (double coated PbI_2)	5% FIm	12.29	870	76.1	8.34	0.976
$(FAPbI_3)_{0.85}(MAPbBr_3)_{0.15}$	0.5% FIm	21.43	1060	66.2	15.03	1
$(FAPbI_3)_{0.85}(MAPbBr_3)_{0.15}$	1% FIm	20.66	1070	69.5	15.38	1
$(FAPbI_3)_{0.85}(MAPbBr_3)_{0.15}$	1% BMIm	20.70	963	65.4	13.04	1

where J_{rev} and J_{fwd} are the current density values measured in the reverse and forward directions, respectively, and V_{OC} is the open-circuit voltage. The fabricated devices show a negligible degree of hysteresis and the calculated HI was found to be 0.011, 0.027, and 0.0274 for 0, 1, and 5% FIm doped $MAPbI_3$, respectively. Pure $MAPbI_3$ based devices (0% FIm), prepared by sequential deposition of perovskites, gave 12.5% of PCE. Doping with 1% FIm had little effect on the PCE, which was measured at 11.55%; however, 5% doping resulted in a lower PCE of 7.2%. The reduced performance with higher doping may be attributed to aggregate formation resulting in non-uniform perovskite layer deposition that hinders the optoelectronic properties. Figure 3 shows that the 5% FIm film is not desirable for the formation of uniform surface coverage. We also observed that a double coating of PbI_2 was required to obtain satisfactory PV performance, and the PCE increased to 13.5% for devices fabricated with 1% FIm perovskite films (Figure 6a).

It is remarkable that doping with the FIm salt has little negative impact on the device PV parameters, which is not general-

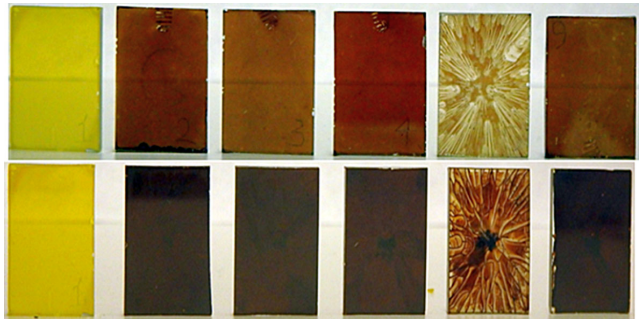

Figure 3. Perovskite film formation. Top, from left to right: PbI_2, $MAPbI_3$, $MAPbI_3$ with 0.5, 1, and 5% doped FIm, and $MAPbI_3$ with 1% BMIm. Bottom, same compositions as in the top row using $(FAPbI_3)_{0.85}(MAPbBr_3)_{0.15}$ perovskites.

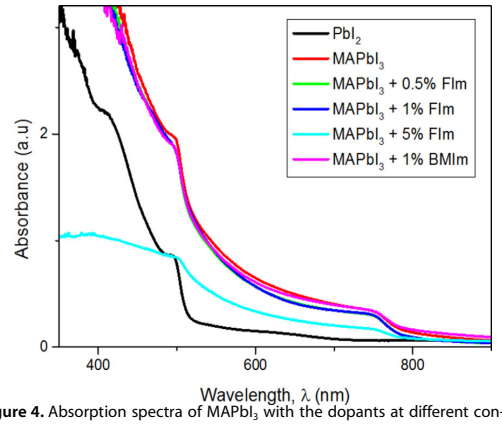

Figure 4. Absorption spectra of $MAPbI_3$ with the dopants at different concentrations.

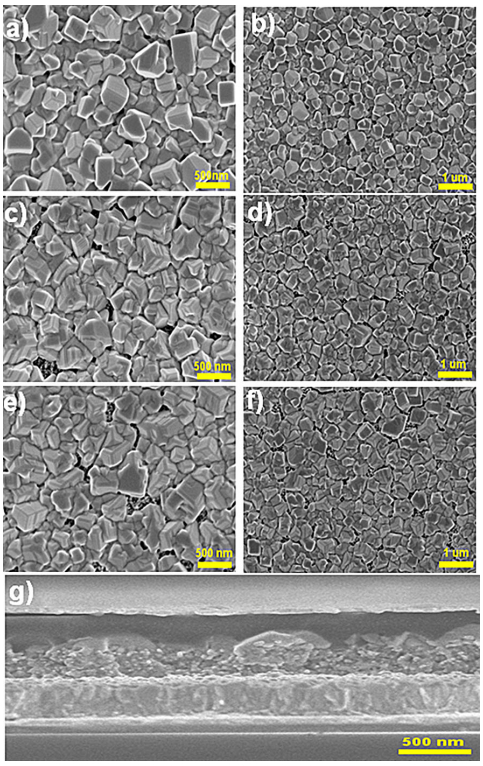

Figure 5. SEM images of a–b) the $MAPbI_3$ film, c–d) $MAPbI_3$ doped with 1% FIm, e–f) $MAPbI_3$ doped with 1% BMIm, and (g) cross section image of TiO_2/1% FIm-doped $MAPbI_3$/Spiro-OMeTAD solar cell.

ly the case for other dopants reported in the literature.[32,33] The fabricated devices show high reproducibility and low standard deviations. The incident photon-to-current efficiency (IPCE) spectra for the devices are shown in Figure 6b, where the integral photocurrent obtained from the IPCE spectra are in good agreement with the experimentally obtained short-circuit current density (J_{SC}) from the current–voltage performance. The perovskites layers doped with 1% FIm yielded improved light harvesting abilities compared to pristine perovskites in the visible range and the conversion rate was over 80%.

FIm- and BMIm-doped devices were fabricated using $(FAPbI_3)_{0.85}(MAPbBr_3)_{0.15}$-based perovskites. This time the FIm concentration was lowered further to establish its effect on the device performance. Whereas $(FAPbI_3)_{0.85}(MAPbBr_3)_{0.15}$-based perovskites demonstrated superior PCE values of 15.4% with 1% of FIm doping (Figure 7), the device more importantly showed negligible hysteresis (Figure S6). The HI value was found to be 0.0028. The IPCE trace was almost flat in the 450–750 nm region with a response over 80% (Figure S7).

Such a low concentration of dopant in the perovskite layer seems to have minimal effect on the surface coverage and maximum surface coverage is achieved, suggesting a uniform distribution of FIm cations in the perovskite structure. Contact angle measurements of the perovskite film were made and show that the hydrophobicity increases systematically with the increase in the doping concentration. Contact angle measurements were performed both instantaneously and 5 min after deionized water was deposited on the surface. The average

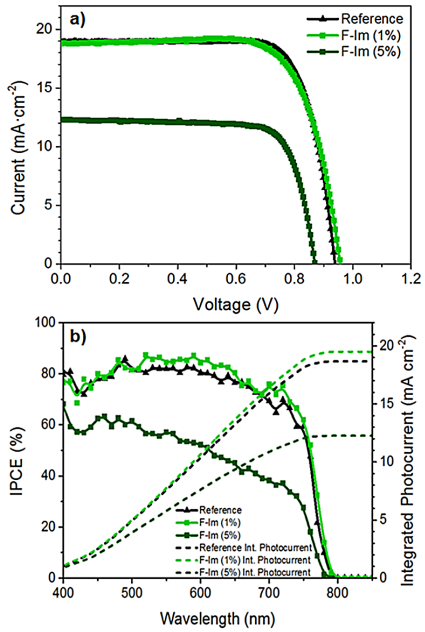

Figure 6. a) *J–V* characteristics for devices with $MAPbI_3$ and with different concentrations of FIm dopant. b) IPCE spectra of the perovskite solar cells using $MAPbI_3$ with different levels of doping under 100 mW cm^{-2} AM 1.5 G irradiation.

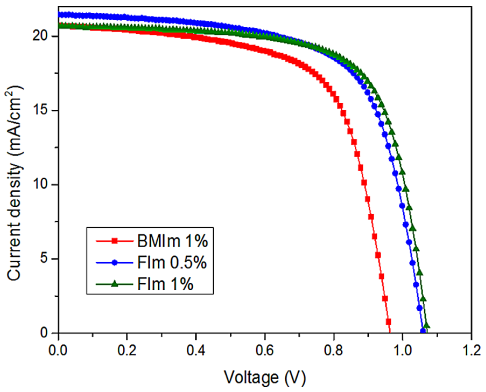

Figure 7. *J–V* characteristics of fabricated mesoscopic devices with the mixed perovskite $(FAPbI_3)_{0.85}(MAPbBr_3)_{0.15}$ as light harvester with different doping concentrations.

contact angle (Table S1) of the functionalized perovskite increases for both the $MAPbI_3$ and $(FAPbI_3)_{0.85}(MAPbBr_3)_{0.15}$ perovskite samples. Improved surface behavior of the perovskites appears to be a result of the hydrophobic nature of the fluorinated compound, which provides a synergistic effect in perovskite formation through the formation of a shield around its crystal structure.

Stability studies

The low stability of perovskite solar cells under ambient conditions is the main concern that prevents this promising technology from commercialization. Figure 8 illustrates the normalized PCE plotted as a function of time to determine the stability of the 1% FIm-doped $MAPbI_3$-based solar cell. The unencapsulated devices were kept in a glovebox under Ar and monitored by measuring the *J–V* characteristics at periodic intervals. In the initial time period of up to 20 days, an increase in the PCE was observed, presumably owing to superior intimate contact of the perovskite layers with the selective charge contacts (electron- and hole-transport materials) and/or owing to residual solvent drying in the perovskite crystals. It is noteworthy that the device was stable even after 90 days of measurements and a gain of 6.5% over the initial PCE value was observed over a period of 95 days. The same devices were exposed to ambient atmosphere after 95 days; after 110 days (15 days at ambient) a loss of 11.6% was observed. Indeed, it is remarkable that an unencapsulated device still works effectively over a total period of 110 days. Figure 9 illustrates the evolution of the normalized PCE with time for unsealed (FAP-

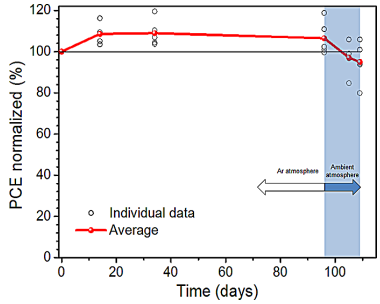

Figure 8. Evolution of stability data for the unencapsulated solar cells with 1% FIm-doped $MAPbI_3$. After 95 days the samples were exposed to ambient conditions (57% relative humidity).

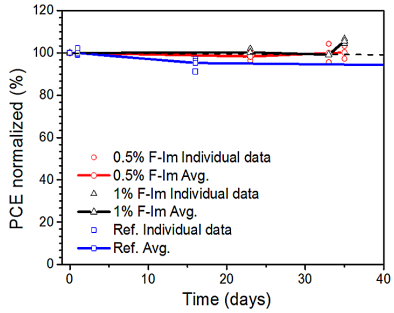

Figure 9. Evolution of stability data for the unencapsulated solar cells with 1% FIm-doped $(FAPbI_3)_{0.85}(MAPbBr_3)_{0.15}$ under ambient conditions (57–60% relative humidity).

$bI_3)_{0.85}(MAPbBr_3)_{0.15}$-based devices under ambient atmosphere; it was found that the FIm-doped devices exhibit enhanced stability over the pristine perovskite. Figure S8 represents the ageing *J–V* curves, periodically recorded for a typical unencapsulated FIm-doped perovskite device and shows negligible loss in PV performance over a period of 52 days.

Conclusions

The influence of varying the composition of a fluorinated dopant was studied in $MAPbI_3$ and $(FAPbI_3)_{0.85}(MAPbBr_3)_{0.15}$ perovskites. XRD data indicates that incorporation of 1-methyl-3-(1H,1H,2H,2H-nonafluorohexyl)-imidazolium iodide (FIm) or 1-methy-3-butyl-imidazolium iodide (BMIm) into the perovskite films has negligible influence on the lattice structure, but leads to an increase in unreacted PbI_2 and changes in the crystallite orientation of the tetragonal perovskite structure. Optimized PCEs of 13.5% for $MAPbI_3$ and 15.4% for $(FAPbI_3)_{0.85}(MAPbBr_3)_{0.15}$ were achieved with 1% doping by FIm. Importantly, the dopant significantly increases the operational stability of the perovskite solar cell.

Experimental Section

All chemicals were procured from Sigma–Aldrich and used without further purification unless otherwise mentioned. MAI and FAI were obtained from Dyesol and 2,2′,7,7′-tetrakis(*N*,*N*-di-p-methoxyphenyamine)-9,9-spirobifluorene (Spiro-OMeTAD) was acquired from Merck KGaA.

Compound synthesis

This synthesis of FIm was based on a modification of a method described earlier[34]. In brief, in a dry flask, 1-methylimidazole (0.82 g, 0.80 mL, 10 mmol) and 1H,1H,2H,2H-nonafluorobutyl iodide (4.66 g, 2.40 mL, 12.5 mmol) were stirred for 100 h at 80 °C. The resulting product was washed with toluene, dissolved in ethyl acetate and washed again with water, before being dried under vacuum for 60 h to afford a brown powder. ^{1}H NMR ([D_6]DMSO, 400 MHz): $\delta = 9.20$ (s, 1H), 7.88 (t, $J = 1.8$ Hz, 1H), 7.72 (t, $J = 1.8$ Hz, 1H), 4.57 (t, $J = 7.0$ Hz, 2H), 3.87 (s, 3H), 3.01 ppm (tt, $J = 19.7$, 7.0 Hz, 2H). ^{13}C NMR ([D_6]DMSO, 400 MHz) ∂: 137.2, 123.7, 122.5, 41.2, 35.9, 29.9.

Device fabrication

Perovskite solar cell devices were fabricated on FTO-coated glass (TEC15, Pilkington) patterned by laser etching. Before deposition the substrates were cleaned using Hellmanex solution and washed with deionized water and ethanol. Next, they were ultrasonicated in 2-propanol and rinsed using ethanol and acetone and then air dried. A TiO_2 compact layer was deposited by spray pyrolysis at 450 °C using 1 mL of titanium diisopropoxide bis(acetyl acetonate) precursor solution (75% in 2-propanol, Sigma–Aldrich) in 19 mL of pure ethanol using dry air as the carrier gas. After deposition of the blocking layer, the substrates were kept for a further 30 min at 450 °C to induce the formation of an anatase phase. Once the samples reached room temperature they were dipped in a 0.02 M $TiCl_4$ solution in deionized water at 70 °C for 30 min to obtain a homogenous layer. Subsequently the samples were then washed with deionized water, heated at 500 °C for 10 min and then cooled to room temperature. Next, a TiO_2 mesoporous layer (Dyesol, 30NRD) was deposited by spin coating (4000 rpm for 30 s) and the samples were annealed by progressive heating up to 450 °C for 2 h.

Perovskite layers were then deposited on the surface. PbI_2 spin coating, MAI dip-coating, and hole-transport material spin-coating depositions were made inside a dry box. For $MAPbI_3$ deposited by sequential method a solution of 1.25 M PbI_2 was used in DMF, while for $(FAPbI_3)_{0.85}(MAPbBr_3)_{0.15}$ 1:4 (DMSO/DMF) was used. The solution was prepared inside an Ar-filled glovebox with moisture and oxygen controlled conditions (H_2O level: <1 ppm and O_2 level: <10 ppm) and stirred at 80 °C overnight to completely dissolve the PbI_2. The deposition of the perovskite was carried out by sequential deposition or using a one-step deposition method.[4, 35] For the deposition of $(FAPbI_3)_{0.85}(MAPbBr_3)_{0.15}$ one-step method together with, solvent engineering approach was adopted, the perovskite precursor solution was spin-coated on top of the mesoporous layer at 1000 rpm for 10 s and then 6000 rpm for 30 s. Following this, the films were transferred onto a hotplate and annealed at 100 °C for 60 min. In the case of $MAPbI_3$, the FIm or BMIm was added in the PbI_2 solution and spin coated, whereas for mixed perovskites, it was directly added to $(FAPbI_3)_{0.85}(MAPbBr_3)_{0.15}$ and was subject to spin coating.

Spiro-OMeTAD was spin coated at 4000 rpm for 30 s by dissolving 72.3 mg of Spiro-OMeTAD in 1 mL of chlorobenzene; 21.9 μL of tris(2-(1H-pyrazol-1-yl)-4-*tert*-butylpyrydine)cobalt(III) bis(trifluoromethylsulphonyl)imide (FK209) from stock solution (400 mg of FK209 in 1 mL of acetonitrile), 17.5 μL of lithium bis(trifluoromethylsulphonyl)imide (LiTFSI) stock solution (520 mg of LiTFSI in 1 mL of acetonitrile) and 28.8 μL of 4-*tert*-butylpyridine were also added to the solution as dopants. Finally, an 80 nm layer of gold was thermal evaporated on the top of the cell as cathode under a vacuum level between 1×10^{-6} and 1×10^{-5} torr.

Characterization

For structural characterization, films were prepared by spin coating of solutions onto coarse glass. XRD scans were recorded on a Rigaku powder diffractometer using CuKα source. The measurements were performed in the Bragg–Brentano geometry. A scan range from $2\theta = 10°$ to 60° was selected with an acquisition time of 1° min^{-1}. A baseline correction was applied to diffractograms to compensate for the noise arising from the substrate.

The transmittance spectra of the perovskite films were collected using an Agilent Carry 60 spectrophotometer. Surface morphology and cross sectional images were obtained using a Hitachi S-4800 field emission scanning electron microscope at power 2 kV, while contact angle measurements were made on Data Physics, OCA15 instrument.

J–V curves were recorded with a Keithley 2400 source-measurement-unit under AM 1.5 G, 100 mW cm^2 illumination from a certified Class AAA, 450 W solar simulator (ORIEL, 94023A). Light output power was calibrated using a NREL certified calibrated monocrystalline silicon solar cell. A black mask (0.16 cm^2) was used over the solar cell active area (0.5 cm^2) to reduce the influence of scattered light.

Photovoltaic parameters including J_{SC}, V_{OC}, fill factor (FF), and PCE were extracted from the *J–V* curves of the solar cells and listed in Table 1. The scan rate and the active area used for measuring the devices were optimized to calculate the real value for efficiencies

without hysteresis effects (active area: 0.16 cm^2, scan rate: 100 $mV s^{-1}$).

The IPCE measurements were performed using a Newport 150 W xenon lamp coupled to an Oriel Cornerstone 260 motorized $^1/_4$ m monochromator as the light source, and a 2936-R Power Meter to measure the short-circuit current.

Acknowledgements

We thank Laura Calio for experimental help, V.M. thanks the Swiss National Science Foundation for financial support and S.A. thanks the European Union Seventh Framework Programme under grant agreement n° 607232 [THINFACE].

Keywords: doping · fluorination · perovskite · solar cells · stability

[1] A. Kojima, K. Teshima, Y. Shirai, T. Miyasaka, *J. Am. Chem. Soc.* **2009**, *131*, 6050 – 6051.
[2] S. Kazim, M. K. Nazeeruddin, M. Grätzel, S. Ahmad, *Angew. Chem. Int. Ed.* **2014**, *53*, 2812 – 2824; *Angew. Chem.* **2014**, *126*, 2854 – 2867.
[3] M. A. Green, A. H-Baillie, H. Snaith, *Nat. Photonics* **2014**, *8*, 506 – 514.
[4] H.-S. Kim, C.-R. Lee, J.-H. Im, K.-B. Lee, T. Moehl, A. Marchioro, S.-J. Moon, R. Humphry-Baker, J.-H. Yum, J. E. Moser, M. Grätzel, N.-G. Park, *Sci. Rep.* **2012**, *2*, 591; J. Burschka, N. Pellet, S.-J. Moon, R. Humphry-Baker, P. Gao, M. K. Nazeeruddin, M. Grätzel, *Nature* **2013**, *499*, 316 – 319.
[5] National Renewable Energy Laboratory Best Research-Cell Efficiencies, can be found under http://www.nrel.gov/ncpv/images/efficiency_chart.jpg.
[6] A. Polman, M. Knight, E. C. Garnett, B. Ehrler, W. C. Sinke, *Science* **2016**, *352*, 307.
[7] S. Brittman, G. W. P. Adhyaksa, E. C. Garnett, *MRS Commun.* **2015**, *5*, 7 – 26.
[8] J. H. Park, J. Seo, S. Park, S. S. Shin, Y. C. Kim, N. J. Jeon, H.-W. Shin, T. K. Ahn, J. H. Noh, S. C. Yoon, C. S. Hwang, S. I. Seok, *Adv. Mater.* **2015**, *27*, 4013 – 4019.
[9] M. R. Filip, G. E. Eperon, H. J. Snaith, F. Giustino, *Nat. Commun.* **2014**, *5*, 5757.
[10] P. Piatkowski, B. Cohen, F. Javier Ramos, M. Di Nunzio, M. K. Nazeeruddin, M. Grätzel, S. Ahmad, A. Douhal, *Phys. Chem. Chem. Phys.* **2015**, *17*, 14674 – 14684.
[11] a) D. Bryant, N. Aristidou, S. Pont, I. S. Molina, T. Chotchunangatchaval, S. Wheeler, J. R. Durrant, S. A. Haque, *Energy Environ. Sci.* **2016**, *9*, 1655 – 1660; b) B. Li, Y. Li, C. Zheng, D. Gao, W. Huang, *RSC Adv.* **2016**, *6*, 38079 – 38091.
[12] N. Pellet, P. Gao, G. Gregori, T.-Y. Yang, M. K. Nazeeruddin, J. Maier, M. Grätzel, *Angew. Chem. Int. Ed.* **2014**, *53*, 3151 – 3157; *Angew. Chem.* **2014**, *126*, 3215 – 3221.
[13] a) N. J. Jeon, J. H. Noh, W. S. Yang, Y. C. Kim, S. Ryu, J. Seo, S. Il Seok, *Nature* **2015**, *517*, 476 – 480; b) Z. Xiao, Q. Dong, C. Bi, Y. Shao, Y. Yuan, J. Huang, *Adv. Mater.* **2014**, *26*, 6503 – 6509.
[14] T. M. Koh, K. Fu, Y. Fang, S. Chen, T. C. Sum, N. Mathews, S. G. Mhaisalkar, P. P. Boix, T. Baikie, *J. Phys. Chem. C* **2014**, *118*, 16458 – 16462.
[15] S. Pang, H. Hu, J. Zhang, S. Lv, Y. Yu, F. Wei, T. Qin, H. Xu, Z. Liu, G. Cui, *Chem. Mater.* **2014**, *26*, 1485 – 1491.
[16] X. Li, M. Ibrahim Dar, C. Yi, J. Luo, M. Tschumi, S. M. Zakeeruddin, M. K. Nazeeruddin, H. Han, M. Grätzel, *Nat. Chem.* **2015**, *7*, 703 – 711.
[17] D. Bi, P. Gao, R. Scopelliti, E. Oveisi, J. Luo, M. Grätzel, A. Hagfeldt, M. K. Nazeeruddin, *Adv. Mater.* **2016**, *28*, 2910 – 2915.
[18] T. Leijtens, G. E. Eperon, N. K. Noel, S. N. Habisreutinger, A. Petrozza, H. J. Snaith, *Adv. Energy Mater.* **2015**, *5*, DOI: 10.1002/aenm.201500963.
[19] J. H. Noh, S. H. Im, J. H. Heo, T. N. Mandal, S. Il Seok, *Nano Lett.* **2013**, *13*, 1764 – 1769.
[20] Y. Chen, B. Li, W. Huang, D. Gao, Z. Liang, *Chem. Commun.* **2015**, *51*, 11997 – 11999.
[21] A. Halder, R. Chulliyil, A. S. Subbiah, T. Khan, S. Chattoraj, A. Chowdhury, S. K. Sarkar, *J. Phys. Chem. Lett.* **2015**, *6*, 3483 – 3489.
[22] A. M. Ganose, C. N. Savory, D. O. Scanlon, *J. Phys. Chem. Lett.* **2015**, *6*, 4594 – 4598.
[23] Q. Jiang, D. Rebollar, J. Gong, E. L. Piacentino, C. Zheng, T. Xu, *Angew. Chem. Int. Ed.* **2015**, *54*, 7617 – 7620; *Angew. Chem.* **2015**, *127*, 7727 – 7730.
[24] M. Daub, H. Hillebrecht, *Angew. Chem. Int. Ed.* **2015**, *54*, 11016 – 11017; *Angew. Chem.* **2015**, *127*, 11168 – 11169.
[25] D. B. Mitzi, D. R. Medeiros, P. R. L. Malenfant, *Inorg. Chem.* **2002**, *41*, 2134 – 2145.
[26] I. Papagiannouli, E. Maratou, I. Koutselas, S. Couris, *J. Phys. Chem. C* **2014**, *118*, 2766 – 2775.
[27] Y. Wei, J. S. Lauret, L. Galmiche, P. Audebert, E. Deleporte, *Opt. Express* **2012**, *20*, 10399.
[28] Y. Wei, P. Audebert, L. Galmiche, J.-S. Lauret, E. Deleporte, *J. Phys. D* **2013**, *46*, 135105.
[29] Y. Wei, P. Audebert, L. Galmiche, J.-S. Lauret, E. Deleporte, *Materials* **2014**, *7*, 4789 – 4802.
[30] J. M. Frost, K. T. Butler, F. Brivio, C. H. Hendon, M. Van Schlifgaarde, A. Walsh, *Nano Lett.* **2014**, *14*, 2584.
[31] T. J. Jacobsson, J. P. Correa-Baena, E. H. Anaraki, B. Philippe, S. D. Stranks, M. E. F. Bouduban, W. Tress, K. Schenk, J. Teuscher, J.-E. Moser, H. Rensmo, A. Hagfeldt, *J. Am. Chem. Soc.* **2016**, DOI: 10.1021/jacs.6b06320.
[32] I. C. Smith, E. T. Hoke, D. Solis-ibarra, M. D. Mcgehee, H. I. Karunadasa, *Angew. Chem.* **2014**, *126*, 11414 – 11417.
[33] D. H. Cao, C. C. Stoumpos, O. K. Farha, J. T. Hupp, M. G. Kanatzidis, *J. Am. Chem. Soc.* **2015**, *137*, 7843 – 7850.
[34] T. L. Merrigan, E. D. Bates, S. C. Dorman, J. H. Davis, Jr., *Chem. Commun.* **2000**, 2051 – 2052.
[35] K. Rakstys, A. Abate, M. I. Dar, P. Gao, V. Jankauskas, G. Jacopin, E. Kamarauskas, S. Kazim, S. Ahmad, M. Grätzel, M. K. Nazeeruddin, *J. Am. Chem. Soc.* **2015**, *137*, 16172 – 16178.

Received: July 28, 2016
Published online on ■■ ▮▮, 0000

FULL PAPERS

*M. Salado, F. J. Ramos, V. M. Manzanares, P. Gao, M. K. Nazeeruddin, P. J. Dyson, S. Ahmad**

■■ – ■■

Extending the Lifetime of Perovskite Solar Cells using a Perfluorinated Dopant

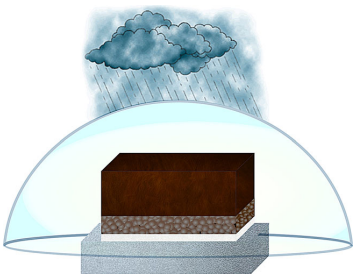

Under cover: Perovskite solar cells are fabricated using perovskite active layers doped with fluorinated imidazolium-based molecules. These additives significantly increase the stability of the resulting solar cell device owing to the electron-withdrawing character of the fluorinated salt together with its hydrophobicity, and induce structural and functional changes to the resultant perovskite, leading to stable power conversion efficiency.

FULL PAPER WILEY-VCH

Towards extending solar cells life time: addition of a fluorous cation to triple-cation based perovskite films

Manuel Salado,[a] M Asunción Fernández,[b] Juan P. Holgado,[b] Samrana Kazim,[a] Mohammad Khaja Nazeeruddin,[c] Paul J. Dyson,[d] Shahzada Ahmad*[a]

Abstract: Organohalide perovskites have emerged as highly promising replacements for thin film solar cells. However, their poor stability under ambient conditions remains problematic, hindering commercial exploitation. Here, we describe our investigation on the addition of a fluorous-functionalized imidazolium cation during the preparation of a highly stable cesium based mixed perovskite material $(Cs_{0.05}(MA_{0.15}FA_{0.85})_{0.95}Pb(I_{0.85}Br_{0.15})_3$ and how it influences on the stability. The resulting materials, which vary according to the amount of the fluorous-functionalized imidazolium cation present during fabrication, display a prolonged tolerance to atmospheric humidity (>100 days) along with power conversion efficiencies exceeding 16%. This work provides a general route which can be implemented in variety of perovskites and highlights a promising way to increase perovskite solar cell stability.

Introduction

Recent years have witnessed an enormous growth in the studies of perovskite materials as light harvesters in solar cells due to their attractive electro-optical properties, cost-effectiveness, facile fabrication,with power conversion efficiencies (PCE) now exceeding 22%.[1]Consequently, perovskite-based solar cells have rapidly become one of the most promising technologies for solar energy conversion. However, perovskite stability remains a problem and research efforts are still needed to overcome this limitation. Several studies have attempted to unravel the origin of perovskite degradation, which has been shown to be favored by moisture, UV irradiation and high temperatures.[2–6] Various strategies to prevent perovskite degradation have also been reported including the use of carbon based compounds[7], inorganic materials[8–10], hydrophobic dopants[11] or the addition of an Al_2O_3 buffer layer.[12] Unfortunately, the addition of an extra layer affects the energy levels or the interface between the hole transport materials (HTM) and perovskite, and induces an increment of transport resistance leading to a reduction in the efficiency of the resulting solar cell devices. Perovskite deposition methods also affect film uniformity and low-pressure chemical vapor deposition has been shown to yieldperovskites with strong light absorption capabilities.[13] Another approach thatavoids exposure to water involves the encapsulation of perovskite devices in hydrophobic polymers[14], which helps to prevent degradation.

Perovskite are highly versatile materialsin which both the organic cation and the anion can be varied. In this context, pseudohalidethiocyanateanions (SCN^-) were used to improve the resistance of perovskites to humidity[15]. It was also shown that chloride- and bromide-based perovskite are more stable than those based on iodide[16],however, the resulting high band gap limits device performance. Although most studies have focused on the well-known methylammonium lead halide ($MAPbI_3$) system, recent studies have shown that mixed cation-anion perovskites are relatively stable and even exhibit improved operational conditions. For example, a triple cation, cesium based perovskite structure resulted in a more UV and thermally stable perovskite-based solar cell.[17–20] Fluorinated salts have also been shown to increase the stability of perovskite-based devices due to their hydrophobic properties.[21,22] For example, incorporation of a multifunctional fluorous-based photopolymer on the front of the device improvesstability as well as the photovoltaic performance.[23] Alternatively, incorporation of fluorinated dopants that modify the perovskite layer, without altering the interface between the charge selective contacts, could be a promising approach.[24]

It has been shownthat even trace amounts of water packed in a closed system will decompose (at least inpart) a perovskite material. Following exposure to waterammonium ions in $CH_3NH_3PbI_3$material will be rapidly deprotonated to form an intermediate phase of formula $[(CH_3NH_3^+)_{n-1}(CH_3NH_2)_nPbI_3][H_3O]$. This intermediate is unstable and decomposes[3,18] further to form HI, CH_3NH_2 and solid PbI_2. The extreme vulnerability of perovskites to moisture has led to efforts to design the materials that defend against attack by moisture. Recently various approaches have shown that it is possible to induce structural stability of the material without compromising device performance. In the case of $MAPbI_3$-type systems, MA^+can discharge a proton under light irradiation, and the resulting proton will combine with I^- to produce HI, which is corrosive,whereas in the case of formamidinium based i.e. $FAPbI_3$ materials, FA^+cannoteasilyrelease protons. $MAPbI_3$systems have been studied most extensively for electro-optical applications, although structurally related $FAPbI_3$materials have a slightly higher tolerance factor (0.88) and radius compared to $MAPbI_3$materials (0.83). The partial substitution of FA^+ by MA^+cationsalso increases device stability and efficiency by increasingentropyin $(FAPbI_3)_{0.85}(MAPbBr_3)_{0.15}$. The use of a triple cation system, e.g. $(Cs_{0.05}(MA_{0.15}FA_{0.85})_{0.95}Pb(I_{0.85}Br_{0.15})_3$,represents another

[a] Mr. M. Salado, Dr. S. Kazim and Dr. S. Ahmad*
Abengoa Research, Abengoa
C/ Energía Solar nº 1, Campus Palmas Altas-41014, Sevilla, Spain
E-mail: shahzada.ahmad@abengoa.com
[b] Prof. M. A. Fernández,and Dr. J. P. Holgado
Instituto de Ciencia de Materiales de Sevilla (CSIC-Univ. Sevilla), Avda. Américo Vespucio 49, 41092-Sevilla, Spain.
[c] Prof. M. K. Nazeeruddin, Group for Molecular Engineering of Functional Materials, Swiss Federal Institute of Technology Lausanne (EPFL), EPFL Valais Wallis, CH-1951 Sion, Switzerland.
[d]Prof. P. J. Dyson, Institute of Chemical Sciences and Engineering, Swiss Federal Institute of Technology Lausanne (EPFL), CH 1015, Lausanne, Switzerland.

approach to increase the stability of 3D perovskites. It was reported that the stability of organohalide perovskites can be increased significantly by the application of three different cations with the inclusion of the Cs^+ ionsuppressing the formation of the photo-inactive yellow phase. The MA^+ cation stabilizes the formation of the black phase within FA^+-based structure as it is smaller (ionic radius 2.70 vs. 2.79 Å). The Cs^+ ionis even smaller with an ionic radius of 1.81 Å, which further suppresses reactions and increases entropy.[18] The addition of a small amount of Cs^+ was reported to afford a stable perovskite and Cs^+/FA^+ mixtures were shown to enhance thermal and humidity stability, with PCEs of 16.5%.[18] Here we demonstrate that $(Cs_{0.05}(MA_{0.15}FA_{0.85})_{0.95}Pb(I_{0.85}Br_{0.15})_3$based perovskites enveloped bythefluorinated salt, 1-methyl-3-(1H,1H,2H,2H-nonafluorohexyl)-imidazolium iodide (Figure 1),exhibit competitive stability without at the cost of device PCE. Notably, at low loadings (0.5% w/w) in the precursor solutiona significant increasein both the stability and the PV performance of the devices was observed. These homoeopathic additive based solar cells show improved stability,which can be attributed to the protection of the surface of perovskite grains by the hydrophobic ionic coating, thus preventing penetration of water into the perovskite crystal. The impact of FIm addition on perovskite microstructure, device PV parameters and electrical properties along with life time is being reported.

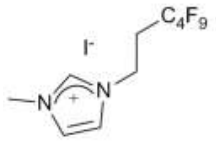

Figure 1. Structure of the1-methyl-3-(1H,1H,2H,2H-nonafluorohexyl)-imidazolium iodide (FIm) dopant used.

Results and Discussion

We added various concentrations of a fluorinated dopant (1-methyl-3-(1H,1H,2H,2H-nonafluorohexyl)-imidazolium iodide, termed FIm, Figure 1) during the preparation of the $Cs_{0.05}(MA_{0.15}FA_{0.85})_{0.95}Pb(I_{0.85}Br_{0.15})_3$ perovskite, in order to increase the stability of perovskite solar cells. The XRD spectra of the resulting doped perovskites under humidity conditions (55-60% RH) were collected at regular time intervals and the patterns obtained after 33 days are shown in Figure 2 (Figure S1 for diffractograms of the un-aged pristine perovskite layers). The characteristic peak at 12.6° corresponding to PbI_2 and indicative of a water-based decomposition pathwaywas not observed in the perovskite prepared with the FIm dopant (1%) following 33 days in a RH environment of 55-60%. In contrast, the perovskites without the FIm dopantcontained a strong peak at 12.6°, indicative ofthe formation of PbI_2 and essentially completely degraded within7days (Figure S1). The 'homeopathic' addition of FImretards the decomposition reaction, but does not suppress it completely.

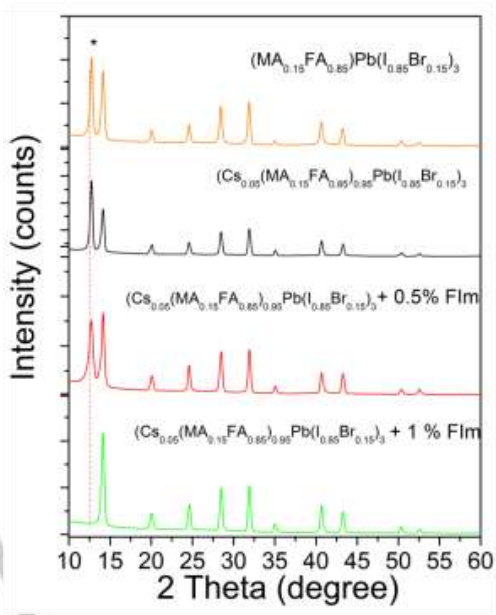

Figure 2. XRD patterns of different % (w/w) fluorinated dopant after 33 days at 55-60%RH. (*) PbI_2 main characteristic peak (12.6°). Figures S1 in the supporting information shows the diffractograms as a function of time.

Spectroscopic studies and device performance

The absorbance spectra of the various perovskites are shown in Figure S2. It was foundthat varying the percentage of theFImdopant has negligible effect on the absorption spectra of perovskites, with no new absorption band observed. However, thedopant compromises the homogeneity of the layers at higherloadings, i.e. 2% (w/w), producing less uniform films withstar-like microstructures seen under microscope.[24] The absorbance spectrum remains unaltered even after 40 days of exposure (Fig. S2). Earlier we have also found that the water contact angle for the different compositional engineering perovskite thin films i.e. $MAPbI_3$ and $(MA_{0.15}FA_{0.85})Pb(I_{0.85}Br_{0.15})_3$ increases systematically as FIm loading increase, however at higher loading film uniformity cannot be achieved and it was a trade off with device PV performance. [24]

Table 1 and Figure 3 summarize the characteristic photovoltaic parameters of the devices. Notably, with 0.5% FIm the photocurrent and fill factor are improved, which indicates lower recombination losses or shunting paths into the solar cell device. Addition of 2% FIm affords a higher V_{oc} (1050mV), compared to pristine or 0.5% FIm (1000mV) devices, possibly due to shifting of the Fermi level, but at the expense of short circuit current density (J_{SC}). The decrease in short circuit current is due to inhomogeneity in the perovskite layers and, consequently, it also showed lowest fill factor (*FF*). The best *FF* and $J_{SC}$was shown by the cell based on the 0.5% FIm. Notably, a FF c.a to 75% was

obtained due to the optimal FIm inclusion in the perovskite lattice, which may be attributed to the formation of more uniform perovskite grains as the addition of FIm will modify the crystallization process. When performing the measurements after 30s light soaking the 0.5% FIm doped devices yielded an improved value of 16.82% (J_{sc} = 21.85 mA/cm^2, V_{oc} = 1060 mV and FF = 72.36) from 16.32%. Table S1 and Fig. S3 illustrates device statistics, which are fairly reproducible, except in the case of 2%FIm doped which shows higher deviation. To observe the hysteresis behavior, a typical device was also measured in the forward and reverse scan direction (Fig.S4), and a negligible degree of hysteresis was found. The hysteresis index (HI) was calculated (Table S2) according to standard method and almost no hysteresis was found, which also remains unchanged over the measured period of 50 days. The HI was also found to be independent of scan rate.

Figure 4 shows the wavelength response of incident photon to current conversion efficiency (IPCE) plots for the different devices. The light to electricity conversion abilities in these systems approaches 90%, in the broad range of visible spectrum, except in the case of devices fabricated from perovskites with higher FIm contents, which show lower IPCE values. The secondary Y-axis represents the derived integrated current value, which is in line with the *J-V* measurements, and supports the legitimate PCE calculations. Relatively flat photon-to-electron conversion profiles were observed between 400 and 750 nm. As expected, 1% and 2% FIm materials, afforded devices with lower IPCE values. A drop in IPCE value in the range 350-450 nm was observed following the use of the FIm dopant, i.e. decreasing as the concentration of the dopant was increased. Nevertheless, these changes are in a very narrow spectral range (350-4500nm) and are not reflected in the overall PV properties of the devices.

Table 1.Photovoltaic parameters of the devices under 100 mW / cm^2.

Doping ratio	V_{oc}(mV)	J_{sc} (mA/cm^2)	FF (%)	PCE (%)
0%	1000	21.55	74.68	16.07
0.5%	1000	21.69	75.19	16.32
1%	980	21.02	72.52	15.06
2%	1050	20.44	71.68	15.41

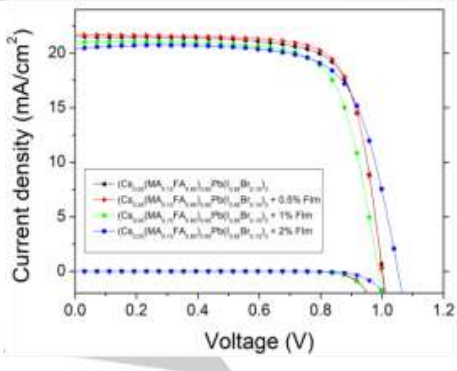

Figure 3. *J–V* characteristics for devices with different concentrations of the FIm dopant under 100 mWcm^{-2} AM1.5G irradiation.

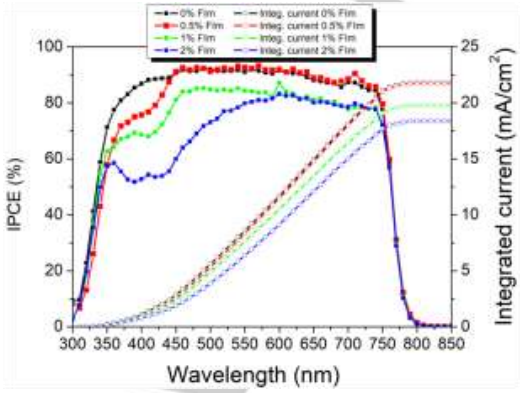

Figure 4. IPCE spectra of the perovskite solar cells under 100 mWcm^{-2} AM1.5G irradiation.

To obtain insights into the role of the fluorinated compound (FIm) in the improved perovskites, an array of techniques was employed. Scanning electron microscopy (SEM) was first used to examine the microstructures and surface texture of the perovskite layers containing theFIm dopant. As the percentage of FIm increases the perovskite film appears to become increasingly smooth (Figure 5a-c), probably due to the effect of the hydrophobic dopant. Grains in the pristine (0% FIm doped) sample (Fig. 5a) appear clearly faceted with sharp grain boundaries. The FIm dopant possibly acts as a passivationlayerat the surface of perovskite grains, smoothing the grain boundaries (Figure 5c), and protecting the perovskitecrystals from direct interaction with water. Figure 5d represents the SEM cross-section image of a complete device, which is in accordance with architecture adopted and represents well connected interlayers. Scheme 1 represents the possible interactions induce by FIm in a triple cation environment.

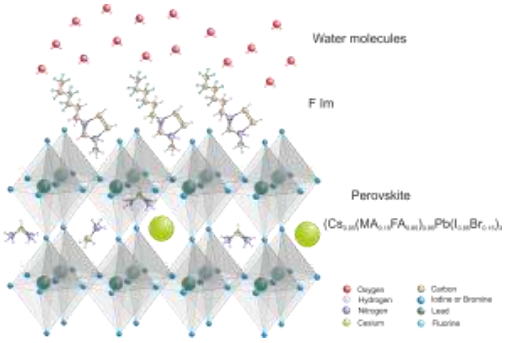

Scheme 1: Representing the possible role and interaction of FIm in a triple cation environment.

To elucidate the location of the FIm dopant, energy dispersive X-Ray (EDX) analysis was carried out in the SEM microscope with only trace-levels of fluorine detected (for a representative spectrumfrom top view analysis of 2% FIm doped sample seeFigure 5e). Elemental map images obtained by SEM-EDX in cross section views are also shown in supporting information (Figure S5) for the complete device.

Transmission electron microscopy (TEM) with an EDXanalyzer was used to further probe the samples(Figure S6). The perovskite films were scratched from the silicon substrate with a diamond pencil and deposited on a carbon coated copper grid without the use of a solvent, i.e. by smooth contact of the grid with the powder. TEM images reveal well defined structures having different textures. The comparative analysis of different samples and textures conceals the presence of a clear peak for fluorine. However, atom segregation was observed (important variations in bromide to iodine signal ratios in different areas of scratched samples) which is in accordance with recent findings[25].

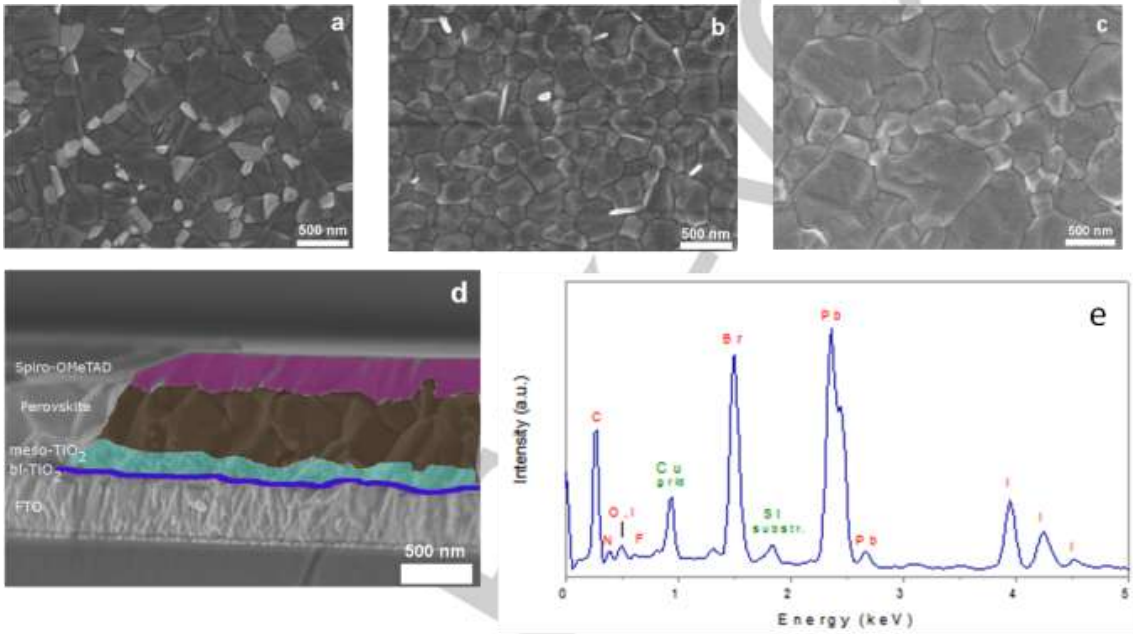

Figure 5. a-c) SEM images (top-view) of perovskite films with a) 0% b) 0.5 % and c) 1% of FIm dopant. d) SEM image (cross-sectional) of device fabricated with 0.5% FIm doped perovskite (FTO/TiO_2 mesoporous/perovskite/Spiro-OMeTAD) and e) representative SEM-EDX spectrum from top view analysis of the 2% FIm doped sample.

X-ray photoelectron spectroscopy (XPS) was also employed to determine the presence of fluorine dopant on the perovskite layer. Table S1 summarizes the atomic percentages obtained from quantification of elements detected, using standard Shirley background and atomic sensitivity factors.

Due to the high difference in atomic weight between F and the main constituent of the sample (Pb, I), a differential sputtering process may have occurred in these samples, that will induce a lower level of light elements after ion bombardment, thus making the fluoride detection difficult. (Figure S8). The molecular interaction mechanisms in these homoeopathic additives based layers were difficult to elucidate, due to the diluted nature of the FIm molecules.

With respect to the remaining the elements, it is also worth mentioning that the signal corresponding to O1s is quite small (c.a 3.0%), suggesting a high stability of the perovskite under atmospheric exposure. This level even decreases to 1.5 – 2.0% in the ion sputtered sample, confirming the purity of the obtained perovskite phase.

To study the photo-physical processes occurring inside the different fabricated solar cells electrochemical impedance spectroscopy (EIS) techniques wereemployed (Figure S10). The device PV properties (*J-V* and IPCE measurements) showed a drop in current density in the devices containing the FIm dopant in higher amounts. Figure 6ashows how the recombination resistance varies depending on the percentage of FIm dopant. The perovskite device fabricated with 2% FImdopant exhibits a higher value which is in accordance with the higher values of V_{oc} obtained in *J-V* measurements. Higher loadings of FImappear to minimize the recombination sites at grain boundaries, which in turn allow higher V_{oc} values to be attained (Table S1).These results are also consistent with the percentage of FIm in the

perovskite stoichiometry. At close to open circuit voltage, identicalvalues of resistance to recombination were observed for all the devices, while the device without FIm shows lowest recombination resistance.

Time constants for the lifetime of the carriers can also be derived from EIS and Figure 6bdepicts the lifetime versus voltage curves. At higher FImcontents,higher lifetimes were observed. Carrier lifetime was calculated from the recombination resistance and geometric capacitance. Since the capacitance in perovskite-based solar cells (Figure S9) remains constant, [26,27] the carrier lifetime shows a similar trend to recombination resistance.Thus, the device with 2% FImhas a longer carrier lifetime and, consequently, the addition of the dopant does not affect the recombination processes that occur in the perovskite layer.

From the electro-optical (*J-V*, absorbance) measurements and the photo-physical (charge transport) experiments it is difficult to establish a clear relationship between the concentration of the FIm dopant and the drop of current observed in the IPCE spectra. The third contribution comprises the injection of carriers from the perovskite to the HTM or TiO_2.

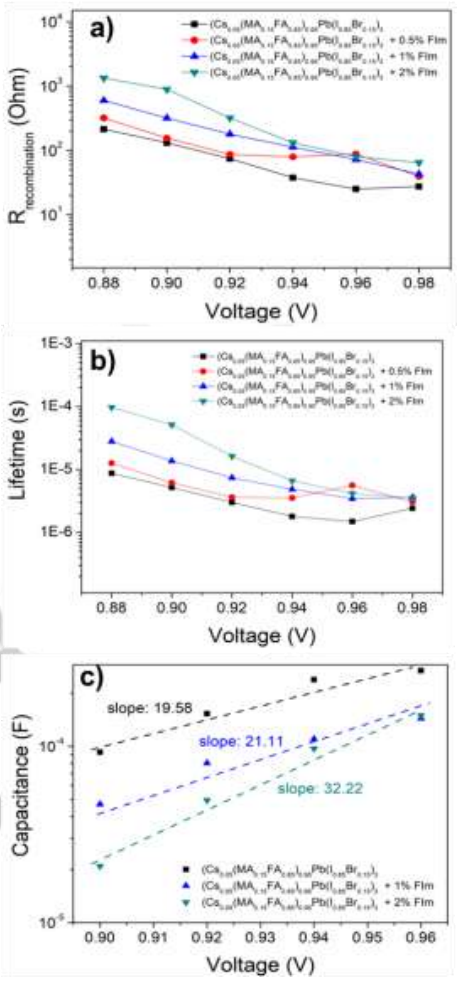

Figure 6.a) Recombination resistance versus voltage of the devices with different FIm loadings, b) carrier lifetime versus voltage obtained by fitting the semicircle (w) on the Nyquist plot and c) low-frequency capacitance values versus voltage of different devices. Measurements were performed at 298K.

As the decay was observed in the blue part of the spectra we focused our study on the low frequency range (Figure S9). The existence of surface recombination sites has been proposed when high capacitance values are observed at low frequencies. [28] This effect could be related to the hysteresis observed in perovskite solar cells. According to this model, capacitance is associated with exponential dependence on voltage with slope $1/2k_BT$ at 298 K. Thus, the existence of electron accumulation at the TiO_2/perovskite interface due to a polarization of the surface caused by ion movement was observed. This phenomenon could explain the drop in current density observed in IPCE

spectra. Arguably, the FIm dopant could be positioned at the interface of charge selective contacts (TiO_2/perovskite) due to its high surface affinity and interact with the TiO_2 surface affecting the electron extraction from the perovskite layer.

Device stability

Long-term ageing studies under high humidity conditions (55-60%RH)were conducted to determine the stability of the devices. Figure 7 shows the characteristic parameters of 0.5 -2% FIm doped devices. The unprotected devices were kept in ambient atmosphere (55-60% RH), notably the devices remain stable over >150 days with all the key PV parameters intact without any significant drop. The noticeable changes were observed (Fig. S12) in the value of current density and *FF* of triple cation based pristine perovskite, which can be ascribed due to lack of protection from FIm. The drop in J_{sc} is due to lower recombination resistance, and a lower *FF* due to the distortion of the crystal structure.

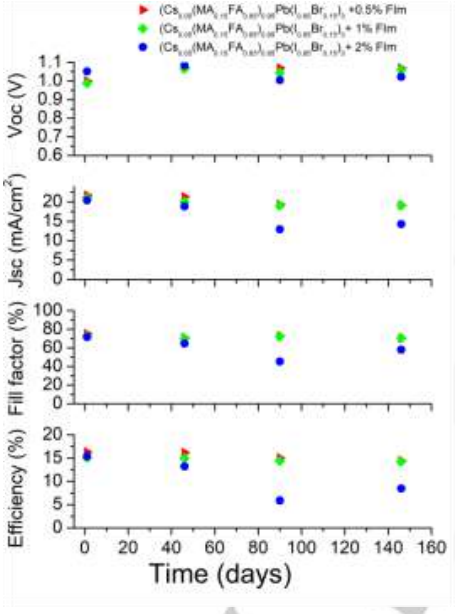

Figure 7. Evolution of the photovoltaic parameters (*PCE*, J_{SC}, V_{OC} and *FF*) for devices doped with 0.5-2% FIm at 55-60% RH measured at 1 sun. Note during 100-150 days the RH was 40-50 % due to winter season.

The stability of the perovskite films was also evaluated using XRD (Figures S1). The perovskite samples were kept inside and outside a glovebox to assess the influence of humidity on perovskite films. Degradation of the films leads to the appearance of a peak in the XRD pattern at 12.6° corresponding toPbI_2(Fig. 1). The perovskite film without a cesium cation rapidly deteriorated, even inside the glovebox. For the 5% Cs^+ containing perovskite degradation was relatively slower. However, the perovskite doped with 0.5% FImdid not show any signs of degradation inside the glovebox, and the 1% FIm-based perovskite remained even more stable for over 1 month in 50-55% RH.The iodide from FIm, will capture the vacant iodide sites, and will help to passivates the iodide vacancies on the perovskite crystal. This will retard the superoxide formation and allow improved moisture tolerance.[29]Recently, the use of quaternary ammonium halides was also shown to passivates the ionic defects[30], which allows to improve the stability. These findings are in accordance with our results.

Conclusions

We have demonstrated that the addition of the fluorinated FIm salt during the preparation of $Cs_{0.05}(MA_{0.15}FA_{0.85})_{0.95}Pb(I_{0.85}Br_{0.15})_3$ based perovskites leads to solar cell devices which remain stable for >100 days when stored in atmospheric conditions (55% RH). A low amount of FIm (homoeopathic additivation) was sufficient to obtain stable devices, whichhelp to keep the crystal structure intact, possibly by acting as a hydrophobic barrier.Grains in the pristine perovskites appear clearly faceted with sharp grain boundaries, while with FIm modified perovskites shows sign of passivation layer at the surface of perovskite grains, smoothing the grain boundaries, this will help to protect the perovskite crystals from direct interaction with atmosphere.By so doing, the iodide from FIm will fill the iodine vacancies and delay superoxide formation. The FIm did not alter the way the charges are transferred at the interfaces while retaining device stability. Combined, these studiessuggest a general approach toimprove thestability of perovskite films for the fabrication of solar cells using hydrophobic fluorous-cations.

Experimental Section

Materials

All chemicals were purchased from Sigma Aldrich and used as received, MAI and FAI were obtained from Dyesol, while PbI_2 was procured from TCI, and were used as such. 2,2',7,7'-tetrakis(N,N-di-p-methoxyphenyamine)-9,9-spirobifluorene (Spiro-OMeTAD) was acquired from Merck KGaA. Synthesis of 1-methyl-3-(1H,1H,2H,2H-tridecafluorooctyl)-imidazolium iodide was based on a modification of a literaturemethod.[27]

Device Fabrication

Pre-patterned laser etched FTO-coated glass (TEC15, Pilkington) was used to fabricate the perovskite solar cells. Initially, the substrates were cleaned using Hellmanex® solution and rinsed repeatedly with deionized water and ethanol. Following this, samples were ultrasonicated in acetone, rinsed using 2-propanol and dried by using compressed air. Compact layer of TiO_2 was then deposited on FTO glasses by spray pyrolysis at 450°Cfrom a precursor solution of titanium diisopropoxidebis(acetyl acetonate) (75% in 2-propanol, Sigma Aldrich) using dry air as a carrier gas. The TiO_2 blocking layer was then annealed for 30 minutes at 450 °C to acquire anatase phase. Once the samples

are cooled to room temperature, a TiO_2 mesoporous layer (Dyesol, 30NRD diluted 1:7) was deposited by spin coating (4000 rpm for 20 s) and were then annealed gradually at 450 °C. Subsequently a 1.4M mixed ($(FAPbI_3)_{0.85}(MAPbBr_3)_{0.15}$) layer was deposited, in a single step. The perovskite solution was spun coated at 1000 and 6000 rpm for 10 and 20s, respectively. During the second step, 100µL of chlorobenzene was dripped as an anti-solvent approach on the spinning substrate (over the last 15 s). The deposited layer was then annealed at 100°C for 1h in an argon filled glove box to form perovskite layer. For the triple cation based perovskite ($Cs_{0.05}(MA_{0.15}FA_{0.85})_{0.95}Pb(I_{0.85}Br_{0.15})_3$), CsI was separately dissolved (1.5 M stock solution in dimethyl sulfoxide (DMSO)), and added to the mixed perovskite precursor to achieve the desired composition (5%). Previously we have varied the Cs^+ content and found that 5% addition provided better efficiencies.[31]In the ($Cs_{0.05}(MA_{0.15}FA_{0.85})_{0.95}Pb(I_{0.85}Br_{0.15})_3$precursor solution FIm was added in different ratio (0.5 − 2%), and the solution was spun coated to yield FIm doped perovskite layers.

Once the perovskite layers were annealed and has acquired a dark color, the material was left to cool to room temperature (RT) and 35 µL of a Spiro-OMeTAD solution was then spun coated at 4000 rpm for 20 s. Spiro-OMeTAD (72.3 mg) was dissolved in 1 mL of chlorobenzeneusing additives: 17.5 µL of a lithium bis(trifluoromethylsulphonyl)imide (LiTFSI) stock solution (520 mg of LiTFSI in 1mL of acetonitrile), 21.9 µL of a FK209 (Tris(2-(1H-pyrazol-1-yl)-4-tert-butylpyridine)cobalt(III)Tris(bis(trifluoromethylsulfonyl)imide))) stock solution (400 mg in 1 mL of acetonitrile) and 28.8 µL of 4-tert-butylpyridine (*t-BP*). To complete the device, 80 nm of gold was deposited as the cathode layer by thermal evaporation under a vacuum, between 10^{-6}– 10^{-5}torr. All the solutions were prepared inside an argon filled glove box under controlled moisture and oxygen conditions (H_2O<1 ppm and O_2<10 ppm).

Characterization

The transmittance spectra of the perovskite films were collected using a Cary 60 spectrophotometer. Current density–voltage (*J–V*) curves were documented with a Keithley 2400 source-measurement-unit under AM 1.5 G, 100 mW cm^2 illumination from a 450 W AAA solar simulator (ORIEL, 94023 A). This was calibrated using a NREL certified calibrated mono-crystalline silicon solar cell. A black metal mask (0.16 cm^2) was used over the square solar cell active area (0.5 cm^2) to reduce the influence of scattered light.

Photovoltaic parameters including J_{sc}, V_{oc}, fill factor (*FF*), and power conversion efficiency (PCE) were extracted from the photocurrent-voltage (*J-V*) curves of the solar cells. The scan rate and the active area used for measuring the devices were optimized as such to calculate the real value for efficiencies without having hysteresis effect. (Active area: 0.16 cm^2, scan rate: 100mV/s). The IPCE measurements were performed using a Newport 150 W Xenon lamp coupled to an Oriel Cornerstone 260 motorized ¼ m monochromator as the light source, and a 2936-R power meter to measure the short circuit current. Electrochemical impedance spectroscopy (EIS) studies were made with the help of Bio-logic (SP-300), and were carried out under illumination of a white LED over a wide range of DC light intensities. Frequency response of the solar cells devices at different positions of the Fermi level, was fixed by the DC illumination intensity (open circuit voltage) to avoid voltage drop. A 20 mV perturbation step in the range 2 MHz – 1 mHz was used to obtain the spectra. Post measurements the data were fitted with the help of Z-view software in order to extract characteristic parameters of the devices.

For structural characterization, films were prepared by spin coating of solutions onto coarse glass. X-ray diffractograms were recorded on a Rigaku powder diffractometer using CuKα source. The measurements were performed in the Bragg-Brentano geometry. A scan range from 10°–60° was selected with an acquisition time of 1 degree/min. A baseline correction was applied to diffractograms to compensate for the noise arising from the substrate. Scanning electron microscopy (SEM) was performed with a high resolution FEG microscope HITACHI S4800 equipped with an EDX detector (Bruker X-Flash 4010). The perovskite layers grown on glass or silicon substrates were directly analyzed in top view. Cleaved samples were used for cross section studies of the complete device grown on glass substrate. Transmission electron microscopy (TEM) was performed in a Philips CM20 microscope operated at 200 kV and equipped with an EDX detector (Oxford Instruments X-Max80-SDD). The perovskite films grown on silicon were scratched from the substrate prior to the analysis (details in the results and discussion section).Conventional XPS measurements were taken on pelletized samples (c.a 100 mg) mounted on a stainless steel sample holder, after evacuation up to ultra-high vacuum ($P < 2\times10^{-9}$ mbar) at room temperature using a non-monochromatized dual X-ray source, with a hemispherical analyzer (SPECS PHOIBOS 100) working at fixed transmission mode and 50 eV pass energy resolution, with an energy step of ca. 0.1 eV. The binding energies were calibrated using internal references, such as the C1s (285.0eV). The energy calibration was necessary because surface charging occurred due to the emission of photoelectrons, although was always in the range of 1–3 eV.

Acknowledgements

MAF acknowledged financial support from the CSIC (PIE-201460E018). Authors thank the Laboratory of Nanoscopies and Spectroscopies LANE at the ICMS and M.C.Jiménez, I. Rosa and O. Montes for their support in electron microscopy measurements, Valentin M. Manzanares for preparing the fluorinated compound. We thank Juan A Anta and Jesus Idigoras for discussions.

Keywords: Perovskite•solar cells • ionic liquids• stability • impedance analysis

[1] L. Calió, S. Kazim, M. Grätzel, S. Ahmad, Angew. Chem. Int. Ed. **2016**, *55*, 14522-14545; Angew. Chem. 2016,*128*,14740-14764.
[2] A. Guerrero, J. You, C. Aranda, Y. S. Kang, G. Garcia-Belmonte, H. Zhou, J. Bisquert and Y. Yang, *ACS Nano* 2016, **10**, 218–224.
[3] T. A. Berhe, W.-N. Su, C.-H. Chen, C.-J. Pan, J.-H. Cheng, H.-M. Chen, M.-C. Tsai, L.-Y. Chen, A. A. Dubale, and B.-J. Hwang, *Energy Environ. Sci.***2016**, *9*, 323-356.
[4] G. E. Eperon, S. N. Habisreutinger, T. Leijtens, B. J. Bruijnaers, J. J. Van, R. A. J. Janssen, A. Petrozza, and H. J. Snaith, *ACS Nano***2015**,*9*, 9380–9393.
[5] Y. Rong, L. Liu, A. Mei, X. Li and H. Han, *Adv. Energy Mater.***2015**, *5*, 15011066.
[6] G. P. Nagabhushana, R. Shivaramaiah, and A. Navrotsky, *Proc. Natl. Acad. Sci.***2016**,*113*, 7717–7721,
[7] A. Mei, X. Li, L. Liu, Z. Ku, T. Liu, Y. Rong, M. M. Xu, M. Hu, J. Chen, Y. Yang, M. Grätzel, H. Han, M. Grätzel and H. Han, *Science* **2014**, *345*, 295–298.
[8] X. Xu, Z. Liu, Z. Zuo, M. Zhang, Z. Zhao, Y. Shen, H. Zhou, Q. Chen, Y. Yang and M. Wang, *Nano Lett.***2015**,*15*, 2402–2408.
[9] W. Yu, F. Li, H. Wang, E. Alarousu, Y. Chen, B. Lin, L. Wang, M. N. Hedhili, Y. Li, K. Wu, X. Wang, O. F. Mohammed and T. T. Wu, *Nanoscale***2016**,*8*, 6173–6179,.
[10] C. Zuo and L. Ding, *Small***2015**, *41*, 5528–5532.
[11] T. Leijtens, T. Giovenzana, S. N. Habisreutinger, J. S. Tinkham, N. K. Noel, B. A. Kamino, G. Sadoughi, A. Sellingerand H. J. Snaith, *ACS Appl. Mater. Interfaces***2016**, *8*, 5981–5989.

[12] S. Guarnera, A. Abate, W. Zhang, J. M. Foster, G. Richardson, A. Petrozza and H. J. Snaith, *J. Phys. Chem. Lett.***2015**, *6*, 432–437.
[13] P. Luo, Z. Liu, W. Xia, C. Yuan, J. Cheng and Y. Lu, *ACS Appl. Mater. Interfaces***2015**,*7*, 2708–2714.
[14] S. N. Raja, Y. Bekenstein, M. A. Koc, S. Fischer, D. Zhang, L. Lin, R. O. Ritchie, P. Yang and P. Alivisatos, *ACS Appl. Mater. Interfaces***2016**, *8*, 35523-35533.
[15] Q. Jiang, D. Rebollar, J. Gong, E. L. Piacentino, C. Zheng and T. Xu *Angew. Chemie - Int. Ed.***2015**, 54, 7617–7620.
[16] A. Buin, R. Comin, J. Xu, A. H. Ip and E. H. Sargent, *Chem. Mater.***2015**, *27*, 4405–4412.
[17] M. Kulbak, S. Gupta, N. Kedem, I. Levine, T. Bendikov, G. Hodes and D. Cahen, *J. Phys. Chem. Lett.***2016**, *7*, 7167–172.
[18] M. Saliba, T. Matsui, J.-Y. Seo, K. Domanski, J.-P. Correa-Baena, M. K. Nazeeruddin, S. M. Zakeeruddin, W. Tress, *Energy Environ. Sci.***2016**, *9*, 1989–1997.
[19] R. E. Beal, D. J. Slotcavage, T. Leijtens, A. R. Bowring, R. A. Belisle, W. H. Nguyen, G. Burkhard, E. T. Hoke and M. D. McGehee, *J. Phys. Chem. Lett.***2016**, *7*, 746–751.
[20] H. Choi, J. Jeong, H. B. Kim, S. Kim, B. Walker, G. H. Kim, and J. Y. Kim, *Nano Energy***2014**, *7*, 80–85.
[21] Q. Wu, W. Zhou, Q. Liu, P. Zhou, T. Chen, Y. Lu, Q. Qiao, S. Yang, ACS Appl. Mater. Interfaces **2016**, *8*, 34464–34473.
[22] J.-Y. Seo, T. Matsui, J. Luo, J.-P. Correa-Baena, F. Giordano, M. Saliba, K. Schenk, A. Ummadisingu, K. Domanski, M. Hadadian, et al., Adv. Energy Mater. **2016**, *6*, 1600767.
[23] F. Bella, G. Griffini, J.-P. Correa-Baena, G. Saracco, M. Grätzel, A. Hagfeldt, S. Turri, and C. Gerbaldi, *Science***2016**, *354*, 203-206.
[24] M. Salado, F. J. Ramos, V. M. Manzanares, P. Gao, M. K. Nazeeruddin, P. J. Dyson and S. Ahmad, *ChemSusChem***2016**, *18*, 2708-2714.
[25] P. Gratia, G. Grancini, J.-N. Audinot, X. Jeanbourquin, E. Mosconi, I. Zimmermann, D. Dowsett, Y. Lee, M. Grätzel, F. De Angelis, K. Sivula, T. Wirtz and M. K. Nazeeruddin, *J. Am. Chem. Soc.***2016**, *18*, 27158-27164.
[26] H.-S. Kim, I. Mora-Sero, V. Gonzalez-Pedro, F. Fabregat-Santiago, E. J. Juarez-Perez, N.-G. Park, and J. Bisquert, *Nat. Commun.***2013**, *4*, 2242.
[27] O. Almora, I. Zarazua, E. Mas-Marza, I. Mora-Sero, J. Bisquert and G. Garcia-Belmonte, *J. Phys. Chem. Lett.***2015**, *6*, 1645–1652.
[28] I. Zarazua, J. Bisquert and G. Garcia-Belmonte, *J. Phys. Chem. Lett.***2016**, *7*, 525–528.
[29] N. Aristidou, C. Eames, I.S.-Molina, X. Bu, J. Kosco, M. S. Islam, S. A. Haque, *Nat. Commun.***2017,** *8*, 15218
[30] X. Zheng, B. Chen, J. Dai, Y. Fang, Y. Bai, Y. Lin, H. Wei, X. C. Zeng and J. Huang, Nat. Energy **2017**, *2*, 17102.
[31] M. Deepa, M. Salado, L. Calio, S. Kazim, S. M. Shivaprasad, and S. Ahmad, *Phys. Chem. Chem. Phys.***2017**,*19*, 4069–4077.

Entry for the Table of Contents

FULL PAPER

Homoeopathic addition of fluorous cation into triple cation based perovskite to increase the stability of solar cells.

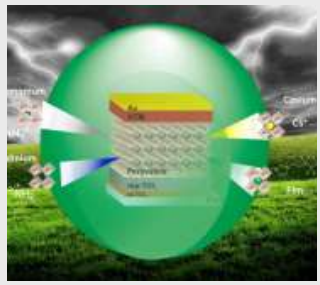

*M. Salado, M. A. Fernández, J. P. Holgado, S. Kazim, M. K.Nazeeruddin, P. J. Dyson, S. Ahmad**

Page No. – Page No.

Towards extending solar cells life time: addition of a fluorous cation to triple-cation based perovskite films.

Part VI
Discussion and general conclusions

5 Discussion and general conclusions

Chapter 1:

"Study of the effect in the selective contacts in the charge extraction process"

In Publication 1, we studied the influence of the hole transport layer on the final performance of devices. Microscopy and spectroscopy techniques were used to unravel the possible charge accumulation at interface due to a poor charge extraction. Our main conclusions are:

1 The quality of the interface (molecular interaction) between the perovskite and the hole selective contact has a profound effect on the photovoltaic performance, in terms of better hole extraction and lower recombination.

2 The nature of the hole transport material (polymer or small molecules) strongly affects the interface with the perovskite. Small perturbation-based optoelectronic and electrochemical measurements reveal that the HTMs that yield a higher open circuit voltage and low hysteresis values have a larger recombination resistance.

3 Among the investigated high-performance and stable HTMs, 2,2´,7,7´-tetrakis(N,N-di-p-methoxyphenylamine)-9,9´-spirobifluorene(Spiro-OMeTAD) and 5,10,15-trihexyl-3,8,13-tris(4-methoxyphenyl)- 10,15- dihydro-5H- diindolo [3,2a : 3´,2c] carbazole(HMPDI) were found to be of significant interest for future perovskite solar cells technology.

In Publication 2, we studied the effect of different electron transport layers morphology in terms of charge extraction and stability. In this work, we compare 3-dimensional mesoporous TiO_2 and 1-dimensional nanoforest like structures of TiO_2 with various lengths where the perovskite solution was infiltrated. Our principal conclusions are:

1 Porous and homogeneous 1-D TiO_2 thin films were fabricated through facile and industrially scalable method with competitive power conversion efficiencies.

2 When 1-D TiO_2 nanoforest structure is employed, the improvement in photovoltaic performance lies in their efficient charge collection/extraction as supported by the impedance spectroscopy. Besides, when these nanoforest having 200 nm lengths are used, less hysteresis and interfacial charge accumulation is achieved, therefore improved efficiency was obtained.

3 Ageing tests carried out on unsealed devices suggests improved stability of these 1D-TiO_2 as compared to 3-dimensional mesoporous structures.

Chapter 2:
"Modification of perovskite composition towards efficient and stable solar cells"

In Publication 3, phase behaviour of mixed A-site cations methylammonium (MA)/formamidinium (FA) were studied with the aim to improve stability and improved optical properties. Our main conclusions are:

1 The addition of the formamidinium cation in the MAI lattice slows down the crystal formation in perovskites and allows the formation of large crystals and a high degree of order.

2 X-Ray and absorption measurements reveal lattice parameters and optical band gap modification when the bigger organic cation was added.

3 The addition of 15–40% FAI in MAI was found to influence the PV performance and dramatically reduced the hysteresis behaviour. $MA_{0.6}FA_{0.4}PbI_3$ (40% FAI) was found to be the best composition, in terms of device performance and less hysteresis effect.

4 The presence of the smaller MA cation in mixed perovskite with FA improves stability even in high humidity conditions, which could be attributed to ten times higher dipole moment of the small sized MA cation than FA.

5 The addition of >50% FAI entails the emergence of δ-phase of formamidinium perovskite mainly due to the difficulty to annealed the samples at the optimum temperature.

In Publication 4, triple cation based perovskite solar cells were fabricated in order to unravel the role of cesium cation in the charge generation process. Two different techniques were employed (kelvin probe force microscopy (KPFM) and electrochemical impedance spectroscopy (EIS)) to analyse the perovskite films. The main conclusions are given below:

1 When we employ the KPFM techniques, it was observed that after the inclusion of 5% Cs cation, the photocurrents are further improved, and have a more uniform delocalized distribution across the surface.

2 In addition, the incorporation of Cs cation increases the contact potential difference (CPD) between the tip and sample at nanometer scale, this CPD further increases when Spiro-OMeTAD was used as a hole transport material.

3 EIS demonstrates that presence of triple cations reduces carrier recombination at the TiO_2 /perovskite interface, which in turn allow achieving higher V_{OC} value.

Chapter 3:

"Study of perovskite selective degradation mechanism under high humidity conditions"

In Publication 5, we studied morphological and charge dynamics changes when samples were exposed to humidity. Different perovskite composition as well as various hole transport materials were used to unravel how the device is affected under unfavourable conditions. Our central conclusions are given below:

1 $Cs_{0.05}(MAPbBr_3)_{0.15}(FAPbI_3)_{0.85}$ perovskite as the active layer and poly(3-hexyl thiophene)P3HT as the HTM presented low degradation rate. However, the effect of the moisture-induced degradation on the electronic processes determines the photovoltaic performance of perovskite solar cells.

2 Although polymeric nature of HTM showed higher humidity resistance, but the interfacial charge accumulation induced fast device degradation.

3 Therefore, after moisture-induced degradation, recombination process changed from a trap-limited mechanism to the surface-mediated recombination, possibly due to an interfacial charge accumulation when crystal structure is affected by degradation.

Chapter 4:
"Improving the stability of the devices"

In Publication 6, a complete study was carried out when ionic liquid such as1-methyl-3-(1H,1H,2H,2H nonafluorohexyl)-imidazolium iodide *(FIm)* or 1-methy-3-butyl-imidazolium iodide *(BMIm)* were added in order to enhance final device stability. A diversity of perovskite composition and deposition methods was compared. Our central conclusions are following:

1 Between pure $MAPbI_3$ or mixed $(FAPbI_3)_{0.85}(MAPbBr_3)_{0.15}$ perovskite and sequential or one-step with anti-solvent deposition method, it was found that mixed perovskite and one-step with anti-solvent deposition method presented higher efficiencies as well as better stability when dopants were added.

2 Remarkable perovskite film stability over 100 days was achieved when only 1% *FIm* dopant was added. On the opposite, higher loads (e.g 5%) presented star-like coverage which provokes detrimental effects in devices as fast degradation and low efficiencies.

In Publication 7, a complex triple cation based (Cs/MA/FA) perovskite was fabricated. New perovskite composition in a one-step deposition process utilizing anti-solvent method was used. It strongly improves the opto-electronic properties of the devices. Moreover, a perfluorinated dopant (FIm) was added in order to enhance moisture stability. We found that:

1 The addition of cesium (Cs) cation in the mixed perovskite environment entails an improvement in thermal stability together with higher power conversion efficiencies

2 A low amount of *FIm* was found to be sufficient to obtain stable devices, which helps to keep the crystal structure intact over >100 days, possibly by acting as a hydrophobic barrier.

3 Higher *FIm* load involves a possible interaction (due to its bigger size) with the TiO_2 interface, inducing charge accumulation and therefore higher hysteresis index values.

Part VII
Other publications

In this part, other publications related with my work are presented although they must not be understood as a part of this thesis as a compendium of publications.

6 Other publications

Publication 8

"Origin and Whereabouts of Recombination in Perovskite Solar Cells"

Lidia Contreras-Bernal, Manuel Salado, Anna Todinova, Laura Calio, Shahzada Ahmad, Jesús Idígoras, and Juan A. Anta. The Journal of Physical Chemistry C 2017 121 (18), 9705-9713

http://dx.doi.org/10.1021/acs.jpcc.7b01206

Publication 9

"Performance and stability of mixed $FAPbI_{3(0.85)}MAPbBr_{3(0.15)}$ halide perovskite solar cells under outdoor conditions and the effect of low light irradiation"

Yegraf Reyna*, Manuel Salado*, Samrana Kazim, Amador Pérez-Tomasa, Shahzada Ahmad, Monica Lira-Cantua. Nano Energy 30 (2016) 570–579. (*equal contribution)

http://dx.doi.org/10.1016/j.nanoen.2016.10.053

Publication 10

"Specific cation interactions as the cause of slow dynamics and hysteresis in dye and perovskite solar cells: a small-perturbation study "

Lidia Contreras, Jesús Idígoras, Anna Todinova, Manuel Salado, Samrana Kazim, Shahzada Ahmad and Juan A. Anta. Phys.Chem.Chem.Phys., 2016, 18, 31033

http://dx.doi.org/10.1039/C6CP05851E

Publication 11

"Universal Features of Electron Dynamics in Solar Cells with TiO_2 Contact: From Dye Solar Cells to Perovskite Solar Cells"

Anna Todinova, Jesús Idígoras, Manuel Salado, Samrana Kazim, and Juan A. Anta. The Journal of Physical Chemistry Letters 2015 6 (19), 3923-3930

http://dx.doi.org/10.1021/acs.jpclett.5b01696

Publication 12

"Unraveling Charge Carriers Generation, Diffusion, and Recombination in Formamidinium Lead Triiodide Perovskite Polycrystalline Thin Film"

Piotr Piatkowski, Boiko Cohen, Carlito S. Ponseca, Jr., Manuel Salado, Samrana Kazim, Shahzada Ahmad, Villy Sundström, and Abderrazzak Douhal. The Journal of Physical Chemistry Letters 2016 7 (1), 204-210

http://dx.doi.org/10.1021/acs.jpclett.5b02648

Publication 13

"Towards a Universal Approach for the Analysis of Impedance Spectra of Perovskite Solar Cells: Equivalent Circuits and Empirical Analysis"

Anna Todinova, Lidia Contreras-Bernal, Manuel Salado, Shahzada Ahmad, Neftalí Morillo, Jesús Idígoras, and Juan Juan A. Anta. ChemElectroChem 2017, 4, 1–12

https://doi.org/10.1002/celc.201700498

Publication 14

"Cesium power: low Cs^+ levels impart stability to perovskite solar cells"

Deepa, M., Salado, M., Calio, L., Kazim, S. Shivaprasad, S. M., and Ahmad, S. (2017). Physical chemistry chemical physics: PCCP, 19(5), 4069.

https://doi.org/ 10.1039/c6cp08022g